DATE DUE	DATE DUE	DATE DUE

MICRO-SCALE *IN VIVO* IMAGING OF FREEZE INJURY IN TISSUES

By

Gloria D. Elliott

A DISSERTATION

Submitted to
Michigan State University
in partial fulfillment of the requirements
for the degree of

DOCTOR OF PHILOSOPHY

Department of Mechanical Engineering

2002

ABSTRACT

MICRO-SCALE *IN VIVO* IMAGING OF FREEZING IN TISSUES

By

Gloria D. Elliott

Cryosurgery is the use of localized freezing to kill undesirable tissue. Although rapid freezing rates are known to create intracellular ice, a phenomenon that correlates highly with cell death, the effects of slow freezing rates and high sub-zero temperatures that characterize the edge of a cryo-lesion are not well understood. Understanding the relationship between thermal history and physiological response in tissues relies on the ability to generate quantitative measures of each.

A novel Green Fluorescent Protein (GFP) transfection based viability assay was developed that allowed the continuous *in vivo* evaluation of injury in the cryo-treated tissue. GFP produced by the transfected cell was found to leak from damaged cells but was retained in living cells. Viability results with this new assay correlated highly with other static indicators of death. A radial mass diffusion and dilution mathematical model was found to adequately explain the transient changes in GFP fluorescence intensity observed following death of cells in suspension and within tissues.

Obtaining accurate thermal measurements within small cryo-lesions is very challenging. Typically only a few thermocouples can be used, and these are prone to fin effects and placement error. To create a cryo-lesion that was thermally well characterized, a novel annular freeze apparatus was developed that minimized the spatial temperature gradients. This device uniformly freezes tissue within a rat skin flap

chamber while allowing optical access to the tissue before, during, and after treatment. Meticulous thermocouple measurements were acquired in phantom tissues and *in vivo*, and results were also compared to a numerical simulation to validate the uniformity of the field.

These new technologies were brought together to investigate the effect of high sub-zero temperatures and slow cooling rates on both the microvasculature and tumor cell viability in a living rodent. The microvasculature was severely disrupted immediately after freezing, evidenced by vessel dilation, hemorrhage, and stasis. The cells survived the freezing, but died several hours after the treatment. These results provide the first direct evidence that cells *in vivo* are not dying immediately after the initial freezing insult, thus implicating the role of secondary effects and possibly solute injury in creating the ultimate cryo-lesion.

To my nephews Cody and Jonathon, for being a

welcomed distraction when I needed to empty my head, and

a motivating influence when I needed to fill it

I

of many

John J. M

and also

my guidan

enabled w

and encou

A

research ef

Hamm, S

Knowing

Black Dam

Six Project

creating an

blacks are

has also be

A m

Supplies, rese

Opportunity

Especially th

Grateful for

ACKNOWLEDGEMENTS

This work could not have been completed without the support and participation of many outstanding individuals. First and foremost I would like to thank my supervisor, John J. McGrath, for his patience and support throughout the duration of my program, and also for setting the bar high and encouraging me to reach for it. I'd also like to thank my guidance committee for their willingness to learn a new 'language' as engineering collided with science in this multi-disciplinary dissertation. Their constructive criticism and encouragement during difficult phases of the research helped me to stay the path.

A number of undergraduate students made many significant contributions to this research effort. I'd like to thank Mandy Miller, Jill Brunner, Maureen Galloway, Sarah Harbin, Suzy Smith, and Diane Doeing for the many long hours they spent collecting or processing data, or in supporting the efforts that first got us to that point. I'd also like to thank Damien Fron, Noelle Frerichs, and Cathy Peltz for their significant involvement in this project. Through their various independent study projects, they were instrumental in creating and developing the cryosurgical probe technology used in this work. Many thanks are due my lab colleagues Al Aksan and Paul Hoke. The many conversations we had about both personal and professional goals were both motivating and inspiring.

A major component of this work was made possible by the generous provision of supplies, research equipment, and lab space by Dr. Elahe Crockett. I've appreciated this opportunity to conduct a major proportion of my work in a surgical environment, but I'm especially thankful for the friendship that developed out of this relationship. I'm also grateful for the opportunity to work with Crystal Remelius. Her willingness to share her

expertise and experience with cell culture and small animal surgical procedures provided me with the skills and guidance I needed to complete this work.

For the many delightful meals and the wonderful company after long days in the lab, I'd like to thank Allan and Colleen. We ate like kings and queens at your house and created many memories that I will always remember as an integral part of my days at MSU.

To my husband Rob, thank you for marrying me amidst the madness of writing this dissertation and conducting those 'last' experiments. Your patience knows no end.

LIST OF

LIST OF

TABLE OF CONTENTS

LIST OF TABLES

LIST OF FIGURES

Figure 5.3
ether than roo
outer jacket of
flasked throug

Figure 5.4
the mean .....

Figure 5.5
model .....

Figure 5.6
odel. Samp
were exclude

Figure 5.7
triangles ar
olution at 2

Figure 5.8
Error bars ar

Figure 5.9
stimate par
n independ
esults are c
roviding a

Figure 5.10
function of
curve. The

Figure 5.11
are indicate

Figure 6.1
temperature
obtain. an
corresponde
N GLP g
average of

Figure 6.2
relationships
function by

Figure 6.3
RCSMAC cells
assessed by Try

Figure 6.4
to 1.6M and 2.

Figure 6.5
cells were hel
conditions. (b
room temper
gas phase con
microscopy.....

Figure 6.6
synthesis inhi
incubated wi
incubated gro
cell boundar

Figure 6.7
ines to the p
D-MEM m

Figure 6.8
Illuminated w
camera. 0.1 s

Figure 6.9
apillary tube

Figure 6.10
gas length, (
gas point m

Figure 6.11
Rows of 4x
impermeable
treated soil
standard err
interval t-

Figure 6.
mi ec ula

Figure 6.
determin

Figure 6.
lowing

Figure 6.
freeze-thi
the measu
error bars
the uncer

Figure 7.
Mark Dev

Figure 7.
Fischer 3-

Figure 7.
story in t
3-b, and

Figure 7.
chamber a
is the sam

Figure 7.
animal stu
sections w
were obta

Figure 7.

Figure 7.
liquid nitr
in

Figure 7.

Figure 7.
maximum

Figure 7.
the phanto

Figure 7.
function c
region ind
and treate

Figure 7.
fluorescer
(b and 6)
demarcate

Figure 7.
tumor afte
b. Dama

Figure 7.
tumor afte
(b) Dama
normal tur

Figure 7.
tumor after
the tissue

Figure 7.
Surrounding
cells are ev
remnants

Figure 7.
near the ed

Figure 7.
arrows).

Figure 7.
diameter
results (app
the case o

Figure 8.
the stainle
ports. A g
DSFC. (b
protruding

Figure 8.2
(AFA). Th
inset diag
and mainta

Figure 8.3

Figure 8.4
an diamet
thermocou

Figure 8.5
material wi
and T, the
of the soli

Figure 8.6

Figure 8.7
material in
boundary c
given by X

Figure 8.8
solidificatio

Figure 8.9
tissue in the
dark dotted

Figure 8.10

Figure 8.11
water used

Figure 8.12
as simulated

Figure 8.
geometry
temperat

Figure 8.
DSFC gl

Figure 9.
Regions
close to t
experien
change te

Figure 9.
from Ma

Figure 9.

Figure 9.
a single t
thermoco
temperat

Figure 9.

Figure 9.
95 are p
the locat

Figure 9
in contac
freezing

Figure 9
to the st
animal d
three an
deviation

Figure 9
located

Figure 9
loss of c

Figure 9.11
chamber. sh
(a) Transver
(b) Fibroblas

Figure 9.12
to -18 °C. (a
nuclei, narrow
necrosis. (b)
severely hem

1.1 M

L

as vast a

ities o

ent ener

temperat

determin

between

Dependin

he materi

ominate

Th

natural u

ints the

Chapter 1

Introduction

1.1 Motivation for the Research

Low temperature injury to bio-materials has wide-reaching significance in arenas as vast as maintaining ecological diversity to preventing death by cancer. Although injuries of this nature have been studied for some decades, there remains considerable ambiguity as to the mechanisms by which these injuries occur (Rubinsky, 1991). As the temperature of a biological material is lowered, the effect can be preserving or deleterious. These conflicting manifestations are the product of an intricate interaction between thermal, chemical, electrical, and mechanical forces (McGrath, 1993). Depending on the degree of cooling, the final end temperature reached, and rate at which the material is cooled, stored, and warmed, different injury or preservation mechanisms dominate.

The primary goal in a cryosurgical process is to use localized freezing to achieve maximal tumor destruction, without injury to healthy tissue. The current state of the art limits the optimization of existing cryosurgical devices and processes as well as the

develop

other ap

thawing

fundam

whether

the dan

injury

contrib

immun

are no

Scient

of dan

cancer

decrea

design

assay

Identif

Prom

Scient

Socio

Pr

Impa

development of new devices and procedures that could extend the use of cryosurgery to other applications. The limiting factor is that the mechanisms by which the freezing and thawing kill the cancerous tissue are not well understood (Bischof *et al.*, 1993, 1997). A fundamental understanding of the response of tissue to freezing and thawing is lacking whether the tissue is normal or neoplastic. To develop a comprehensive understanding of the damage inflicted by cryosurgery, it is necessary to understand the direct cellular injury caused by the decreased temperature and the formation of ice, and also the contribution of secondary effects such as cell-mediated inflammatory response, host immune response, and vascular damage to the overall injury. The mechanisms of injury are not well understood primarily because the tools to easily delineate direct kill and ischemia and inflammatory effects do not exist. As well, understanding the time course of damage is difficult and requires the sacrifice of many animals. This lack of understanding means that sub-optimal results are obtained from procedures designed to destroy tumors by freezing (cryosurgery) or, conversely, the development of protocols designed to preserve tissues and organs for storage. Development of a non-toxic viability assay that can provide information about the vital state of a tissue over time, without sacrifice of the animal, can significantly improve experimental efficiency as well as provide continuous viability information that can begin to uncouple direct injury from secondary effects.

Understanding the thermal history that gives rise to the freeze injury is also a fundamental aspect of what will hereafter be generally referred to as 'the cryosurgery problem'. Quantifying the thermal history eliciting the particular tissue response is an important and non-trivial task. For example, Bischof *et al.*, 1997, predicted that the

density

range

surface

temper

the spa

history

can be

questio

gradien

only be

In addi

Thermo

Introdu

a thorm

Mathem

Resear

Mathem

Mathem

Mathem

Thermo

Navigat

Lecture

Practice

cooling rates in biological tissue treated with a 3-mm liquid nitrogen-cooled probe would range from >1000 °C/min to 5 °C/min, with temperatures ranging from –196° C at the surface of the cryosurgical probe to ~0 °C at the edge of the ice ball. These extremes of temperature and freezing rates are manifested in an ice ball of order 1 cm. To understand the spatial variation in cell death that occurs in cryosurgically-treated tissue, the thermal history must be understood throughout the cryo-lesion. Although discrete thermocouples can be used to record local temperatures, the accuracy of the measurements are somewhat questionable due to inherent difficulties in acquiring measurements in steep spatial gradients of temperature that are rapidly changing in time. Thermal field information can only be obtained by interpolating between these discrete measurements and/or theoretical modeling. Not only is this temperature field estimation challenging due to tissue inhomogeneities and a lack of reliable thermal property data, but the warming effect of circulating blood, as well as metabolic heat generation must be considered when freezing a biomaterial *in situ*. This results in complicated governing equations, limiting most mathematical models of biological freezing to numerical solutions. Optimizing the measurement of temperature in biological materials and/or developing suitable mathematical models are thus important complementary aspects of creating technologies to improve the understanding of thermal history-viability functional relationships.

The cryosurgery problem presented here represents a sub-class of bio-heat problems in which the primary objectives are to quantify a transient temperature field in a biological material and understand the associated biophysical response. Thus, developing technologies to address challenges of this nature in the cryosurgery problem will have positive implications for other bio-heat transfer problems as well.

1.2 Intra-vital Microscopy

Just as the march of engineering technology of recent decades has been towards smaller, better, and faster, so has medical treatment and sensing progressed from gross anatomical assessment to the scale of sub-cellular structures. Disease is treated at the genetic level and molecular imaging is providing us with unprecedented information about the molecules that comprise our tissues and organs. The bulk of biomedical research addresses in some way the impaired transport of molecules or loss of cellular control. Consequently, engineering tools developed to study disease are geared towards micro-scale cellular sensing, imaging, or manipulation.

Intra-vital preparations are becoming exceedingly popular as a tool to understand cellular injury, dysfunction, and repair. The complex interplay of inflammation and direct cell injury following ischemia-reperfusion has been studied using intravital microscopy in rodent models for direct visualization of cellular and tissue response by way of neutrophil infiltration and vessel leakage of fluorescently-labeled macromolecules (Schuder *et al.*, 1999). Trans-illuminated tissue model systems such as the dorsal skin flap chamber (DSFC), hamster cheek pouch, and rabbit ear preparations have been used effectively for many types of studies. Such systems provide direct, in vivo optical access to tissue and vasculature. These intra-vital approaches have been utilized to understand the extravasation of chemotherapy drugs (Gaber *et al.*, 1996), micro-vascular permeability (Yuan *et al.*, 1993), angiogenesis (Li *et al.*, 2000), and vascular injury following burn injury (Aggarwal *et al.*, 1989), laser treatment (Gourgouliatos *et al.*, 1991), cryosurgery (Hoffman and Bischof, 2001ab), and radiation (Wu *et al.*, 1994). However, the single feature missing from all of these studies was the ability to monitor cell death *dynamically*

in the same animal. Independent of the observation period for the phenomena under investigation, cell death could only be established at a single end point in a given animal, either by delivery of a vital dye and subsequent termination, or by termination and biopsy for standard pathological analysis.

Because of the preponderance of intra-vital preparations and techniques currently being utilized to study a range of tissue injury phenomena, and also because of the immediate impact that a new intra-vital continuous viability assay could have in these systems, the *in vivo* model used in this work will implement the dorsal skin flap chamber.

1.3 Viability Assays

Evaluation of the viability of individual cells, as well as cells within tissues and organs after freezing is of fundamental importance for cryopreservation and cryosurgery research. Although cryopreservation seeks to sustain cell and tissue viability and conversely, cryosurgery seeks to devitalize neoplastic tissue, both rely on some measurable function of viability to determine protocol success. Measuring viability is a difficult task whether single cells or tissues are under consideration, partly because viability is often poorly defined and can be associated with many different aspects of the cell or tissue (Pegg, 1989). These aspects include morphology, cell attachment, motility, chemotaxis, fertilization capacity, membrane integrity, enzyme activity, protein synthesis, metabolism, reproduction, etc. Although there is no universally agreed upon definition for viability that suits all contexts, and perhaps none possible, the convention adopted by Pegg (1989) is embraced in this work. That is, viability can be considered "the ability of a treated sample to exhibit a specific function or functions, expressed as a

proportion

identical fr

of the cell

cell membr

limited nur

none that p

In t

dyes and th

targeting dy

is that app

small tissue

histopathol

the cellular

organization

infectious s

incubation

detected in

is a dynam

days, with

To

intervention

necessary.

per group

proportion of the same function exhibited by the same sample before treatment, or an identical fresh untreated sample". There exist a number of assays that evaluate functions of the cell, such as metabolic activity (e.g., MTT, Alamar Blue), and others that indicate cell membrane integrity (e.g., Ethidium Bromide, Trypan Blue). However, there are a limited number of assays available for determining tissue viability, especially *in situ*, and none that provide continuous dynamic measurements.

In the case of single cells it is relatively easy to add substrates such as fluorescent dyes and these often correlate well with other accepted measures of viability. In contrast, targeting dyes and substrates for tissue viability applications is difficult. A major problem is that application of the dye or substrate is often diffusion-limited even for seemingly small tissue sizes. The current gold standard for evaluating tissue injury is histopathology. This biopsy and stain approach provides very detailed information about the cellular characteristics of the injury (vacuolization, membrane disruption, nuclear coagulation, vascular congestion, etc.) but the information is static, and represents the injurious state of the tissue only at the time of biopsy. Moreover, there is a significant incubation time following injury before the damage progresses to an extent that it can be detected in histopathology specimens using standard light microscopy evaluation. Injury is a dynamic phenomenon occurring immediately after the insult, and progressing for days, with tissue remodeling continuing for weeks and months.

To understand the dynamics of this tissue injury, as well as when other interventions can accelerate or ameliorate its progression, the sacrifice of many animals is necessary. Because of variation from animal to animal, the number of animals included per group needs to be large to ensure statistical significance. To provide comprehensive

information about injury progression requires experimental groups that span the range of the phenomenon in small increments of time. This can translate into hundreds, and perhaps even thousands of animals to effectively understand the development of the injury. The consequence is either interpolation between discrete static measures or else exorbitant research costs. The latter case is especially so with the current trends toward utilization of 'knock-out' or transgenic animal models, with a cost per animal as much as 5-50 times that of the wild-type. The histological processing of tissues may also introduce artifacts and it is often difficult to correlate the processed tissue in space and time with other phenomena of interest that were applied to or occurred within the tissue.

Intra-vital dyes used in conjunction with microscopy, without fixation, are now the state of the art for dynamic viability imaging (Schuder *et al.*, 1999; Wanner *et al.*, 1999). However, the techniques for dye perfusion and observation are invasive and the dyes can be toxic, consequently requiring termination of the host before recovery from anesthesia. This restricts the duration of dynamic evaluation to experiments that can be completed within a single anesthesia period. These *in situ* assays do not permit dynamic and long-term evaluation of viability.

To date, most of the studies attempting to address the morphological, biophysical, and thermal response of mammalian tissues to freezing have been done using tissue slices or cell monolayers and suspensions. It is well known however, that models based on parameters derived from these in vitro studies under-predict the extent of damage that occurs in an actual cryosurgery (Bischof, 1997). It has been suggested that this differential is due to a vascular mechanism of injury, yet the nature of the injury has not been well-characterized due to a lack of adequate *in vivo* assays. Conventional

fluorophores and chromophores are inserted into cells using microporation techniques or via passive transport by incubation of cells in culture containing the probe. Although, tissues can be suffused with assay solution, often the result is toxic to the tissue, and there is difficulty with close-packed cells (Muldrew, 1994). Moreover it becomes difficult to distinguish tumor and healthy tissue margins. A different class of fluorescent biomarkers, called Green Fluorescent Proteins (GFP) may be able to furnish this very necessary tissue assay.

The assay proposed in this work does not require staining or fixation of the tissue to indicate viability, but relies on the expression and retention of an intracellular protein, GFP, produced by a transfected cell. Because the fluorescent compound is produced intracellularly, there is no requirement for electroporation techniques or diffusion (passive or active) to insert the probe into the cell. Moreover, no exogenous substrate is required to produce the fluorescence. The cells can be assayed without altering the system in any way, other than illuminating with light of the proper excitation wavelength. This allows continuous, real-time, non-destructive evaluation of GFP fluorescence when optical access is possible. These features may provide the basis for a powerful tissue viability assay as well as an assay for isolated cells. Because the introduction of dyes is not required, limitations associated with diffusion of dyes are superceded. Moreover biopsy is not necessary to assess viability. The GFP fluorescence may be assessed in real-time, in a living host, without sacrificing the animal, allowing the study of host-mediated effects on the protocol of interest. This would also permit chronic and long-term studies on the same animal or system.

A

he relev

proposed

inserting

protein.

1.4 S

B

problem

vital im

was cho

on seve

regions

techniq

assay ca

been p

charac

therma

cytosol

1.4.1

Although GFP has been shown to be non-toxic to cells, toxicity to an animal may be relevant in a system where GFP can be released from cells, as in the case of the proposed system. The fact that GFP mice and GFP bunnies have been produced by inserting GFP into embryonic cells suggests that organisms can be very tolerant of this protein. This aspect of toxicity will be discussed in further detail in Chapter 4.

1.4 State of the Art in Cryosurgical Research

Because the proposed research has been motivated by a class of bio-heat transfer problems that are large in scope, to provide comprehensive validation for the new intra-vital imaging techniques and yet ensuring a tractable problem, the cryosurgery problem was chosen. The injury phenomena associated with cryosurgery are complex and occur on several time scales and there are ambiguities about the nature of injury in certain regions of the cryo-treated tissue. These features will serve to illustrate the power of the technology developed in this work. It is believed that a GFP-based intra-vital viability assay can provide new information about the cryosurgery problem that has not previously been possible. Because the GFP intra-vital technology will be developed and characterized in the context of low temperature injury with specific attention to the thermal conditions of relevance to cryosurgery, a review of the state-of- the-art in cryosurgery research is warranted.

1.4.1 Historical Perspective

The use of low temperatures to treat pathological conditions dates back to the 1850's when iced saline solutions (-18 to -20 °C) were used to irrigate cancers of the

breast and

advent of

liquefied

now poss

of topical

White, 18

al., 1985

then rem

technolog

body, in

probe an

resulted

(

the brai

Breast e

clinical

incision

but pos

undesir

pleasin

alternat

recurre

require

breast and cervix, primarily for palliative purposes (Gage, 1992; Bird, 1949). With the advent of liquefied gases came the ability to apply much colder temperatures (e.g. liquefied N_2, -196 °C). Thus, freezing at faster rates and to much lower temperatures was now possible in the tissue. As a direct result of this innovation, successful cryosurgeries of topical cancers, primarily dermal and opthamalgic, were reported (Gage, 1992, 1998; White, 1899). In the mid-80's breast cancer cryolumpectomies were performed (Rand *et al.*, 1985, 1987) wherein the tumorous mass was first frozen through an open wound and then removed as in a normal resection procedure. Later, with advances in imaging technology (Hong *et al.*, 1994; Gilbert *et al.*, 1997), cryosurgery moved deeper inside the body, in the treatment of visceral disease. The ability to monitor location of the freezing probe and the position of the advancing ice front permitted much greater control and resulted in much less invasive procedures.

Cryosurgery has been successfully performed on a diversity of organs including the brain, liver, bronchus, prostate, pancreas, and oral and nasal cavities (Gage, 1992; Baust *et al.*, 1997). Moreover, liver and prostate cryosurgeries are becoming routine in clinical settings (Baust *et al.*, 1997). The ability to perform cryosurgeries through stab incisions has allowed the cryosurgical treatment of awkwardly seated tumors and lesions not possible to treat using an open wound conventional approach. Because the undesirable tissue is not removed from the body, post- surgical results are cosmetically pleasing with less tissue loss than surgical excision. In addition to being a primary care alternative, cryosurgery has also been shown to be beneficial in the management of recurrent carcinomas following standard excisions. Cure of metastases has also been reported in rare cases.

Although cryosurgery has been shown to be an effective means of treating various cancers (Gage, 1992; Baust *et al.*, 1997), there are still many ambiguities about the nature of the freeze injury that occurs and the best approach to maximizing the damage accruing in a single freeze-thaw cycle (Gage and Baust, 1998). To improve the state-of–the art in cryosurgical research, there is a need for an improved understanding of the response of tumor tissue to freezing and thawing *in vivo*. Studies on biopsied tissues have contributed significantly to our understanding of the biophysical response of healthy and tumor tissue to freezing (Rubinsky and Ikeda, 1985; Bischof *et al*, 1993). However, i*n vitro* cell and tissue studies cannot account for cell-mediated immunological responses or the presence of circulating blood. Both of these can significantly impact cryosurgical outcome (Gage and Baust, 1998). Additionally, information from post-operative tissue biopsy is constrained to the time it was obtained and therefore offers only a static interpretation of tissue response to cryosurgery. However, evidence suggests that cell death following cryosurgery is not a discrete phenomenon, but that ischemic necrosis, occurring on a longer time scale than direct injury, contributes to the overall lesion size (Hoffman *et al.*, 1999, 2001b). This not only complicates the assessment of cryosurgical success, but also makes it difficult for the surgeon to delineate suitable margins for debridement of dead tissue following frostbite injury (Zook *et al.*, 1998). Understanding the dynamics of tissue degeneration following freezing injury thus has important clinical ramifications.

It is known that in tissues such as the liver (Bischof *et al.*, 1993) and prostate (Bischof *et al.*, 1997) regions near the cryosurgical probe experience fast freezing rates and are associated with intracellular ice formation. Peripheral regions of the tumor

experience slower rates and tissue death in this region is typically related to solution effect or solutes injury. A vascular mechanism of injury has also been suggested as accounting for some of the necrosis at the edge of the cryo-lesion (Bischof *et al.*, 1997). The precise conditions that give rise to these types of damage are not well-understood (Rubinsky and Onik, 1991; McGrath, 1993; Bischof *et al.*, 1997) and they vary from tissue to tissue (Shepherd and Dawber, 1984). More complete knowledge of thermal damage in any system affords a greater sense of control and can result in more effective tumor de-vitalization and less damage to healthy tissues.

1.4.2 Direct Cellular Injury

Considerable knowledge has been obtained from freezing studies on isolated cells (Mazur, 1977, 1984; McGrath *et al.*, 1975; Smith *et al.* 1999). At fast rates of freezing, heat transfer dominates. Water is trapped within cells and thermodynamic equilibrium is attained by intracellular ice formation (IIF), which is generally lethal (Mazur, 1984). This type of damage is considered to be primarily due to mechanical forces on membranes and organelles. At slow rates of freezing mass transfer dominates, the cell becomes severely dehydrated and the cells are exposed to high solute concentrations for extended periods at relatively high subzero temperatures. This can cause both chemical and mechanical membrane stress (McGrath, 1993). Mazur (1984) has referred to this phenomenon as the two-factor hypothesis; viability as a function of cooling rate is described as an inverted-U-shape, representing a fairly universal trend to low viability at the extremes of freezing rates.

Fo

the forma

and Pegg

become c

cell memb

the cell to

are expo

numerous

effect in

cooling d

viability

plasma-le

Stepenk

membran

changes

changes

A

keep pa

to offset

Experim

darkenin

somewh

Rapid w

For slow cooling rates, the immediate effect of temperatures lower than 0 °C is the formation of ice crystals in the extracellular space and microvasculature (Rubinsky and Pegg, 1988). As liquid water is converted to ice, solutes in the extracellular fluid become concentrated, causing a decrease in chemical potential of water external to the cell membrane. As the concentration of solutes steadily increases, water begins to leave the cell to osmotically equilibrate this imbalance. During this slow freezing process cells are exposed to progressively damaging hyperosmotic conditions. There have been numerous observations made and mechanisms proposed to explain the nature of solutes effect injury. Reduction of the cell volume past a critical level during slow cooling/dehydration has been thought to be associated with a significant drop in cell viability (Meryman, 1970). It has also been proposed that damage to or alteration of the plasma-lemma membrane may be related to solutes injury (Gordon-Kamm and Steponkus, 1984). Steponkus *et al.* (1983) indicated that an irreversible loss of membrane material due to excessive shrinkage could result in irreversible and destructive changes to the cell. Additionally precipitation of buffering salts can cause damaging changes in pH (McGrath, 1993).

At fast freezing rates, the rate at which water can leave the cell cannot adequately keep pace with the departure from osmotic equilibrium and intracellular freezing occurs to offset the imbalance in chemical potential across the membrane (Toscano *et al.*, 1975). Experimentally, this formation of intracellular ice has been described as a sudden darkening of the cell, or "flashing". The precise nature of how IIF relates to injury is somewhat controversial. There is disagreement as to whether the force generated by rapid water flux in and of itself causes lethal membrane damage and then this

permeabilization of the membrane allows intracellular ice to subsequently form (Muldrew *et al.*, 1990, 1994), or if the intracellular ice is indeed precipitating the cell damage (Mazur, 1984). This can be generalized as a cause versus consequence debate. Steponkus *et al.* (1983) have provided substantial evidence for the membrane rupture hypothesis, suggesting a critical temperature at which the membrane fails. Mazur (1966) has theorized that at a certain critical temperature the radius of ice crystals will match the radius of aqueous pores in the *intact* membrane and intracellular ice will be subsequently seeded by extra-cellular ice. During warming, re-crystallization or fusion of small non-lethal ice crystals to form large crystals can be quite destructive (Mazur, 1977). The more slowly these are warmed, the greater the likelihood that this type of re-crystallization will occur. Although recognized as being an important component of the injury, few studies investigate the thawing process with the level of detail given to the freezing rates and minimum temperatures. Toner *et al.* (1990) proposed a nucleation theory of IIF that suggests that at certain critical temperatures the plasma membrane can change in such a way that it becomes an effective ice nucleator. An alternative theory by Muldrew *et al.* (1994) suggests that membrane rupture may occur due to the osmotically driven water efflux, consequently allowing extracellular ice to propagate into the cell. Despite the divergence of opinion on how ice manifests intracellularly, it is generally agreed that IIF does correlate strongly with cell injury (Toner, 1993). Figure 1.1 summarizes the physical nature of the damage that is found at the different freezing rates.

Although the aforementioned theories offer plausible explanations to describe the two classes of injury there is still much to be learned about the mechanisms that precede or supersede cell damage and about the primary sites of injury.

Figure
dissertia

1.4.3

micro-v

White e

1989;

compre

and mu

tempera

characte

relied o

injury (

1991). v

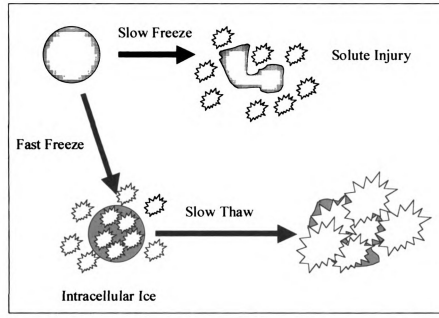

Figure 1.1 Location and size of ice crystals at different freezing rates. Images in this dissertation are presented in color.

1.4.3 Secondary Injury

Frostbite research has contributed significantly to the understanding of how the micro-vasculature responds to freezing (Sjostrom *et al.*, 1964; Reite, 1965; Weatherly-White *et al.*, 1964, 1969; Snider *et al.*, 1975; Waris and Kyosala, 1982; Marzella *et al.*, 1989; Manson *et al.*, 1991; Bourne *et al.*, 1986). A common problem with comprehensively interpreting the results of these studies is the absence of thermal control and monitoring of the freezing process during the experiments. Oftentimes the temperature of one discrete point in the tissue was monitored and data then generalized to characterize the entirety of the frostbite injury. A number of the experimental techniques relied on immersion of extremities in liquids of varying sub-zero temperatures to create injury (e.g. Sjostrom *et al.*, 1964, Weatherly-White *et al.*, 1964, 1969; Manson *et al.*, 1991), with temperature histories in the actual tissue not documented.

In addition to the preponderance of data available from frostbite studies, investigations into the effects of lower temperatures and faster freezing rates characteristic of cryosurgery procedures have also been performed. Zacarian *et al.* (1970) and Rabb *et al.* (1974) have utilized liquid-nitrogen cooled copper probes to directly examine the effects of cryogenic temperatures on microcirculation in the hamster cheek pouch. More recent efforts by Schuder *et al.* (1999) and Hoffman *et al.* (1999, 2001b) have begun to explore micro-vascular changes in response to cryosurgically relevant freezing in rat models.

These different experimental approaches to understanding the effects of freezing on the micro-vasculature has resulted in the emergence of a general pattern of vascular freezing injury. As the tissue is cooled, the initial thermoregulatory physiologic response is increased blood flow to the tissue (Weatherley-White, 1969), termed the "rewarming" response. With sustained cooling the biological system begins to lose its protective function, and blood flow to the cooled site is reduced. When the phase change temperature is reached, the tissue begins to freeze first in the extra-cellular space (Rubinsky *et al.*, 1987, 1988, 1990). Circulatory stasis occurs in the affected tissue. Vascular distention has been observed both in frozen section (Rubinsky *et al.*, 1990, 1997) and intra-vitally post-thaw (Schuder *et al.*, 1999). During thawing, circulation is temporarily restored to the previously frozen tissue however progressive failure of the micro-circulation is observed. Edema develops (Weatherley-White *et al.*, 1964; Reite, 1965; Marzella *et al.*, 1989; Zook *et al.*, 1998; Manson *et al.*, 1991; Zook *et al.*, 1998), vascular permeability is increased (Waris and Kyosala, 1982), impaired platelet function and platelet aggregation leads to thrombosis and vascular occlusion (Weatherley-White *et*

Zoo

[96

tiss

seve

vend

occl

end

hem

to

dista

How

dista

and

endo

to oc

of g

some

intra-

[96,

al., 1964; Reite, 1965; Zacarian *et al,* 1970; Bourne *et al.*, 1986; Marzella *et al.*, 1989; Zook *et al.*, 1998), and endothelial cells die (Waris and Kyosala, 1982; Marzella *et al.*, 1989; Manson *et al.*, 1991). With failure of circulation, nourishment of tissues is lost and tissue death is certain. Adverse microvascular changes have been observed to occur on several time scales. Changes have been observed as early as immediately after freezing (endothelial cell damage) by Manson *et al.* (1991) or 3-min after thawing (small vessel occlusions) by Bellman *et al.* (1956) to as long as 24 hours after freezing (necrosis of endothelial cells) by Waris and Kyosola (1982).

Recent efforts to provide more control over freezing protocols applied as well as better accuracy in the registration of temperatures that are reached in the tissues, have led to the formulation of freezing rate and temperature sensitive models of vascular distention occurring during freezing (Rubinsky *et al.*, 1988, 1989; Bischof *et al.* 1993). However, many questions remain as to how thermo-physical effects such as vascular distention and the physiological effects of cell-mediated changes in vascular permeability and platelet function inter-relate to give the final microvascular lesion.

The acute inflammatory response, characterized by neutrophil adhesion to the endothelium and subsequent transmigration into the tissue following thawing are reported to occur at different time points following cryosurgery. The magnitude and localization of this inflammatory response can affect the ultimate size of the lesion, though this contribution has not been well studied. Recently some investigators are beginning to use intra-vital models to study the magnitude of this contribution however (Shuder *et al.*, 1999).

Hoffman and Bischof (2001ab) have used the transparent skin flap model to assess vascular integrity following freezing in a Copenhagen rat / AT-1 tumor model. Their results indicate that at the edge of the cryo-lesion where high sub-zero temperatures are predicted, vascular damage correlates with histological assessment of cellular damage 3 and 7 days following treatment. The temperatures recorded at the edge of the lesion were shown to be considerable higher than those necessary to kill cells *in vitro*, suggesting that the injury in this region was associated with the secondary effects of vascular injury as opposed to the immediate effect of freezing on the cells. This study begins to decouple the effects of direct cellular injury and the secondary ischemia effects of freeze injury. Development of a continuous tissue viability assessment technique would enhance the utility of this experimental system and could provide the first direct evidence that cells at the edge of a cryo-lesion die not as a result of the initial freezing insult, but instead by the secondary effects of ischemia.

2.1 GFI

Gree

gene respon

subsequentl

Although G

al., 1994; Y

current use

ion channel

(Xian *et a*

cytoplasm

1997a-e). a

Tra

foreign DN

323β) adeno

Chapter 2

Molecular and Physical Basis for the Proposed GFP Technique

2.1 GFP Transfection

Green Fluorescent Protein is native to the jellyfish species *Aequorea victoria.* The gene responsible for the production of GFP was first cloned by Prasher *et al.* (1992), and subsequently expressed in both prokaryotic and eukaryotic cells by Chalfie *et al.* (1994). Although GFP was first implemented as a reporter molecule for gene transfer (Chalfie *et al.*, 1994; Zhang *et al.*, 1996), this molecule's unique fluorescent properties underlie its current use in a diversity of applications such as protein localization (Cubitt *et al.*, 1995), ion channel expression (Marshall et al, 1995), cardiac development and pathophysiology (Xian *et al.*, 1999), erythroid differentiation (Chida *et al.*, 1999), measurement of cytoplasm viscosity (Swaminathan *et al.*, 1997), tumor metastasis (Chishima *et al.*, 1997a-e), and angiogenesis (Li *et al.*, 2000).

Transfected cell lines are produced by introducing a GFP-encoding segment of foreign DNA into the cell line of interest. This study utilizes the GFP-transfected Rat 3230 adenocarcinoma (R3230AC) tumor cell line. A GFP-transfected cell manufactures

the GFP protein using its inherent protein synthesis mechanism and native amino acids. Furthermore, the vector can remain stably expressed in successive generations, which makes it especially attractive for studying tumor metastasis. Chishima *et al.* (1997a-e) and Yang *et al.* (1998b) have effectively utilized transduction of a GFP vector to characterize successive stages of metastatic colony growth of human lung adenocarcinoma, and the metastatic potential of hamster ovarian tumors. More recently this group has been developing a GFP-based mouse model of metastatic human prostate cancer (Yang *et al.*, 1999). Higashijima *et al.* (2000) have used GFP transfection to study cranial motor neurons. Others have used GFP transfection to monitor herpes virus transmission (Brewis *et al.*, 2000). This protein has recently been used to study gap junctions (Falk and Lauf, 2001). Despite their relative novelty, the use of GFP proteins is wide and varied.

The water-soluble cylindrical GFP monomer, comprised of 238 amino acids (Prasher *et. al.*, 1992), is 3 nm in diameter and 4 nm long (Yang *et al.*, 1996). The reported molecular weight of the GFP ranges from 27,000 (Shimura, 1979) to 30,000 (Prendergast and Mann, 1978). GFP and its mutants can be fused with other proteins both at the N- and C- terminus without loss of biological activity of either protein and without loss of fluorescent properties (Cubitt *et al.*, 1995; Marshall *et al.*, 1995; Yokoe and Meyer, 1996; Rizzuto *et al.*, 1995; Windoffer and Leube, 1999). However in some instances the biological function can be attenuated to some extent (Yokoe and Meyer, 1995), therefore preliminary screening for functionality as well as fluorescence is important.

compr

and sh

barrel

utilizi

in Fig

residue

barrel

exclud

Figure
of fi-sh
protect

Yang *et al.* (1996) describe the tertiary structure of GFP as cylindrical, and comprised of a tightly woven, 11-stranded β- sheet, with an α-helix inside the cylinder and short helical segments on each end. This structure is frequently referred to as a β-barrel or β-can. The fluorophore portion of the protein is encapsulated within the barrel, utilizing the α end-segments as scaffolding (Yang *et al.*, 1996). This structure is pictured in Figure 2.1. Although truncations of the protein can be tolerated, they are minimal, and residues 7-229 must be maintained (Li *et al.*, 1997) to ensure proper formation of the β-barrel. The protective barrel ensures the proper environment for stable fluorescence by excluding oxygen and adverse solvents.

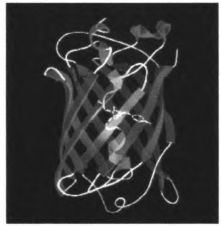

Figure 2.1 Tertiary structure of a GFP molecule: a tightly-packed 'β-can' comprised of β-sheets (green) which enclose an alpha helix (red) with the appendaged chromophore protected in the center of the β-barrel. (From Yang *et al.*, 1996)

Although the nascent protein is itself not fluorescent, the formation of the chromophore that imparts the fluorescence occurs autocatalytically (Chalfie *et al.*, 1994; Heim *et al.*, 1994; Kolb *et al.*, 1996), requiring only molecular oxygen to complete this post-translational modification. The tripeptide chromophore depicted in Figure 2.2, p-hydroxybenzylidineimidazolidinone, is generated by post-translational cyclization and oxidation of a Ser-dehydroTyr-Gly sequence at residues 65-67 (Cody *et al.*, 1993). This chromophore is responsible for the fluorescent absorption bands at 280, 395, and 480 nm, as well as the emission maximum at 508-509 nm (Morise *et al.*, 1974) in wild-type GFP. The chromophore is only fluorescent when embedded in the GFP protein in its fully folded state.

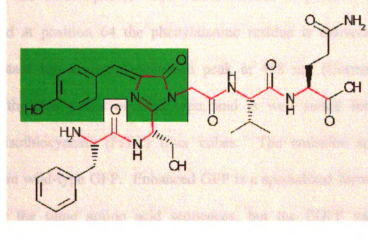

Figure 2.2 The GFP chromophore, highlighted in green is comprised a cyclic tripeptide (Ser-dehydroTyr-Thr). (From Cody *et al.*, 1993; www.biochemtech.uni-halle.de/PPS2/projects/jonda/chromoph.htm).

2.2 Enhanced Green Fluorescent Protein

Wild-type GFP does not have high levels of expression in higher eukaryotes such as human and primate cells (Kain, 1999). It also has a relatively low level of fluorescence when compared to some of the variants of GFP that have been recently been constructed. These mutants are now preferred for many applications. There are numerous variations or mutants of the wild-type GFP (e.g. Heim et al., 1994). The GFP mutant used in this work is the Enhanced GFP (EGFP), which is a red-shifted variant of wild type GFP that has been engineered for brighter fluorescence. 'Red-shifted' refers to the direction of the change in spectral properties that occur as a result of the point mutations, with the excitation peak shifted towards the red end of the photodynamic spectrum. The mutant GFPmut1, described by Cormack *et al.* (1996), contains two point mutations in the chromophore. The serine residue at position 65 is replaced with threonine and at position 64 the phenylalanine residue is converted to leucine. The resulting mutant has a single excitation peak at 488 nm (Cormack *et al.*, 1996) as opposed to the two peaks of wild type, and is well suited for use with standard fluoroscein isothiocyanate (FITC) filter cubes. The emission spectrum is basically unaltered from wild-type GFP. Enhanced GFP is a specialized form of GFPmut1. They have exactly the same amino acid sequences, but the EGFP variant has also been optimized for improved expression in mammalian cells by the replacement of some of the native codons (i.e. originating in the jellyfish) with codons that are highly expressed in human proteins (Zhang *et al.*, 1996; Haas *et al.*, 1996; Clonetech Protocol # PT2040-1). A related mutant worth mentioning is the S65T mutant that includes the Ser to Thr substitution at position 65 but without the position 64 mutation. The Phe-64 to Leu

mutation imparts a thermo-tolerance not present in the wtGFP. Patterson *et al.* (1997) have shown that on the basis of protein folding studies, the EGFP fluorescence intensity expressed at 28 °C and 37 °C are equivalent. In the case of wtGFP the exhibited fluorescence of transfected cells has been shown to diminish at higher culture temperatures (Lim et al., 1995).

The spectral resolution achieved by such alterations in the excitation spectra makes the red-shifted mutants more readily utilized in conjunction with other probes. Crossover-free dual labeling experiments with EGFP and DsRed, a novel red fluorescent protein, in *E. Coli* were recently performed by Jakobs *et al.* (2000). Triple combinations of red, green, and blue proteins have also been reported (Beavis and Kalejta, 1999).

The mutant EGFP retains the same tertiary structure as the wild-type protein (a β-barrel configuration), but is 35X brighter than wild- type GFP when excited with blue light (Cormack *et al.*, 1996). The extinction coefficient (E_m) of EGFP is ~55,000 $cm^{-1}M^{-1}$ compared to 7000 $cm^{-1}M^{-1}$ for wild-type GFP (wtGFP). The mutant EGFP also has improved solubility and reduced photo-bleaching rates when compared to wild type GFP (Jain, 1999). The pH stability for EGFP is also different. Although wtGFP fluorescence has been reported to be stable between pH 6 to 10 (Ward, 1981), EGFP fluorescence begins to decrease below pH 7 (Patterson *et al.*, 1997). This sensitivity to pH is shown in Figure 2.3. Haupts *et al.* (1998) demonstrated that the drop in fluorescence at lower pH is evident in the excitation, emission, and absorption spectra, as shown in Figure 2.4. The authors suggest that a single protonation step (protonation of the hydroxyl group of Tyr-66) is responsible for conversion of the protein into a non-fluorescent state. The pK_a of this reaction is given as 5.8. Wachsmuth et al. (2000) have also examined this pH

phen

b.f

Figu
wit
nm.
to de

phenomemon using Fluorescence Correlation Spectroscopy (FCS) and give the value as 6.0 ± 0.4. Fluorescence of EGFP was found to be independent of the ionic strength (Haupts et al., 1998).

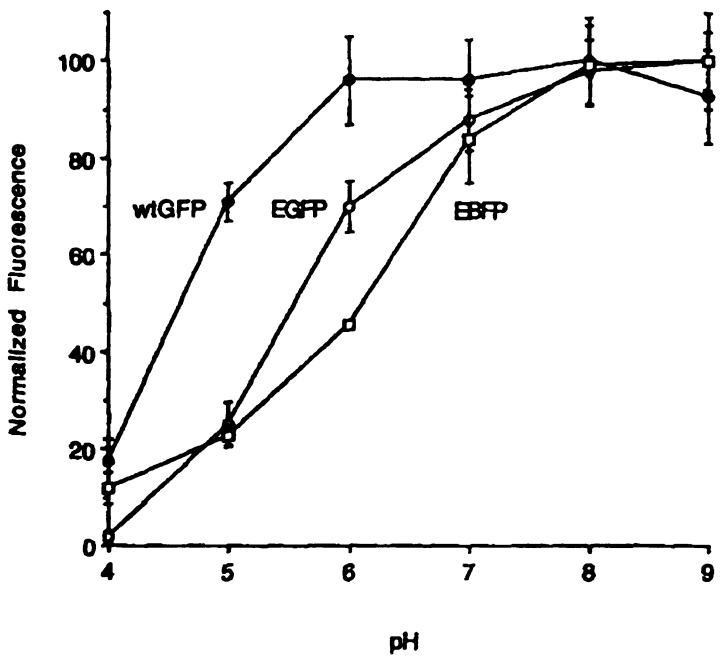

Figure 2.3 Effect of pH on fluorescence of wtGFP and some of its mutants. For wtGFP and EGFP, excitation was at 488 nm and emission was collected from 490-650 nm. Maximum signal strength was normalized to 100. EGFP fluorescence can be seen to decrease in intensity at a higher pH than wtGFP. From Patterson *et al.*, 1997.

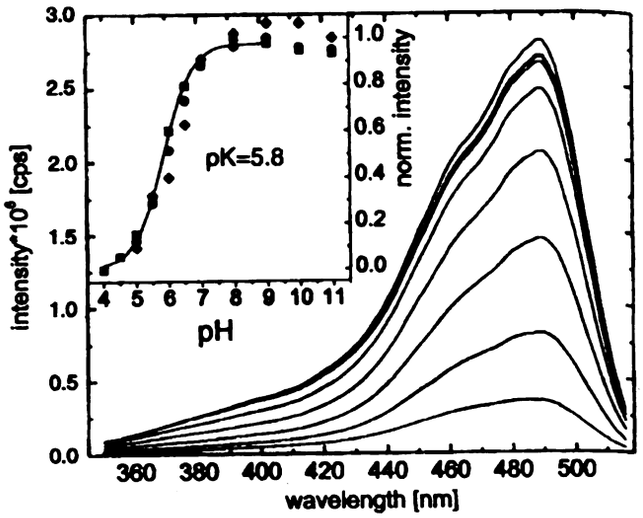

Figure 2.4 Fluorescence excitation spectra of EGFP as a function of pH. From the top: 9.0, 8.0, 11.0, 7.0, 6.5, 5.5, and 5.0. Inset: fluorescence emission intensity at 510 nm (■) fluorescence excitation intensity at 490nm (●) and absorption at 488nm (♦). From Haupts *et al.*, 1998.

Other mutants have been optimized for localization within particular organelles and cell compartments (De Giorgi *et al.*, 1999), as well as for different spectral ranges (Cormack *et al.*, 1996; Heim *et al.*, 1994), which indicates many possibilities for specifically targeting damage following insults of the nature explored in this work.

2.3 Photodynamics

Swaminathan et al. (1997) have used fluorescence recovery after photo-bleaching (FRAP) and anisotropy decay techniques to study the translational and rotational diffusion of green fluorescent protein in solution and biological cells. The GFP mutant used in their study was S65T. The FRAP technique involves irradiation of a small area in a larger sample of aqueous or *in situ* fluorophore, using laser excitation of suitable wavelength, power, and duration to induce photo-bleaching. The laser intensity is then

attenu

during

protei

fluores

area.

fluoro

bleachi

be 86.7

reversib

increase

differen

photo-b

As expe

of the c

differen

3.2. Be

the prin

Recover

concent

1994; d

A

Spiral d

attenuated significantly to allow subsequent monitoring of the fluorescent intensity during the recovery period without causing further photo-bleaching. Since the GFP-S65T protein was found to irreversibly photo-bleach in aqueous solution, recovery of fluorescence was assumed to be dependent only on translational diffusion into the probed area. This recovery was also found to be independent of concentration of the fluorophore. Based on the half-life of the fluorescence recovery following photo-bleaching, the diffusion coefficient of GFP-S65T in aqueous solution was determined to be 86.7 $\mu m^2/s$.

The Swaminathan *et al.* (1997) study also demonstrated that the absence of reversible photo-bleaching was evident only in dilute solutions. When the viscosity was increased with glycerol, a rapid recovery process was observed. However, the significant difference in time constants for the rapid recovery process (reversible and irreversible photo-bleaching) allowed the determination of diffusion coefficients in viscous media. As expected, the same time-resolved phenomena were observed in the viscous cytoplasm of the cell. Based on $t_{1/2}$ of the reversible recovery process, the relative viscosity difference between cytoplasm of CHO cells and aqueous solution was determined to be 3.2. Because the diffusivity was found to vary directly with viscosity, this suggests that the primary barrier to GFP diffusion is interaction with macromolecular solutes. Recovery curves were not affected by the concentration of GFP-S65T, suggesting that a concentration-dependent monomer-to-dimer transition characteristic of wtGFP (Chalfie, 1994) does not occur in this mutant.

As mentioned previously, Wachsmuth *et al.* (2000) have used FCS to study the spatial diffusion of EGFP in cellular environments. Because the time resolution of video

microscopy does not permit observation of the motion of a single molecule, they use fluorescence intensity fluctuations in laser-irradiated femtoliter volumes of fluorochrome solutions, which contain just a few fluorophores, to determine hydrodynamic and photophysical properties of the molecules. These fluctuations in intensity are caused by Brownian motion of the molecules, as the fluorophores move into and out of the observation window. Based on the lifetime of fluorescence decay it was possible to compute diffusion coefficients. Similar to the results of Swaminathan *et al.* (1997) the diffusion coefficient of EGFP in aqueous solutions was determined to be 87 $\mu m^2/s$. In cells, the autocorrelation function (ACF), which characterizes the fluctuations in fluorescent intensity, generally lent itself to a single freely diffusing species model in the cytoplasm, and either a two-species model (model 1) or obstructed diffusion model (model 2) in the nucleoplasm. However, there were variations that suggested the organelles in the cell or some other cytoplasmic structure caused some hindered diffusion in the cytoplasm as well. On average, using the fast component of the two-species model or the obstructed diffusion model gave very similar results for diffusion of EGFP in two types of cells (less than 5% variation). Based on the reported ratios of diffusion coefficients, the diffusivity of EGFP in AT-1 cells was given as 15.8 (model 2) or 16.4 $\mu m^2/s$ (model 1), and in COS-7 cells it is 19.3 $\mu m^2/s$ (model 2) or 18.5 $\mu m^2/s$ (model 1). In the same study, based on the amplitude of the ACF and the size of the detection volume, the Wachsmuth group (2000) found the average GFP protein concentrations in the AT-1 cell to vary between 10 and 150 nM.

cyt

tar

iR

me

res

ba

de

exc

we

sol

The

Co

Co

ass

uti

del

ev

to q

fl

ori

2.4 GFP as the basis for a Viability Assay

Wild-type GFP, as well as EGFP, is known to be distributed throughout the cytoplasm and nucleus when expressed in mammalian cells (Cubitt *et al.*, 1995). With targeted mutations to the vector, GFP can also be tagged specifically to other organelles (Rizzuto *et al.*, 1995, 1996). Because GFP accumulates in the cytoplasm of normally metabolizing transfected cells, it seems likely that damage to the plasma membrane could result in leakage of cell contents, including GFP. In this work, a GFP viability assay, based on a loss of GFP fluorescence in damaged cells, is compared to the viability results determined by a number of classical indicators of viability, including Trypan Blue exclusion, Ethidium Bromide exclusion, and standard histopathology. Cells and tissues were stressed by treatment with a range of freezing protocols and ice-free hyper-osmotic solutions with concentrations similar to those that might be experienced during freezing. These conditions have implications for both cryosurgery and cryopreservation.

A cell viability assay based on a transfection process has also been explored by Coombe *et al.* (1998) and Baumstark-Khan *et al.* (1999). The assay developed by Coombe is based on the expression of luciferase that has been transfected into cells. This assay requires addition of a substrate however, and as currently implemented, has little utility as an *in situ* viability assay for tissues because it has the same limitations of delivery as any other viability probe. A similar GFP-based assay, requiring no exogenous substrate, was developed for biotechnology applications by Hunt *et al.* (1999) to quantitatively assess colony growth in bioreactors. Their studies indicated that GFP fluorescence increased with cell concentration to a maximum that was dependent on the original plating density. The high correlation of GFP fluorescence to cell number

(R^2=0.9

propose

the sam

and GF

survivi

transfe

the bas

Purifie

5.5 to

will re

encaps

recove

metho

less o

stored

not a

(R^2=0.997) supports the use of GFP fluorescence as an indicator of cell viability as proposed in this work. The assay utilized by Baumstark-Khan *et al.* (1999) was based on the same concept but implemented differently. The colony forming ability of wild-type and GFP-transfected CHO cells was measured after irradiation. They found that colonies surviving radiation expressed GFP and that the surviving fractions were comparable for transfected and wild-type cells. None of these transfection-based assays were explored as the basis for a tissue viability assay.

As the tertiary structure suggests, GFP is physico-chemically very stable. Purified samples of GFP have been shown to be highly fluorescent at pHs ranging from 5.5 to 12, and thermally stable to 65 °C (Bokman *et al.*, 1981). Denaturation of the GFP will result in a loss of fluorescence, primarily because the chromophore is no longer encapsulated and protected (Cody *et al.*, 1993; Prasher *et al.*, 1992). Fluorescence is recovered upon renaturation however (Bokman *et al.*, 1981). The successive freeze-thaw method typically used to isolate proteins has also been employed to isolate GFP without loss of fluorescence (e.g. Gonzalez and Ward, 2000), and purified GFP is shipped and stored in the frozen state (e.g. Clonetech, Palo Alto, CA), suggesting cold-denaturation is not a problem when using GFPs at low temperatures.

Su

producing

opportunit

compared

a)

living tiss

histologica

b)

living tissu

c)

animal rath

reduces the

that can be i

d)

Chapter 3

Significance of the Research

Successful development of a GFP fluorescence-based viability method capable of producing instantaneous *in vivo* viability data within tissues would create future opportunities for many researchers. The GFP method has numerous advantages compared to traditional viability assessment methods. These advantages include:

a) Instantaneous, quantitative, non-invasive viability determination within living tissues. This would eliminate the need for labor-intensive, time-consuming histological processing of tissues, and avoid the possibility of fixation artifacts.

b) Continuous monitoring of spatio-temporal viability relationships within living tissue.

c) Ability to monitor complex time-course experiments within a single animal rather than having to use many animals sacrificed at sequential times. This reduces the number of animals required for experimentation and eliminates ambiguities that can be introduced by animal-to-animal variations.

d) Possibilities to combine optically-based GFP tissue cell viability method

with other optical methods (fluorescence-based or otherwise) for simultaneous measurements of physio-chemical, thermal, morphological, physiological, inflammatory and immunological responses to freezing/thawing or other processes by using multi-spectral probes, infrared thermography, and other existing technologies.

e) Improved knowledge of spatial relationships that are difficult to track after histological processing (e.g. accurate positioning of tissue and/or vascular damage relative to location of frozen regions).

There are some limitations to the use of GFP for viability assessment. The stable transfection of cells with GFP is not a trivial task, and reselection may be necessary periodically to ensure that a portion of the colony has not lost the GFP vector. The use of a GFP viability assessment technique in a quantitative way will also be limited to situations in which optical access with exciting wavelength light is possible.

The use of GFP-transfection techniques can provide a non-toxic way of introducing fluorescent markers into living tissue and thereby offers the potential to examine cryosurgery phenomena *in vivo*, in real time. This approach can provide more realistic information about the effects of low temperature on tumor tissue as it relates to cryosurgery because the studies are being conducted in a living and normally functioning system. Prior to this study, GFPs had not yet been evaluated as a marker/viability indicator in the low temperature regime. If this application is successful, GFPs can provide a means of directly observing freeze injury phenomena, dynamically, in a living system. Not only is there potential to develop an *in vivo* viability marker, but this technique simultaneously provides a means of studying the effects of freeze-induced

vascula

followi

freezing

correlat

utilized

during c

constitu

function

The firs

and the

vivo. T

vivo. A

impleme

events r

damage

develop

simultan

the imm

case of t

specific

antigenic

vasculature damage on tumor devitalization as well as the risk of tumor metastasis following a cryosurgical procedure. To date, this has not been possible in a living host.

The current work seeks to provide the first *in vivo* evidence that following freezing, fluorescent intensity changes of tumors grown from GFP-transfected cells correlate with tissue damage as assessed by histological methods. The freezing protocols utilized were chosen to span the range of damage (both type and severity) experienced during cryosurgery. The experimental assay proposed to evaluate viability relies on the constitutive expression and retention of stable GFP. The GFP molecule therefore functions primarily as an indicator of membrane integrity and normal anabolic activity. The first part of this study looks at the effectiveness of the GFP assay in individual cells, and the second part of the work investigates the validity and limitations of the assay *in vivo*. This approach thus answers questions pertaining to its utility both *in vitro* and *in vivo*. Additionally it may highlight potential differences in how the assay should be implemented for maximum reliability in isolated cells and cells within tissues.

The GFP method described here provides an exciting new possibility to monitor events relevant to improving our understanding of the mechanisms of cryosurgical damage at the tissue level. In addition to immediate applications, it should be possible to develop different GFP mutants with different wavelengths which may make it possible to simultaneously label and observe multiple cell types such as endothelial cells and cells of the immune system via transfection into embryonic cells such as has been done in the case of the GFP mouse (Okabe, 1997) and the GFP bunny (Kac, 2000). If such cell–specific GFP mutants become available, it may be possible to observe the absorption of antigenic material into the lymphatic channels and lymph nodes, as well as observe cell-

mediated immune response to the cryosurgical assault, thus providing additional tools for understanding cryo-immunologic phenomena. Although the thermal conditions used to challenge the cells in this work corresponds to the injury experienced during cryosurgery, and to some extent during cryopreservation, the assay is not limited to these applications. It may also prove to be a valid viability assay for a wide range of phenomena, including tissue hypoxia, drug-induced tissue death, and hyperthermia, and do so dynamically, *in vivo*, without sacrifice of the host animal.

Chapter 4

Cell Line and Animal Model

4.1 GFP-Transfected Rat 3230 Mammary Adenocarcinoma Cell Line

A GFP-transfected rat mammary adenocarcinoma (R3230AC) cell line was provided as a gift from Drs. Chuan-Yuan Li and Mark Dewhirst, Dept. of Radiation Oncology, Duke University Medical Center. This cell line can be utilized to grow transplantable fluorescing mammary adenocarcinomas in the Fischer 344 rat. The cells had been transfected with a pEGFP-NI plasmid using DMRIE liposomes and G418 selection (Li *et al.*, 2000). The R3230AC cell line is a subline of a R3230AB cell line originally derived from a spontaneous mammary adenocarcinoma in the Fischer rat and characterized by Hilf *et al.* (1964). Like its parent line, the R3230AC line is hormone-sensitive, responding to both estrogen and androgen. This cell line has extensive secretory activity, and can be induced to lactate by estrogen. This R3230AC cell line does not grow as fast as the parent R3230AB, and has biochemical and morphological characteristics similar to normal breast tissue (Hilf *et al.*, 1965).

4.1.1

C

suppl

units

fungi

incub

trypsi

subseq

minute

in supp

cells a

were p

box in

4.1.2

the wild

plated a

after pla

interval

curves fo

for each

line was

4.1.1 Cell Culture

Cells were cultured in T-flasks in Dulbecco's Modified Eagle Medium (D-MEM) supplemented with 10% fetal bovine serum, 4% penicillin streptomycin solution (10,000 units/ml penicillin G sodium and 10,000 μg/ml streptomycin in 0.85% saline) and 1% fungizone (250 μg/ml) [all products from Gibco BRL, Grand Island, NY], with incubation at 37°C and 5% CO_2 atmosphere. Cells were harvested by exposure to 0.25% trypsin solution (Gibco BRL, Grand Island, NY) for 2 minutes at room temperature, subsequently removing the trypsin solution by pipette, and then incubating the flask for 3 minutes at 37°C to release the cells from the flask surface. Cells were then re-suspended in supplemented D-MEM and diluted 1:10 for normal cell passage. To cryo-preserve the cells a solution of 10% DMSO, 30% fetal bovine serum, and 60% media was used. Cells were prepared to $1x10^6$ cells/ml and then immediately placed inside a cardboard storage box in a –80 °C freezer.

4.1.2 Doubling Time

To understand the growth characteristics of the cells, the doubling time for both the wild-type and transfected cell lines was determined. Five flasks per cell line were plated at a density of 0.5-1 x 10^4 cells/ml then incubated at 37 °C. Beginning 24 hours after plating, the cells were released from the flask using trypsin and counted at regular intervals, using a hemacytometer and Trypan Blue. Figures 2.1 and 2.2 give the growth curves for the wild-type and transfected R3230AC cells, respectively. The doubling time for each line was calculated from the exponential fit of the growth data. The wild-type line was determined to have a doubling time of 16 hours whereas the doubling time for

the trans

differenc

cells tha

dividing

Figure 4.1

Figure 4.2

the transfected line was determined to be 20 hours. There is no apparent reason for the difference in growth rates. However one might speculate that in the process of selecting cells that were brightly fluorescing during the transfection process, a more rapidly dividing colony was isolated from the parent line.

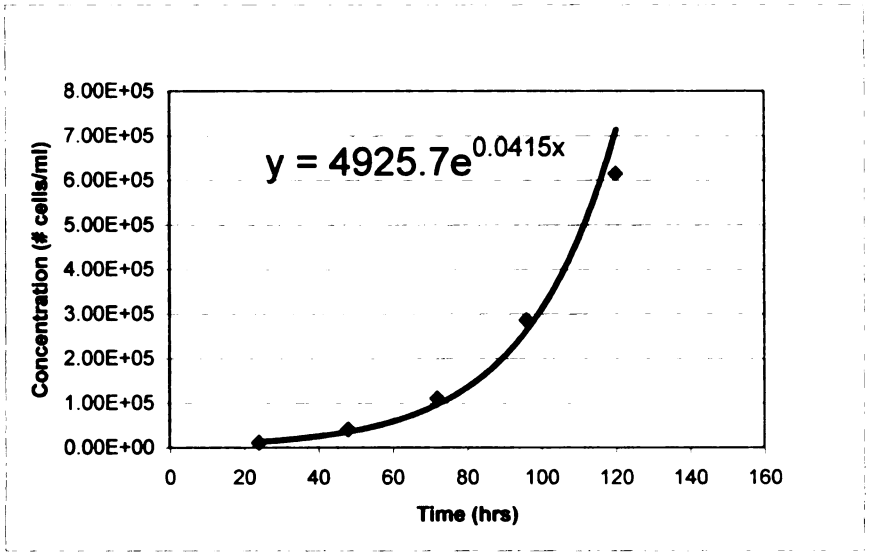

Figure 4.1 Growth curve for the wild-type R3230AC cell line.

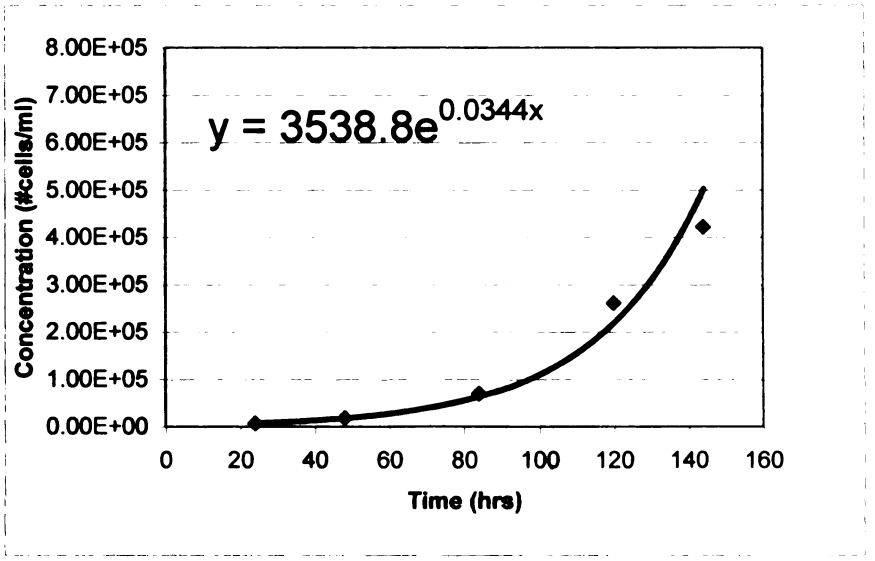

Figure 4.2 Growth curve for the transfected R3230AC cell line.

4.1.3 C

E

water (d

ice, an

Immedia

cells still

(Mager S

Scientific

cells had

diameter i

camera so

then taken

4.3. The

calculated

also plotted

coincide wi

microns, do

deviation w

4.1.3 Cell Size Distribution

Because the size of a cell figures significantly into how fast a cell can transport water (discussed further in Chapter 5), and consequently its tendency to form intracellular ice, an understanding of the average cell diameter and its distribution was desired. Immediately following a routine cell passage, a culture flask containing GFP-R3230AC cells still in suspension was placed on the stage of a Nikon Diaphot inverted microscope (Mager Scientific, Sterling Heights, MI). Using a SPOT digital camera (Mager Scientific, Sterling Heights, MI) seven images were acquired of the suspension before the cells had time to attach to the flask. Images of these cells were then measured for diameter in both the horizontal and vertical axial direction of the image, using the SPOT camera software and the appropriate stage micrometer-based calibration. An average was then taken of the two values. A histogram created from the results is shown in Figure 4.3. The total number of cells measured was 327. A probability distribution was calculated based on the assumption that the population was normally distributed and was also plotted in Figure 4.3. As can be seen from these results, the sample does not coincide with a perfect normal distribution. The mean diameter of the population, 14 microns, does not correspond with the mode of the population, 15 microns. The standard deviation was calculated to be 2 microns.

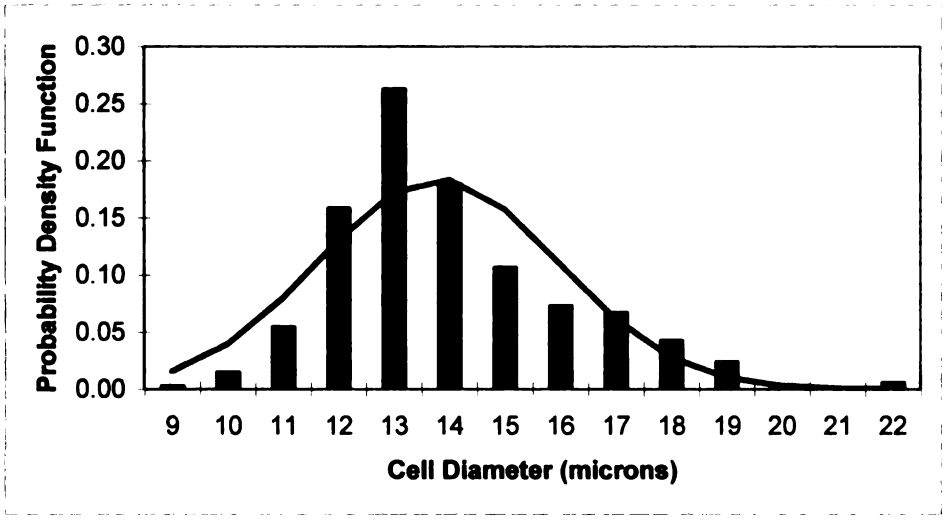

Figure 4.3 Histogram and probability density function based on n=327 individual cell diameter measurements from a single sampling of the cell population acquired during routine cell passage. The probability density function assumed the population was normally distributed.

4.2 Fischer 344 Female Rat

Female Fischer 344 rats, originating from Harlan (Indianapolis, IN) and Charles River Laboratories (Raleigh, NC) were used in this study. Female Fischer rats are an inbred species with a high incidence of naturally occurring mammary tumors (41%) that are also receptive to growth of transplantable R3230 mammary carcinomas (Altman and Katz, 1979). Because R3230 cells were to be used in this study, this species was chosen as the animal model for experiments.

4.3 Immune Response to EGFP

One of the applications motivating the *in vivo* assay proposed in this work is the study of the secondary effects of freeze injury (ischemia and inflammation). Consequently it is important to understand how a possible immune response to GFP released from cells could complicate the tissue response.

The recent interest in GFP co-expression as a means of optimizing therapeutic gene delivery and expression in humans (Levenson *et al.*, 1998, Aran *et al.*, 1998) has prompted the investigation of the immune response to GFP. Stripecke *et al.* (1999) have studied T cell immune response against EGFP+ cells in murine (mouse) models. As indicated by Stripecke, other non-GFP transgene constructs have been shown to evoke T-cell mediated toxicities in patients. As an example, in clinical trials with HIV positive patients, Riddell *et al.* (1996) found that five out of six of their patients developed T-lymphocyte responses specific for a novel protein produced by the intentionally transduced genes. Novel protein by-products can present themselves at the T-receptor sites, thus potentially stimulating the immune system to produce antibodies to this antigen, as well as elicit an immediate strike on the cell containing the protein, by way of the killer T-cells.

Stripecke *et al.* were able to establish that when EGFP-expressing leukemia cells (EGFP+ BM185 pre-B) were grown in syngeneic BALB/c mice there was a marked decrease in the kinetics of leukemia growth over the wild-type cells. Only one of twelve mice developed a tumor, and this lymphoma was considerably smaller than normal, and over time regressed in size. Several further experiments supported the hypothesis that the effect was due to a T-cell response. The same EGFP+ line was injected in

immunodeficient Nu/Nu mice, which by definition lack T cells. Normal lymphomas developed, indicating that T-cells were likely the cause of decreased tumor growth in the immunocompetent BALB/c mice. Cytotoxic T lymphocyte (CTL) lytic activity experiments were also supportive of this hypothesis.

Although these experiments were performed in mouse models, it is interesting that a significant T-cell mediated immune response is not detected in the RC3230 AC cell line/Fischer Rat syngeneic system. The Fisher rat is immunocompetent, yet readily grows EGFP+ adenocarcinomas. It is possible that there are enough differences in the immune systems of the rat and mouse that the observations of Stripecke in the BALB/c mouse model will not be representative of the expected response in the rat. More likely the differences are at the cellular level. Stripecke did evaluate tumor growth kinetics using a different EGFP+ tumor cell line, the T cell lymphoma EL-4, and found generality of results. However these cell lines are both of lymphoma origin and certainly do not represent a good cross-section of existing tumor cell lines.

In light of these results however, if GFP-transfected cells were to be used in studies related to immune response where low level T-cell effects could be significant, a closer investigation along the lines of Stripecke's study is warranted.

Chapter 5

Characterization of Water Transport in GFP-R3230AC Cells

5.1 Overview

If the goal of an *in vivo* model is to determine the role that secondary injuries such as the inflammatory response and vascular injury play in the determination of the ultimate cryo-lesion size, then to begin with, the basic freeze injury response in the isolated cell system must be well characterized. Limitations in existing technologies require the extrapolation from isolated cell and tissue slice behavior to expected *in vivo* response. The rates and end temperatures that cause both intracellular ice and damaging dehydration must be understood in order to separate direct cell injury from host-mediated responses or secondary ischemic effects that arise from progressive failure of the micro-circulation. The manner in which a cell responds to freezing protocols is directly related to the cell's ability to transport water. Presently data pertaining to the water permeability of R3230AC cells exists neither above nor below the freezing temperature of water. Comprehensive viability information at a variety of freezing rates spanning the range of the different types of freeze injury is also lacking. The goal of this research component is

to delineate these freezing regimes for the R3230 AC cell line using biophysical modeling. Determining membrane transport properties allows the utilization of predictive models to understand when cells can be expected to dehydrate in response to extra-cellular ice formation, or when IIF would be more probable.

The focus of this component of the work is to develop an understanding of the thermal histories that result in the two distinct classes of direct freeze injury (solute injury and IIF). Generally, the goal is to understand what constitutes 'slow freezing' and 'fast freezing' for these cells. This knowledge will help in the interpretation and application of GFP fluorescence signal intensity changes following injury by these two modes, and will also assist in the uncoupling of direct and indirect damage in later *in vivo* studies.

There are two key parameters that are recognized as characterizing the response of cells to freezing, namely the hydraulic conductivity of the plasma membrane, L_p, and the activation energy of the hydraulic conductivity, E_{Lp} (Schwartz and Diller, 1983). The surface area to volume ratio (S/A) also plays an important role in governing how a cell responds to freezing (Toner, 1990). Although these parameters are of critical importance for thermodynamic modeling of the response of cells to freezing, most of the data available are for properties measured above the freezing temperature of water. Once L_{pg} and E_{Lp} have been determined for a particular cell type, thermodynamic models of volume change during freezing can be used to predict intracellular concentration changes during freezing for those cells.

The development of successful cryo-preservation and cryosurgery protocols can be accelerated by knowledge of the cell parameters that govern the transport of water during freezing. Using models of water transport that have been developed in the past few

decades (e.g. Mazur, 1963; Levin, 1976), the amount of water inside a cell at a given temperature during freezing can be predicted. Knowledge of these parameters can provide considerable insight into the probability as well as type of injury that would be expected for given thermal processing conditions.

When the temperature of a cell suspension is lowered, freezing preferentially begins in the extra-cellular space. As liquid water is converted to solid water in the extra-cellular solution, a difference in water activity is produced across the plasma membrane. The water activity of the extracellular solution is lowered in comparison to the intracellular water activity. If the freezing rate is slow enough, this thermodynamic imbalance results in an efflux of water from the cell. The rate at which the water can leave the cell is governed by the parameters L_p and E_{Lp}. When no further water can be removed from the cell, the remaining volume is referred to as V_b, the osmotically inactive volume. This is an important experimentally determined parameter that is utilized in most thermodynamic models of freezing (e.g. Mazur, 1963; Schwartz and Diller, 1983; Levin, 1976).

If the cooling rate is rapid, water cannot leave the cell fast enough to satisfy equilibrium, the consequence of which is the formation of intracellular ice to reduce the water activity inside of the cell. The probability for IIF thus increases with increasing freezing rate. However, 'fast' is relative to the particular cell type, and is intricately tied to the water permeability of the cell. For example, the cooling rate yielding 50% IIF in red blood cells is over 3 orders of magnitude greater than for mouse and hamster oocytes (Toner, 1993). Red blood cells are known to have unusually high water permeabilities and high surface area-to-volume ratios.

Although the membrane permeability of a cell plays a very important role in determining the fate of water inside the cell during freezing, most measurements of this value have been obtained at temperatures above zero. There are a few cryomicroscopy-based approaches for determining permeability values at sub-zero temperatures that have been described in the literature. In 1979, Levin *et al.* determined sub-zero permeability values for yeast, as did Schwartz and Diller in 1983. Levin's estimation of sub-zero permeability parameters was based on the experimental data of Ushiyama and Cravalho (1973), wherein cells were suspended in distilled water and frozen at various freezing rates. L_p and E_{Lp} were then estimated by fitting the volume change data as a function of temperature to a thermodynamic volume regulation equation using multiple non-linear regression fitting schemes. Papanek (1978) measured the permeability of the human erythrocyte down to –10 °C using a stopped flow-light scattering approach. Schwartz and Diller (1983) used a similar approach to Levin (1979) but instead super-cooled the cell suspensions to temperatures between –2 and –10 °C, and then nucleated ice formation. In this manner the sudden change of extra-cellular concentration induced by the freezing effected a mass transfer response by the cell. A novel approach by Bischof and colleagues uses differential scanning calorimetry to estimate the membrane transport properties during freezing (Devireddy *et al.*, 1998).

In this work measurements of L_p were undertaken in the non-frozen state. It is recognized that the extrapolation of membrane permeability values determined at supra-freezing temperatures may not be representative of permeability values at sub-zero temperatures. However, at present there is no permeability information available for R3230AC cells at any temperature. Therefore, the approach of determining L_{pg} and E_{Lp}

at temperatures in the range of 0 °C to 22 °C using diffusion chamber methods will be taken as a first step to understanding the response of cells to hypertonic stress and consequently freezing conditions.

5.2 Biophysical Model

Considering the cell as an open thermodynamic system, with the cell membrane represented as a semi-permeable barrier (permeable to water but not to salt) across which we describe water transport, the equation describing the volume flux of water, J_v (μm/s), is given as:

$$J_v = \frac{1}{A_c}\frac{dV_c}{dt} = -L_p\left(c^{ex}_{salt} - c^{in}_{salt}\right) \qquad [5.1]$$

where A_c is the surface area of the cell (μm^2), V_c is the volume of the cell (μm^3), t is time (s), L_p is the hydraulic permeability (μm/atm-min), c^{ex}_{salt} is the extracellular salt concentration (Osmoles) and c^{in}_{salt} is the intracellular salt concentration (Osmoles). An increase in the extracellular salt concentration will cause water to leave the cell thereby increasing the intracellular salt concentration. This change in intracellular salt concentration can be related to the changing volume of the cell according to:

$$c^{in}_{salt} = \frac{n^{in}_{salt}}{V_c - V_b - n^{in}_{salt}\upsilon_{salt}} \qquad [5.2]$$

where V_b is the osmotically inactive volume (μm^3), n^{in}_{salt} is the number of moles of intracellular salt, and υ_{salt} is the molar volume of salt (μm^3/mol).

When the change in extracellular concentration is also accompanied by a temperature change (such as can occur in the case of freezing) the temperature dependence of the water activity needs to be considered in the derivation of water transport equations. The first equation to quantify the relationship between temperature and the amount of water leaving a cell during freezing was developed by Mazur (1963). This mathematical relationship has provided the basis for almost all subsequent thermodynamic models of cellular dehydration related to freezing (Mansoori, 1975; Silvares *et al.*, 1975; Levin *et al.*, 1976; Shabana and McGrath, 1988; Toner *et al.*, 1990). There are a number of assumptions used to develop this model including: (1) absence of hydrostatic pressure gradients across the membrane, (2) negligible temperature gradients across the membrane, (3) concentration gradients existing only across the membrane, (4) infinite extracellular space, (5) constant surface area, A_c, (6) spherical cellular space, (7) ideal and dilute intracellular solution, and (8) a constant latent heat of fusion (McGrath, 1985). These assumptions together with basic thermodynamic laws permit an expression of water flux across the cell membrane as:

$$\frac{dn_w}{dt} = \frac{-L_p RT}{\upsilon_w^2} A\left(\ln \frac{a_w^{in}}{a_w^{ex}}\right) \qquad [5.3]$$

where a_w is the activity of water, n_w is the number of moles of water, T is absolute temperature (K), R is the universal gas constant (cm^3atm/mol-K), and υ_w is the molar

volume of water (μm^3/mol). The intracellular water activity, if modeled as an ideal solution, can be given by the mole fraction of available water, X_w:

$$a_w^{in} = X_w^{in} = \frac{n_w}{n_w + (\nu_s n_{salt})} \quad [5.4]$$

where n_w is the number of moles of water and ν_s is the dissociation constant of the solute. In this work the solute is sodium chloride, which is assumed to undergo complete ionic dissociation to yield a dissociation constant of 2. Using the molar volume of water Equation 5.4 can be rewritten as:

$$a_w^{in} = X_w^{in} = \frac{V_w}{V_w + (\upsilon_w \nu_s n_{salt})} \quad [5.5]$$

The water content of a cell is composed of both free and bound water, as well as salt, proteins, and other components that make up cell membranes and organelles. It is convenient to express this relationship as:

$$V_c = V_w + V_b \quad [5.6]$$

where V_w represents the volume of free water, or water available for transport across the cell membrane, and V_b is the volume of the remaining components of the cell once all possible free and unbound water has left the cell. This allows equation 5.5 to be reformulated as:

$$a_w^{in} = \frac{(V_c - V_b)}{(V_c - V_b) + \upsilon_w(\nu_s n_s)} \qquad [5.7]$$

The extracellular water activity can be related to the extracellular concentration and temperature, assuming constant pressure, using a Gibbs-Helmholtz relationship:

$$\frac{\partial}{\partial T}(\ln a_w^{ex})_P = \frac{\Delta H_f}{RT^2} \qquad [5.8]$$

Assuming constant ΔH_f, this can be integrated to yield an expression for extracellular water activity:

$$a_w^{ex} = \frac{\Delta H_f}{R}\left(\frac{1}{T_R} - \frac{1}{T}\right) \qquad [5.9]$$

where ΔH_f (J/mol) is the latent heat of fusion for water, and T_R is the reference temperature of 273.15 °K, the freezing point of pure water.

At constant cooling rates, B, the temperature is related to time according to:

$$B = -\frac{dT}{dt} \qquad [5.10]$$

Combining Equations 5.3, 5.7, 5.9, and 5.10 results in the following water transport equation, expressed as a function of temperature:

$$\frac{dn_w^{in}}{dT} = \frac{L_p ART}{\upsilon_w^2 B}\left[\ln\frac{(V_c - V_b)}{(V_c - V_b) + \nu_s \upsilon_w n_s} - \frac{\Delta H_f}{R}\left(\frac{1}{T_R} - \frac{1}{T}\right)\right] \qquad [5.11]$$

If V_b is independent of time and temperature then:

$$\frac{dV_c}{dt} = \frac{dV_w}{dt} = \upsilon_w \frac{dn_w}{dt} \qquad [5.12]$$

and equation [5.11] can be rewritten as:

$$\frac{dV_c}{dT} = \frac{L_p ART}{\upsilon_w B}\left[\ln\frac{(V_c - V_b)}{(V_c - V_b) + \nu_s \upsilon_w n_s} - \frac{\Delta H_f}{R}\left(\frac{1}{T_R} - \frac{1}{T}\right)\right] \qquad [5.13]$$

The temperature dependence of L_p can be given by an Arrhenius mathematical description (Levin *et al.*, 1976):

$$L_p = L_{pg} \exp\left[\frac{E_{Lp}}{R}\left(\frac{1}{T_R} - \frac{1}{T}\right)\right] \qquad [5.14]$$

where L_{pg} is the membrane permeability at the reference temperature, T_R, and $E_{l,p}$ is the activation energy of L_p.

5.3 Materials and Methods

5.3.1 Determination of V_b, Osmotically Inactive Volume

The osmotically inactive volume can be determined by a number of different experimental approaches. A microscope diffusion chamber, which utilizes a change of extracellular solute concentration to effect a change in cell volume, was utilized in this work. The model of diffusion chamber utilized is depicted in Figure 5.1. The microdiffusion chamber allows cells to be directly observed with a microscope as they respond to changing osmotic conditions produced by an external flow. This apparatus was described in detail by McGrath (1985). The cells are separated from the bulk flow region by a semi-permeable dialysis membrane. As the bulk flow concentration is changed, the change in the local environment of the cell (sample region, Figure 5.1) can be quantified using a simple mass transfer analysis across this membrane.

Cells were cultured according to the methodology described in Chapter 4. Cells were detached from the flask with trypsin when they had grown to nearly a monolayer and were then concentrated by centrifugation. The supernatant was decanted and the cells were then re-suspended in ~1 ml of un-supplemented DMEM media. The cells were placed on the thin plastic window of the diffusion chamber and then covered with a semi-permeable dialysis membrane. The assembly was then inverted and inserted into the customized stage component. The dialysis membrane mechanically separates the cells from the bulk fluid flow, but allows the hypertonic solution to diffuse across the membrane in a quantitative rate-limited manner. A Sony charge-coupled device (CCD) video camera was mounted on the camera port of a Zeiss Universal microscope and the video signal merged with the output of a video timer, the final image being recorded on a

Sony SLV-420 videocassette recorder (VCR). A 25x microscope objective was used together with a 1.25x microscope tube head magnifying lens. The cells were then exposed to and equilibrated in progressively hypertonic solutions (308-1200 mOsm) and the change in cell dimensions monitored microscopically and videotaped for offline analysis. Offline images were obtained using a video capture board and then processed with Image Pro® PLUS software (Media Cybernetics, Silver Spring, MD). Following the 1200 mOsm equilibration step, the cells were returned to isotonic concentration. Only cells that maintained a spherical shape throughout this process and subsequently returned to the starting volume at the end were selected for further analysis.

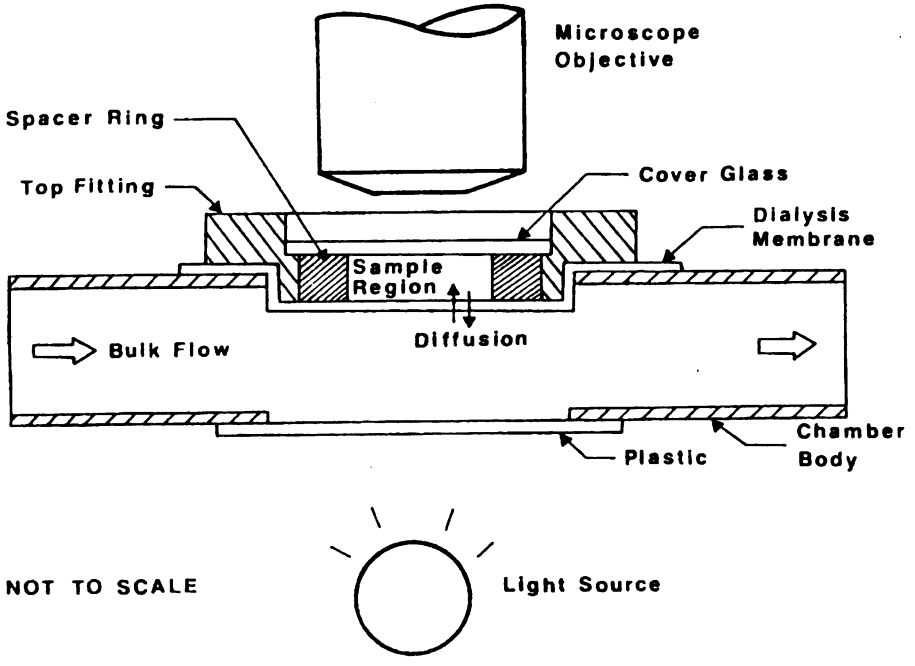

Figure 5.1 Schematic of a microscope diffusion chamber. The semi-permeable dialysis membrane allows solute in the bulk flow region to passively diffuse across the membrane while containing the cells in the sample region. (From Sherban, 1987).

Cell volumes were determined from 2-D image area measurements by manually tracing the outline of the cell three consecutive times and then computing the average of these measurements. With the assumption that the cells were spherical, these circumference measurements were then converted to volume measurements using the following relationship:

$$V = \frac{C^3}{6\pi^2} \qquad [5.15]$$

where V is volume, and C is circumference. The computed volumes were normalized to the starting cell volume and then plotted as a function of inverse osmolarity and a linear regression analysis of the data was performed. The linear equation was then solved for infinite osmolarity (x-intercept = 1/Osm = 0) to obtain the osmotically inactive volume V_b.

$$\frac{V}{V_{iso}} = \frac{M_{iso}}{M}\left(1 - \frac{V_b}{V_{iso}}\right) + \frac{V_b}{V_{iso}} \qquad [5.16]$$

5.3.2 Determination of L_p and E_{Lp}

The microdiffusion chamber used in this work has channels incorporated in the assembly to allow for a temperature regulating fluid to be circulated around the exterior of the sample region. This concept is depicted in Figure 5.2. In the current study the L_p

value was desired at temperatures ranging from ambient to near the freezing temperature of water. Cooled ethylene glycol refrigerant was circulated through the diffusion chamber channels using a circulating programmable refrigeration bath (RTE-140). The bath temperature was maintained at a slighter cooler temperature than the desired operating temperature of the microdiffusion chamber to compensate for heat losses in the Tygon™ tubing used to deliver the refrigerant. The hypertonic solutions were maintained at the desired operating temperature in a reservoir containing ethylene glycol refrigerant. The temperature of this fluid was regulated using a second Neslab circulating refrigeration bath, also maintained several degrees below the desired operating temperature of the microdiffusion chamber. This set-up is depicted in Figure 5.3. The refrigeration baths were mechanically isolated from the microscope to prevent undesirable vibrations in the microdiffusion chamber. The gravimetric flow of fluids to the chamber was controlled by a set of solenoid valves that allowed rapid switching from one solution to another. A bleed line was placed between the solution bottles and the solenoid valves to allow the release of standing solution in the hose before switching from isotonic to hypertonic flow.

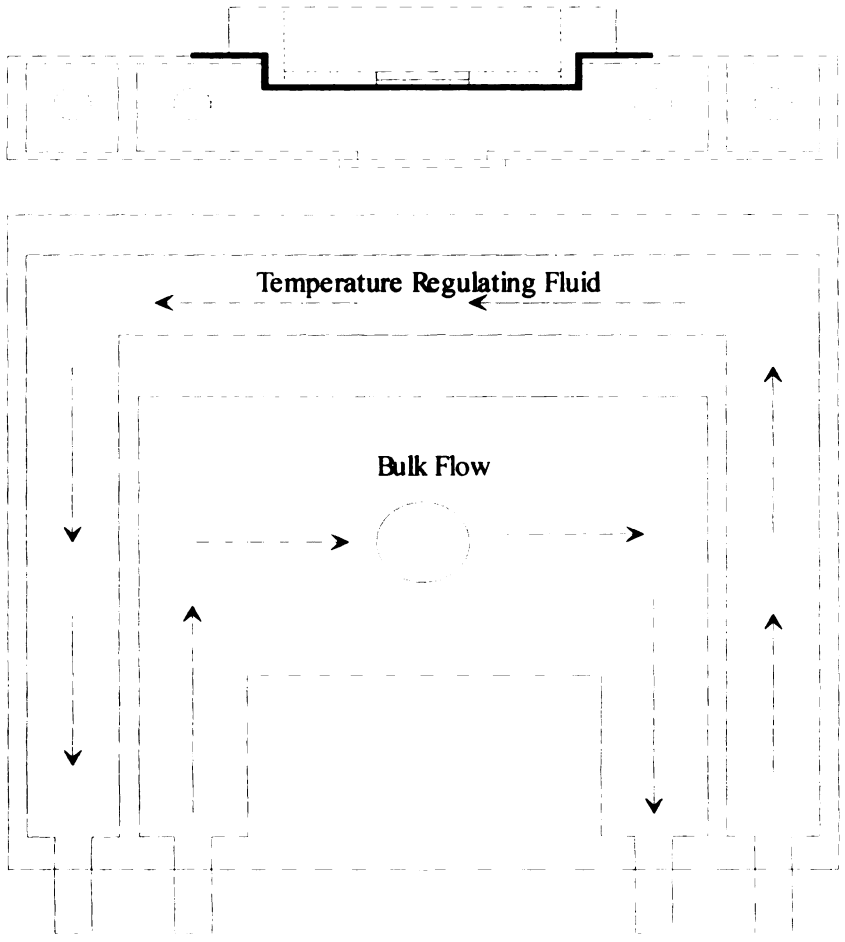

Figure 5.2 Schematic of the temperature regulating channels and bulk flow experimental solutions channels in the microscope diffusion chamber.

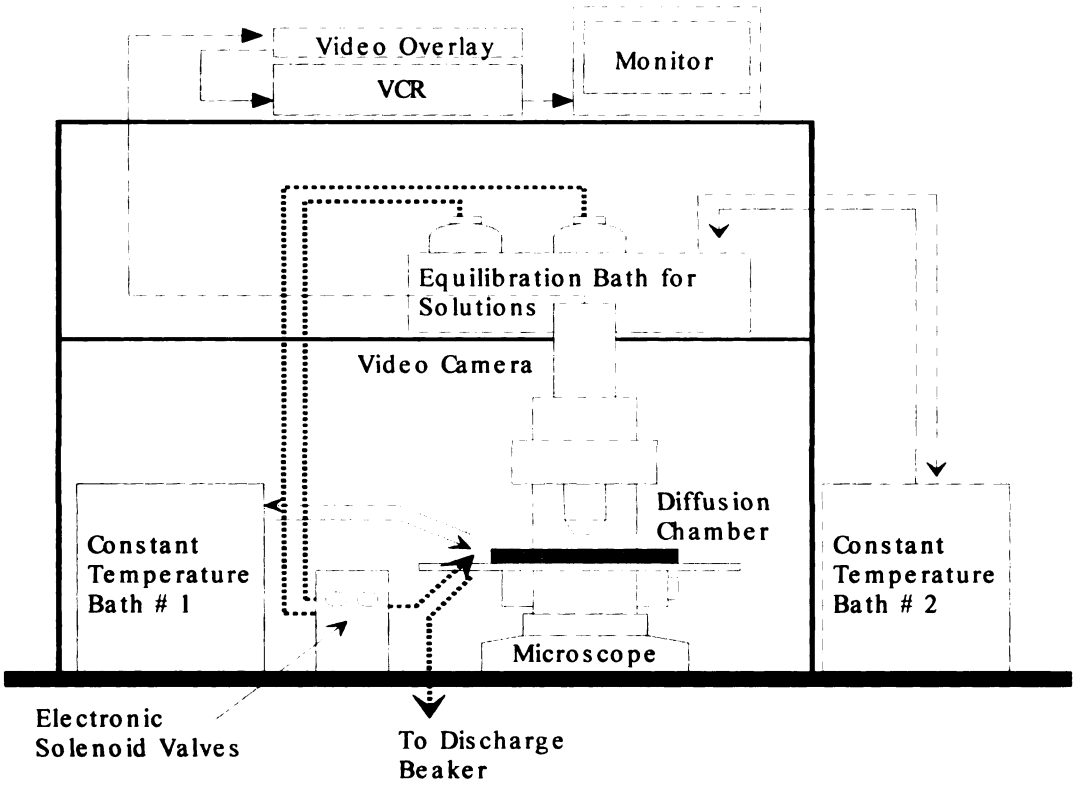

Figure 5.3 Apparatus set-up for acquiring diffusion chamber data at temperatures other than room temperature. Two refrigeration baths are used; the first to cool the outer jacket of the diffusion chamber, and the second to cool the solutions that are flushed through the optical region of the diffusion chamber.

To determine E_a, the activation energy of the membrane permeability, L_p, was determined at 22, 9.5, and 1 °C. The 22 °C data was acquired with the device and fluids at ambient temperature with only air in the temperature regulating channels. In the case of the 9.5 and 1 °C data, the temperature was recorded at the inlet and at the outlet of the microdiffusion chamber and the average temperature chosen to be representative of the thermal environment of the cells in the sample chamber. The temperature difference between the inlet and the outlet was on average 1.5 °C.

Cell suspensions were prepared in the same manner as in the previous section. The cells were placed in the diffusion chamber and first equilibrated in isotonic saline. Next, the cells were exposed to a 900 mOsm hypertonic solution by switching the flow from the isotonic line to the hypertonic line using the solenoid valve switch. The corresponding osmotic response of the cell over time was recorded. The data were quantified by post-processing with Image Pro® Plus software as previously described, except a time course of volume measurements was obtained instead of equilibrium volumes. Based on a measured flow rate through the chamber an adjustment was made in the data to account for the lag time for the solution to traverse the short length of tubing from the solenoid valve to the chamber.

The volume history in the form of radius as a function of time was entered into DIFFCHAM, a parameter estimation program that implements the Kedem-Katchalsky (K-K) model of passive coupled transport across the plasma membrane (Kedem and Katchalsky, 1958; McGrath, 1992). In the absence of a permeating cryoprotectant the K-K model reduces to equation 5.1. The DIFFCHAM program has a built-in routine that compensates for the lag in solute diffusion across the dialysis membrane. The Box-

Kanemasu method of parameter estimation was utilized together with the Gauss method of linearization and ordinary least squares. The L_p coefficient was determined by minimization of the sum of squares:

$$S = \sum_{i=1}^{n} \left\{ Y_i - \eta_i\left(\bar{\beta}\right) \right\}^2 \qquad [5.17]$$

where Y_i is the volume history datum at time i, and η_i the corresponding predicted cell volume at that time, which is based on the current estimate of parameters, given by the vector $\bar{\beta}$. To minimize the sum of squares, the following conditions must be simultaneously satisfied for p, the number of parameters being estimated:

$$\frac{\partial S}{\partial \bar{\beta}_k} = 0 \qquad [5.18]$$

where k=1 to p.

Values of L_p obtained at these different temperatures were then plotted as a function of inverse temperature, and E_{Lp} was determined from a linear fit of this data according to equation 5.13. The slope of this line provided the activation energy.

To ensure that the use of trypsin was not affecting the measured permeability values, a series of measurements was made using cells that had been mechanically removed from the flask. When the cells had grown to nearly a monolayer, the medium was removed and the flask surface was gently scraped with a sterile disposable cell

scraper (Costar, Cambridge, MA). The detached cells were then collected by adding culture media and the cells were transferred by pipette to a centrifugation tube. The rest of the procedure was identical to the trypsin protocol. Because some mechanical damage of cells was expected, cells were evaluated for the presence of GFP fluorescence prior to analysis. A GFP positive cell was considered to have an intact and normal cell membrane as will be validated in Chapter 6. Only GFP positive cells were used for experimentation.

5.3.3 Mathematica™ Programs

5.3.3.1 Validation of Diffcham Results

Because the results of the L_p measurements were unexpected, a check of DIFFCHAM results was performed. Assuming that the sample area chemical profile predicted by DIFFCHAM was correct, an exponential fit to this extracellular concentration history was obtained and implemented in a Mathematica™ program, Diffcham _Check. This simple Mathematica program models cell volume response when provided with concentration histories and parameters. This program is given in Appendix A.

5.3.3.2 Simulation of Water Transport During Freezing

With knowledge of the values L_p and E_a for the GFP-R3230AC cell line, it was possible to predict cell volume change as a function of cooling rate according to Equations 5.13-5.14. A Mathematica™ program was written to simulate the cell volume change at a variety of cooling rates. This program, Vc _Freeze, is given in Appendix B.

5.4 Results

5.4.1 Boyle Van't Hoff Plot

A Boyle Van't Hoff plot was constructed from the equilibrium cell volumes at concentrations ranging from 308 to 1200 mOsm, as shown in Figure 5.4. Each data point represents the average of 13 cells and 3 separate experiments. The y-intercept yields an osmotically inactive volume of 32.7% of the isotonic volume. The correlation was high (R^2=0.9832) supporting the validity of results.

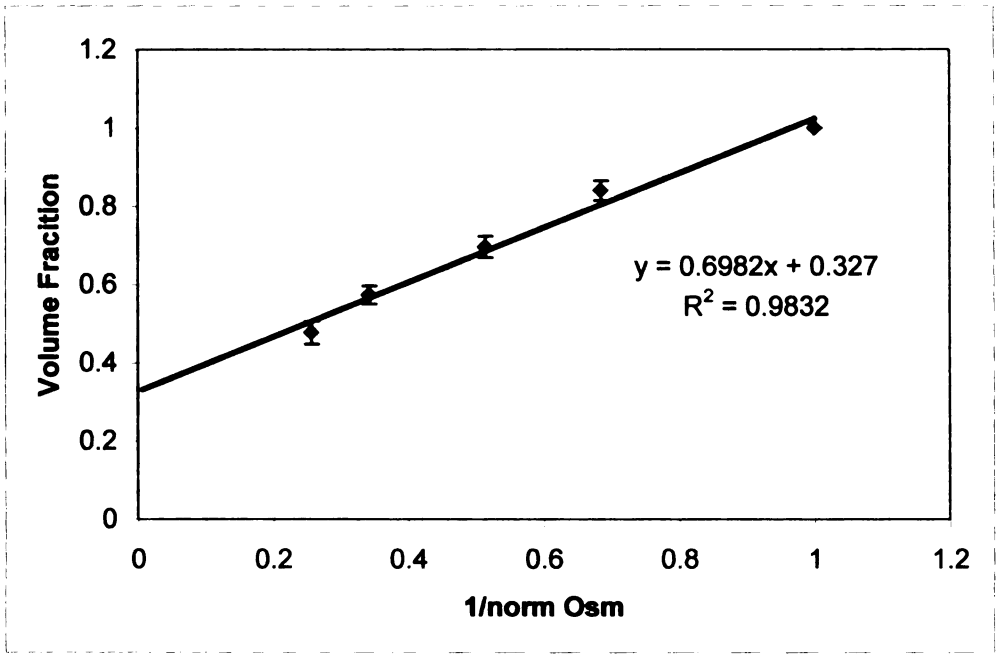

Figure 5.4 Boyle Van't Hoff plot. Errors bars represent standard error of the mean.

5.4.2 Estimates of L_p and E_{Lp}

The cell volume curves obtained for the purposes of estimating Lp did not all fit the simplified K-K model implemented in DIFFCHAM. Data were removed from the final data set on the basis of: (1) blatant deviatory behavior from the expected volume curve, and (2) inability of the program to fit the data to the model. Deviatory behavior was characterized by what appeared to be overshoot and re-swelling behavior near the equilibrium volume. An example of what is considered a good fit to the data is shown in Figure 5.5. In contrast, a poor fit of data classified as 'deviatory' and not included in average Lp results is shown in Figure 5.6. Approximately 50% of the data sets had to be removed due to deviatory behavior or inability of the program to fit the data.

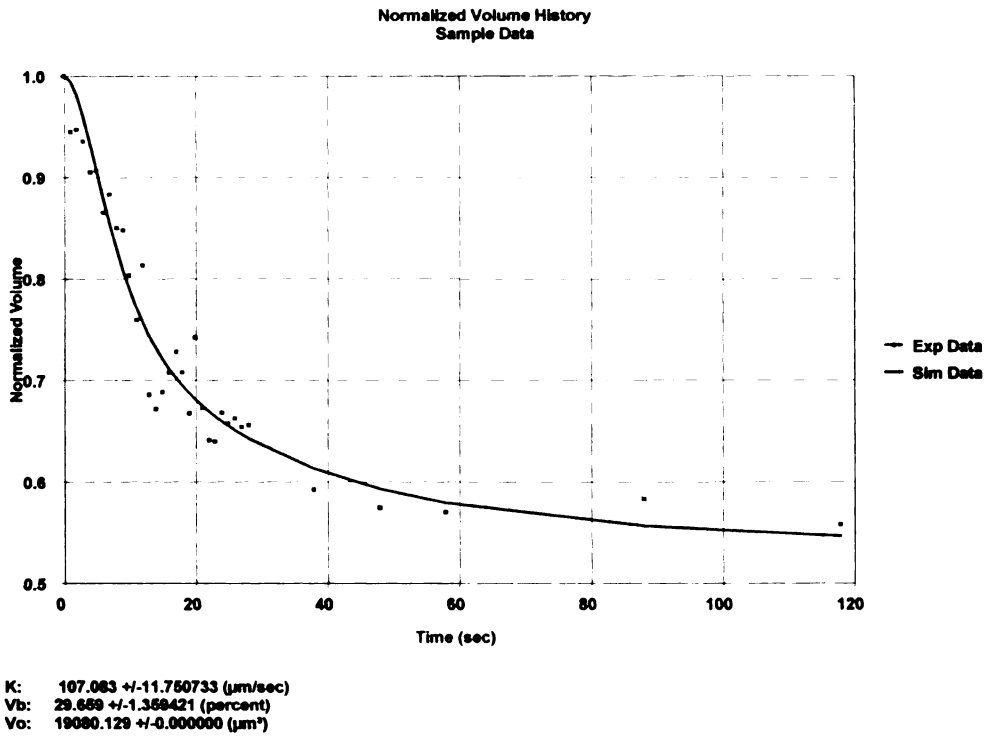

Figure 5.5 An example of a good fit of experimental data to the biophysical model.

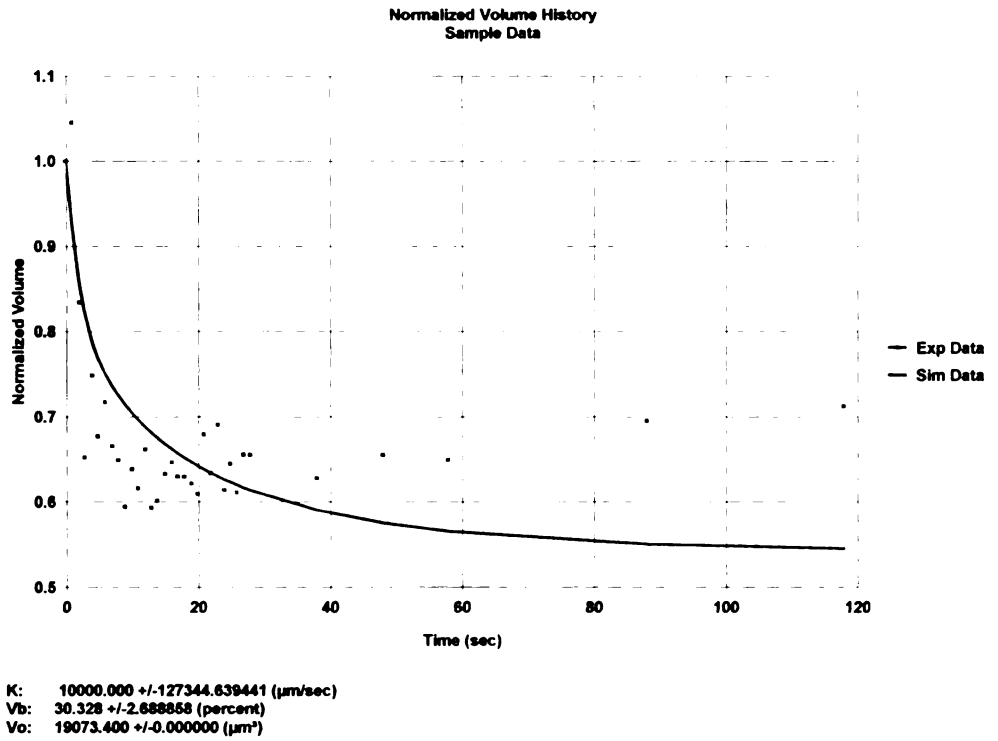

Figure 5.6 An example of a poor fit of experimental data to the biophysical model. Samples with volume histories characterized by a rising volume at the end were excluded from the data set.

To understand if the use of trypsin could change the basic osmotic response of cells, the averaged volume histories and L_p estimates were compared to those of cells that had been prepared for analysis by mechanical scraping instead of trypsin exposure. As can be seen in Figure 5.7, at 22 °C the cell volume histories were similar. Statistically identical estimates of L_p were obtained for these cells as well, as can be seen in Table 5.1.

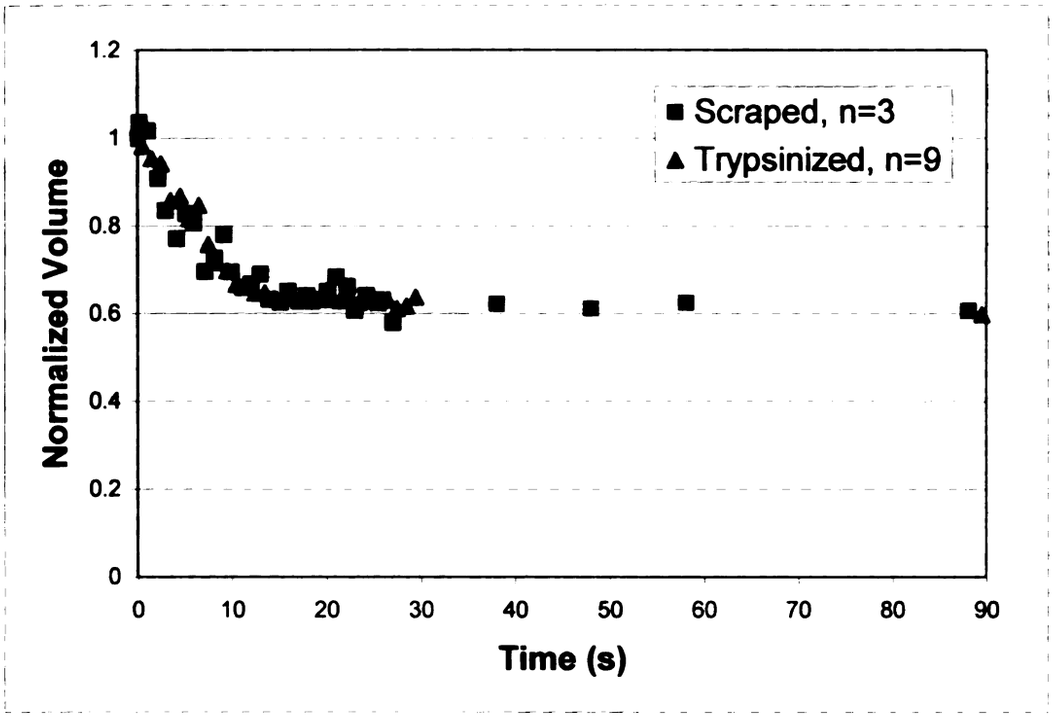

Figure 5.7 Volume histories of cells prepared for analysis by trypsin exposure (triangles) and by mechanical scraping (squares) following exposure to hypertonic solution at 22 °C.

Table 5.1 L_p Estimates (μm/s). (T) and (S) referred to trypsinized cells and scraped cells, respectively.

Temperature (°C)	n	Average L_p	SD	SEM
1 (T)	6	164	283	115
9.5 (T)	10	197	158	50
22 (T)	9	302	274	91
22 (S)	3	305	215	124

The L_p values determined for each temperature are shown in Table 5.1 and are also plotted as a function of inverse temperature in Figure 5.8. A linear regression was used to determine the activation energy from this plot. An E_{Lp} value of 4.2 kcal/mol was obtained. It is important to note that the temperature dependence cannot be considered statistically significant due to the large standard deviations of L_p values. This value of E_{Lp} is consistent with the presence of aquaporins in the cell membrane, as will be discussed shortly.

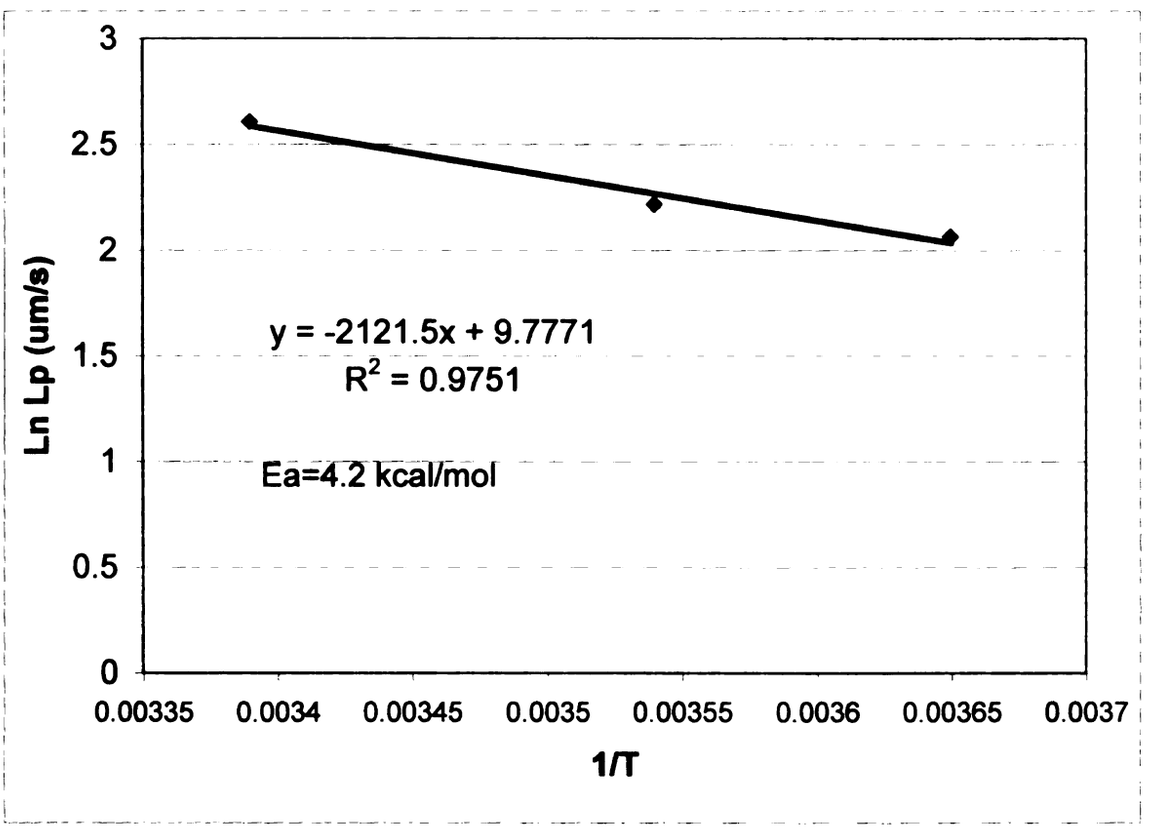

Figure 5.8 L_p as a function of temperature. E_{Lp} is estimated to be 4.2 kcal/mol. Error bars are not shown on the plot but are on the order of the mean.

5.4.3 DIFFCHAM Check

The average volume history of trypsinized cell data (22 °C) used to estimate parameters in DIFFCHAM was plotted together with the simulated results of Diffcham_Check. The predicted local extracellular concentration history and the estimated parameters generated in DIFFCHAM were used in Diffcham_Check. The predicted results from Diffcham_Check were consistent with the original data used to estimate the parameters. Sample results are shown in Figure 5.9. This agreement suggests that DIFFCHAM was providing acceptable estimates of the parameters. It does however assume that the local concentration history in the sample chamber provided by the DIFFCHAM program is accurate.

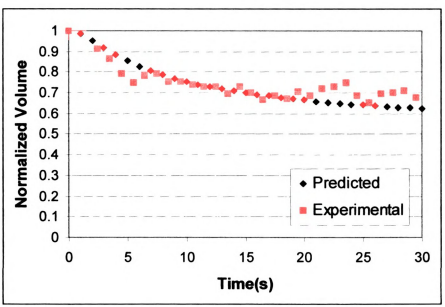

Figure 5.9 Volume histories of trypsinized cells (22 °C) that were used to estimate parameters in DIFFCHAM are plotted together with simulated results from an independent program implementing the DIFFCHAM parameter estimates. The results are consistent, indicating that the DIFFCHAM estimation program is providing accurate estimates.

5.4.4 Water Transport During Freezing

The predicted normalized water volume was plotted as a function of temperature and cooling rate in Figure 5.10. As can be seen in the figure, even at cooling rates as high as 100 °C/min there is very little deviation from the equilibrium curve, suggesting that intracellular ice formation would be unlikely at any rate equal to or less than this. This is further illustrated in Figure 5.11. Using the volume-concentration relationship in the Boyle van't Hoff plot shown in Figure 5.4, the static intracellular concentration can be estimated from the predicted volume curves in Figure 5.10. This osmolarity information, together with the phase change relationship $T_f = -1.858 \times Osm$ (for NaCl), allows the equilibrium phase change temperature to be estimated from the predicted cell volume. This can then be used to compute the amount of under-cooling, or deviation from equilibrium, at a given temperature and freezing rate. The under-cooling represents the difference between the actual temperature and the equilibrium freezing temperature for a given cytoplasmic concentration. The probability of IIF will increase as the amount of under-cooling increases. The results in Figure 5.11 suggest that cooling rates of at least 500 °C/min are necessary to achieve more than a few degrees of undercooling and thereby increase the likelihood of intracellular ice formation. This is similar to the freezing rates predicted by Toner *et al.* (1992) for hepatocytes, also reported to have a high L_p value ($L_{pg} = 1.5 \times 10^{-12}$ m^3/Ns).

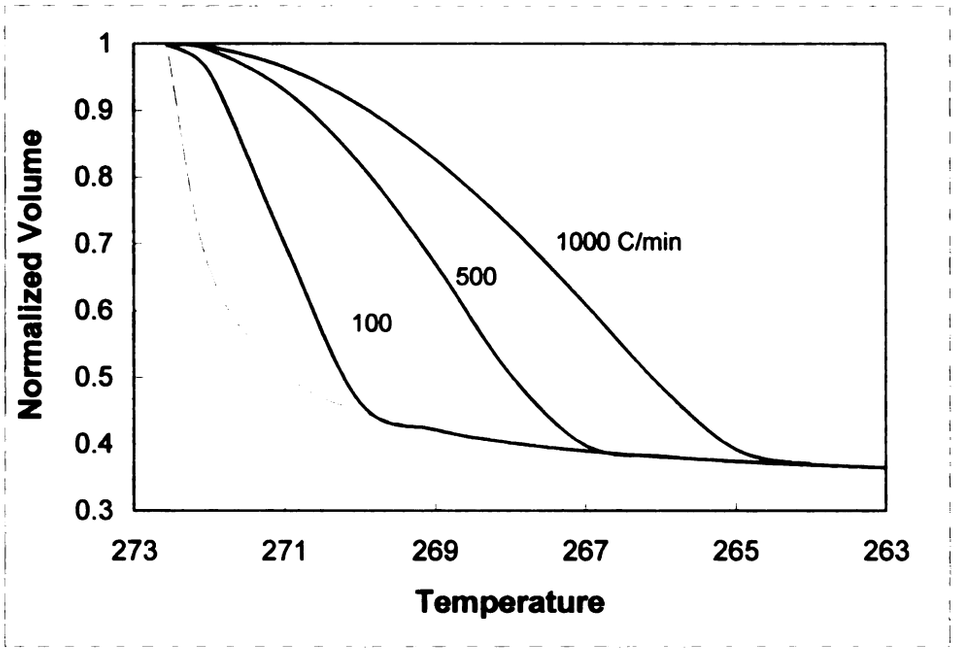

Figure 5.10 Predicted temperature dependence of normalized water volume as a function of cooling rate for R3230AC cells. Cooling rates are indicated on each curve. The dashed line represents the equilibrium response.

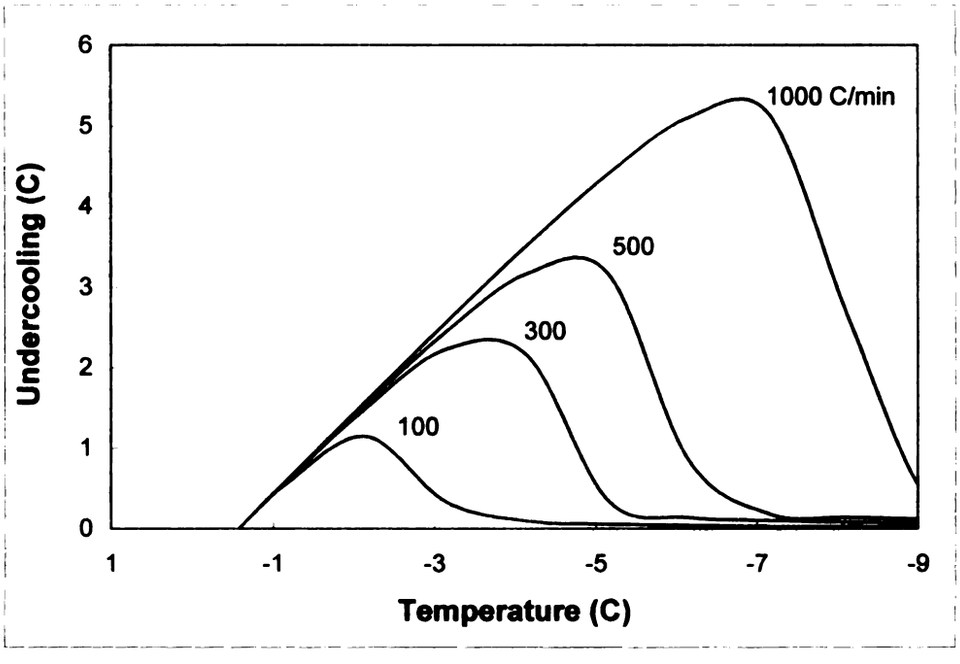

Figure 5.11 Predicted cytoplasmic undercooling of R3230AC cells. Cooling rates are indicated on each curve.

5.5 Discussion

Approximately 50% of the volume histories curves obtained did not fit the K-K model of water transport. The non-K-K behavior could indicate that cell membrane damage may be present, however the basic appearance of the cell and its ability to respond osmotically when returned to isotonicity suggested otherwise. It would be desirable to explore the behavior of these deviatory cells to understand if the observations are artifactual or if they are representative of phenomenological behavior of a portion of the population. If the latter case proves to be true, it is important to understand this behavior in the context of cryo-sensitivity.

The volume response of scraped cells was seen to be more erratic than in the case of trypsinized cells. This may be a phenomenon related to the method of cell preparation or it may be accounted for by the different cell numbers included in the averages, with the trypsinized cell response more effectively 'smoothed' by the larger data set.

The water permeability value estimated for R32230 AC cells is quite high when compared to many of the published L_p values for other cell types. Other cell types characterized as having high water permeabilities include red blood cells (Terwillinger and Soloman, 1981), tumor ascites cells (Hempling, 1977), human myelogenous leukemia K562 cells (Martinez de Maranon *et al.*, 1997), and *Saccharomyces cerevisiae* yeast (Martinez de Maranon *et al.*, 1997). Many of these high permeabilities have been associated with the presence of aquaporin water channels (Martinez de Maranon *et al.*, 1997).

Aquaporins are a class of trans-membrane water selective transporter proteins that facilitate the rapid transport of water both across cells and across vascular structures by causing the formation of channels in the cell membrane (Agre *et al.*, 1995). Aquaporins are widely expressed in epithelia and endothelia that have a fluid-transporting physiologic role (Chou et al., 1999). The presence of aquaporin in cell membranes tends to correlate with high cell membrane or transepithelial water permeability values. For example, Chou *et al.* (1998) demonstrated a fourfold reduction in trans-epithelial water permeability in the inner medullary collecting duct of aquaporin-4 knockout mice. However, there are many tissues that have not yet been examined for the presence or localization of water channels, and pathological tissues have been studied even less. The immunoblot and immunofluorescence study by Endo *et al.* (1999) was the first to examine Aquaporin-1 (AQP1) expression in different types of pathologically altered tissues. They found that AQP1 was not expressed in the cell membranes of normal epithelial cells but was expressed in the cell membranes of tumor cells to varying degrees. A dependence of AQP1 expression on location of the tumor in the animal (cranial or subcutaneous) was found for two out of three of the glioblastomas that were investigated. The protein AQP1 was found to be expressed in the mammary carcinomas they studied, which included the R3230AC cells used in this work. The presence of aquaporins explains the high permeability values measured for R3230AC cells as well as the magnitude of the activation energy. Cells with water channels are known to have low activation energies, due to the insensitivity of water channel transport to temperature (Kleinhans, 1998).

The bulk of studies to characterize the water permeability of biological cells has been performed for a limited range above 0 °C. However when using this information for freezing studies it is necessary to extrapolate these data to sub-zero temperatures. There are many potential dangers in doing so. The activation energy for L_p above and below zero can be markedly different. For example, changes in water conductivity due to phase changes in membranes at sub-zero temperatures or due to increasing solute concentrations, desorption of membrane (Pegg, 1988), or formation of external ice may result in substantial polarization of the membrane proteins and lipids (Toner *et al.*, 1990). The complexity introduced by the behavior of aquaporin water channels as the phase change temperature is traversed is also not well-studied, further complicating the extrapolation of data from above zero to sub-zero. Kleinhans (1998) has indicated that the temperature dependence of L_p for aquaporin-containing cells would be expected to be non-linear due to the different temperature dependences of membrane diffusion and water channel diffusion that give rise to the overall effect.

5.6 Conclusions

The high membrane water permeabilities measured for the R3230AC cell line suggest that cooling rates on the order of 500 °C/min will be necessary to induce the formation of intracellular ice in these cells. The conclusions drawn are meant to be a general guideline for future experimental design, not a definitive indicator of when particular modes of injury are expected. Further cryomicroscopy studies are necessary to determine phenomenological parameters that can be used in the IIF probability models of Toner (1990).

Chapter 6

Validation of a GFP-Based Viability Assay at the Cellular Level

6.1 Assessment of Injury in R3230 AC Cells

6.1.1 Comparison of GFP-based Imaging to Standard Viability Assays Following Freezing

Cells transfected with GFP and cells without the GFP vector were prepared to a concentration of 1 x 10^5 cells/ml in D-MEM culture media. Aliquots of 220 µl were added to 5 x 50 mm plastic vials (Corning, NY), and placed in a programmable refrigeration bath (Neslab RTE-140) at -5°C for 2 minutes. Ice formation was initiated by touching the solution with a cold probe, and a 1-min period allowed for the latent heat of fusion to dissipate. A convenient range of freezing damage was produced in both of these cell lines by freezing from –5°C to minimum temperatures between –10°C and –30°C at 1°C/min. When the bath temperature reached the desired minimum temperature, samples were held in the bath for 10 seconds. The samples were then rapidly thawed by immersion and agitation in a 37°C water bath. After thawing, 20 µl of the cell suspension were added to 20 µl of Trypan Blue solution (0.1% in PBS) and a portion of

the solution was then placed in a hemacytometer. Viability was assessed by counting the number of cells excluding Trypan Blue approximately ten minutes after thaw. Data points represent the average of 3 replicates, each replicate representing the average of sixteen 1 x 10^{-4} ml volume hemacytometer well counts (~80 cells per replicate). The remaining 200 µl of cell suspension (for transfected R3230 AC cells only) were added to one well of a 96 well tissue-culture microplate and either 20 µl of 1.25 mM Ethidium Bromide in D-MEM media (EtBr assay) or 20 µl of D-MEM media (GFP assay) was added. Following a 10-15 minute period of incubation, the microplates were transferred to a Nikon Diaphot inverted fluorescent microscope equipped with a 100 W mercury arc lamp. The wells were illuminated with blue light (450-490 nm) by inserting a FITC filter cube (Chroma Technology Corp., Brattleboro, VT) into the light path. Seven color digital images were captured from approximately the same regions within each well using a SPOT thermoelectric cooled color CCD camera (Diagnostic Instruments, Inc., Sterling Heights, MI). It took approximately 10 minutes to locate each assay region, focus the frame of interest, and obtain a 3-channel RGB image of each test area. The average cell count per control well image was 133 (absolute range: 86-253 cells) therefore each control replicate represented the average of approximately 1000 cells. Images were later analyzed using Image Pro software (Media Cybernetics, Silver Spring, MD). The total number of fluorescent green cells was counted in the GFP assay, and the total number of fluorescent green, EtBr negative (non-red) cells was counted in the EtBr assay. Although the number of EtBr stained cells was not explicitly counted, control wells were generally observed to have less than 3% EtBr positive cells and this percentage increased with decreasing minimum temperature. A color-cube-based counting method, which

identifies all cells within the color range selected by the user was utilized. In this case the cells with the brightest and weakest GFP fluorescence were used to set the color limits. In all assays, cell counts were normalized to non-frozen control counts. Each assay point represents the average of 3 replicates.

The recovery of cells frozen at 1°C/minute to various end temperatures, as assessed by the three assays, is shown in Figure 6.1. A freeze damage curve was obtained, with recovery decreasing as the minimum temperature decreased. For all minimum temperatures there was no statistical difference between the three methods used to assess recovery (Students t-test, p=0.05). It was assumed that in all cases the sample parameter was normally distributed. A linear regression analysis of GFP viability as a function of ethidium bromide viability yielded a correlation coefficient of 0.95 (y=1.1271x). A similar correlation coefficient of 0.97 was obtained for a linear regression analysis of GFP viability as a function of Trypan Blue viability (y=1.0628x).

Figure 6.2 illustrates the change in GFP fluorescence intensity of cells after freezing to different end temperatures. The total number of cells in each template was approximately equal. The GFP intensity in the damaged cells is so low that the cells are undetectable without counterstaining or use of phase-contrast microscopy.

The response of non-transfected R3230AC cells, as assessed by Trypan Blue exclusion (n=3), was comparable to that of transfected cells, as show in Figure 6.3. A correlation of recovery of transfected cells as a function of recovery of wild-type cells yielded a high correlation coefficient (R= 0.98) and a nearly perfectly linear relationship (slope= 0.95). This suggests that, as expected, the presence of GFP does not alter the basic freeze-thaw response.

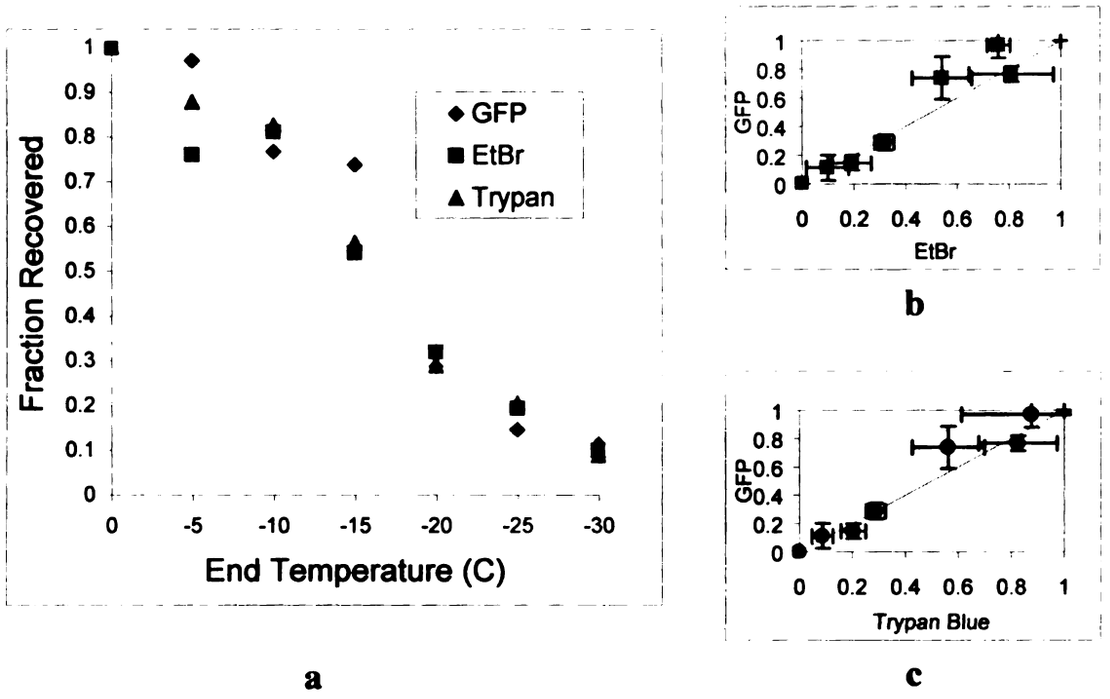

Figure 6.1 (a) Recovery of cells frozen at 1 °C/min to various minimum temperatures, as assessed by GFP fluorescence, GFP Fluorescence with EtBr co-stain, and Trypan Blue Exclusion. (b) Correlation of recovery assessed by GFP fluorescence with recovery assessed by EtBr. (c) Correlation of recovery assessed by GFP fluorescence with recovery assessed by Trypan Blue. Data represent average of three replicates +/- one standard error of the mean.

Fig
var
(b)

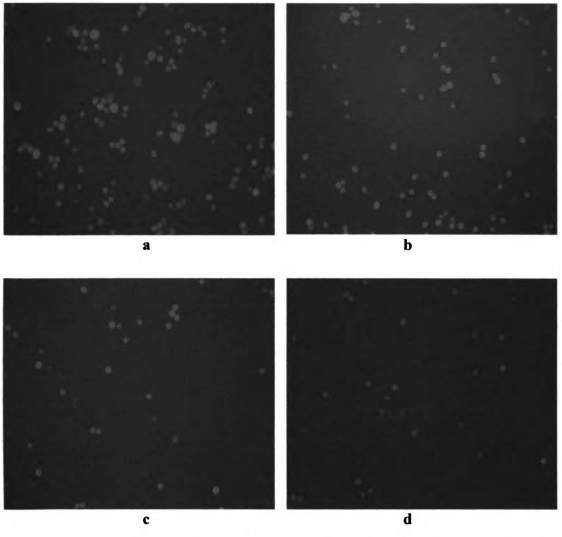

Figure 6.2 Fluorescent images of GFP-transfected R3230 AC cells after freezing to various minimum temperatures and thawing in a 37°C water bath: (a) unfrozen control (b) –10°C (c) –20°C (d) –30°C.

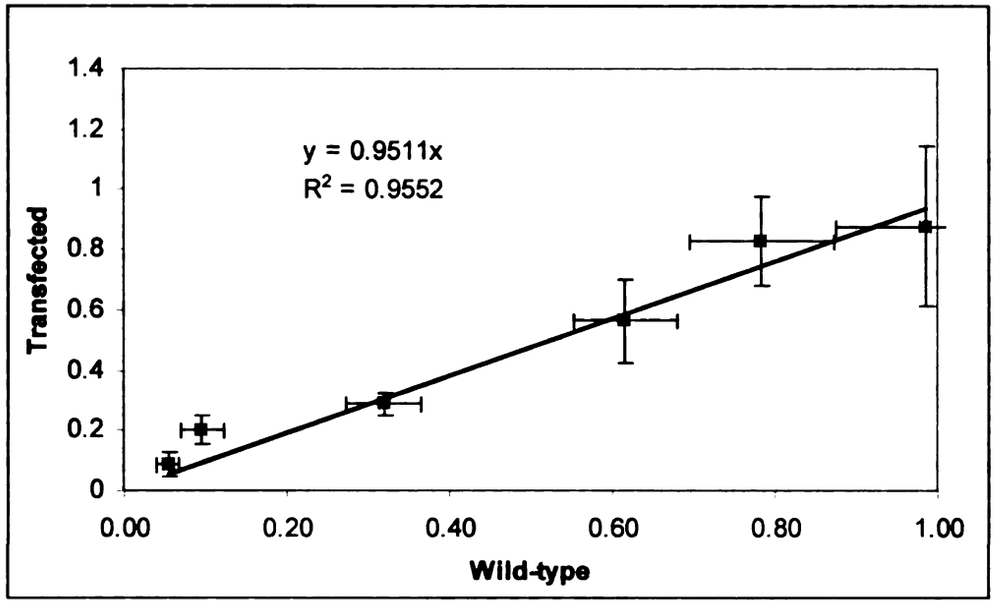

Figure 6.3 Correlation of post-thaw recovery of GFP-transfected and wild-type R3230AC cells frozen at 1 °C/min to various minimum temperatures. Recovery was assessed by Trypan Blue exclusion.

Good agreement between GFP and conventional membrane integrity indicators was obtained as is evident from the correlations (R = 0.95 EtBr; R = 0.97, Trypan Blue) for freeze injury at slow freezing rates. Although the slope of the correlation curves was greater than 1 in both cases, the deviation from the ideal fit is thought to be a dynamic effect, resulting from a slight variation in the time for GFP to diffuse into and ethidium bromide out of the cells. The water-soluble cylindrical GFP monomer is 3 nm in diameter and 4 nm long (Yang *et al.*, 1996). Calculations based on the proposed structure of wild-type GFP yield a molecular weight of 26,862 g/mol (Inouye *et al.*, 1994). Because GFP is a much larger molecule than ethidium bromide (MW: 394.3 g/mol) or Trypan Blue (MW: 960.8 g/mol) it can be expected to diffuse more slowly out of the cell. This combination of diffusion dynamics can give rise to small differences in recovery at a given assay time. Recovery measured with the GFP assay would be expected to be

higher than recovery with EtBr or Trypan Blue assay at a specific point in time, giving a slope greater than 1 in the regression analysis, as observed.

Image-Pro analysis was performed in a way such that the threshold for distinction of GFP-positive cells was chosen as 1 color index (of 10 possible) above background. This was a very conservative measure and included as viable, cells with fluorescence diminished by as much as 90%. A less stringent threshold (eg. 50% of average starting fluorescence) would have resulted in uniformly lower values of recovery. Alternatively, the threshold value could be specifically determined by fitting the GFP recovery data to the recovery data of another viability indicator, such as ethidium bromide or Trypan Blue as used in this study. From a statistical standpoint however, these assays were found to yield equivalent results (Students t-test, $p=0.05$) and therefore the threshold value of 1 color index above background was maintained throughout all experiments.

Some semi-quantitative observations were made over the course of these experiments that also support the use of GFP as a viability indicator. No intracellular GFP fluorescence was observed following rapid freezing by plunge freezing (~500°C/min) in liquid nitrogen (-196°C) and slow thawing (~10°C/min). The EtBr assay also revealed 0% viability for these conditions, suggesting that the GFP assay will be a valid viability assay at rapid freezing rates as well. Overgrowth of cells or lack of fresh media can give rise to nutritional stresses that eventually lead to cell death. When these circumstances were allowed to occur, the GFP fluorescence was found to decay in time as long as these conditions were allowed to persist. At various stages ethidium bromide was added to the flasks and the relative fraction of EtBr(+) cells was qualitatively comparable to the disappearance of GFP fluorescence.

6.1.2 Comparison of GFP-based Imaging to Standard Viability Assays Following Solute Injury

24-well flat bottom tissue-culture-treated polystyrene cell wells (Corning, NY) were plated at a density of 1 x 10^4 cells/mL and incubated at 37°C for a minimum of 24 hours. For the GFP assay the old media was removed and 1 mL of fresh media added. In the ethidium bromide assay, 1 mL of media with ethidium bromide (2.5 μM) was added. This solution was prepared fresh daily. In both assays a region of non-confluent colonies was selected and an image acquired with a Spot digital color camera. The media was then removed and 1.6M or 2.7M NaCl solution added to the well for a total exposure time of 30 seconds. The NaCl solution was then removed and fresh media (GFP assay) or media with ethidium bromide (EtBr Assay) added to the well. Images were acquired at 15, 30, 60, and 90 minutes following return to isotonicity. All assays were performed between 24 and 60 hours after plating, and all solutions were at room temperature. Images were later analyzed using Image Pro Software. In the GFP assay the total number of green fluorescent cells was counted. In the ethidium bromide assay the number of green fluorescent, ethidium bromide negative (non-red) cells were counted. Cell counts were normalized to the starting cell counts to determine the fraction recovered in plated colonies.

Figure 6.4 gives the viability response following exposure of cells to two different concentrations of NaCl solution, as assayed with GFP fluorescence and with ethidium bromide. There are no statistically significant differences between the two assays in time, or with solute strength. The standard deviation of the data for the 2.7M experimental series is substantially higher than the 1.6M series. This is thought to be attributed to the sensitivity of the experiment to human error involved in delivering and

removing the hypertonic solution. As more damage is expected at higher concentrations, error in the time of exposure (estimated at +/- 6%) will result in larger absolute standard deviations under these conditions. Mechanical delivery/removal of solutions would be necessary to improve upon the accuracy of these results. Because the assays tracked reasonably well despite these limitations, an extension of the 2.7 M experiments was not pursued.

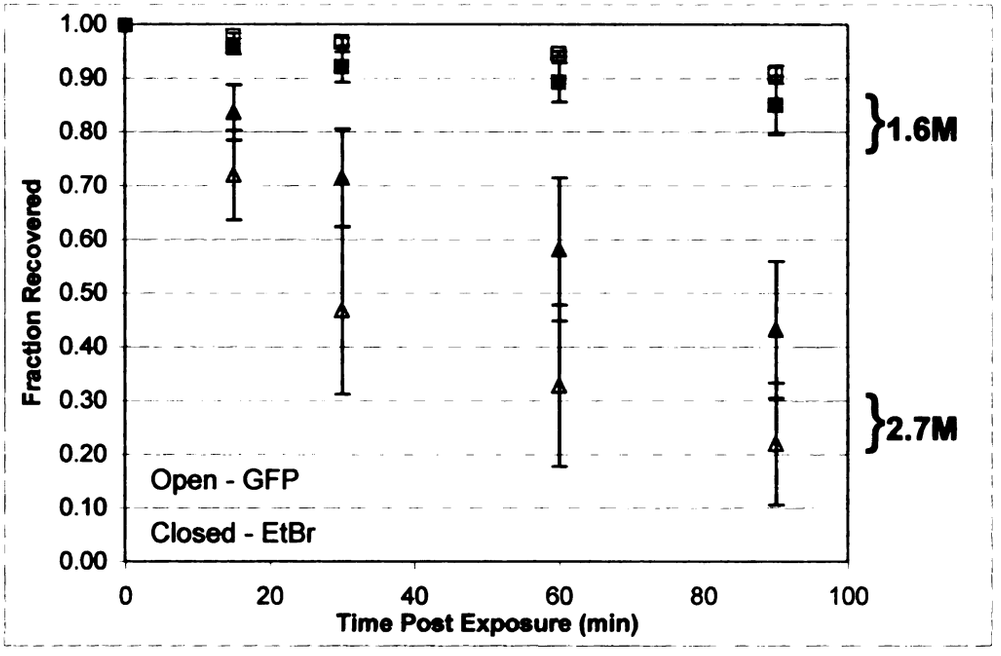

Figure 6.4 Viability of GFP-transfected R3230AC cells following 30 s exposure to 1.6M and 2.7M NaCl.

6.1.3 Clonogenic Assay

Practical experience with GFP transfected cells in culture has revealed that plated cells that have been stressed by overgrowth and lack of fresh media will eventually lose their fluorescence. Cells that reach this stage have not survived subsequent passage and/or supplementation with fresh media. To understand if this observation was also consistent with freezing-induced loss of GFP fluorescence, cells that were predicted to be dead on the basis of GFP assay were subsequently cultured to test for positive cell growth.

One ml of cell suspension (~ 1 x 10^5 cells) was placed in six 1.5 ml eppendorf tubes. Three tubes were held at room temperature for 30 minutes and three were immersed in liquid nitrogen for 2.5 minutes followed by passive thawing at room temperature. Three cycles of freezing and thawing were performed on the contents of these vials. The contents of each vial were then added to a separate T-50 culture flask and 9 ml of D-MEM added. Prior to culture, images were acquired of all flasks using both phase contrast and epi-illumination fluorescence microscopy. Although cells could be identified in the frozen-thawed samples using phase contrast microscopy, they did not have the appearance of control cells, as can be seen in Figure 6.5. Furthermore, fluorescence microscopy revealed dim fluorescence levels in only a few cells in the entire flask, suggesting the population was irreversibly damaged. All cells were then cultured under normal conditions for 3 days (normal passage schedule). On day 3 flasks were removed from the incubator and imaged in the same manner as day 0 cells. The flasks containing the frozen-thawed cells had no identifiable green fluorescing cells and phase contrast microscopy did not reveal any cell growth. Control flasks had reached

confluency. Flasks containing the frozen-thawed cells were cultured for three more days with no growth observed.

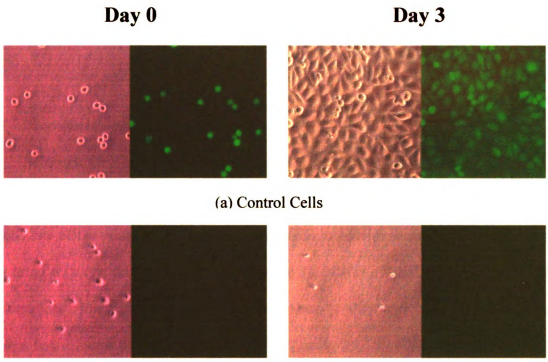

Figure 6.5 Images of cells in culture following different conditions. (a) control cells were held at room temperature for 30 minutes then cultured under normal conditions. (b) test cells were frozen in liquid nitrogen followed by passive thawing at room temperature for three cycles prior to normal culture. The left image of each pair: phase contrast microscopy, right image: epi-illumination fluorescence microscopy.

This experiment demonstrated that for the freezing conditions examined, when GFP fluorescence was lost from cells, the cells were irreversibly damaged. To date, it has not been possible to sub-lethally damage a cell, with loss of GFP. Although the results support the hypothesis that GFP fluorescence loss is indicative of cell death, it

does not definitively answer the question of whether it is possible that GFP loss can occur without cell death. Such an experimental condition is difficult to contrive using freezing as the modality of injury. However, because of the lack of any results to suggest otherwise, it is reasonable to assume this is not a high probability occurrence in the GFP assay.

6.1.4 Photobleaching and Photodamage

Although GFP is known to be resistant to photo-bleaching (Cubitt *et al.*, 1995) this effect needs to be evaluated in the context of each system of study. Additionally, because one of the goals of developing this assay is to provide a means of continuously monitoring cells and tissue, the potentially damaging effects of photo-absorption warrant consideration. For example, Miller and Silverston (1979) were able to kill neurons within a few minutes by pre-loading them with Lucifer Yellow CH and irradiating with blue light from a fluorescent microscope. Although bright GFP fluorescence is desirable for most applications, the capacity to absorb exciting energy can cause damage to system of study if the exposure time is excessive. The limiting total exposure time before the irreversible photo damage occurs is therefore a parameter of interest.

To assess the effects of continuous exposure on the intensity of GFP fluorescence, as well as on the viability of the cells, 24-well flat bottom tissue-culture-treated polystyrene plates were plated at a density of 1 X 10^4 cells/ml. After 24 hours of incubation at 37°C, a population of plated cells was continuously exposed to blue light with the shutter fully open, and digital images were taken of this same population at regular intervals over a time span of 40 minutes. An equivalent assay was performed,

with 2.5 μM ethidium bromide present in the media. Four replicates of the EtBr assay were performed. Images were later analyzed using Image Pro Software. In the GFP assay the total number of green fluorescent cells was counted. In the EtBr assay the number of green fluorescent, ethidium bromide negative (non-red) cells were counted. Cell counts were normalized to the starting cell counts to determine the fraction recovered in plated colonies.

Because GFP is thought to leak out of cells with a damaged membrane, to assess photo-bleaching it is necessary to evaluate fluorescent intensity in cells that are not membrane-compromised. The ethidium bromide assay images that were captured at 40 minutes were examined to isolate specific cells that remained viable throughout the test period. In each test series 3-5 fluorescing cells were selected in the 40 minute images and identified and marked in all of the preceding images using Image Pro software. All images were then converted to gray-scale and the gray-scale intensities of fluorescence of these specific cells were determined as a function of time.

At full illumination (shutter completely open) with blue light, the critical limit before detectable damage accrued was 15 minutes (3% of cells ethidium bromide positive). Significant damage (>10% of cell ethidium bromide positive) was observed beyond 30 minutes. Controls, which were not illuminated, but were incubated at room temperature, did not show any evidence of damage at the end of the 40-minute period, and also displayed bright fluorescence.

Normalized gray scale intensity measurements are shown in Table 6.1 as a function of time for cells that remained viable after 40 minutes of exposure. Data beyond 30 minutes was not reported due to the possibility of photodamage artifacts in the

intensity data. A steady decrease in fluorescent intensity over time can be observed for these cells. At 20 minutes the fluorescent intensity has decreased by 15%. This is comparable to the approximate 20% decrease in fluorescent emission at 510 nm measured with a monochromator by Cubitt et al. (1995) when the S65T mutant of GFP was irradiated at 280 nm with light from a xenon lamp.

Although it can be difficult to separate photobleaching effects from leakage due to photodamage, some degree of distinction was achieved by measuring the decrease in fluorescence intensity for cells that remained viable after 40 minutes of exposure. A steady but slight decrease in fluorescent intensity was observed for these cells over the time interval assayed, indicating that the fluorescence is quite stable for reasonably long exposure times (1-5 minutes). It is possible that this decrease in intensity is due to slight leakage of cytoplasmic GFP caused by damage to the membrane that has not fully manifested itself yet. Given the relative size of the viability markers however, red fluorescence from ethidium bromide would likely be detected before significant loss of fluorescence due to diffusion of the much larger GFP molecule. To avoid photo-induced damage, cells assayed in this work were exposed to blue light illumination for the minimum possible times.

Table 6.1 GFP fluorescence intensity as a function of exposure time for a select population of plated GFP-transfected R3230 AC cells. Data represent averages of four replicates.

Time (min)	Normalized Fluorescent Intensity	SEM
0	1.000	0.000
1	0.980	0.019
2	0.987	0.007
3	0.988	0.009
4	0.986	0.015
5	0.983	0.017
6	0.970	0.017
7	0.968	0.015
8	0.964	0.024
9	0.970	0.026
10	0.964	0.015
15	0.928	0.020
20	0.848	0.018
30	0.783	0.012

6.2 Characterization of the GFP Assay

The loss of GFP fluorescence following exposure of cells to subzero temperatures was rapid in cell suspensions, with dramatic decreases in intensity observed directly after freezing and thawing. It was not immediately obvious whether or not this loss of fluorescence was due to destruction of the chromophore and/or denaturation of the protein, or if it is was simply a leakage and dilution phenomenon. The results of section 6.1 suggest that the GFP may be functioning as a membrane integrity indicator because of the close agreement of damage predictions as assessed by other viability dyes that fall into this category. However, a more systematic approach to understanding the source of GFP fluorescence loss after injury was sought.

Three testable hypotheses were identified that could possibly explain the source of GFP fluorescence loss following exposure of cells to lethal subzero temperatures. These were:

(1) shutdown of protein synthesis

(2) protein denaturation

(3) leakage of GFP from the damaged membrane

Each of these hypotheses was evaluated in an attempt to develop a mechanistic understanding of the basis of the GFP assay.

6.2.1 Intracellular GFP Half-life

Proteins are not immortal. Each protein has a characteristic rate of proteolytic degradation into constituent amino acids for a given set of physiological circumstances (Creighton, 1996). This turnover rate can vary widely for different proteins. For example, ornithine decarboxylase in the rat liver has a half-life of 11-min. By contrast, actin in rabbit skeletal muscle has a half-life of 50-days (Kay, 1978). Because the GFP molecule is extremely robust to thermal denaturation, temperature extremes, and pH extremes (see Chapter 4), it seems likely that the GFP molecule would have a relatively long turnover rate. Determination of the GFP half-life in R3230 AC cells is important in terms of establishing whether protein synthesis shutdown can contribute to fluorescence loss immediately following freezing, but also in determining the limits and maximizing the utility of a GFP viability assay.

To determine the half-life of GFP in R3230 AC cells, cells were incubated in cycloheximide, a protein synthesis inhibitor. When using a protein synthesis inhibitor to

determine the rate of GFP turnover, it is essential to differentiate cytoplasmic GFP loss as a consequence of cell death and possible leakage, with true turnover of GFP resulting from degradation or metabolism of the protein. To do this it was important to establish the integrity of the cell membrane with an indicator other than GFP fluorescence intensity. Ethidium bromide was used to identify a membrane breach.

Twenty-four well plates were plated at a density of 1 x 10^4 cells/ml two days prior to use and incubated at 37°C. At the time of experiment the cells were washed twice with D-MEM media then 900 µl of fresh media was added. A 100-µl aliquot of cycloheximide solution (10 mg/ml) was added to each test well. The control wells were supplemented with 100 µl of media. Plates were then incubated at 37°C for 0, 2, 6, 16, and 24 hours. Prior to imaging the phenol red containing media was removed and replaced with colorless media. Images were acquired using the Spot digital camera, and a 20x objective. Seven images per well were obtained. Characteristic results are shown in Figure 6.6. It can be seen that the control cells (without inhibitor) are growing normally, whereas the cycloheximide-incubated cells do not double as rapidly, and at 16 hours are showing signs of cell death. The GFP fluorescence appeared more diffuse and the location of the boundaries of the cells were more ambiguous.

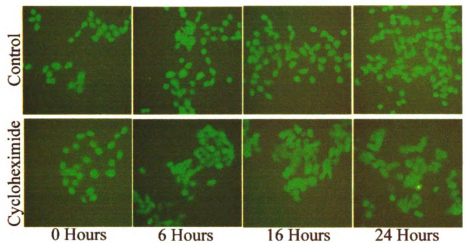

Figure 6.6 Plated R3230AC cells were incubated in cycloheximide, a protein synthesis inhibitor and assayed at several time points in a 24-h period. Control cells (incubated without inhibitor) appear normal whereas the cells in the cycloheximide-incubated group were fewer in number and appeared slightly swollen with indistinct cell boundaries (potentially due to leaky membranes) at the 24-h point.

Images were converted to 16 bit gray scale using Image Pro software. Intensity thresholding tools were utilized to create a photo-mask that fixed all background pixels at zero intensity. Histogram data of the entire field were then obtained to determine the cumulative fluorescent intensity of the cell population. This value was then divided by the area of the un-masked area (the cells), to yield a value of gray scale intensity per sq. pixel for the population. This procedure was reversed to determine a value for the background intensity.

A complementary set of experiments was performed to establish the effect of long cycloheximide incubation times on the viability of the cell. The inhibition of protein synthesis by cycloheximide will certainly affect the vitality of the cell at some stage, as proteins critical for the integrity and normal functioning of the cell will no longer be manufactured. Cells were plated as described above, with identical experimental design.

After incubation at 6, 16, and 24 hours, viability was assessed using ethidium bromide to detect membrane-compromised cells. Seven images were obtained per well yielding approximately 700 total cells per data point.

The results of the viability assessment are given in Figure 6.7. A dramatic decrease in viability is seen between the 16 and 24-hour data points. This viability assessment suggests that analysis of cells for evidence of protein turnover beyond 16 hours will give ambiguous results. Using the methodology described here, after 16 hours of incubation, it would not be possible to discern whether GFP intensity loss in cells was due to leakage from damaged cells or from GFP turnover.

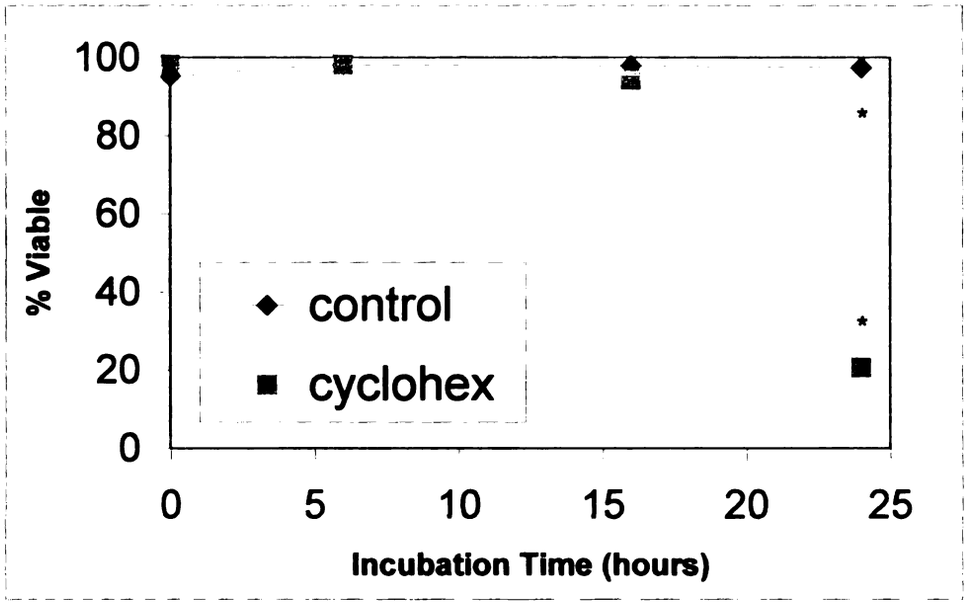

Figure 6.7 Viability assessed with ethidium bromide after different exposure times to the protein synthesis inhibitor cycloheximide. Control cell were incubated in D-MEM media with no cycloheximide present. (* t-test, $p<0.0005$).

The data are plotted in Table 6.2. There was no statistically significant difference between control wells and the cycloheximide-incubated wells at all time points prior to 16 hours, however a small but significant decrease was found at 16 hours (student t-test, $p<0.01$). This suggests that the half-life of GFP exceeds 16 hours. Because cells begin to die after 16 hours of incubation in cycloheximide, persistence of GFP beyond this time is difficult to measure. These results are qualitatively comparable to the half-life of 20 hours reported by Li *et al.*, 1998. Their study did not address the possibility of cell death giving rise to decreased GFP signals, therefore it is possible that GFP does persist much longer than can be effectively measured using protein synthesis inhibitors.

These results establish that the loss of fluorescence directly following freezing cannot be accounted for by a failure of the protein synthesis mechanisms. Even if new protein is no longer manufactured because of damage to the cell components involved in protein manufacture, the GFP produced prior to injury will continue to fluoresce.

Table 6.2 Cell fluorescence intensity as a function of exposure time to cycloheximide. AFU, arbitrary fluorescent units.

	Fluorescence Intensity (AFU)			
	Control		Experiment	
Time(h)	Ave	SD	Ave	SD
0	3.2	0.4	2.9	0.4
2	3.3	0.4	3.2	0.3
6	3.2	0.3	3.2	0.2
16	3.6*	0.1	3.4*	0.1

(t-test, $p<0.001$)

6.2.2 Stability of GFP to Low Temperatures

There is considerable information in the literature regarding the stability of GFP at high temperatures, at high and low pH, and in the presence of denaturants (Bokman *et al.*, 1981). To the author's best knowledge there exists no information on the stability of GFP at low temperatures. Unfortunately there is no structural feature of proteins that definitively indicates a propensity for stability at high or low temperatures, as there are many molecular features contributing to stabilization of molecules at physiologic extremes. Some of these factors include the number of disulfide bonds, the number of salt bridges, the preponderance of ion-pair networks, the inaccessibility of hydrophobic groups, and compactness of the molecule (Scandurra *et al.*, 2000). Proteins that are stable at extremes of temperature and other adverse environmental conditions (termed extremophilic proteins) each contain different manifestations of these characteristics. Thus a detailed examination of the various levels of structure of the EGFP molecule may serve to explain observed stability phenomena, but it does not provide predictive power for a range of conditions, such as expected low temperature behavior.

Generally protein functionality or activity at low temperature is achieved at the expense of stability at high temperature, because the molecular flexibility required for catalytic activity (the raison d'etre for many proteins) at low temperatures is in opposition to the rigid nature of proteins that are stable at high temperatures. Conversely, the rigidity associated with high temperature proteins can result in a non-functional protein at low temperatures. From an evolutionary standpoint however, GFP does not have a catalytic role *per se*. It serves as an energy transfer molecule, producing a shift in light emission from blue to green when combined with luciferin and luciferase (Ward and

Cormier, 1979). Rigidity that might be associated with the molecule's reported high temperature stability may not necessarily result in a stability or fluorescence functionality trade-off at the low end of the temperature spectrum.

Despite the complexity of structure-stability relationships that exist in proteins, there is one structural feature of GFP worth highlighting that may suggest expected low temperature behavior. Because the chromophore is encapsulated within the GFP 'β-can' (see Chapter 2), in general the fluorescence functionality will likely be protected until such time that the protein molecule either becomes completely denatured by normal thermodynamic means or the tertiary structure becomes significantly altered by mechanical forces that might be associated with ice crystal formation.

Nardid *et al.* (1997) studied the effect of freezing and thawing on the fluorescent proteins P450 and spectrin using fluorescent spectroscopy. They specifically examined the structural state of the molecules as measured by changes in the location and magnitude of spectroscopic peaks. Their results revealed a small shift towards longer wavelength of the emission peak maximum following liquid nitrogen immersion and subsequent thawing of these proteins in buffer solution. The authors suggested that freezing and thawing induced macromolecule surface loosening and consequently a conformational change that exposed the protein chromophores to the solution molecules. These changes were irreversible. Although studies of this nature have not been performed for a wide variety of fluorescent proteins, the fact that both spectrin and P450 had similar structural changes resulting in mildly altered fluorescent spectra parameters suggests that this phenomenon might be a minor factor in decreased fluorescent intensity measured in EGFP-transfected cells following freezing.

All experiments performed up to this point suggest that the absence or dramatic decrease of green fluorescence from a transfected cell that was fluorescent prior to the event, means the cell is dead. However, it is critical to understand if, following freezing conditions that are non-lethal to GFP-transfected cells, fluorescence can be diminished by denaturation or degradation of the protein to an extent that a live cell can be deemed non-viable by the GFP assay. The high correlations of the GFP assay with other viability assays together with the results of clonogenic assays suggest that this would be highly improbable. However, this hypothesis was tested directly with pure EGFP in solution.

Before using the expensive recombinant protein, troubleshooting of the experimental system was performed using InSpeck Green (505/515 nm) calibration beads of fixed intensity [Molecular Probes, Eugene, OR]. A small amount of each calibrated bead solution (~ 5 μL sample) was placed on a microscope slide and allowed to dry before mounting and sealing with a cover slip. The mounted samples were then placed on the stage of a Nikon Eclipse Fluorescent microscope [Mager Scientific, Detroit, MI] equipped with a 460-500 nm excitation filter, a 505 nm dichroic mirror, and a 510-560 band pass filter. Images were taken using a 12-bit Cooke SensiCam [Cooke Corp., Auburn Hills, MI] with a 0.1 s exposure time. Using Image Pro software [Media Cybernetics, Silver Spring, MD] to obtain measurements of gray scale intensity of the central portion of the beads, a calibration curve was constructed and is shown in Figure 6.8. Each data point represents the average of 5 calibrated beads. The correlation obtained was consistent with the manufacturer's specifications.

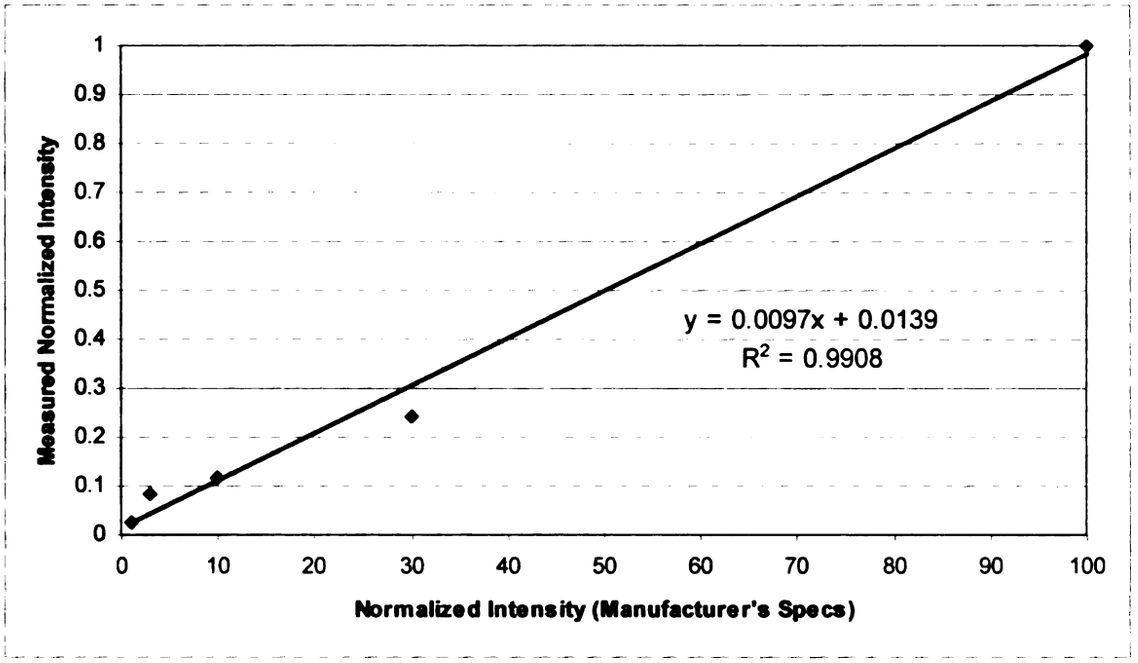

Figure 6.8 Calibration curve obtained with InSpeck Green calibration beads illuminated with blue light (510-560 BP filter), and detected with a Sensicam camera, 0.1s exposure time.

The stability of the Opti-Quip Kobosha light source was tested by examining one set of beads over an extended time period to identify drift or fluctuations in the intensity measured. Images were obtained every 30 seconds for a 3 minute period for the 30% intensity beads. Small bitmaps (4x4) of the central portion of 5 beads were obtained and analyzed for gray scale intensity. The average deviation of measured intensity was 1.1% (one standard deviation from the average) during this time period, with a maximum deviation of 1.8%, suggesting that the light source was relatively stable over short periods of time.

Because the rEGFP measurements were going to be performed on liquid solution samples contained in capillary tubes, sodium fluorescein solutions were implemented to understand any complexities that might be introduced by this approach. Serial dilutions of sodium fluorescein were made up in distilled water, to bracket the concentration range

0.02 to 0.1 mg/mL. Samples were drawn up in 0.1 mm path length capillary tubes (In Vitro Diagnostics, NJ), sealed on both ends, and placed on a glass microslide. Upon illumination with blue light (ex. 460-500 nm; em. 510-560 nm), images were captured with the Cooke SensiCam with a 0.1 s exposure time. A 250 pixel x 250 pixel bitmap of the capillary tube was analyzed with Image Pro for average gray scale intensity. The calibration curve is plotted in Figure 6.9. As evidenced by the value of the coefficient of variation (0.98), the calibration curve was quite linear, which suggested that the experimental system was adequate for attempting to construct a similar curve for rEGFP in solution.

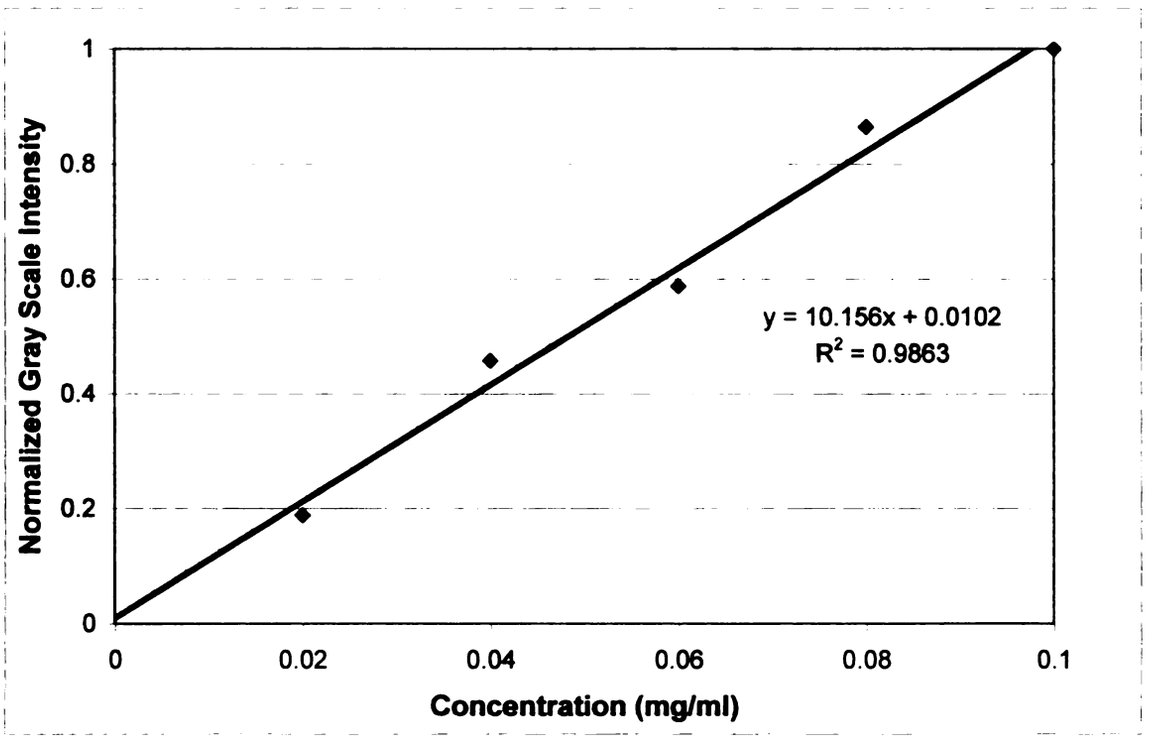

Figure 6.9 Calibration curve obtained with Sodium Fluoroscein solutions in capillary tubes, path length 0.1 mm, 0.1 s exposure time.

A calibration curve of fluorescence as a function of concentration of pure GFP was constructed to understand the levels of EGFP that can be detected with the equipment currently available, and to serve as a standard for estimation of EGFP concentrations in the population. In the case of liquids, the fluorescent signal comes from both in-focus and out-of-focus regions of the sample, with light absorption and scattering also influencing the overall fluorescence measured (Yuan *et al.*, 1993). To avoid possible artifacts from light attenuation differences associated with scattering and reflectance, 20 μm capillaries were chosen for determination of calibration curves. These capillaries are within a few micrometers of the diameter of a suspended cell. The intensity from the center of cells in suspension would be expected to represent an integrated intensity over the nominal 14- micron diameter. In this manner the calibration curve can be used to directly estimate the concentration of EGFP in cells based on gray scale levels.

Calibration curves were constructed using recombinant EGFP (rEGFP) [Clontech Laboratories Inc., Palo Alto, CA]. Capillary tubes very close to the diameter of the cells were used to contain the samples of rREGP for determination of sample intensity. Serial dilutions of rEGFP were made up in 10 mM TRIS-HCl buffer (pH 8.0) to bracket the concentration range 0.0025 to 1 mg/mL. Similar to the procedure for preparing sodium fluorescein solutions, small samples of protein solution were drawn up into 0.02 mm capillary tubes [Vitro Dynamics Inc., Rockaway, NJ] and placed on a microscope slide. Upon illumination with blue light, images were captured with the Cooke Sensi-cam camera with a 0.4 s exposure time and analyzed with Image Pro. Three images of each sample were taken at approximately the same depth in the capillary with a 0.4 s exposure time. Three images of each capillary were taken and test area bitmaps of 249 pixels x

251 pixels were acquired of the imaged capillaries. Gray scale intensity results of the three areas were averaged to obtain each data point. Data to construct the calibration curve was also acquired after the solutions were held at 5 hours at room temperature in light-impermeable containers. This curve deviated less than 3% from the original curve, hence the two sets of data were pooled to obtain the calibration curve plotted in Figure 6.10. Data represents the average of six bitmap images from two separate capillary tubes. Background corrections based on blank capillary intensity levels were applied to the data in Figure 6.10

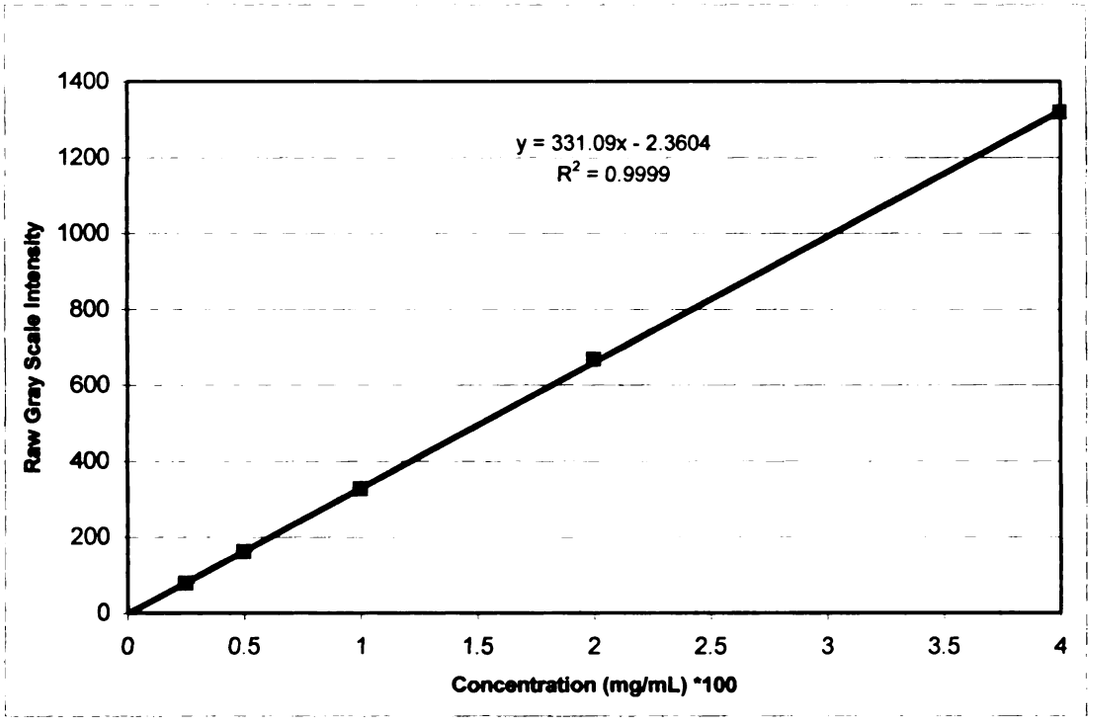

Figure 6.10 Calibration curve obtained with rEGFP solutions in capillary tubes of path length 0.02 mm using a 0.4 s exposure time. Error bars are smaller than the data point markers.

Patterson (1997) has indicated a cytoplasmic concentration threshold of ~200 nM for EGFP (approximately 10,000 GFP molecules per cell) versus ~1 μM for wild type (Niswender *et al.*, 1995) is necessary to detect a fluorescent signal that is twice the autofluorescence level. These studies were performed in HeLa cells. The detection threshold determined in these experiments with capillary tubes was similar to the results of Patterson, with a threshold of 220 nM to detect a signal that is twice the auto-fluorescence level of capillaries filled with buffer solution.

To test the stability of the EGFP protein to extreme low temperatures a dilute sample of rEGFP was treated with what considered in the cryosurgery literature to be a highly damaging freezing protocol. A 0.5 mL Eppendorf tube containing a 50-μl sample of 4×10^{-2} mM rEGFP was plunged into liquid nitrogen and held for 2.5 minutes, followed by uncontrolled warming at ambient room conditions. Ten minutes after the sample had melted it was plunged into liquid nitrogen and the procedure repeated for a total of three freeze-thaw cycles. Control samples were maintained in a light impermeable container at room temperature and sampled at the same time as the treated solutions. For intensity analysis, samples were drawn up into small capillaries of path length 0.05 mm (Vitro Dynamics Inc., Rockaway, NJ) and placed on the stage of a Nikon Eclipse Fluorescent microscope [Mager Scientific, Detroit, MI] equipped with a 460-500 nm excitation filter, a 505 nm dichroic mirror, and a 510-560 band pass filter. Three images of each sample were taken at approximately the same depth in the capillary using a 12-bit Cooke SensiCam [Cooke Corp., Auburn Hills, MI] with a 0.4 s exposure time. The test was performed in triplicate with a fresh working solution of rEGFP. Test area bitmaps of 250 pixels x 250 pixels were acquired of the imaged capillaries using Image

Pro software [Media Cybernetics, Silver Spring, MD] and the gray scale intensity results of the three areas were averaged to obtain each data point. The resultant decrease in intensity is presented in Figure 6.11. Error bars represent the coefficient of variation based on one standard deviation of nine bitmaps.

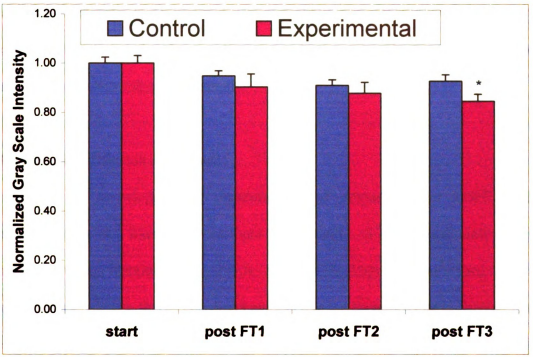

Figure 6.11 Decrease in intensity measured following multiple freeze-thaw (FT) cycles of $4x10^{-2}$ mM rEGFP solution. Control samples were maintained in a light impermeable container at room temperature and sampled at the same time as the treated solutions. Error bars represent the coefficient of variation based on the standard error of n=9 bitmaps. *Significant difference against control ($p<0.01$, one-sided t-test).

Results from direct freezing of rEGFP solutions suggest that damage or denaturation of the protein would be expected to contribute very minimally to a decreased fluorescence signal in cells following freezing. Based on a one-sided t-test of treated and control samples, a significant decrease ($p<0.01$) was not observed until the

end

of a

iden

likel

follo

cell

ques

fluo

the

6.2.

tem

resp

auth

of

lack

mer

not

mer

dilu

sho

diff

end of three freeze-thaw cycles. The level of decrease measured even after three cycles of aggressive freezing and thawing (~15%) was not of a magnitude that would result in identification of a cell as non-viable per the GFP assay. This result suggests that there is likely a more pronounced mechanism responsible for the GFP intensity change in cells following freezing. Because membrane breach is widely accepted as a consequence of cell injury following freezing, it is logical to assume that GFP leakage would occur. The question now remains as to whether or not leakage and subsequent dilution of the fluorescence signal can take place on a spatial and temporal scale that is consistent with the loss of signal observed experimentally.

6.2.3 Diffusion-Dilution Hypothesis

With the knowledge that denaturation and degradation of EGFP at low temperatures was not likely to contribute significantly to the overall cell intensity response following freezing, the question of EGFP leakage was addressed. To the author's best knowledge, there is no direct evidence in the literature that indicates the size of lesion that might be induced in a cell membrane following freezing. Because of this lack of information, for the time being it is assumed that damaged cells will have a membrane breach of adequate size such that diffusion of EGFP into the aqueous media is not inhibited. Thus, the hypothesis is that EGFP can diffuse through a damaged membrane immediately upon thawing, on a time and distance scale that would result in dilution of the EGFP concentration to an extent that it falls below a certain threshold shortly after cell injury. This concept will subsequently be referred to as the dilution-diffusion hypothesis.

A series of experiments was performed next to establish the concentration of EGFP in EGFP-transfected R3230AC cells. Concentrated solutions of EGFP-transfected R3230 cells were drawn up into capillaries and images acquired under identical conditions as the calibration curve. A total of nine images were acquired of three separately drawn capillaries. The fluorescent intensity of the cells was determined by averaging the pixels in an 11x11 bitmap positioned at the center of the cell. This bitmap size was chosen because it covered approximately 30% of the cell area and was relatively uniform in intensity. In this manner 345 cells were analyzed and a histogram of the results are plotted in Figure 6.12. There appears to be two distinct peaks in the histogram. The bulk of the population (90%) is distributed in the 850- 3650 range and is positively skewed, but the remaining population appears to be centered near 4050. Because the population goes off-range at this point it is difficult to describe its distribution. All cells that were off-scale were lumped together at the theoretical 4150 level, as only 4096 levels of gray scale are possible with a 12-bit camera. It is likely that cells in this region of the distribution represent the fraction of the population undergoing mitosis, with an effective doubling of the cytoplasmic contents, including EGFP. Using the mean gray scale intensity level of the first segment of the distribution, 2075, one would expect the mitotic sub-fraction to have a mean gray scale intensity level of 4150. This is consistent with the observed histogram. The median and mode of the main population (850-3650) are 2027 and 1550, respectively. The mean of the entire population was 2295. Based on the mode of the main population shown, this direct gray scale intensity level, when corrected for background media fluorescence, would yield a

cellular EGFP concentration of 0.044 mg/mL according to the calibration curve in Figure 6.10.

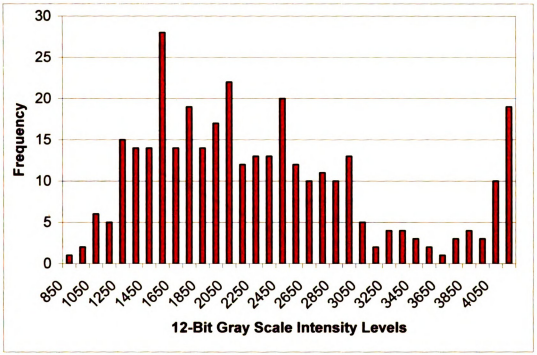

Figure 6.12 Histogram of 12-bit gray scale intensity levels measured in a population of R3230 AC cells.

A simple mathematical model of EGFP diffusion was desired to probe the dilution-diffusion hypothesis. Although an understanding of nominal EGFP concentrations in cells was now possible with the available experimental data, a value of EGFP diffusivity was necessary for the calculations.

To obtain an estimate of the mass diffusivity coefficient for EGFP, known values of diffusivity for other proteins were plotted as a function of molecular weight of the molecule. As can be seen from Figure 6.13, the value of diffusivity for proteins tends to

correlate highly with molecular weight. Based on a molecular weight of 27,000 g/mol, the diffusivity of EGFP would be estimated as 9.24 x 10^{-7} cm^2/s in aqueous solution if the linear best-fit line in Figure 6.11 were used. As discussed in Chapter 2, the diffusivity coefficient measured for the GFP mutant S65T, a protein very similar to EGFP, was 8.67 x 10^{-7} cm^2/s. These values are very similar. The average of these two values, 9.0 x 10^{-7} cm^2/s, will be used in subsequent calculations.

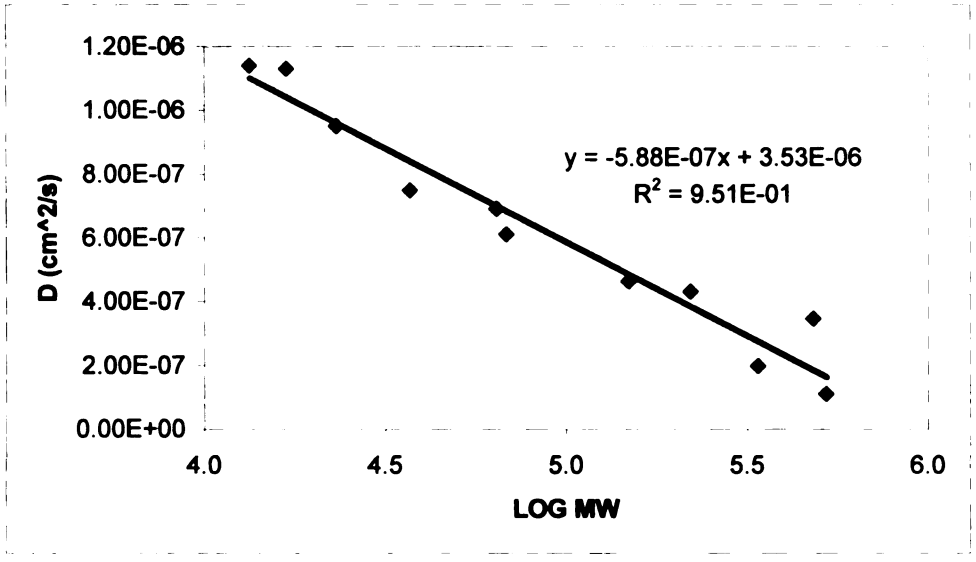

Figure 6.13 Curve-fitting was used to estimate a diffusivity value on the basis of molecular weight. Data for plot was obtained from Lehninger, 1976.

A 1-D radial diffusion model was used to calculate the expected time constant for diffusion of GFP into the extracellular space:

$$\frac{\partial C}{\partial t} = D\left[\frac{1}{r^2}\frac{\partial}{\partial r}\left(r^2\frac{\partial C}{\partial r}\right)\right] \qquad [6.1]$$

In this equation C is the concentration of GFP, r is radius, and t, time. Laws of scaling analysis were used to simplify the derivatives and achieve an order-of-magnitude estimate of the time constant for radial diffusion. The derivatives in Equation 6.1 were simplified as follows:

$$\frac{C}{t} \sim D \frac{1}{r^2} \frac{1}{r} \frac{r^2 C}{r} \qquad [6.2]$$

that leads to a characteristic diffusion time of:

$$t \sim \frac{r^2}{D} \qquad [6.3]$$

The characteristic radius used in this calculation can be understood from the diagram in Figure 6.14. Using the mode of the population described by the histogram in Figure 6.12, and the rEGFP calibration curve given in Figure 6.10 to determine the concentration, a 1:20 dilution factor would be necessary to result in a decrease of the fluorescence of an average cell to background intensity levels (i.e. that of culture media in capillaries). The radius of a sphere that would result in this decrease in intensity was computed based on the change in volume necessary to achieve the 1:20 dilution. The characteristic radius to be used in Equation 6.3 is not the radius of this sphere, but the difference between the starting radius and the final radius necessary to achieve this dilution. This is the distance that the outermost molecule would have to travel to reach the outermost edge of this sphere. This characteristic radius was determined to be 12 μm.

Using this value together with a diffusivity value of 90 $\mu m^2/s$ yields a characteristic time for diffusion of 1.6 s. This is consistent with the observation that GFP fluorescence following cell injury is of order seconds to minutes in cell suspensions.

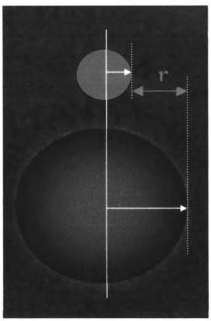

Figure 6.14 Schematic to illustrate the characteristic radius required for determination of the time constant for diffusion of GFP.

In an attempt to extrapolate to expected *in vivo* behavior it is important to understand that cells in a tumor are close-packed with only a finite amount of extracellular space into which the GFP could diffuse. Using a cell volume fraction of 0.5, we could thus expect a dilution factor of approximately 1:2. The diffusivity value would also be expected to be higher because the transport *in vivo* would be expected to be more hindered than in a pure aqueous environment. In choosing an appropriate estimate of

GFP diffusion *in vivo*, several models were examined which are summarized in Table 6.3. It is noteworthy that the values listed are within a narrow range. The Nugent and Jain (1984) value was chosen as the situation most closely resembling the steady state *in vivo* environment. Their value represents the diffusion coefficient of a 27 kD molecule in the interstitium of intact tissue. The situation following freezing *in vivo* would be expected to be more hindered however, as cell debris and extravasated red blood cells would serve to slow the movement of the GFP molecule. Of the values considered, the AT-1 nucleoplasm model provided the most hindered environment. A value intermediate to these, 1.9×10^{-7} cm^2/s, was therefore chosen to determine the expected time constant for GFP diffusion *in vivo*, following freezing. Because the expected dilution factor *in vivo* is expected to be only 2-fold, the *in vivo* characteristic radius was calculated to be 2 μm. The time for diffusion to occur to an extent that the signal drops 50% is calculated to be 0.2 s. This indicates that if freezing *in vivo* directly damages cells, the characteristic drop in fluorescence (~50% decrease) would be very rapid.

Table 6.3 Literature diffusivity values applicable to GFP diffusion *in vivo*.

D^*1x10^7 (cm^2/s)	Molecule	Matrix	Source
2.23	27kD (1)	Carcinoma	Nugent and Jain (1984)
2.71	EGFP	Cells	Swaminathan, (1997)
1.64	EGFP	AT-1 cytoplasm	Wachsmuth *et al.* (2000)
1.85	EGFP	COS-7 cytoplasm	Wachsmuth *et al.* (2000)
1.58	EGFP	AT-1 nucleoplasm	Wachsmuth *et al.* (2000)
1.93	EGFP	COS-7 nucleoplasm	Wachsmuth *et al.* (2000)
1.97	IgG (2)	Human Adenocarcinoma	Netti *et al.* (2000)
1.89	IgG	Mouse Carcinoma	Netti *et al.* (2000)

(1) D calculated on the basis of molecular weight of GFP
(2) IgG has a molecular weight of ~150kD

6.2.4 Mass Conservation

Based on the evidence presented so far, the diffusion-dilution hypothesis best explains the loss of GFP fluorescence following freezing. To further test the validity of these results, a mass conservation type of experiment was performed. Cells were grown to confluence in 50 ml Falcon flasks (Becton Dickinson, Lincoln Park, NJ) and 800 ml Corning flasks (Corning, NY) and following detachment from the flask with trypsin, cells were concentrated by centrifugation and then re-suspended in 500 µl of D-MEM media. Cells were prepared to varying volume fractions. The volume fraction of cells in solution or 'cytocrit' was measured using an International Equipment Company Model MB micro-capillary centrifuge (International Equipment Company, Needham Hts, MA) and a Lancer Spiracrit micro-hematocrit capillary tube reader (St. Louis, MO). Following volume fraction determination, samples for imaging were drawn up in three 20-µm microcapillary tubes and placed on a microslide on the stage of the Nikon microscope. Samples were illuminated with blue light and images were acquired in three areas of each

capillary. Aliquots of 30-50 μl of cell suspension were then transferred to 0.5 ml micro-eppendorf tubes and the samples immersed in liquid nitrogen for 2.5 minutes followed by passive thawing at room temperature. Freezing and thawing was repeated for an additional cycle. The samples were briefly mixed on a Fisherbrand Vortex Genie 2 (Fischer Scientific, Pittsburgh, PA) and then three fresh capillaries drawn from the solution. Again, 3 images were acquired of each capillary. In this manner, for each volume fraction studied, 9 images were obtained for analysis both before and after the freezing and thawing protocol.

Images were analyzed using Image Pro Plus. Using a rectangular area of interest (AOI) of 49x50 pixels (~50 μm^2), 20 separate bitmaps were acquired of the background fluorescence in the cell suspension. This AOI size was specifically chosen to allow bitmaps to be collected between suspended cells. This concept is illustrated in Figure 6.15. In the case of frozen-thawed cells, no intact cells were ever visible and therefore bitmaps were collected in a systematic 5 x 4 array covering the field of interest. An average 'before' and 'after' intensity was calculated from the appropriate set of 180 bitmaps. The difference in intensity was plotted as a function of cell volume fraction and is shown in Figure 6.16. Also plotted was a predicted intensity curve that was calculated using the following equation:

$$I_{lysed} = \overline{V}_{Cells} I_{Cells} + \overline{V}_{Media} I_{Media} \qquad [6.4]$$

where I_{lysed} is the GFP fluorescent intensity predicted for the solutions following lysis of the cells, I_{Media} is the mean starting background intensity as measured in the current

experiments, I_{Cells} is the mean cell fluorescent intensity computed from the entire population represented in the Figure 6.12 histogram, and $\overline{V}_{Cells}$ and $\overline{V}_{Media}$ are the volume fraction of cells and media, respectively. The error in I_{lysed} was predicted on the basis of one standard error of the mean of both I_{Cells} and I_{Media}. Error was calculated according to:

$$s_{I_{lysed}} = I_{lysed}\sqrt{\left(\frac{s_{I_{Cells}}}{I_{Cells}}\right)^2 + \left(\frac{s_{I_{Media}}}{I_{Media}}\right)^2} \qquad [6.5]$$

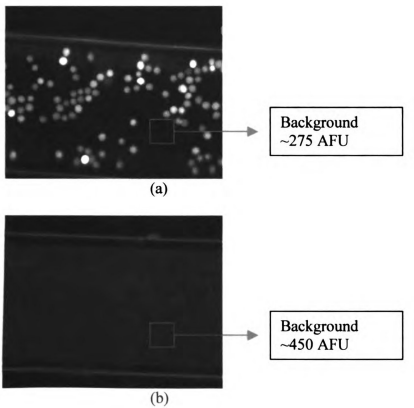

Figure 6.15 Photomicrographs demonstrating conservation of GFP fluorescence following lysis of GFP-R3230AC cells: (a) before freezing, (b) post-lysis.

As can be seen in Figure 6.16, the data are in reasonable agreement with the predicted curve, with a correlation coefficient of 0.95, suggesting that the estimate of the mean fluorescent intensity in previous experiments is in good agreement with current data. The average percent difference between calculated and experimental data was determined to be 12.4 %. The slope of the line originating from a linear fit of the experimental data in Figure 6.16 revealed that within the magnitude of the experimental error, a doubling of the volume fraction yields a 2-fold increase in fluorescence intensity. This result provides direct evidence for the validity of the diffusion-dilution hypothesis by establishing that fluorescence lost from the cells following freezing is quantitatively accounted for by the magnitude of the increase in fluorescence intensity in the extra-cellular space.

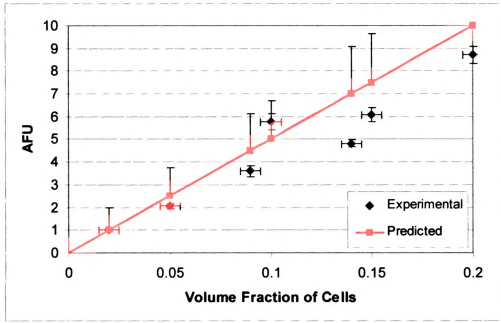

Figure 6.16 Change in GFP fluorescent intensity of background media following freeze-thaw lysis of suspended cells. Arbitrary fluorescent units (AFU) represent the measured gray scale intensity normalized to the initial data point. All y-axis error bars represent the standard error of the mean. The x-axis error bars represent the uncertainty in measuring volume fraction.

6.2.5 Conclusions

The previous results provide support for the hypothesis that diffusion and dilution of the GFP molecule is the basis for the GFP fluorescent intensity loss observed following freeze-thaw injury. Experiments using pure rEGFP demonstrated that the molecule was robust to multiple cycles of freezing to extreme temperatures and therefore cold denaturation of protein was not a relevant aspect of this application of GFP. The GFP was shown to persist in cells that are not membrane-compromised, at least for as long as 16 hours and probably for much longer. Order-of-magnitude estimates on the characteristic time for GFP to diffuse to an extent that significant changes in fluorescence

are observed were consistent with experimental observation. Furthermore, mass conservation experiments performed on the basis of quantification of GFP intensity further indicated that the GFP molecule was not being destroyed but was transported into the extra-cellular space. All experimental results and theoretical predictions were consistent with GFP leakage following freeze-induced injury.

If cells become irreversibly damaged but not immediately membrane-compromised, the GFP will likely persist until the necrotic pathway reaches the stage of membrane degradation. This suggests that although the GFP assay has two hypothesized features: (1) GFP will leak from membrane-compromised cells (2) GFP will not be manufactured in cells that are metabolically damaged, the latter feature seems to be difficult to practically capitalize on due to the long (>16 hours) turnover time of GFP in the cell. Necrosis will probably progress to the extent that membrane damage manifests prior to this latter mode becoming a rational basis for deeming a cell non-viable.

Chapter 7

Validation of a GFP-based Viability Assay *in vivo*

7.1 R3230 AC Tumors Grown in the Dorsal Skin Flap Chamber: Implant Procedure

The current work seeks to establish that following freezing, changes in the fluorescent intensity of tumors grown from GFP-transfected cells will correlate with tissue damage as assessed by other independent measures of viability, thereby evaluating the use of a transfection-based assay for in vivo purposes. To achieve these ends the dorsal skin flap chamber (DSFC) was utilized to grow and treat microscopically observable tumors. The DSFC has been recently implemented by several researchers for the study of freezing injury in rodents (Hoffman and Bischof, 1999, 2001ab). Following injury the tissue was evaluated using GFP intravital fluorescence, and histopathology.

Female Fischer 344 Rats weighing between 150 and 180 grams were implanted with dorsal skin flap chambers. Because this chamber permits chronic optical access to subcutaneous or other implanted tissues, it is very desirable for studying both frostbite and cryosurgery-induced tissue injury phenomema. Tissue integrity and microscale hemodynamics can be studied without sacrifice of the animal. This procedure has been

described by Papenfuss (1979) and few deviations from the methodology were made. The primary modification was that one-sided preparations were utilized instead of removal of the dermis on both sides of the skin flap. The traditional preparation involves removal of the epidermal layer of opposing skin flaps, leaving a thin layer of vascularized dermal tissue. Because this study focused on fluorescent epi-illumination of tumor preparations, thin sections for trans-illumination were not necessary, and the less traumatic one-sided preparations were found to be most suitable. All of the experimental procedures were carried out under aseptic conditions using sterile surgical instruments and reagents. A sketch depicting an implanted skin flap chamber is shown in Figure 7.1.

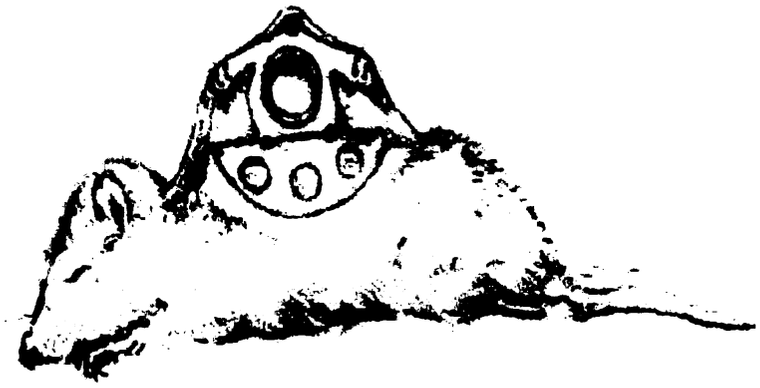

Figure 7.1 Sketch of Implanted Dorsal Skin Flap Chamber, Courtesy of Dr. Mark Dewhirst, Duke University.

Animals were injected subcutaneously (sc) with 0.3 mg/kg of buprenorphine hydrochloride analgesic (Reckitt & Colman Pharmaceuticals, Inc., Richmond, VA). Ten minutes later animals were anesthetized with sodium pentobarbitol (35 mg/kg

intraperitoneal (ip), diluted 1:5 in 0.9% NaCl). The dorsal side fur was clipped and depilatory used to remove the fine hair. The dorsal skin flap was then sterilized and aseptically sutured to a stainless steel frame to allow through-the-skin visualization of vasculature. Upon selection of a suitable vascular bed, the skin was dissected away on one side of the dorsal flap (~1 cm diameter) using a scalpel and micro scissors, exposing the microvasculature and subcutaneous tissue. The hypodermal tissue was trimmed until the microvasculature on the opposing side was neatly exposed.

Holes were made at three sites surrounding the dissected region and the two halves of the chamber assembly inserted and mounted together. A glass window was then placed over the exposed subcutaneous tissue and it was sealed in place with an E-ring. Three sutures were added to stabilize the chamber. At the time of chamber implant, using a sterile syringe, the tissue was bathed with a small bolus (~200 μL) of GFP-transfected R3230 AC tumor cells in DMEM media (1×10^5 cells/ml) before sealing the preparation with a glass window. Prior to implantation Trypan Blue was used to discriminate live and dead cells, and cells were counted with a hemacytometer and prepared to the desired concentration in fresh supplemented D-MEM. In sham experiments sterile saline was used instead of a cell suspension. An implanted chamber (animal 1 hour post-operative and still anesthetized) is shown in Figure 7.2.

Animals were placed on an insulating pad and 4.5 mL of Ringer's lactate was administered every 2 hours until animals were ambulatory. They were then moved to a room maintained at 91°F and ambient humidity and housed there for the remainder of the tumor incubation period. Animals were monitored for tumor growth activity until the tumor tissue dominated the viewing area, creating a relatively uniform spatial

fluorescence signal. This was achieved in a 6 to 9 day time period. The tissue was then treated with cryosurgery.

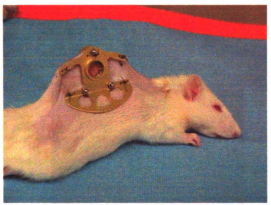

Figure 7.2 Recently implanted dorsal skin flap chamber in an anesthatized Fischer 344 rat.

The growth of implanted tumor cells was monitored in the first few animals that were studied to understand the appropriate incubation time to achieve a substantial tumor size. Shown in Figure 7.3 is a series of images that reflect a typical growth pattern. Although quantification was not attempted, in areas of adequate blood supply, growth *in vivo* tended to parallel growth in culture, with a doubling time on the order of 20 hours.

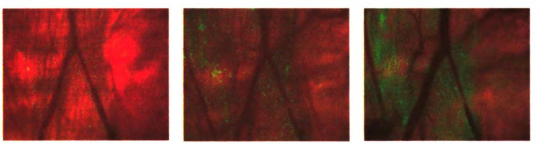

Figure 7.3 Series of images depicting growth of a solid tumor from a tumor slurry in the dorsal skin flap chamber: fresh tumor preparation (a), the tumor at day 3 (b), and day 6 (c).

The tissue shown in Figure 7.3 was biopsied at day 6, fixed in 10% formalin, embedded in paraffin, sectioned and stained with hematoxylin and eosin (H&E). The same region of the tissue identified in Figure 7.3 was also located in the fixed specimen and is shown in Figure 7.4.

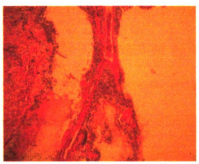

Figure 7.4 H & E section of the tissue contained in the dorsal skin flap chamber at day 6 after implant of chamber and tumor slurry. The vessel pictured is the same vessel seen in the Figure 7.3 series.

7.2 Experimental Design

Four groups were evaluated in this study. To determine baseline levels of fluorescence in the tissue, independent of any fluorescent tumor growth, chambers were implanted and were analyzed for fluorescent intensity over a 6-hour period (Sham, n=3). Following the observation period, tissues were biopsied and fixed. To determine the effect of treatment on this background level of fluorescence, several animals without tumors were treated with cryosurgery (Sham Treated, n=3). Tumors were raised in another group of animals (Control, n=5) that served as controls. The tissue in n=2 of the animals in this group were biopsied in the plane of the chamber, whereas the other n=3 were biopsied in such a way to allow observation through the thickness of the chamber

tissue (cross-section). See Figure 7.5 for an illustration of the biopsy procedure. For animals in this category, the tumor tissue was not treated but exposed to the same period of fluorescent light illumination (intensity, magnitude, and frequency), and then at 6 hours the animal was euthanized and the tissue within the chamber biopsied, fixed in formalin, and stained for histological analysis. The final group received both a tumor preparation and a cryosurgery treatment (Cryosurgery, n=9). Fluorescent images of the tumors were acquired at the center of the viewing area before, during, and for 6 hours following the freezing procedure. In some instances images were acquired of the entire field to allow visualization of lesion diameters. Following the 6-hour observation period the animal was immediately euthanized and the tissue within the chamber was fixed in formalin and stained for histological analysis. The experimental design is summarized in Table 7.1.

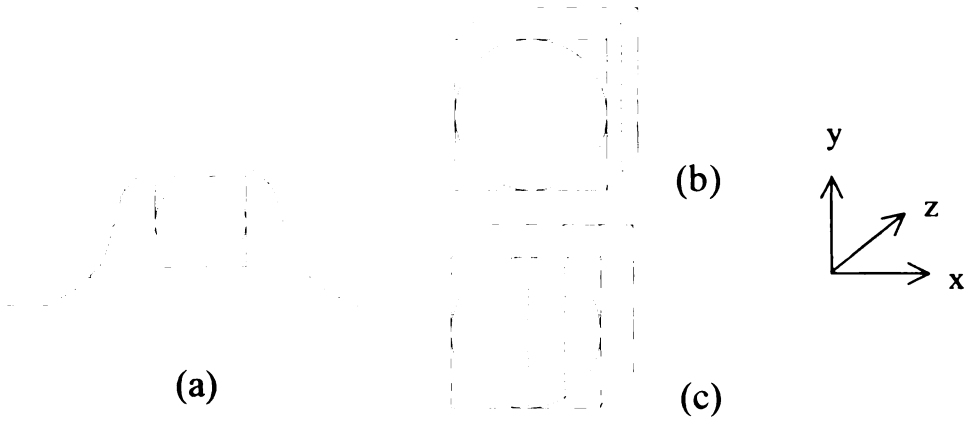

Figure 7.5 Illustration of the two different biopsy techniques used in the first animal study. (a) Square tissue section was first removed from the skin flap. Tissue sections were cut (b) in-the plane of the tissue (x-y) and also (c) cross-sections were obtained at x = 0 and x = 2.5 mm.

Table 7.1 Experimental Design

Group	**Acronym**	**# Animals**
Control: tumor, 6 hr observation	**C**	n=5
Sham: no tumor, 6hr observation	**S-**	n=3
Sham Treated: no tumor, cryosurgery, 6 hr observation	**S+**	n=3
Cryosurgery: tumor, cryosurgery, 6 hr observation	**CS**	n=9

Although not part of the original experimental design, the absence of a second glass window on the non-dissected side occasionally resulted in considerable non-tumor cell proliferation. This resulted in tissues two to three times the intended thickness, as illustrated in Figure 7.6. All tissues, independent of thickness, were treated with an identical freezing protocol.

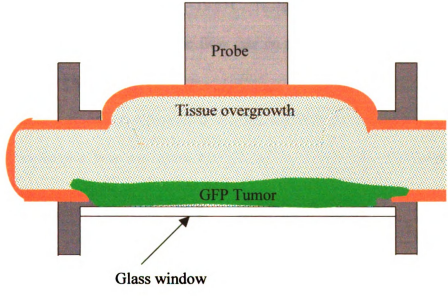

Figure 7.6 Depiction of tissue that was overgrown at the time of treatment.

7.3 Cryosurgical Probe Development

As part of a MSU indepedendent study, Fron (2000) created a simple cryosurgical probe that was manufactured to achieve a range of cryosurgically relevant end temperatures (lower than -20 °C) and freezing rates (faster than -50 °C/min) (Gage and

Baust, 1998) in the tumor tissue within the dorsal skin flap chamber. The body of the probe was manufactured from 0.5" OD copper tubing. The 12 mm length probe tip was made of 6 mm diameter brass stock. Extending from the top end of the probe were short lengths of 1/8" diameter brass tubing, which provided connections for the liquid nitrogen supply and return. Mixed phase nitrogen was circulated through the cryosurgical probe using a variable flow rate Linkam LNP9311 Cryopump. The probe was insulated with 3/8" thick foam tubing. The evaporation of liquid nitrogen in the body of the probe provided a minimum tip temperature of –192 °C. Different tip temperatures and cooling rates could be achieved by adjusting the flow rate on the Cryopump. The cryosurgery system is depicted in Figure 7.7.

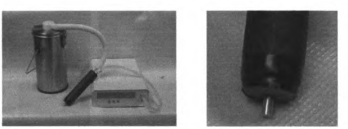

a b

Figure 7.7 Cryosurgical probe system. (a) Linkam LNP9311 Cryopump with liquid nitrogen dewar and probe. (b) Close-up of 6 mm diameter cryosurgical probe tip.

7.4 Thermal History: Tissue Phantom Measurements to Characterize Cryosurgery Treatment

To achieve the most accurate record of thermal history without invasively instrumenting the tissue within an implanted window chamber, a phantom system was used to optimize the cryosurgery protocol. A stage was built to facilitate instrumentation of the interior ring of the window chamber with Omega 0.001" and 0.005" wire thermocouples (see Figure 7.8) and subsequent measurement of freezing histories. Biopsied rat skin samples from the Fischer 344 rat were utilized to achieve estimates of the freezing rates and end temperatures that would be expected *in vivo*. It was assumed that the effects of microvascular blood flow that were not accounted for in this phantom system would not contribute significantly to the thermal resistance of the tissue for the *in vivo* case. The interior ring and glass window of the DSFC was instrumented with thermocouples as shown in Figures 7.8 and 7.9.

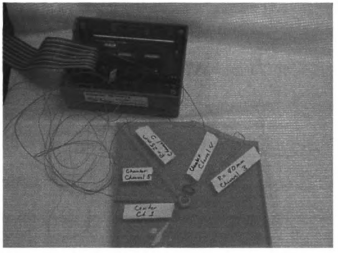

Figure 7.8 Phantom set-up for acquiring thermal data.

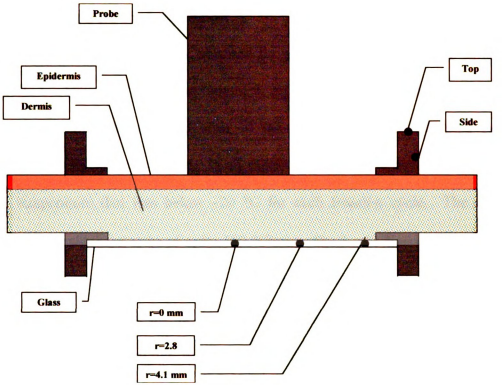

Figure 7.9 Location of thermocouples and cryosurgical probe during the phantom measurements.

The stage was draped with thick absorbent paper towels in the same manner as the animal would be draped during the procedure. The flow rate of the cryopump as well as the duration of freezing and thawing were optimized to create freezing rates with a magnitude of -50 °C/min or greater and end temperatures lower than -20°C, without extending the ice ball to the edge of the metal chamber. After a series of trials a protocol involving three twenty-second freezing cycles was selected, while allowing 2 minutes between freezing for the tissue to thaw completely. This protocol did not create sub-zero temperatures on the surface of the metal chamber, yet created a well-circumscribed lesion

in the viewable area (~6-8 mm diameter). This optimized freezing protocol was applied *in vivo* to tissue within the window chamber.

Characteristic freezing curves obtained for phantom skin samples are shown in Figure 7.10. The most variation amongst replicates occurred at the minimum temperature. Therefore the standard error of the mean is reported at these points. Measurements are for three replicates. In all cases the center thermocouple registered a minimum temperature that was below –20 °C for each freezing cycle. The average freezing rate was calculated to be of order 100 °C/min. The 2-min thaw time was chosen to provide enough time for the tissue to completely thaw and return to above 5 °C. Thermal measurements taken on the surface of the metal chamber indicated that the draping used to protect the animal from cold air shedding from the probe was adequate, as sub-zero temperatures were not recorded in the metal insert at any point during the simulated procedure (data not shown).

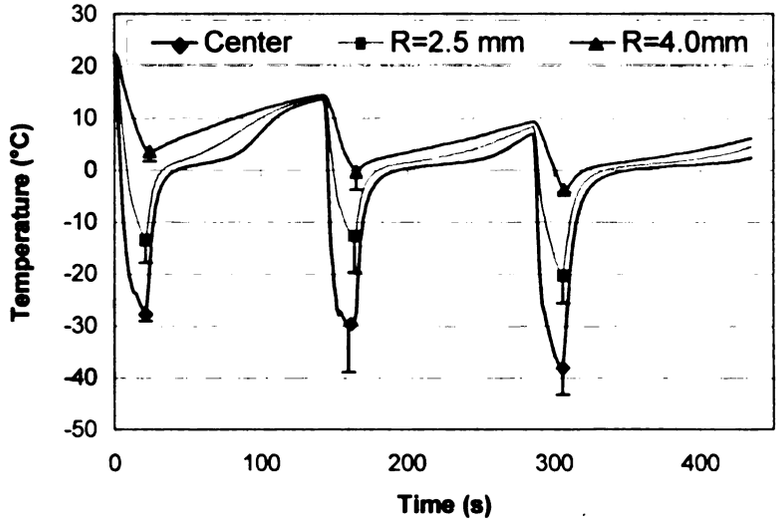

Figure 7.10 Characteristic freezing curves measured at specific locations in the phantom tissue system.

7.

7.

its

se

SI

m

In

in

pa

th

1.

fo

an

av

at

co

cr

mi

for

the

cr

7.5 Post-Cryosurgical Damage to GFP Fluorescing Tumor Tissue

7.5.1 Intravital GFP Intensity Assessment

The animal was anesthetized with sodium pentobarbital (35 mg/kg) and placed on its side on a modified microscope stage. Images were acquired of a centrally located test section (directly beneath the cryosurgical probe) before, during, and after freezing using a SPOT thermoelectric cooled color CCD camera and a Nikon Diaphot inverted fluorescent microscope equipped with a 100 W mercury arc lamp (both from Diagnostic Instruments, Inc. (Sterling Heights, MI). The tissue was illuminated with blue light (450-490 nm) by inserting a FITC filter cube (Chroma Technology Corp., Brattleboro, VT) into the light path. Three-channel RGB fluorescent images of the tumor were acquired at the center of the viewing area before, during, and for 6 hours following freezing (exposure times, Red: 1.533 sec, Green:1.538 sec, Blue: 2.307 sec). These test area images were then evaluated for changes in fluorescent intensity. The test area images were converted to gray scale and analyzed using Image Pro software (Media Cybernetics, Silver Spring, MD). The average fluorescent intensity/ sq. pixel of tissue was measured in each of the test sections at key time points. The area analyzed was 775 microns x 612 microns. Representative composite images spanning the viewable area (~1.0 cm diameter) were also taken before cryosurgery and at 2.5 and 6 hours following the procedure for some of the animals.

The gray scale intensities per square pixel were measured for intravital microscopy images. Intensities were normalized to the starting local intensity measured for each animal. The normalized results for animals that experienced lethal freezing on the basis of histopathology are shown in Figure 7.11. The results of five identical cryosugeries for five different animals with tissue of comparable thickness are shown

(CS1-CS5). These results reveal a large reduction in fluorescent intensity immediately following the final freeze-thaw cycle, with little subsequent change for the duration of the 6-hour observation period. Data from treated (S+) and untreated (S-) sham animals (animals received no tumor implant but were incubated for 6-9 days) were also plotted in this figure. These data were normalized to the average starting intensity of tumor-bearing treatment and control animals. At the 6-hour point all of the cryosurgery data from cryosurgically-treated tumor-bearing animals fell within the limits of these average autofluorescence intensity levels. The difference between these intensities was observed to be directly related to the amount of hemorrhage and blood pooling in the observation area, which served to moderately attenuate the fluorescence levels. For treated animals, the x-axis represents the time following the last of three freeze-thaw cycles. The untreated control animals received an equivalent time series of blue light illumination (~60 minutes total) but did not undergo cryosurgery. Some variation was noted in the intensity of the control tissue but the deviation was small. The average variation was 3% from the average starting intensity of 14 animals. This indicated that the GFP expressing tumor tissue was robust to photo-bleaching effects and that the excitation source was relatively stable.

Composite tiled images of the viewing area are shown in Figure 7.12 for intravital images acquired before cryosurgery and 6 hours following treatment for the same animal. Note the retaining ring at the edge of the images in Figure 7.12. This ring has an ID of 10.6 mm. The cryolesion in Figure 7.12 (b), judged by fluorescence decay, was measured to be ~7.5 mm in diameter. The 6-hour images were similar to the 2.5-hour images.

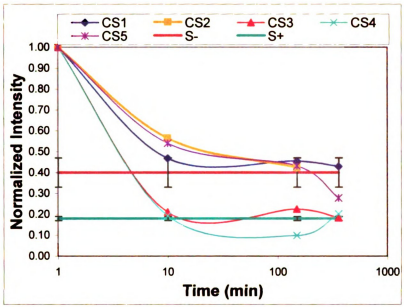

Figure 7.11. Normalized gray scale intensity of GFP fluorescing tumor as a function of time for cryosurgically treated animals (CS1-CS5). The rectangular region indicates the average upper and lower autofluorescence levels of untreated and treated normal tissue, respectively.

a

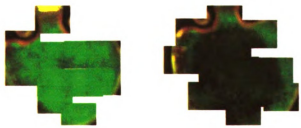

b c

Figure 7.12 Image of the glass window and e-clip (a) and tiled composite fluorescent images of the entire window chamber viewing field: before cryosurgery (b) and 6 hours after the last freeze-thaw cycle (c). The cryo-lesion is clearly demarcated in (c).

7.5.2 Histopathology Assessment

Following the cryosurgical protocol the animal was immediately euthanized and the tissue within the chamber was fixed in 10 % formalin and embedded in paraffin. To establish the relationship between the presence or absence of GFP fluorescence and cell devitalization *in vivo*, 5-micron thick tissue sections were obtained either in the plane of the skin flap or in cross-section, and stained with hematoxylin and eosin.

Before the fixed specimens were dissected for paraffin embedding, the impressions that the window chamber left in the tissue were used as markers to estimate the amount of tissue shrinkage that occurred during the fixation process. Shrinkage varied across the specimen. The inner tissue with the dermis dissected away had an average shrinkage of 2.5%, the outer non-dissected tissue had a value of 4.5 %.

As previously indicated, some tissues experienced overgrowth. They were treated with the same protocol but as expected, little damage occurred. In five of the nine animals treated the tissues were of normal thickness. In these cases the GFP intensity was seen to drop by 50% or more within 10 minutes after treatment. Histopathology confirmed the necrosis or ablation of this tissue. In the remaining cases, cell death either did not occur or was partial. In each of these cases histopathology correlated with intravital observations. Characteristic results are shown in figures 7.13 through 7.15.

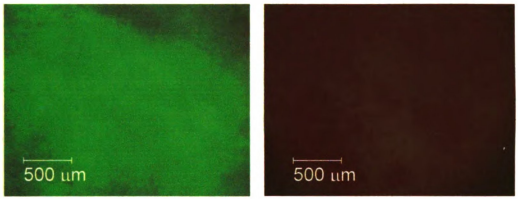

(a) (b)

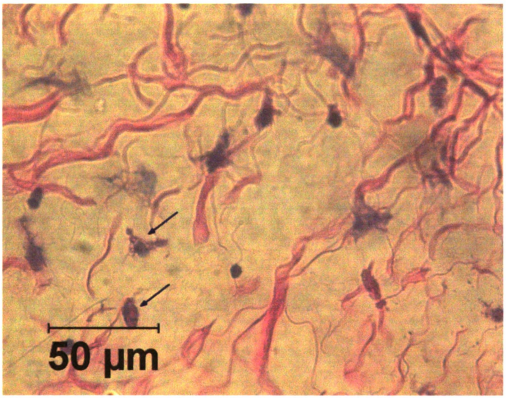

(c)

Figure 7.13 (a) GFP-fluorescing tumor before treatment. (b) GFP-fluorescing tumor after treatment. (c) histpathology micrograph from the center of the tissue in (b). Damage is complete, with only cell debris and necrotic cells (arrows) present.

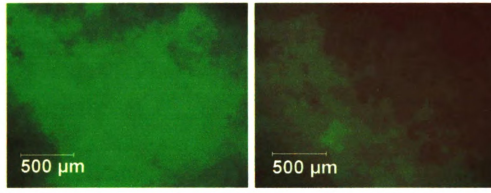

(a) (b)

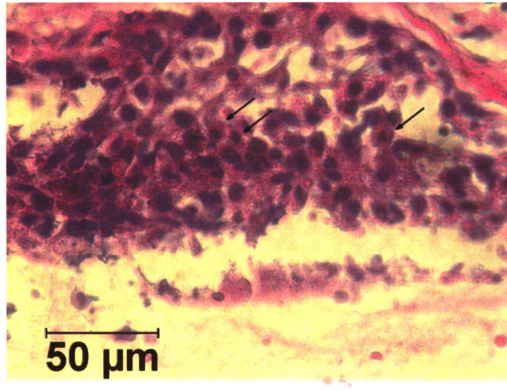

(c)

Figure 7.14 (a) GFP-fluorescing tumor before treatment. (b) GFP-fluorescing tumor after treatment. (c) Histpathology micrograph from the center of the tissue in (b). Damage is partial with some necrotic cells (arrows) present amidst a group of normal tumor cells.

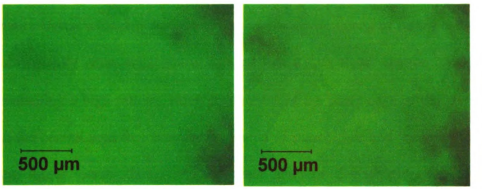

(a) (b)

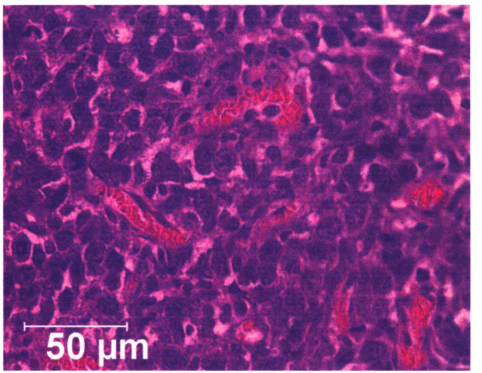

(c)

Figure 7.15 (a) GFP-fluorescing tumor before treatment. (b) GFP-fluorescing tumor after treatment. (c) histpathology micrograph from sample at the center of the tissue in (b). No damage is observed.

The remaining observations will focus on the tissues in which distinct cryo-lesions were formed. In the center of the targeted tissue there was near complete ablation of the tumor tissue with only nuclear and cytoplasmic remnants of tumor cells scattered within a markedly edematous and congested connective tissue matrix. Viable tumor tissue containing a high mitotic index circumscribed the outer edge of the targeted area. Between the central area that was nearly devoid of tumor cells and the outer edge of the remaining tumor tissue, there was a distinct zone of degeneration and necrosis of individual tumor cells, vascular congestion and hemorrhage, and a conspicuous influx of neutrophils with lesser numbers of mononuclear cells (i.e. acute inflammation). Characteristic results are shown in Figures 7.16-7.18.

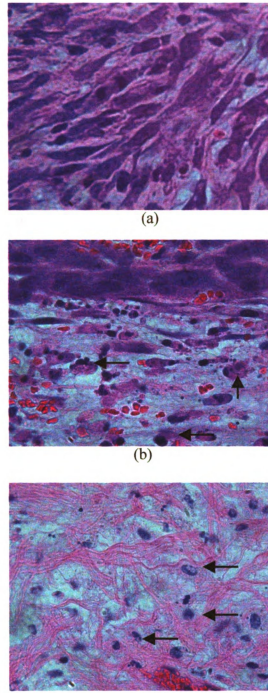

Figure 7.16 H&E micrographs of cryo-treated tumor tissue: The tissue surrounding the lesion (a) is undamaged. At the margin of the lesion (b) necrotic cells are evident (arrows). In the central region (c) nuclear and cytoplasmic remnants are evident.

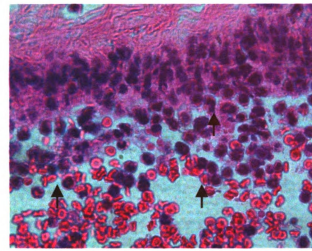

Figure 7.17 H&E micrographs of acute inflammatory cells (neutrophils) located near the edge of the cryo-lesion (arrows).

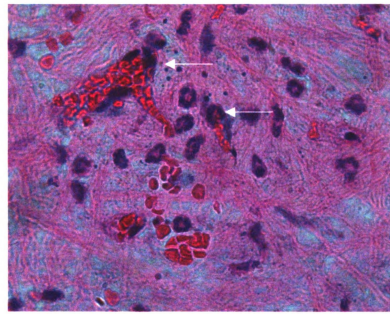

Figure 7.18 H &E micrograph of neutrophils phagocytosing red blood cells (arrows).

7.5

con

nor

the

crea

regi

fina

GFP

prec

norr

caus

tum

leak

GFP

obse

this

to be

perio

tissue

freezi

fluore

7.5.3 Comparison of Results

The freezing protocol applied to the tissue was expected to create a region of complete tissue damage in the center of the tissue. In the tissues that were considered normal thickness, H&E analysis confirmed that significant tissue damage was present in the central region of the tissue, which suggests that the protocol was successful in creating a well-circumscribed cryo-lesion in a subset of the tissues studied. In the central region of the tissue, GFP fluorescence intensity decreased dramatically following the final freeze-thaw cycle, consistent with the proposed basis for the GFP assay: leakage of GFP from cells with damaged membranes. The freezing rates and end temperatures predicted at the center of the tissue were of order -100°C/min and –30°C, respectively for normal thickness tissues. Multiple applications of this thermal history were likely to have caused some intracellular ice formation and other damaging events in the cells within the tumor. Membrane damage on the thaw cycle was thus expected, giving rise to GFP leakage into the extracellular fluid. This would cause a dilution of GFP and a decrease in GFP fluorescence signal, as observed. Although a dramatic decrease in signal was observed immediately following the cryosurgery treatment for all four cases included in this group, the absolute signal observed varied between animals. This was established to be due to the fluorescent dampening effects of blood pooling in the observation area.

In some of the cryosurgery cases the tissue had 'overgrown' during the incubation period, and had pushed out the back of the chamber. The general appearance of this tissue was shown conceptually in Figure 7.6. These tissues were treated with the same freezing protocol as the 'normal thickness' tissue. The pattern of disappearance of GFP fluorescence was not the same. Obviously with a thicker tissue section, the penetration of

the freezing front was not as deep, and the tissue thus was likely to have experienced benign thermal histories. What is important is that the intravital images qualitatively agreed with the histopathology results. In specimens where the tissue presented as viable in intravital GFP microscopy, the tissue resembled that of control tissues, with no damage observed. As can be seen from the characteristic results shown in figures 7.13-7.15, the gradiation in damage observed over the set of GFP intravital images can also be seen in histopathology in the same region of the tissue.

The spatially distributed percent change of GFP fluorescence after cryosurgery was evaluated for the 2.5 and 6-hour composite images for a number of cases, and compared to histopathology. For a sample case shown in Figure 7.19, it can be seen that the lesion diameter predicted by GFP was larger than that predicted by histopathology (image dimensions corrected for shrinkage). It seems likely that the cells will exhibit evidence of damage by GFP assay more quickly than histopathology can reveal at the same time point. It is interesting to note that in both cases, the assays reveal an area of tissue with a gradiation of damage, suggesting that the GFP assay might be used to quantify partial damage in whole tissues as well as complete damage, on the basis of normalized intensity change.

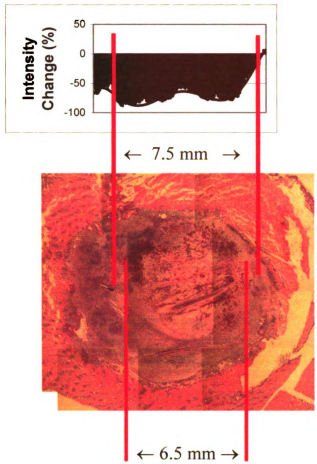

Figure 7.17 Spatial comparison of GFP intensity changes (approximate lesion diameter ~7.5 mm based on magnitude of intensity change) and histopathology results (approximate lesion diameter 6.5 mm based on region of hemorrhage) for one case of tumor cryosurgery treatment.

7.6 Dynamics of Fluorescence Intensity Change *in vivo*

How would the dynamics of GFP intensity change be expected to change *in vivo*? Instead of having an aqueous pool of media or buffer to diffuse into, as in the case of many of the *in vitro* experiments performed to date, the EGFP molecules must diffuse through a normal or disrupted tissue matrix upon leaking from a damaged cell. In the case of *in vitro* studies the volume fraction of cells was such that there was an ample sink for the EGFP molecules. It is necessary to understand the capacity for dilution *in vivo*. The volume fraction of the interstitium in tumors was determined to be in the range of 0.35 – 0.55 by Jain *et al.* in 1987. The values reported for the vascular component by Jain *et al.* in 1988, were 0.01-0.2. This results in a cellular fraction of 0.25-0.64. Thus if all cells in the center treatment region were to be completely lysed following three freeze-thaw cycles, the dilution factor would be somewhere between 1.3 and 4. This is consistent with *in vivo* observations, as GFP fluorescence intensities have been seen to decrease up to ~60% following lethal freezing. As demonstrated in Chapter 6, this could be achieved on the order of seconds, consistent with some of the observations *in vivo* that demonstrate a loss of fluorescence directly following the thaw.

Chapter 8

Design and Characterization of an Annular Freezing Apparatus for the Dorsal Skin Flap Chamber

8.1 Motivation

The time course of freeze injury *in vivo*, as well as the magnitude of inflammatory and ischemia contributions to overall injury are not well understood. Traditional *in vivo* approaches for studying cryosurgery frequently involve inserting a cryosurgical probe into a lesion, evoking several freeze-thaw cycles, and then biopsying the treated tissue at discrete time points after the cryosurgery to obtain histopathology specimens. Species such as sheep (e.g., Rabin *et al.*, 1998) have frequently been used as animal models for cryosurgery studies because their size allows the use of traditionally sized cryosurgical probes in large tumor masses. In these types of animal models, tumors can be grown that are analogous to human tumors, both in size and character. However in terms of evaluating the temporal nature of tissue injury, use of large animals to achieve statistically significant data at a large number of time points can be prohibitively expensive. Scaling down the clinical situation to smaller animals such as rodent models makes the evaluation of injury dynamics more accessible, however new challenges are

introduced. Large animal studies allow the placement of discrete thermocouples, or permit simultaneous imaging of the procedure (e.g. ultrasound, MRI) so that phase change boundaries (the ice front) can be tracked. In contrast, small animals create difficulties for monitoring thermal histories during cryosurgeries, and when treating large tumors the risk of hypothermic shock is high. The use of small optical chambers, while providing excellent detail regarding the microvascular injury, does not facilitate thermal history measurement. Numerical simulations of the thermophysical response are thus useful for generating thermal field information in these systems.

Thermocouples have been used to measure temperatures within the dorsal skin flap chamber, both for cryosurgery studies (Hoffman *et al.*, 1999) and high temperature studies such as hyperthermia (Gross *et al.*, 1982) and burn injury (Diller and Hayes, 1991). Thermal measurement within the DSFC and other optical chambers is non-trivial because of the small scale of the system. Since large temperature gradients are typical in scaled-down cryosurgery model, small thermocouples are required to achieve a localized temperature measurement. Thermocouples with bead diameters smaller than the tissue thickness (0.2 to 2.0 mm) are difficult to handle and they are fragile. Moreover, accurately locating the measurement junction once it has been inserted into the tissue can be problematic. Although some have used 'needle' sensors, thermocouples embedded in the shafts of needles, these constructions are known to introduce significant 'fin effects' error into the measured temperature value (Rabin, 1998). Thermal contact resistance is also an issue when thermocouples are used to measure surface temperatures. Generally the number of thermocouples used is limited and interpolation, extrapolation, and symmetry arguments are invoked to infer the desired thermal field information. For the

specific case of using a dorsal skin flap chamber (DSFC) for studying cryosurgery, the Bischof group has used thermocouples as a means of quantifying the thermal field so that the physiological and biophysical responses can be correlated with defined thermal histories (Hoffman *et al.*, 1999, 2001ab). This approach has already contributed to an improved understanding of the importance of the vasculature in tissue freezing response. On the other hand, fin effect errors in these thermocouple measurements are estimated to be of order 10°C, which limits the utility of such an approach. Moreover, instrumenting tissue within the DSFC with thermocouples is an invasive process. The author experienced inadvertent hemorrhage of blood vessels during instrumentation of some of the chambers used in this study, and some minor problems were also noted in the Hoffman and Bischof study (2001b).

In this work, the focus of the first animal series (Chapter 7) was to determine the correlation of the GFP assay with histopathology at different extremes of damage (i.e. complete, partial, none) to validate its use *in vivo*. Knowledge of the precise thermal history was not important as long as it was within a cryosurgically relevant regime. Repeated cycles of freezing, following the protocol optimized in the phantom system, had a high probability of creating damage in the area directly beneath the cryosurgical probe in thin tissue sections. This was observed in all of the animals included in the normal tissue thickness group. Although observations at the edge of the cryolesion were made during the first experimental animal series, the focus of the study was the utilization of GFP as a cellular viability assay, and not correlating thermal history with the pathophysiology of injury at the edge of the cryo-lesion. Nevertheless, it was possible to gain valuable insight into the challenges inherent in achieving viability-thermal history

correlations. Using this same approach for inducing freeze injury would result in difficulties in reproducibly localizing the cryo-lesion edge for intra-vital experiments, as the diameter of the lesion ranged by as much as 10 mm for the animals treated (i.e. no lesion to complete ablation). Although much of this variability was due to the tissue thickness, even if the tissue thickness was constrained, tracking the interface remains challenging. Localizing a region of tissue experiencing temperatures within the narrow range considered to characterize the edge of the cryo-lesion in such a scaled-down system, would equate to trying to identify the temperature gradients and viability response within a region of sub-mm dimensions. Certainly from the standpoint of thermocouple measurements this is nearly impossible.

Another one of the challenges in using the dorsal skin flap chamber to study cryosurgically relevant low temperature processes is the difficulty in achieving a controlled and well-characterized cryolesion within the ~1 cm viewing area. The structural complexity of the microscale system limits the size of the ice-ball that can be created within the chamber before the boundary conditions become extremely complicated and extrapolation from thermocouple measurements questionable. These complexities also present challenges in implementing numerical models to predict thermal histories in the treated tissue. Development of technologies that would allow better control and resolution of temperature gradients and temperatures in the DSFC would thus be advantageous from many standpoints.

To produce a means of studying vascular injury, ischemia, and inflammation at temperatures and freezing rates consistent with the edge of a standard cryo-lesion, a non-conventional approach was used. Instead of creating a spherical tumor, a disk tumor, a

characteristic of tumors grown in a dorsal skin flap chamber, is chosen as the model system. The cryosurgical probe was not inserted into the center of the lesion or placed on the surface of the tumor as performed in the first animal series, but instead a novel probe was developed to create a lesion by applying a uniform and controllable thermal history. Although devices of this nature have been created to study freezing of tissues in vitro (e.g. Rubinsky, 1995), *in vivo* devices are less common.

The device in this study was annular in design, thereby permitting optical access to the tissue during treatment. By creating a device that could provide uniform and reproducible high sub-zero temperatures and slow freezing histories *in vivo*, the possibility of freezing tissue within the chamber without eliciting significant direct cell injury was feasible. Cooling rates and temperatures could be applied that would not result in significant direct cell injury. This provided a measure of 'uncoupling' not possible with the more conventional scaled-down cryosurgery approach. In this latter case, both fast and slow freezing rates are experienced in the same system, and therefore spatial resolution of the high sub-zero temperature range is necessary. A novel freezing device as described would allow a direct means of determining both the extent and dynamic nature of the ischemic injury that occurred following freezing. The remainder of this chapter details the construction, characterization, and numerical modeling of this novel Annular Freeze Apparatus (AFA).

8.2 Design Objectives

A freezing device was desired that attempted to maximize the utility of the DSFC for studying low temperature injury. Fast freezing injury, such as occurs at the center of

a typical cryolesion, is well-characterized but there are many ambiguities associated with injury at the edge of the cryolesion where slow freezing rates and high sub-zero temperatures dominate. Injury in this region tends to be associated with loss of vascular integrity, ischemia, and inflammation, but this complex pathophysiology is not well-characterized. Even less is known about the range of thermal conditions that elicits the response. For this reason the design goal was to create an apparatus that could reproducibly achieve slow freezing rates to minimum temperatures in the -5 to –60 °C range, in a large portion of tissue in the DSFC. By creating a thermal history in the tissue that was the same on both sides of the chamber, temperature measurements could be made on one side of the chamber while microscopic observations (brightfield and epi-illumination) were made on the opposing side. Symmetry of thermal response was also desired to simplify the modeling of tissue freezing within the DSFC. If symmetry arguments can be evoked, the size of the mesh necessary to solve the heat transfer problem can be reduced by a factor of 2. This results in a decrease in computational time.

The design objectives for the AFA were:

1. Controllable and reproducible slow freezing (1-10 °C/min) of tissue in the optically accessible region of the DSFC to high sub-zero temperatures (-5 to –60 °C).

2. Symmetry of device and/or symmetry of temperature response at the interior surface of the DSFC annulus profile.

3. Spatial uniformity of temperature over the annulus.

4. Minimization of frozen tissue in the region surrounding the DSFC.

8.3 Construction of the Annular Freeze Apparatus

Several prototypes were investigated as part of an MSU independent study (Frerichs, 2001), with designs falling into two distinct classes: those that directly implemented the annulus of the DSFC as a cooling chamber and those that used an external device. The latter category was preferred because it involved the construction of a single device as opposed to the retrofit of individual chambers to suit the design requirements. A final design was selected from this category.

The final freezing apparatus design was comprised of two stainless steel symmetrical rings that have an internal 2.3 mm channel for circulation of cold nitrogen vapor. The mechanical drawing for this device is given in Appendix D. A Linkam LN2 Cryopump was used to pull cold nitrogen vapor through the apparatus, via inlet and outlet ports manufactured from hypodermic needles. Stainless steel parts were assembled and attached using Omegabond 400 high-temperature air-set cement (Omega Engineering, Stamford, CT). Although the cement was effective at low temperatures, condensation and associated moisture adversely affected the bonds; hence the cemented regions were sealed with acrylo adhesive prior to repetitive use. An external groove on the surface of these rings provided the point of attachment for interfacing with the DSFC. When implemented *in vivo* the symmetrical annular probes are attached to the exterior surface of the protruding annulus of the DSFC. Use of the AFA together with the DSFC is pictured in Figure 8.1. The extraction of heat from the tissue is achieved via the DSFC annulus, therefore the optical port is not obstructed during the freezing procedure. Cooling begins in the tissue at the point where the annulus of the DSFC contacts the tissue, followed quickly by extraction of energy from the center of the chamber. In this

situation the optical access area of the DSFC can be fully utilized during the freezing protocol, thereby permitting the use of various imaging methods (e.g., fluorescence, infrared) throughout the freezing procedure to identify ice front position or thermal gradients. This apparatus was designed to have flexibility of imaging modes, i.e. microscope-mounted or otherwise. Care was taken to ensure that the AFA did not directly contact the metal surrounding the annulus, by providing a clearance between the AFA and the metal region surrounding the DSFC annulus. This design aspect minimizes adverse heat conduction from regions of the chamber that contact the tissue at other sites.

Figu
stainl
A gr
The
annul

8.4

syste

expe

resen

two

appr

diam

surfa

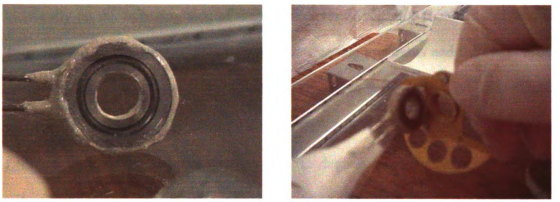

(a) (b)

Figure 8.1 Annular Freeze Apparatus (AFA). (a) Cold N_2 vapor passes through the stainless steel freezing apparatus by means of hypodermic needle inlet and outlet ports. A groove on the surface of the annuli provides the point of attachment to the DSFC. (b) The symmetrical annular probes are attached to the exterior surface of the protruding annuli of the DSFC.

8.4 Thermal Characterization of the Annular Freeze Apparatus

To assess a number of features related to the thermal behavior of the AFA-DSFC system, processed meat was used to simulate tissue. In all of the characterization experiments, thick slices of chicken bologna (~2 mm thickness) were trimmed to resemble the hemispherical shape of a dorsal skin flap and then sandwiched between the two aluminum frames that comprise the DSFC. This caused the tissue to compress by approximately a factor of two.

In the first series of characterization experiments, thermocouples with bead diameters of ~ 0.01" diameter were attached to the center of the annulus on the interior surface of the dorsal skin flap chamber using acrylo adhesive at three equidistant

locations, as shown in the inset picture of Figure 8.2. Thermocouples were placed identically on the opposing side of the chamber for a total of 6 mounted thermocouples. To maximize the thermal contact between the freezing apparatus and the annular portion of the DSFC, Omegatherm 201 thermal paste (Omega Engineering, Inc., Stamford, CT) was applied to the internal groove of the freezing device, the surface that contacts the DSFC. This provided approximately 10 °C degrees of further cooling capacity by reducing the contact resistance between the chamber and the freezing device. The AFA was attached to the DSFC and cooling initiated by increasing the power of the Linkam Cryopump to its maximum setting. Temperature was recorded in 1 s intervals using a DAS-TC/B data acquisition board (Keithley Instruments, Cleveland, OH). Cooling was maintained for 20 minutes and then the Cryopump was turned off. The apparatus was not removed from chamber during the passive thaw period. This protocol was repeated three times with a fresh sample placed in the chamber after each experiment.

A characteristic thermal history is given in Figure 8.2. The similarity of temperature measurements at each of the three locations on the surface of a single annulus indicated that the temperature distribution over the surface was uniform. The average spatial variation (measured as differences between thermocouples at a single time) when comparing thermocouples attached on a single side of the DSFC was 0.68 ± 0.44 °C (average ± standard deviation). Of the 3 tests performed, the maximum temperature difference recorded amongst all 6 thermocouples (excluding the sharp discontinuity region around the latent heat release) was 4.0 °C. To test for differences between temperatures recorded on opposing halves of the DSFC, the thermocouple readings on each side were averaged and compared. The temperatures measured on

opposing sides were in very good agreement. When the three thermocouples measurements per side were averaged and the difference compared, the average difference over all three experiments was 1.8 ± 1.0 °C (average ± standard deviation). The most significant differences were recorded at the lowest minimum temperatures reached. This indicated that the freezing apparatus was in good contact with the chamber throughout the protocol and that the cooling power delivered to each side of the device was effectively the same. This was the desired result. The minimum temperature reached was –83.4 ± 2.96 °C (average ± standard deviation) after 20 minutes of thawing. A detailed summary of the data is given in Appendix E.

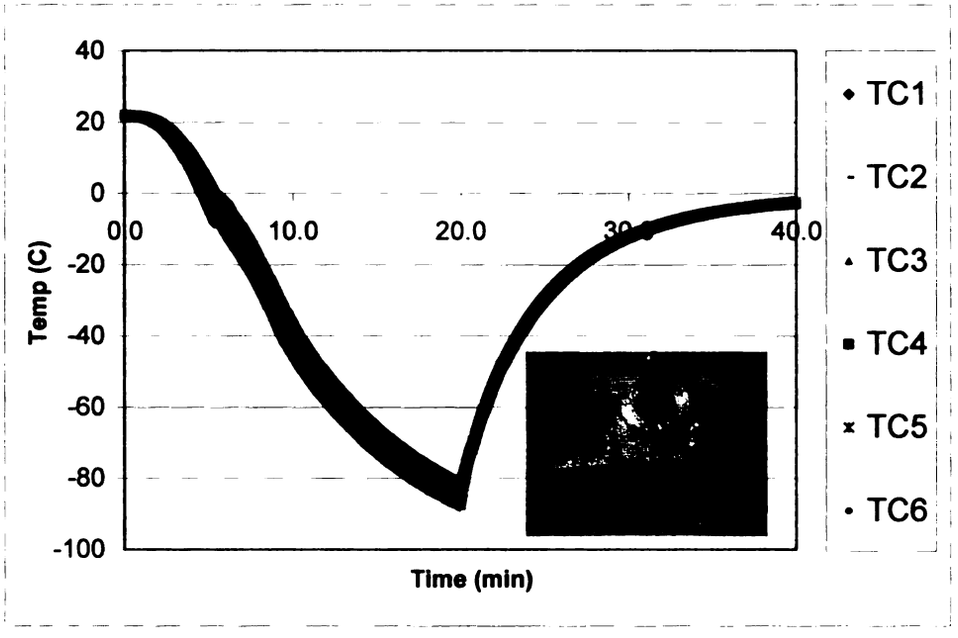

Figure 8.2 Characteristic data obtained with the Annular Freezing Apparatus (AFA). Three thermocouples were attached to each side of the DSFC (per the insert diagram) prior to assembly. The AFA was attached and cooling was initiated and maintained for 20 minutes.

As shown in Figure 8.3, hold periods were possible with the AFA by manually adjusting the pumping rate once the desired temperature was achieved. Cooling was initiated in the AFA attached to a dorsal skin flap chamber containing processed meat. Temperature was recorded in 1 s intervals. When the sample reached – 44.5 °C the pump speed was decreased until temperature stabilized. The pump speed was then adjusted as needed to maintain the temperature during the hold period.

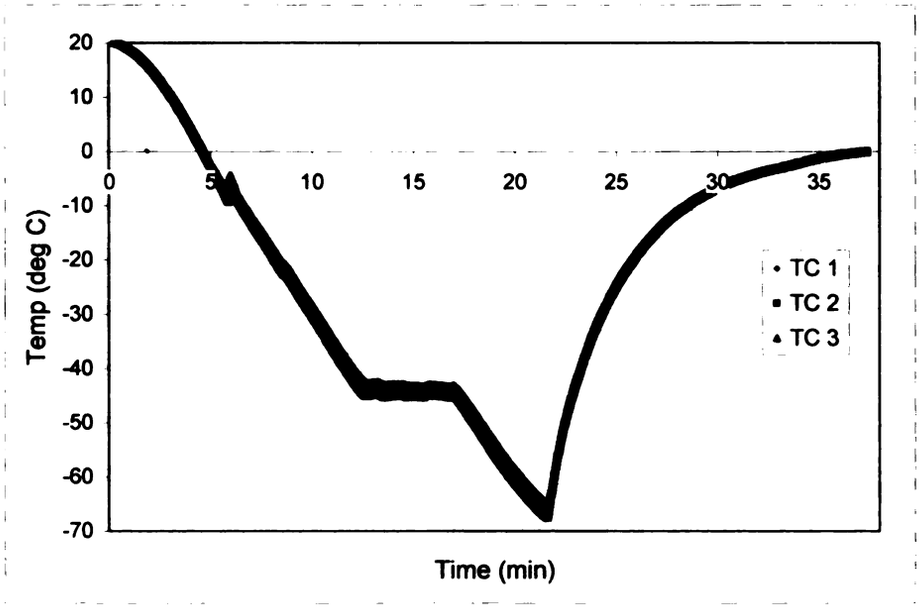

Figure 8.3 Demonstration of thermal control possible with the AFA system.

Once acceptable uniformity of cooling over the surface of the DSFC annulus and symmetry of response between both halves of the DSFC was established, the next goal was to determine the magnitude of the temperature gradient within the viewing region of the DSFC. A grid window was used to position a central thermocouple. This grid is

pictured in Figure 8.4. Thermocouples were mounted on the annular surface as previously described together with a centrally located thermocouple on the grid window. The window was placed groove-side down, with the thermocouple in contact with the tissue. Cooling was initiated and the sample cooled until the central thermocouple reached a temperature of –20.0 °C. This temperature was held for several minutes and then cooling discontinued. This procedure was repeated three times. During cooling, the maximum variation between the temperature of the annulus and the temperature recorded at the central thermocouple was 2.2 °C (range: 1.7-2.6 °C). If the temperature gradient is approximated as a linear function of distance from the center, these results suggest that the temperature gradient is of order 0.5 °C/mm. The actual nature of the temperature distribution will be discussed further in Chapter 9.

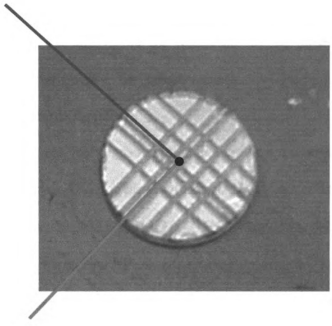

Figure 8.4 A DSFC glass window implemented with machined grooves of 400 μm diameter. The red and blue lines overlaid on the image illustrate how thermocouples can be mounted on this window.

In the Hoffman and Bischof study (2001a) involving freezing in the DSFC, large thermocouples were implemented for measurements. These were mounted with the thermocouple bead on the surface of the tissue, with the remaining lead wires at ambient conditions. Conduction error was considered to be significant and so they performed an experiment to quantify this contribution. For a thermocouple of the size used in this work (0.22 mm), the conduction error reported at –10 °C was 3 °C. In the present study the temperature gradient in the environment of the thermocouple wire is an order of magnitude smaller than in the Hoffman study, much more favorable for accurate temperature measurements. Since the temperature gradient is the driving force for

conduction errors, the error due to conduction can be approximated to be an order of magnitude less. This would yield conduction errors of approximately 0.3 °C. All thermocouple measurements would be expected to be affected similarly in the configuration described, hence fin effects should not be significantly altering the character of the temperature gradient.

Temperatures and freezing rates characteristic of the edge of a cryolesion were achieved using the novel AFA together with the DSFC. The initial design objective was met and freezing rates between 1 and 10 °C/min were achieved. Rates faster than 5 °C/min require the probe to first be cooled and then attached to the surface of the DSFC. At the fastest pumping rates the freezing apparatus is capable of achieving a temperature of –130 °C on the surface of the AFA. When the apparatus was connected to the DSFC, it was possible to achieve –110 °C on the inner annulus of the DSFC. Temperature gradients within the optical port of the DSFC were determined to be small (<1 °C/mm) thereby facilitating a more accurate experimental determination of localized thermal history. The symmetrical nature of the apparatus, and the reproducibility and uniformity of freezing rates achieved on the inner ring of the DSFC, resulted in a much more tractable computational problem compared to a conventional miniaturized ice-ball approach, which can lead to significant improvements in numerical efficiency of modeling efforts.

8.5 Bioheat Transfer Model Development

In previous experiments the AFA was characterized by obtaining thermocouple-based temperature measurements on the surface of the AFA, on the surface of the DSFC inner annulus (i.e. the side that contacts the tissue), as well as in phantom material and living tissue within the DSFC. This experimental information can be used to develop a numerical heat transfer model of freezing in the DSFC geometry that can provide field information not possible using discrete thermocouples. The mathematical model can subsequently be used to help design better *in vivo* experiments. With knowledge of the expected temperature gradients, thermocouples can be localized to areas that support effective extrapolation or provide representative temperature measurements. A numerical model can also be helpful for understanding how cryosurgical probes and window chambers of various designs influence the tissue thermal response.

8.5.1 Mathematical Models of Biological Tissue Freezing in the Literature

Mathematical models exist that predict the thermal field in tissue surrounding a cryosurgical probe (Cooper and Trezek, 1970). Numerical methods for solving multidimensional phase change problems of inanimate materials (Rabin and Korin, 1993) as well as biological materials with temperature-dependent thermophysical properties, metabolic heat generation and blood perfusion have been published (Rabin and Shitzer, 1998). Budman *et al.* (1995) developed a one-dimensional integral solution for the inverse Stefan problem for a non-ideal binary solution with a phase change occurring over a range of temperatures. Rabin and Shitzer (1995) published an exact analytical solution to the one-dimensional inverse Stefan problem in tissues with a non-ideal phase

change over a range of temperatures. The same authors also produced a one-dimensional combined integral solution in the frozen region and a numerical enthalpy-based integral solution in the unfrozen region for the inverse Stefan problem for freezing/thawing in biological tissues (Rabin and Shitzer, 1997). Non-ideal phase change over a range of temperatures was included, as were the effects of metabolic heat generation and blood perfusion in the unfrozen region. The author has also recently published a morphology-specific solidification model of mammary tissue freezing based on the Neumann exact solution for 1-D freezing (Elliott and McGrath, 1999). A numerical phase change model, specific to the DSFC geometry, was published by Hoffman and Bischof (2001a). These authors used a 2-D transient numerical solution incorporating blood flow for a cylindrical geometry. While providing a useful conceptual framework, this body of published work cannot be applied in any detailed fashion to the specific case of freezing tissue within the DSFC as imposed by the AFA. Consequently a geometry specific numerical solution was desired that could adequately represent the current situation. Before proceeding to the geometry of the chamber, exact solutions from the literature provided a means of benchmarking to verify that the numerical models were adequately predictive.

8.5.2 Governing Equations

Prediction of thermal fields that are generated in biological tissues during cryosurgery generally rely on solutions of conduction heat transfer governing equations that include the effects of latent heat evolution that occur during phase change. The initial condition is typically one of uniform temperature, T_o, often ambient temperature

(20-25°C) or physiologic temperature (37°C). In practice the material is subjected to a low temperature probe located centrally or distally, which is generally modeled as either a temperature or heat flux boundary condition. These can be steady or transient boundary conditions. Beginning from ambient or physiologic conditions, energy in the form of sensible heat is thus removed from the tissue/material until the solidification phase change temperature (T_f) is reached. As the material begins to solidify, latent heat is released in the process.

The geometry of a typical 1-D problem is shown in Figure 8.5.

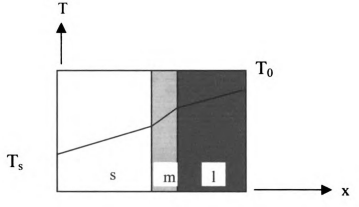

Figure 8.5 Schematic illustrating solidification of a homogeneous semi-infinite material with a phase change region. T_s represents the surface temperature imposed and T_o the initial temperature. The mushy region (m) is identified by the positions of the solidus and liquidus phase change boundaries.

The governing equation for heat transfer in the solid region is given by the simple heat conduction equation:

$$\rho_s c_s \frac{\partial T_s}{\partial t} = \frac{\partial}{\partial x}\left(k_s \frac{\partial T_s}{\partial x} \right) \qquad 0 < x < X_s, \qquad [8.1]$$

where ρ_s , k_s, and c_s, are the density (kg/m^3), thermal conductivity (W/mK), and specific heat (J/kgK) of the solid, respectively. These properties may vary spatially and can be temperature-dependent. The position of the solidus interface is given by X_s. The governing equation in the liquid region will contain a buoyancy term that represents convection due to a change in density as the material changes from solid to liquid. This term can be neglected if the change in density is not significant. The energy equation in the liquid region, including this term, is:

$$\rho_l c_l \frac{\partial T_l}{\partial t} - \rho_l c_l u \frac{\partial T_l}{\partial x} = \frac{\partial}{\partial x}\left(k_l \frac{\partial T_l}{\partial x} \right) \qquad X_l < x < \infty, \qquad [8.2]$$

where the subscript l denotes the liquid values of the previously defined properties, and u is the bulk velocity of the liquid region where X_l defines the location of the liquidus interface.

Although pure materials undergo phase change at a single temperature, many materials solidify over a temperature range. Thus as the material changes phase three distinct regions are observed: a solid region, a liquid region, and a region that contains both the solid and liquid phase. This concept was illustrated in Figure 8.1. A liquidus phase change temperature, T_{fl}, and a solidus phase change temperature, T_{fs}, are defined to describe the thermal limits of the phase change process. This region is commonly termed the 'mushy zone'. The governing equation for the mushy region is given by:

$$\frac{\partial^2 T_m}{\partial x^2} + \frac{\rho_m L}{k_m}\frac{df_s}{dt} = \frac{1}{\alpha_m}\frac{\partial T_m}{\partial t} \qquad X_s < x < X_l \qquad [8.3]$$

where subscript m refers to the mushy zone properties, f_s is the fraction of solid in the mushy zone, and L is the latent heat of fusion (kJ/kg). The thermal diffusivity, denoted by α, represents the thermal conductivity divided by the product of density and specific heat. The various solutions available for solidification problems can generally be classified in terms of how the mushy region is modeled. Specifically they vary in how the contribution from the latent heat term is handled.

8.5.3 Latent Heat Effects

Biological solutions and tissues contain water, salts, proteins, sugars and many other bio-molecules. In such complex mixtures, freezing does not occur at a single temperature but rather spans a range of temperatures, and the evolution of latent heat has a functional relationship with temperature in this freezing range (Voller and Prakash, 1987).

8.5.4 Benchmark Solutions

Analytical solutions do not exist for complex geometries such as those of the DSFC. Consequently a numerical solution was desired to provide thermal field information for freezing in DSFC tissue. To generate thermal field information of tissue frozen in the DSFC, a computational fluid dynamics (CFD) software program, Fluent™ 5.0 was utilized. Fluent utilizes the finite volume method (FVM) of discretization based

on a fixed grid to arrive at a numerical solution to the governing equations of the field of interest. Fixed grid methods are routinely used for numerical solutions of phase change phenomena (Voller *et al.*, 1990). The alternative is to use a front-tracking method that employs a deforming grid scheme. The front-tracking approach works well for isothermal phase change of a pure material. However, for a multi-component solidification problem involving a mushy region, tracking an interface becomes computationally challenging (Voller *et al.*, 1990). Other commercial packages can be used or a specific numerical analysis code can be written that adequately generates solutions to solidification heat transfer problems. Fluent™ was chosen on the basis of its availability, and the author's familiarity with this software package.

Before beginning to develop complex geometries for Fluent™ analysis it was necessary to ensure that the numerical solver was producing accurate results. The disadvantage of numerical models is that they frequently produce 'reasonable' results regardless of how accurately the problem is specified. Consequently it is the task of the user to validate their accuracy by whatever means possible. A benchmark case was solved using three different 1-D solutions, an apparent C_p method in Fluent, the simplified 2-phase Neumann solution (Lunardini, 1981) and the 3-phase Cho and Sutherland solution (Cho and Sutherland, 1969). The properties used in the solution are given in Table 8.1.

Table 8.1 Properties and Conditions Employed in the Benchmark Solution

Initial Temperature (K)	310	
Upper Limit of Phase Transition (K)	272	
Lower Limit of Phase Transition (K)	265	
Surface Temperature (K)	77	
Thermal Conductivity – frozen (W/mK)	1.88	
Thermal Conductivity – unfrozen (W/mK)	0.61	
Thermal Conductivity - mush (W/mK)	1.245	
Specific Heat – frozen (kJ/kgK)	2.04	
Specific Heat – unfrozen (kJ/kgK)	4.18	
Specific Heat – mush (kJ/kgK)	3.11	
Density (kg/m^3)	1000	
Latent heat (kJ/kg)	334	
Time(s)	22	

8.5.4.1 Apparent C_p Method with Fluent™

The apparent C_p method involves the representation of the latent heat effect as a component of the specific heat, C_L. That is:

$$C_L = \frac{L}{\Delta T} \qquad [8.4]$$

or some other function of temperature, where ΔT is the temperature range over which the latent heat is released. The latent heat effect can then be incorporated into an 'apparent' C_p that will have a functional relationship with temperature that varies from phase to phase. The apparent specific heat, C_a, is thus given as:

$$C_a = \begin{cases} C_s & \text{(solid)} \\ \dfrac{C_s + C_l}{2} + C_L & \text{(mush)} \\ C_l & \text{(liquid)} \end{cases} \qquad [8.5]$$

Consequently the governing equation in the mushy region takes the form of that in the solid and liquid region equations. The latent heat release was modeled as a piecewise linear function between –8 and –1 °C with the peak $C_L(T)$ value occurring at –3 °C. This functional relationship is plotted in Figure 8.6. This relationship is a geometrically simple representation that closely mirrors the more complex pattern of latent heat evolution. It was used by Rabin and Shitzer (1997) with good results. Bonacini *et al.* (1974) demonstrated that the shape of the assumed curve does not matter as long as the area beneath the specific heat curve accurately reflects the magnitude of the latent heat effect.

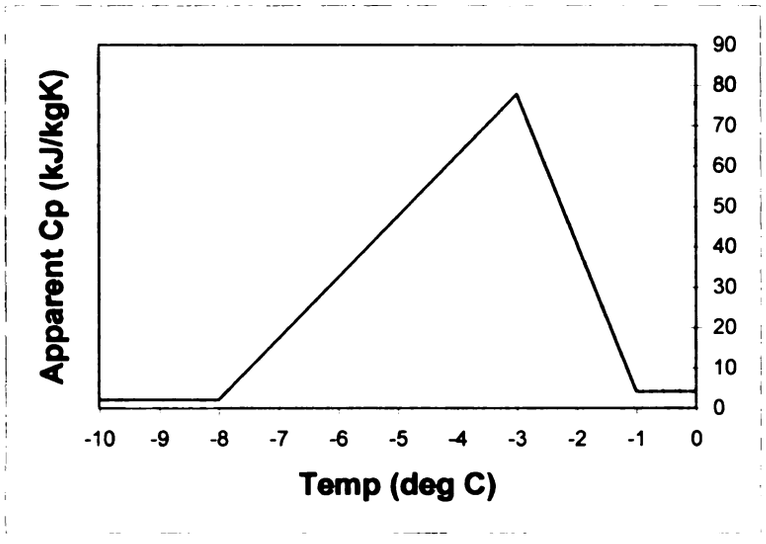

Figure 8.6 Functional relationship of apparent C_p with temperature.

The geometry representing the physical situation was first constructed in Gambit™, a preprocessor for CFD analysis. A 0.25 cm x 2.0 cm geometry was used. A mesh resolution of 10 microns was chosen with quadrilateral volumes. This yielded a 5000 element mesh. Boundaries were assigned using the pre-processer, with one surface at T_s and the remaining boundaries assigned as adiabatic. The solution was then generated using a second order upwind scheme with a convergence criterion of $1x10^{-7}$ and a time step of 1s.

8.5.4.2 Neumann Solution: 2-Phase

The Neumann solution, an exact solution for 2-phase solidification in a semi-infinite tissue slab, was also used to solve the benchmark phase change problem (Lunardini, 1984). In the Neumann solution the mushy zone is reduced to a single phase-change interface. An illustration of this is given in Figure 8.7. The Neumann formulation is characterized by a distinct moving phase change boundary at which the heat in the solid and liquid phases must balance.

In the solid and liquid region the governing equations are given by Equations 8.1 and 8.2, respectively, however convection transport due to change in density is neglected. In the following derivation the numerical subscripts are assigned as follows: (1) liquid (2) solid. The energy balance at the phase change interface is given as:

$$k_1 \frac{\partial T_1}{\partial x} - k_2 \frac{\partial T_2}{\partial x} = \rho L \frac{dX}{dt} \qquad [8.6]$$

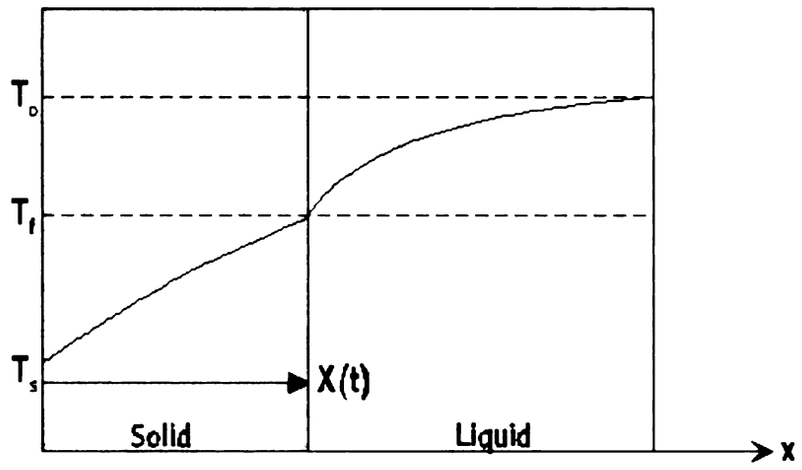

Figure 8.7 Schematic illustrating solidification of a homogeneous semi-infinite material initially at T_o with a single-phase change temperature, T_f, and a temperature boundary condition $T=T_s$ at $x=0$. The position of the phase change boundary is given by $X(t)$.

At the interface of the solid and liquid region the temperature is given by the phase change temperature of the material:

$$T_1(X,t) = T_2(X,t) = T_f \qquad [8.7]$$

The governing partial differential equations can be transformed into an ordinary differential equation using the following similarity transformation:

$$\eta = \frac{x}{2\sqrt{\alpha_1 t}} \qquad [8.8]$$

Direct integration of the resulting ordinary differential equation for either region, yields the solution:

$$T_1 = C\int_0^{\eta} e^{-\beta^2}\,d\beta \qquad [8.9]$$

The error function is defined as:

$$\operatorname{erf}\eta = \frac{2}{\sqrt{\pi}}\int e^{-\beta^2}\,d\beta \qquad [8.10]$$

which, when implemented with the boundary condition at x = 0 allows us to express the temperature distributions in each region as:

$$T_1 = T_s + \frac{(T_f - T_s)}{\operatorname{erf}(\lambda)}\operatorname{erf}\frac{x}{2\sqrt{\alpha_1 t}} \qquad [8.11]$$

$$T_2 = T_o - \frac{(T_o - T_f)}{\operatorname{erfc}(\lambda\sqrt{\alpha_{12}})}\left(\operatorname{erfc}\frac{x}{2\sqrt{\alpha_1 t}}\right) \qquad [8.12]$$

The constant λ can be determined from:

$$\frac{e^{-\lambda^2}}{\mathrm{erf}(\lambda)} - \frac{k_{21}\sqrt{\alpha_{12}}(T_o - T_f)e^{-\alpha_{12}\lambda^2}}{(T_f - T_s)\mathrm{erfc}\lambda\sqrt{\alpha_{12}}} = \frac{L\lambda\sqrt{\pi}}{C_1(T_f - T_s)} \qquad [8.13]$$

where $\alpha_{12}=\alpha_1/\alpha_2$, and $k_{21}=k_2/k_1$. This constant can then be implemented in the expression:

$$X = 2\lambda\sqrt{\alpha_1 t} \qquad [8.14]$$

to determine the location of the phase-change front with time.

The previously defined thermal properties and conditions were implemented in Equation 8.13. Using Mathematica™ software to determine the root of this equation (see Appendix E for program), the location of the solidification interface with time was determined from equation 8.14. The position of the interface delineates the appropriate spatial range for each of the temperature equations, thereby allowing the continuous temperature distribution to be plotted.

8.5.4.3 Cho and Sutherland Solution: 3-Phase

Cho and Sutherland (1969) developed an exact solution to the Neumann problem for the case of a latent heat being evolved over a phase change region. This solution is reviewed in Lunardini (1981). In the following solution the numerical subscripts refer to each phase as follows: (1) solid, (2) mush, (3) liquid. At the solid-mush and mush-liquid interfaces, the temperatures are given by the solidus and liquidus phase change temperatures of the material:

$$T_1(X_s,t) = T_2(X_s,t) = T_{fs} \qquad [8.15]$$

$$T_2(X_l,t) = T_3(X_l,t) = T_{fl} \qquad [8.16]$$

The energy balance at the solidus front is given by:

$$k_1 \frac{\partial T_1}{\partial x} = k_2 \frac{\partial T_2}{\partial x} + \rho_1 L \frac{dX_s}{dt} \quad \text{at } x = X_s \qquad [8.17]$$

Similarly, the energy balance at the liquidus front is given by:

$$k_2 \frac{\partial T_2}{\partial x} = k_3 \frac{\partial T_3}{\partial x} \qquad \text{at } x=X_l \qquad [8.18]$$

In the same manner as the Neumann solution presented previously, the energy balance at each phase change interface provides constants that are used to determine the position of each interface. The resultant equations that must be simultaneously solved for λ and η are:

$$\frac{\exp(\lambda^2)}{\operatorname{erf}(\lambda)} + \frac{\sqrt{\pi} k_{21} fl}{2C_2(T_{fs} - T_s)(\eta - \lambda)} - \frac{k_{21}}{\sqrt{\alpha_{21}}} \frac{\left(T_{fl} - T_{fs} + \frac{lf}{c_2}\right) \exp\left(\frac{-\lambda^2}{\alpha_{21}}\right)}{(T_{fl} - T_{fs})\left(\operatorname{erf}\frac{\eta}{\sqrt{\alpha_{21}}} - \operatorname{erf}\frac{\lambda}{\sqrt{\alpha_{21}}}\right)} = \frac{l\lambda\sqrt{\pi}(1-f)}{c_1(T_{fs} - T_s)} \qquad [8.19]$$

and

$$\frac{\left(T_{fl}-T_{fs}+\frac{lf}{c_2}\right)\exp\left(\frac{-\eta^2}{\alpha_{21}}\right)}{\left(\operatorname{erf}\frac{\eta}{\sqrt{\alpha_{21}}}-\operatorname{erf}\frac{\lambda}{\sqrt{\alpha_{21}}}\right)}-\frac{\sqrt{\pi\alpha_{21}}lf}{2c_2(\eta-\lambda)}=(T_o-T_f)k_{32}\frac{\sqrt{\alpha_{23}}\exp\left(\frac{-\eta^2}{\alpha_{31}}\right)}{\operatorname{erfc}\frac{\eta}{\sqrt{\alpha_{31}}}} \quad [8.20]$$

Once these roots have been determined, they can be implemented to determine the position of each interface according to:

$$X_s = 2\lambda\sqrt{\alpha_1 t} \quad [8.21]$$

$$X_l = 2\eta\sqrt{\alpha_1 t} \quad [8.22]$$

as well as the temperature profiles in each region. The final expressions for the temperature distribution in each region are given by:

$$\frac{T_1-T_s}{T_{fs}-T_s}=\frac{\operatorname{erf}\left(\frac{x}{2\sqrt{\alpha_1 t}}\right)}{\operatorname{erf}\lambda} \quad [8.23]$$

$$\frac{T_2-T_s}{T_{fs}-T_s}=1-\frac{lf\left(\frac{x}{2\sqrt{\alpha_1 t}}-\lambda\right)}{c_2(T_{fs}-T_s)(\eta-\lambda)}+\left(\frac{T_f-T_{fs}+\frac{lf}{c_2}}{(T_{fs}-T_s)}\right)\frac{\operatorname{erf}\left(\left(\frac{x}{2\sqrt{\alpha_2 t}}\right)-\left(\frac{\lambda}{\sqrt{\alpha_2 t}}\right)\right)}{\operatorname{erf}\left(\frac{\eta}{2\sqrt{\alpha_2 t}}\right)-\operatorname{erf}\left(\frac{\lambda}{\sqrt{\alpha_2 t}}\right)} \quad [8.24]$$

and

$$T_3 = T_o - (T_o - T_{fl}) \frac{\operatorname{erfc}\left(\frac{x}{2\sqrt{\alpha_2 t}}\right)}{\operatorname{erfc}\left(\frac{\eta}{\sqrt{\alpha_{31}}}\right)} \qquad [8.25]$$

The Mathematica™ program written to solve for the roots and to generate this solution is given in Appendix F.

8.5.4.4 Comparison of Results

The results of all three solutions are plotted together in Figure 8.8 for a solution at t = 22s. The solutions of Neumann and those of Cho and Sutherland are in very close agreement. In the phase change region the two solutions are expected to vary, as the latent heat is being released over a range of temperatures in the latter solution and at a single temperature in the former. This is indeed the case, however the deviation is very small, with a percent difference of < 2.5 % in the freezing range. The apparent C_p solution using Fluent™ is expected to more closely resemble that of Cho and Sutherland. The results of the Fluent™ solution are very similar to the 3-phase exact solution, however the region of latent heat release does not track exactly. The maximum percent difference between temperatures for these two solutions is 3.3 % and this occurs in the phase change region. The average difference over the temperature range in the plot is 1.4%. These results suggest that the apparent C_p method with Fluent™ is providing acceptable estimates of temperature.

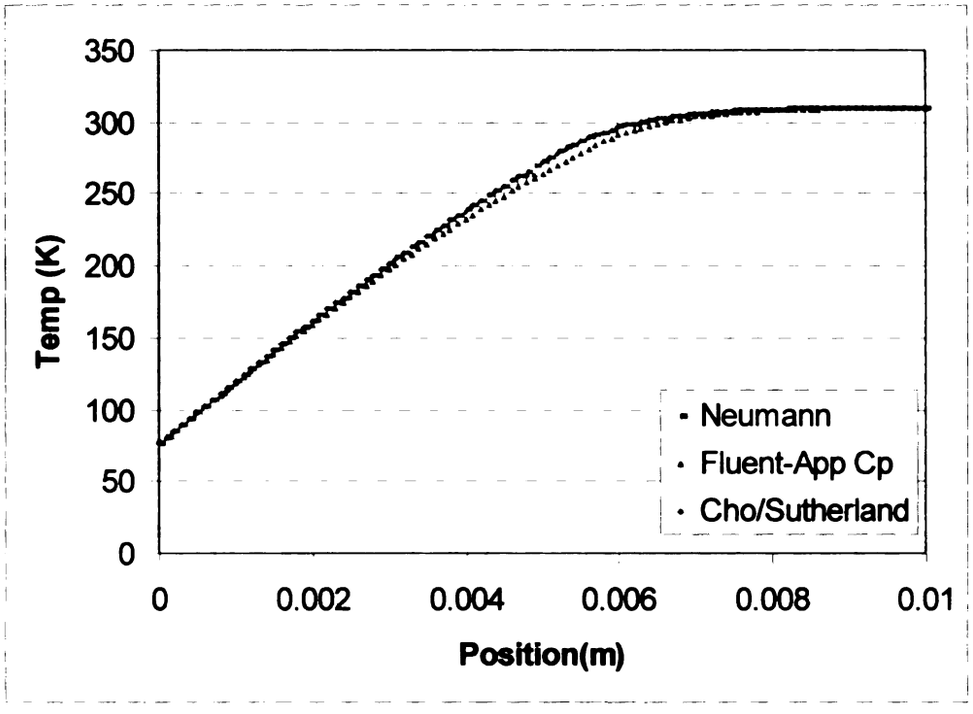

Figure 8.8 Predicted thermal profiles using three different solutions for solidification in a rectilinear semi-infinite geometry.

8.5.5 Thermal Response in DSFC Tissue: Apparent C_p Method

The apparent C_p method for a 1-D solidification problem (solved for a 2-D geometry) appeared to give reasonable estimates of the thermal field when compared to 1-D exact solutions. This was taken as adequate verification that the numerical model and apparent C_p approach was valid. It was assumed that using this same solution method (Fluent™ numerical solution with apparent C_p) would produce accurate results for a 2-D solidification problem in a more complex geometry.

A simplified 2-D model of the DSFC and tissue was created using Gambit. Based on the characterization work of previous sections, it was decided that the thermal response of the DSFC was adequately symmetrical to model the tissue according to the schematic in Figure 8.9. The tissue thickness varied in experiments. For the purposes of

understanding the temperature gradient through the thickness of the tissue as well as the temperature distribution over the viewing field, a representative tissue thickness of 1 mm was chosen. The thickness of the glass window in the DSFC was 0.9 mm. The mesh is pictured in Figure 8.10.

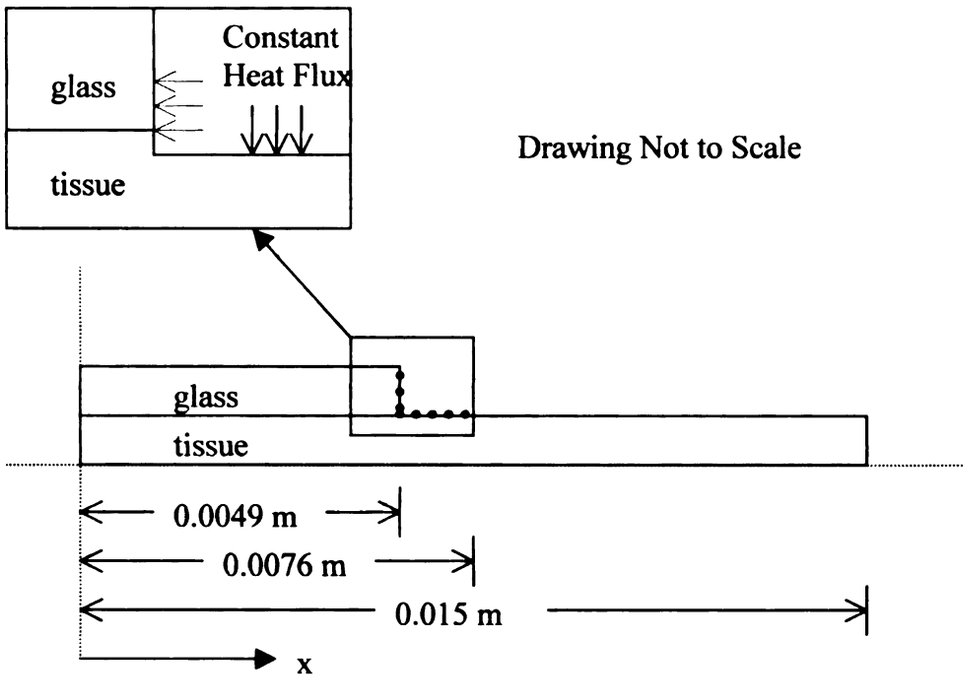

Figure 8.9 Schematic illustrating the geometry used to represent a ¼ section of tissue in the DSFC. The point of contact of the DSFC annulus, indicated with the dark dotted line, was modeled as a constant heat flux boundary condition.

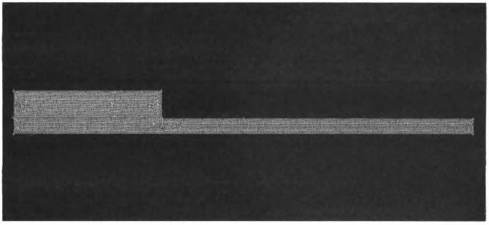

Figure 8.10 Mesh used to generate solidification solution.

Because the amount of tissue surrounding the DSFC varies depending on the location, selecting the appropriate length of the tissue required some approximation. The side of the annulus closest to the body of the animal might be modeled as a semi-infinite, whereas because of the paucity of tissue on the uppermost side, this area can be considered of finite length. A tissue length that was twice the diameter of the skin flap tissue was chosen to represent the extent of tissue surrounding the chamber in an attempt to create a boundary condition that represented an average of the two conditions described.

The glass and tissue were meshed separately using a 50-micron triangular mesh. This yielded a 5855-node mesh, with 6918 elements comprising the tissue, and 3930 elements comprising the window. The metal annulus was not represented by elements in the mesh but instead was modeled as a constant heat flux boundary condition. This was a reasonable approximation of the thermal situation and it was simpler to implement than a prescribed cooling rate. All other boundaries not represented by a symmetry condition

were considered adiabatic. The heat flux boundary condition was adjusted in the model until a cooling rate on the order of that seen on the surface of the annulus during characterization measurements (~5 °C/min) was achieved. This resulted in a heat flux condition of -1600 W. A second order upwind scheme was used to generate an energy solution. The convergence criterion was set at $1x10^{-7}$ and time steps of 1 s were used. Properties of water as used in the benchmark solution were utilized. The starting temperature implemented was 295 K. Solutions were generated at periodic intervals and are plotted in Figure 8.11.

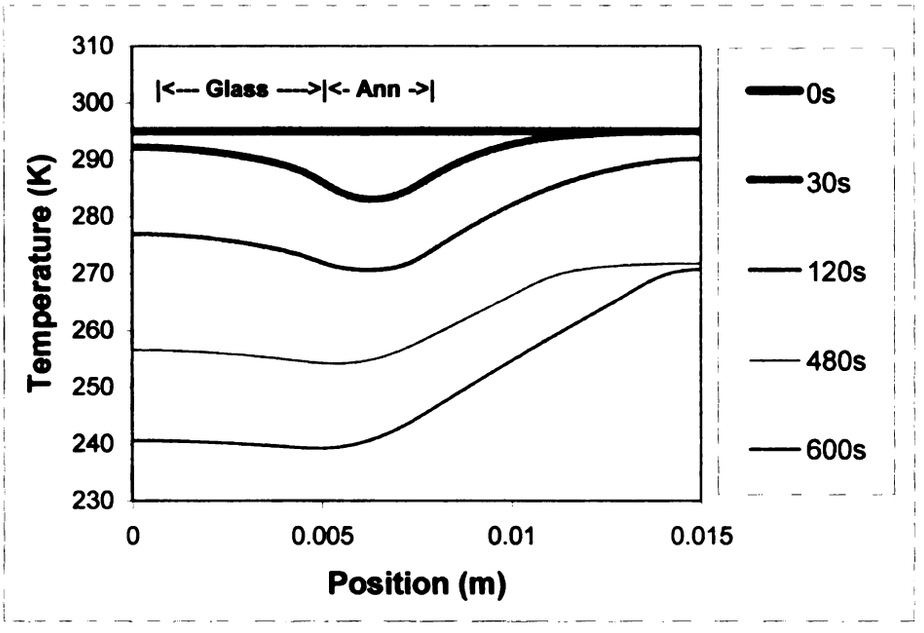

Figure 8.11 Temperature profiles generated for phantom tissue (properties of water used) in the tissue geometry depicted in Figure 8.9.

As expected, the temperature can be seen to be minimal directly beneath the surface of the annulus, which is centered at x = 0.0625 m (see schematic in Figure 8.9 for orientation). As cooling progresses the temperature gradient within the chamber is seen to decrease. The rate of cooling in the tissue decreases when the phase change temperature region is reached. Latent heat release in this region serves to slow down the advance of the freezing front. By the time the chamber tissue reached –18 °C, the temperature gradient was very flat, with a spatial variation of < 0.5 °C/mm. Even at the beginning of the freezing process the temperature difference between the center and the edge of the chamber was seen to be small (~5 °C after 30 s).

In the simulation the tissue surrounding the optical area of the chamber appears to cool significantly as well. This has also been observed in the course of *in vivo* experiments, as will be discussed in Chapter 9. Future probe or protocol designs could benefit from modifications that minimize the cooling in the region outside the chamber.

The temperature distribution through the thickness of the tissue was studied to understand if significant temperature gradients existed in the axial direction. It is generally assumed that the temperature gradient is negligible through the thickness of thermally treated intra-vital preparations of the type used in this work. Using the numerical simulation, this assumption was explored for the present case involving a relatively thick preparation (1 mm). For illustration purposes the predicted thermal field at 240s is displayed on the grid geometry in Figure 8.12. Evident from this plot is the nature of the temperature gradient through the thickness of the tissue. The temperature difference between the top surface of the tissue and the midline of the tissue (i.e. the bottom symmetry plane in the mesh geometry) was calculated for various times and the

results are plotted in Figure 8.13. Temperatures were seen to be effectively constant in the axial direction, suggesting that measurements taken on the surface of the tissue would be representative of those throughout the thickness. The largest temperature difference was observed around the edge of the window, suggesting this would not be a good location for a thermocouple if a representative tissue temperature was desired.

The temperature difference across the thickness of the glass was also examined. The difference in temperature between the top surface and the bottom surface of the glass window was determined and is plotted in Figure 8.14. Again the temperature can be seen to be effectively uniform through the thickness of the glass, with the temperature differing by less than 0.2 °C. The area near the edge of the DSFC annulus has a higher variation in temperature through the thickness of the glass, as was observed for the tissue. Still this variation is less than 1 °C.

Two key observations come from these simulations: (1) the temperature throughout the thickness of the tissue and glass appears to be uniform, and (2) the temperature gradient is less than 1 °C/mm in the window chamber. These are important observations that can be used in the design of experiments for future studies. The prediction of uniform temperature through the thickness of both the glass and tissue is an interesting result relevant to the potential use of optical techniques that can measure surface temperatures in these systems. This observation was consistent at all time points. These results suggest that optical methods for measuring surface temperature would be highly successful in this system, as the measured surface temperature would be representative of the tissue temperature, and extrapolation or interpolation would not be necessary.

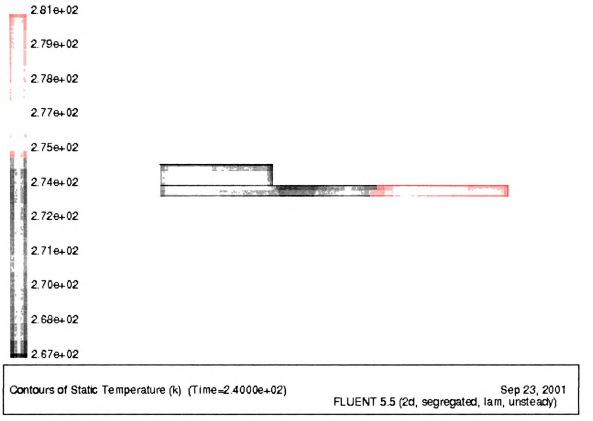

Figure 8.12 Temperature distribution in DSFC tissue (properties of water used) as simulated at 240 s.

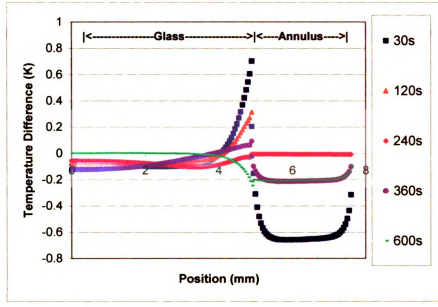

Figure 8.13 Temperature difference between the top surface of the chamber geometry (glass and annulus regions) and the tissue midline as a function of temperature.

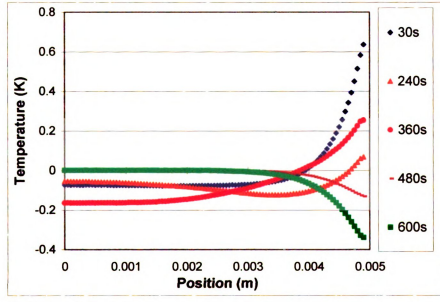

Figure 8.14 Temperature difference between the top and bottom surfaces of the DSFC glass window as a function of time and radial position.

Chapter 9

Application of the GFP Intra-vital Viability Assay: Injury Following Slow Freezing to High Sub-Zero Temperatures

9.1 Motivation

The deleterious effects of freezing on biological tissue can be sub-divided into two main categories, direct cell injury, and secondary injury associated with micro-vasculature damage and host response. Although the nature of direct cell injury has been well-studied (Meryman, 1970; McGrath *et al.*, 1975; Mazur, 1977; Bischof *et al.*, 1997) comprehensive information on the contribution of secondary injury to the ultimate size of the cryosurgically induced lesion is not available (Gage and Baust, 1998).

Because of the high correlation between intracellular ice formation and cell death, cryosurgery instrumentation is generally designed to maximize this mode of direct cell injury. Cryosurgical probes are created with increasingly colder operating temperatures and increased cooling power (Baust *et al.*, 1997). However, when applying rapid freezing rates and low temperatures to tissues using a conventional cryosurgical probe, basic heat transfer principles dictate slower freezing rates and high sub-zero temperatures in distal areas of the tissue as a natural consequence of the treatment. Treated tissue thus

experiences different thermal histories at different spatial locations and this thermal history will depend on the thermal properties of the tissue, as well as the location, shape, and cooling power of the cryosurgical probe. This general concept is illustrated in Figure 9.1 for a cylindrical probe. Although this clinical approach yields acceptable levels of certainty about cell death at the center of the lesion where the probability of intracellular ice formation is high (Whittaker, 1974ab), in peripheral areas the injury is complex and not very predictable. Consequently clinical protocol involves extending the ice ball into the healthy tissue circumscribing the tumor to ensure that critical isotherms (discussed shortly) reach the edge of the diseased tissue.

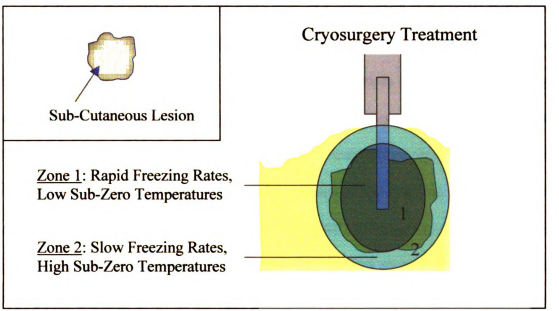

Figure 9.1 Conceptualization of a cryosurgically treated subcutaneous lesion. Regions close to the probe will experience rapid cooling and reach temperatures close to the temperature of the probe; tissue further away from the probe will experience slow cooling rates and will have temperatures closer to the phase change temperature of water.

Many early *in vitro* studies suggested that –20 °C was the necessary critical temperature to achieve certain cell death (Mazur, 1963; Meryman, 1956; Cooper, 1964), hence many clinical protocols were designed to ensure that the entirety of the lesion experienced temperatures at least as low as –20 °C. More recent *in vitro* studies suggest that this critical temperature is as low as – 40 °C (Tatsutani *et al.*, 1996; Roberts *et al.*, 1997) or – 50 °C (Jacob *et al.*, 1985), and in their review on mechanisms of cryosurgically relevant tissue injury, Gage and Baust (1998) recommend a critical temperature of –50 °C to be certain of achieving a good clinical outcome when treating neoplastic tissue. To achieve this temperature at the edge of the lesion requires the freezing of a large margin of healthy tissue.

Although the nature of injury at the edge of a cryo-lesion is not well understood, it is recognized that micro-vascular damage occurring at slow freezing rates and high sub-zero temperatures may contribute to tumor de-vitalization, and therefore can figure significantly into the size of the ultimate lesion that develops. Consequently, estimation of cryosurgical success using a lethal temperature prescribed on the basis of intracellular ice formation *in vitro* can under-predict the amount of damage that will occur *in vivo*. Recent attempts to understand the lethal temperature for cell injury *in vivo* suggest that the lethal temperature *in vivo* is considerably higher than prescribed on the basis of *in vitro* tests (Hoffman, 1999, 2001ab; Schuder, 2000). The results of such studies should not necessarily result in the prescription of a higher sub-zero temperature criterion for clinical usage, but rather serve to provide a more comprehensive understanding of how all of the various cellular responses inter-relate to create the final lesion. In this manner rationally based adjuvant therapies or variations of the traditional algorithm can be

identified and implemented to possibly improve clinical outcome and prevent secondary recurrence. Understanding the relationship between thermal history and tissue injury *in vivo,* in lieu of *in vitro* extrapolation, would thus help advance the state of the art in cryosurgery research.

Tumor cells are generally more resistant to intracellular ice formation (IIF), as evidenced by both direct experimental observation and a trend towards higher membrane water permeability values (McGrath, 1988). Cells with a greater ability to dehydrate in the presence of extra-cellular ice are less likely to super-cool and the formation of intracellular ice is thus less probable. In light of this tendency, the secondary role that vascular injury plays in destroying the treated neoplastic tissue is important to understand so that in the development of new therapies appropriate end-points for evaluation of therapeutic success are chosen. Also, if microvascular damage is a significant mode of injury, adjuvent therapies such as the use of anti-angiogenic drugs may be desirable to improve clinical success. Combined chemical and cryosurgery therapies such as this are currently under investigation (Baust *et al.*, 2000; Clarke *et al.*, 2001). It is especially important to understand the balance of primary and secondary contributions to tissue destruction where treatment of aggressive and rapidly proliferating cancers is concerned. If the time course of injury following cryosurgery is such that the destruction of cells by ischemia is outstripped by the rapid growth and spread of these cells into a well-vascularized region, then cryosurgery without other interventions may not be the best treatment option.

9.2 Relationship between micro-vascular injury and thermal history *in vivo*

It is well known that the thermal processing conditions causing cell death vary enormously from cell-type to cell-type. The relationship between freezing rate and survival for various cells has been comprehensively studied. Figure 9.2 illustrates this relationship for a number of different cell types. The variation evident in this figure demonstrates the difficulty in generalizing the relationship between freeze injury and thermal history in just a direct cell injury sense. Cell injury is not just a function of freezing rate. It is also a function of the minimum temperature, the thaw rate, and the hold time at a given temperature, and these variables are often intricately interrelated. For example, a recent study indicates that the minimum lethal temperature for human primary prostatic adenocarcinoma cells depends on freezing rate (Tatsutani et al., 1999), suggesting there isn't a single critical isotherm associated with cell death. In addition to these thermal variables there are certain host features that become important *in vivo*. The local tissue environment can impact how well a cell can recover from an applied freezing stress (Jacob *et al.*, 1985). Immune response can result in cell de-vitalization above and beyond that inflicted directly by freezing. The local blood vessel architecture can also figure significantly into the problem by creating heat sinks that make it difficult to cool certain regions of tissue, leading to thermal histories that are difficult to quantify and relate to clinical outcome. Understanding the importance of thermal history variables, *in vivo*, where the effects of cell-communication, cell immune response, and micro-vascular contributions are in play, is an important goal if the state of the art in cryosurgery is to be advanced. However, uncoupling direct cellular injury *in vivo* from the secondary cell

injury brought about by a myriad of host factors can be a daunting task. The technologies available to researchers have precluded such a comprehensive investigation to date.

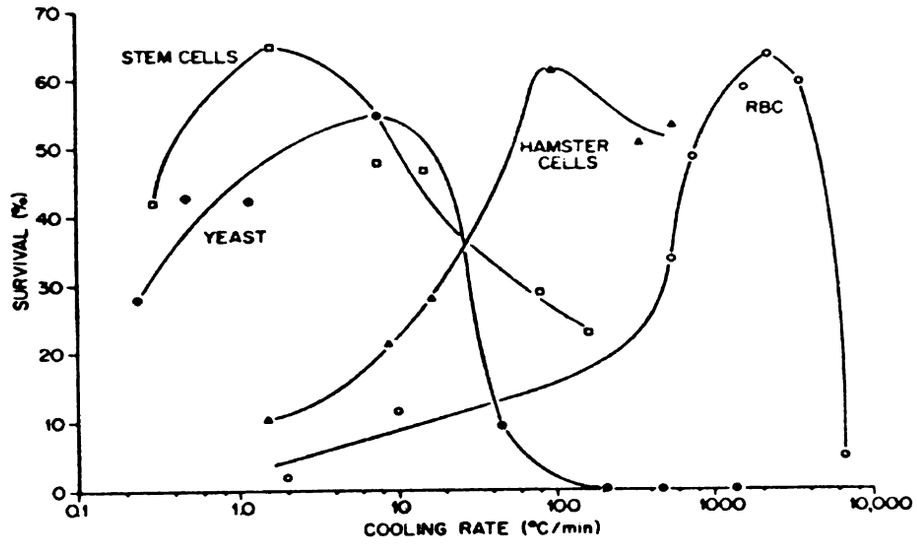

Figure 9.2 Relationship between freezing rate and survival for various cell types. From Mazur, 1970.

It is well-established that malignant tumor tissue requires a significant blood vessel supply to meet the high metabolic demands of continuously dividing cells (e.g. Li *et al.*, 2000). A number of interventive therapies exploit this fact. For example, anti-angiogenic drugs are specifically designed to inhibit the growth of new vessels (angiogenesis) thereby preventing the tumor from uninhibited growth. When cells aren't adequately nourished they will die from ischemic injury, a lack of adequate nutrition. This concept is illustrated in Figure 9.3. Ischemic injury is hypothesized to contribute in part to the overall damage that accrues during cryosurgery, as impaired blood flow has been demonstrated to be a consequence of the freezing process. For example, Brown *et*

al. (1993; 1994) have demonstrated reduced and complete shutdown of perfusion in cryo-treated liver, and cremaster muscle, respectively, following cryosurgery. Also, there exists a preponderance of evidence in the frostbite literature that implicates the role of micro-vascular damage in freezing induced injury. Although frostbite injury is generally associated with slow freezing to sub-zero temperatures that are considerably higher than typically desired for a cryosurgery treatment, frostbite injury does mirror the character of freezing at the margin of a cryo-lesion. Despite the cornucopia of studies detailing the existence of micro-vascular damage and reduced or absent flow for many hours following cryosurgical intervention, none of these studies provide direct evidence that necrosis is caused by ischemia and not other injuries such as slow freezing 'solutes injury' damage, or an increased cryo-sensitivity of cells growing in an *in vivo* environment. Consequently the balance of direct cellular injury versus ischemic necrosis is not well understood.

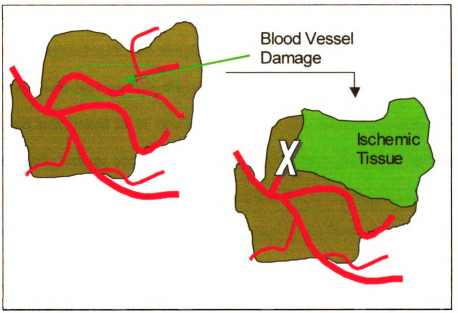

Figure 9.3 Illustration of ischemic injury caused by damage to blood vessels.

Most attempts to study the relationship between thermal history and vascular injury that leads to tissue necrosis have the general weakness of inaccurate temperature sensing. Although there have been several studies done in the last 2 years that attempt to quantitatively correlate thermal history and micro-vascular injury (Hoffman *et al.*, 1999, 2000ab; Schuder *et al.*, 2000), the experimental design and temperature sensing technologies utilized resulted in an ambiguous determination of lethal temperatures for freezing induced micro-vascular injury.

In the study by Hoffman et al. (1999, 2001ab), a dorsal skin flap chamber (DSFC) system was utilized with an AT-1 tumor in the Copenhagen rat. Thermocouples embedded in the tumor tissue, using a polycarbonate window as a guide, were used to measure the temperature history at several radial locations during freezing with a small diameter cylindrical cryoprobe. Because the thermocouples were mounted perpendicular to the tissue surface, fin effects were significant hence a theoretical correction based on a steady state conduction fin model was applied to the experimental measurements. These data were compared with two simple analytical heat transfer models to interpolate the temperature field between the discrete thermocouple measurement sites. This thermal information was linked to *in vivo* measurements of vascular disruption determined by macromolecule leakage and to histological assessment of the tissue after sacrificing the animal. It was found that the region of vascular stasis (determined by macromolecule leakage) correlated with the region of tissue necrosis (determined by histology) for both normal tissue and tumor tissue. Correlation of lesion size with thermal modeling suggests that the minimum temperature required for tissue necrosis is in the range of -10°C to -13°C which is a much higher range than the temperatures near -40°C required to kill

single cells of this cell line *in vitro*. The results suggested that vascular injury may be the dominant mechanism for determining the size of the cryolesion due to freezing *in vivo*. However, difficulties in making the thermocouple measurements as well as modeling assumptions and simplifications in the thermal models combined to produce an estimated temperature uncertainty of at least 7°C. Also, no direct *in vivo* evidence was given to support the hypothesis that cells in the lesion periphery did not die from direct cell injury. The steep gradients within the small working area of the DSFC make it very difficult to localize the lesion periphery and even more difficult to obtain accurate temperature measurements. With these limitations it can be inferred that the minimum temperature required for AT-1 tumor tissue necrosis *in vivo* was in the range of –5 °C to –20 °C. The cooling rate experienced by the tissue was not explored.

Despite the fact that the specific goal of the Schuder study (Schuder *et al.*, 2000) was to determine a lethal temperature for vascular injury in a rat hepatic model, the attempts to measure temperature were coarse. Although they used a plastic guide for thermocouple placement normal to the surface, no adjustment was made for fin effects. Details of the thermocouple size and construction were also not provided; hence other errors may be present in the data. The high treatment temperatures they predict as characterizing the edge of the ultimate lesion (~8°C), were likely caused by conduction along the thermocouple wires that caused a warming of the thermocouple junction. Although the intra-vital aspect of their work was sound, the correlation with temperature can be considered qualitative at best.

In an earlier study Rabb (1974) studied the effects of freezing and thawing on the microcirculation in a hamster cheek pouch using a cold block freezing device with

freezing rates controlled by regulating the flow of cold helium. In this model the cheek pouch was everted and pinned over the cold block. A 0.05" thermocouple was placed between the pouch and block and this was used as the basis for thermal control. No experimental or theoretical validation was presented that indicated this temperature was representative of the temperature history throughout the thickness of the sample, nor was there any mention of the thermal contact resistance that would be inherent in such a set-up. In light of this, one would expect that the temperatures recorded were probably colder than those actually experienced in the bulk of the tissue. However, the protocol used involved freezing at 1 °C/min therefore at this slow rate, barring significant contact issues, it is not unreasonable to assume that the thermal history in the tissue was reasonably close to that reported. Although this study demonstrated that micro-vascular changes are extensive and would likely lead to cell necrosis, at –30 °C it is not uncommon for cells to already be damaged from the direct effects of freezing. No evidence was presented that demonstrated cells were not already dead from direct cell injury (solute injury or otherwise).

The study by Le Febvre (1971) also lacks detail about the thermal history actually experienced by the tissue undergoing cryosurgery. Using the hamster cheek pouch method, different depths of cooling were achieved in the tissue via the use of a stainless steel trough circumscribing the cheek pouch preparation. A solution consisting of 40% propylene glycol in Ringer's solution that had been cooled in an alcohol-dry ice bath was used to charge the trough and elicit temperature changes in the tissue. Because a combined forced-air vacuum system was used to change the freezing solution from 37 °C Ringer's solution to the cooled propylene glycol solution, the trough temperature likely

responded quickly and might be modeled as a step change in temperature. However, the thermal diffusivity of the tissue is an order of magnitude less than that of the stainless steel and thus the tissue will experience a transient change in temperature. The freezing rate in the tissue was not reported, nor was the spatial distribution of temperature in the optically studied section. However, the strength of this paper lies in the correlation between duration of freeze at given trough temperature and tissue necrosis as determined over a 30-day period following cryosurgical treatment. What can be concluded from the reported results is that –15 °C is the critical 'trough' temperature below which a significant degree of necrosis can be expected with a minimum time of exposure. Complete necrosis was reported for any exposure to –18 °C trough temperatures and below. If these trough temperatures are accurate, the critical 'tissue' temperatures are expected to be somewhat warmer. At such high sub-zero temperatures, generally speaking, cell viability *in vitro* is quite high (e.g. Elliott *et al.* 2000), and thus the necrosis observed can be supposed to be originating primarily from the observed microcirculatory stasis and associated ischemia.

The Zacarian *et al.* hamster cheek pouch study (1970) was similar to that of Hoffman *et al.* (1999) in the sense that a 'traditional' cryosurgery was performed. In this case however a single thermocouple was used to record the temperature at various locations distal to the cryosurgical probe. The thermocouple was located in the plane of the tissue, beneath the surface of the cheek pouch. Temperatures reached in the tissue were likely colder than actually recorded by the temperature sensor, as the cryosurgical probe was applied on the opposing side of the tissue. The authors noted that 'a single freeze-thaw experience between the temperature range of -20 to -30 °C to the vascular

network of the cheek pouch affords as much lethality as would be expected from extreme temperatures, suggesting the dominant role that micro-vascular effects can play in tissue necrosis. Temperatures in the –20 to –30 °C range can also elicit direct cell injury, making it difficult to discern the actual contribution of micro-vascular injury to overall tissue necrosis.

Based on these previous studies that have examined cellular and micro-vascular injury following freezing at high sub-zero temperatures, it appears that the temperature regime least likely to cause direct cell injury, but still having a high likelihood of causing stasis and significant micro-vascular injury is the –10 to –20 °C regime. Studies in this temperature regime may be able to effectively uncouple direct cell injury from secondary effects and allow the investigation of both the extent and the time course of cellular injury following freeze-induced ischemia. At these temperatures, some cell death may occur, but the bulk of cells in the tumor mass should remain viable immediately after the initial freeze-thaw cycle.

9.3 Patho-physiology of Cellular and Vascular Injury Following Freezing

The general pattern of vascular injury following freeze injury was delineated in the first chapter of this dissertation, as gleaned from both the frostbite and the cryosurgery literature. As a tissue is cooled, the initial thermoregulatory physiologic response is increased blood flow to the tissue (Weatherley-White, 1969). Continued cooling produces vasoconstriction and a decrease in blood flow. When the phase change temperature is reached, freezing is expected to begin to freeze first in the extra-cellular space (Rubinsky *et al.*, 1987, 1988, 1990). Depending on the rate of cooling and the

temperature reached, ice may also form intracellularly. During thawing, circulation is temporarily restored to the previously frozen tissue. However, progressive failure of the micro-circulation is observed. Vascular distention has been observed both in frozen section (Rubinsky *et al.*, 1990, 1997) and intravitally (Schuder *et al.*, 1999). Edema develops (Weatherley-White *et al.*, 1964; Reite, 1965; Marzella *et al.*, 1989; Zook *et al.*, 1998; Manson *et al.*, 1991; Zook *et al.*, 1998), vascular permeability is increased (Waris and Kyosala, 1982), impaired platelet function and platelet aggregation leads to thrombosis and vascular occlusion (Weatherley-White *et al.*, 1964; Reite, 1965; Zacarian *et al,* 1970; Bourne *et al.*, 1986; Marzella *et al.*, 1989; Zook *et al.*, 1998), and endothelial cells die (Waris and Kyosala, 1982; Marzella *et al.*, 1989; Manson *et al.*, 1991). The increased vascular permeability appears to be a result of damaged endothelial cells and defects in the endothelial cell junctions. This endothelial damage also results in platelet aggregation and micro-thrombus formation. This, in turn, causes blood flow stagnation (stasis) that ultimately deprives cells of oxygen, nutrients and a sink for waste products. The cells die of ischemia. The time scale on which damaging micro-vascular changes occur has been observed as early as immediately after freezing (endothelial cell damage) by Manson *et al.* (1991) or 3-min after thawing (small vessel occlusions) by Bellman *et al.* (1956) to as long as 24 hours after freezing (necrosis of endothelial cells) by Waris and Kyosola (1982).

While this general pattern is understood, the specific thermal history, or the minimum thermal insult to elicit this general response has not been well-studied. Also the bulk of studies have demonstrated that micro-vascular injury exists, but few have provided any direct evidence that micro-vascular injury is responsible for tumor cell

death. The lack of efficient methods to study the time course of cellular injury has precluded researchers from directly establishing the relative contributions of direct cellular injury and the secondary effects of vascular injury and ischemia to overall lesion size. Also because of the lack of correlation with thermal data, cryosurgical technology has not advanced to the point where the secondary aspects of cryosurgery injury can be predicted and controlled.

9.4 Hypothesis and Experimental Design

There were several objectives in this experiment. The first was to determine the extent of microvascular damage that can be achieved by slow cooling to –18 °C *in vivo*. The second objective was to provide the first direct *in vivo* evidence that cells in tissue frozen slowly to high sub-zero temperatures are not immediately injured by the freezing insult. If the microvascular damage from this protocol was determined to be substantial, a final objective was to determine the time course of cellular injury that might occur due to the possible secondary effects of ischemia.

Dorsal skin flap chambers bearing tumor slurries as described in Chapter 7 were implanted in eight animals. Five chambers were treated with a freezing protocol using the annular freeze apparatus described in Chapter 8, and the remaining three animals were used for sham experiments, in which identical procedures were used except the annular freeze apparatus was not cooled.

9.5 Materials and Methods

9.5.1 Chamber Implant and Tumor Propagation

Similar to the methodology described in Chapter 7, female Fischer 344 Rats weighing between 150 and 180 grams were implanted with dorsal skin flap chambers, according to the procedure described by Papenfuss (1979). In the chapter 7 animal series the thickness of the tissue was unrestricted because the non-dissected side was not sealed in any matter. In the current animal series the traditional double-sided preparation was constructed, with epidermis being removed from both sides of the skin flap. This technique involves dissection of opposing skin flaps, leaving a thin layer of vascularized dermal tissue. At the time of chamber implant a small bolus (~200 μL) of GFP-transfected R3230 AC tumor cells was injected into the chamber before sealing the preparation with a glass window. The tumor cell suspensions were prepared by counting cells with a hemacytometer, using Trypan Blue to discriminate live and dead cells, and if necessary concentrating by centrifugation to achieve cell counts of 1-2 x 10^5 cells/mL in D-MEM. In previous work, this protocol has resulted in high tumor take rates and predictable tumor growth (Elliott *et al.*, 2000).

Animals with dorsal skin flap chambers were maintained in a 90 °F room at ambient humidity. The warm room was necessary to maintain circulation in the skin flap chamber. The integrity of tissue in the chamber was macroscopically monitored until tissue could be seen to entirely fill the viewing area. This generally required a minimum of 10 days. The tissue was then treated with freezing.

9.5.2 Development of Freezing Protocol

To optimize the operating conditions of the annular freezing apparatus for intra-vital studies, three animals were implanted with dorsal skin flap chambers containing tumor slurries and incubated for 20 days. These animals were used to understand the temperature distribution that could be expected *in vivo*. Animals were anesthetized with sodium pentobarbital (35 mg/kg) and placed on their side on a stack of towels. Polyethylene bags containing 37°C water were used to prevent hypothermic shock in the rat, and these were changed frequently. The window on one side of the chamber was removed and replaced with the thermocouple grid window described in Chapter 8. Calibrated T-type thermocouples constructed from 0.005" wires had been previously localized at radial positions of 2, 3, and 4 mm (+/- 200 microns). Use of this grid minimized the problem of thermocouple positioning error, as well as positioned the thermocouples in the most favorable way for minimizing fin effects error (i.e. in the direction of minimal temperature gradient). After threading the thermocouple wires through the center of the annular freeze apparatus (AFA), this freezing device was attached to both sides of the dorsal skin flap chamber. Cooling was initiated and temperature measurements recorded with a DAS-TC/B board.

9.5.3 Measurement of Thermal History During Intravital Studies

For intra-vital studies, the animals were identically prepared and kept warm, except the thermocouple grid window was not implemented. The glass window on the one side of the chamber was removed and replaced with a glass window containing a central 1-mm hole. A T-type thermocouple was inserted into the hole and sealed laterally

against the surface of the window using a thin layer of transparent nail enamel. The e-clip used to keep the window fixed in place in the DSFC facilitated positioning the thermocouple in the manner depicted in Figure 9.4. The lead wires were then threaded through the annular freezing device and attached to the appropriate T-type connecter. Measurements were recorded manually at 30-s intervals using a hand-held Omega model CL24 calibrator-thermometer (Omega Engineering Inc., Stamford, CT). Cooling was initiated and maintained until an end temperature of −18 °C was reached at the central thermocouple. Cooling was then discontinued and the tissue was allowed to passively thaw with the annular freeze apparatus remaining in place.

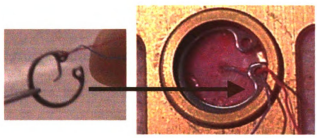

a

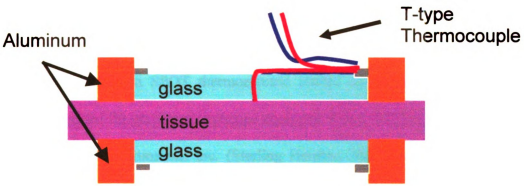

b

Figure 9.4 (a) Photomicrograph demonstrating the location and positioning of a single thermocouple for *in vivo* temperature sensing. (b) Schematic of thermocouple positioning for the purpose of minimizing fin effects of *in vivo* temperature measurements.

9.5.4 GFP-based Intravital Microscopy

A freezing protocol, designed to achieve –18 ˚C in tissue at the center of the DSFC with a minimal temperature gradient across the entire viewing surface, was applied to five animals. Where possible a selected area in the central region of the tissue was monitored for both GFP intensity and vascular injury by alternating between fluorescent and transmitted light. These circumstances occurred in only two out of five animals.

Some preparations did not adequately grow into tumors. Others were not of suitable clarity for vascular monitoring. The maximum information possible was obtained from each preparation. The group of three sham animals were prepared identically to the experimental group animals but cooling was not initiated in the AFA. None of these animals grew tumors, but all provided good microvascular information.

Cell viability was monitored using the GFP intra-vital technique before, during, and after the cryosurgery procedure for pre-determined observation periods to determine if cell death is immediate and associated with direct cell injury from the freezing insult, or delayed and consistent with ischemic injury. Images were acquired before, during, and after freezing using a SPOT thermoelectric cooled color CCD camera and a Nikon Diaphot inverted fluorescent microscope equipped with a 100 W mercury arc lamp (both from Diagnostic Instruments, Inc. (Sterling Heights, MI). The tissue was illuminated with blue light by inserting a FITC filter cube (ex. 450-490 nm, em. 510-540 nm) (Chroma Technology Corp., Brattleboro, VT) into the light path.

The blood vessels were also monitored for evidence of stasis before, during, and after the cryosurgery procedure, using only brightfield illumination. Images were acquired at predetermined times over a 10-hour period to allow for offline analysis of blood vessel dimensions. These images were later analyzed for evidence of vascular distention.

9.5.5 Histology

At the end of the 10-hour observation period the animal was immediately euthanized by cardiac puncture and injection of an overdose of sodium pentobarbitol.

The tissue within the chamber was fixed in 10 % formalin for a minimum of 20 hours and then embedded in paraffin. Tissue sections of 5-micron thickness were obtained and stained with hematoxylin and eosin.

9.6 Results

9.6.1 Cryosurgical Protocol

Using the grid window for thermocouple measurements, it was found that similar to results with phantom tissue, the DSFC tissue in living animals could be reproducibly cooled to high sub-zero temperatures with a minimal temperature gradient across the field. As can be see in Figure 9.5, thermocouples positioned at the center and at a 2 mm radial position, record nearly identical profiles. This was true in all three animals that were studied. The thermocouple positioned at 4-mm recorded temperatures that were seen to deviate from the central thermocouple by up to 2 °C (excluding the region of latent heat release). Unfortunately the 4 mm thermocouple was damaged in two of the three experiments. Repeated attempts were made to maintain three working thermocouples in the configuration described. This task proved to be extremely difficult, and therefore measurements were focused on the central region of the tissue where intravital imaging was performed. The single result from the 4 mm thermocouple does suggest however that the temperature gradient within the chamber is less than 1 °C/mm. Because of the small field examined during intravital studies (<1 mm), the area of analysis can safely assumed to be isothermal.

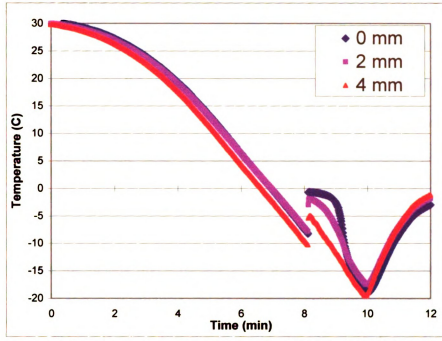

Figure 9.5 Characteristic freezing curves measured *in vivo* at specific locations.

For comparison purposes the previous results were plotted together with the predicted temperature at x = 0 and x = 0.004 m originating from the numerical model developed in Chapter 8. These combined results are given in Figure 9.6. In the experimental case neither the thickness of the sample nor the thermal properties were known precisely. However, since the water content of biological tissue is generally quite high, the simulation should be reasonably representative of the experimental situation, certainly in an order-of-magnitude sense. When comparing results it could be seen that the simulation predicted that the temperature difference between the center and edge thermocouples would be minimal at later times (< 2 °C), and this was indeed observed to be the case in experiments. There is a considerable deviation when comparing these results in the region of phase change. Whereas the model predicts a smooth evolution of

latent heat over a 7 °C freezing range, results measured in samples have been seen to have considerable variability in terms of the onset of freezing. In the case of the experiment shown in Figure 9.6, freezing did not begin until –8 °C. At this temperature all of the latent heat in the model had been released already. It should also be emphasized that the constant heat flux condition chosen to represent cooling at the surface of the annulus is an approximation. Because the AFA system is itself at ambient conditions at the beginning of the procedure, the initial cooling load delivered to the system first cools the hosing and attachments of the AFA before beginning to extract significant heat from the annular components of the device. This results in a heat flux condition that will increase as the system approaches it steady operating condition. Results of the simulations are thus expected to be less representative of the experimental situation at early times. In future models, precise cooling histories could be implemented in the model, via the use of user defined-functions (separately compiled programs). Also, for purposes of comparisons, the use of materials with well-defined thermal properties would be more suitable. Despite these limitations, the results shown in Figure 9.6 demonstrate reasonable agreement at the later times.

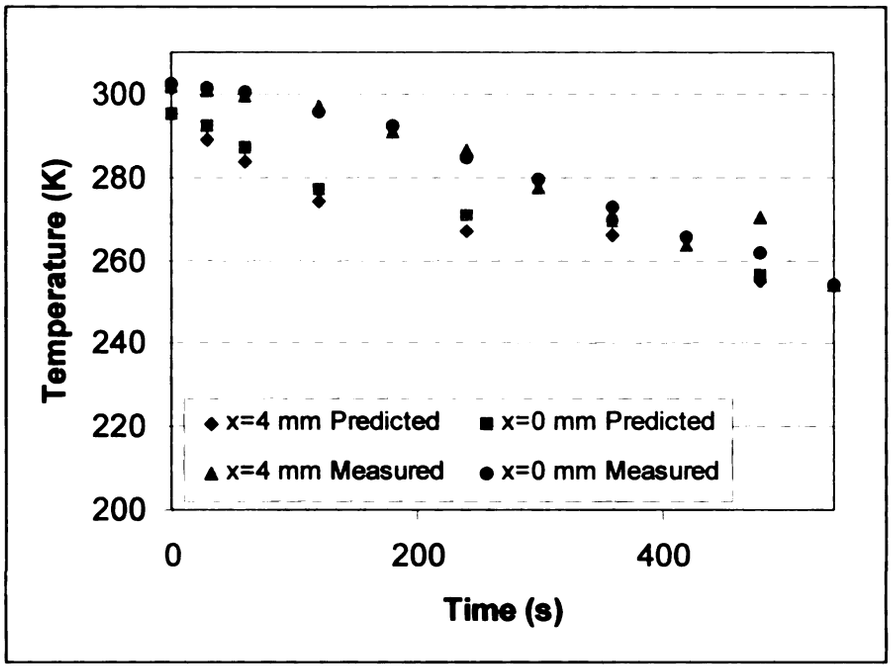

Figure 9.6 Experimental measurements for the *in vivo* case presented in Figure 9.5 are plotted against predicted measurements (properties of water used) for two locations on the surface of the tissue.

9.6.2 Thermal History Measured During Intravital Studies.

Characteristic results of temperature measured at the center of the tissue during the freezing protocol are shown in Figure 9.7. This general pattern of freezing was observed in each animal. In Figure 9.7 it is evident from the temperature data that latent heat was evolved at ~ -8 °C and that thawing occurred around 0 °C. In all cases it was possible to identify the latent heat release region based on the sudden spike in the temperature data. The onset of freezing occurred within 8.5 to 10.5 minutes after cooling was initiated, which corresponded to an onset temperature range of –1.0 to –9.7 °C. The starting temperatures of all the skin flaps were between 25 °C and 28 °C. The

nominal freezing rate was determined to be ~ 4 °C/min. The nominal thaw rate was also ~ 4 °C/min.

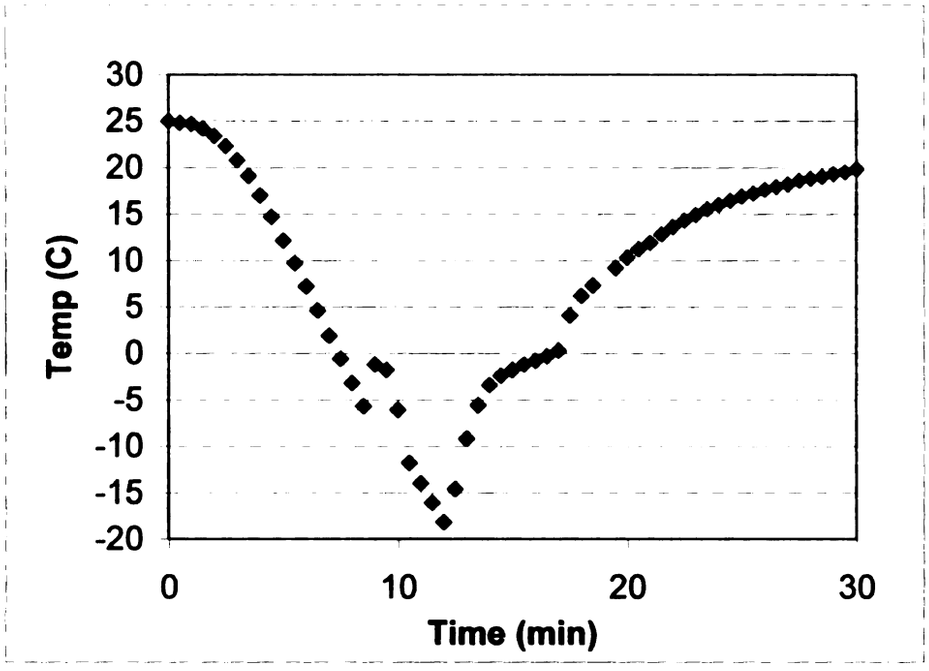

Figure 9.7 Characteristic thermal history measured using a T-type thermocouple in contact with the tissue at the center of the annulus in the DSFC during slow freezing.

9.6.3 Post-Freezing Vascular Changes

Images that were acquired during the experimental observation period were analyzed for blood vessel diameter using Image Pro Plus software. Two to four vessels were identified in each series of images. At every time point, five measurements of diameter were made of each vessel at the same location for both sham animals and treated animals. The vessel diameters of sham animals were observed to undergo very little deviation over time and so for presentation purposes in Figure 9.8, the results of sham animals were averaged. The vessels in the treated animals were all examined individually to define the extent of distention and the nature of the variation amongst vessels. Experimental samples were not pooled because the combination of unequal sample numbers per time point and the large variation between vessels obscured the observed response. The results displayed in Figure 9.8 demonstrate that vessel distention following freezing is a frequently observed phenomenon, with 7 out of the 8 vessels demonstrating vessel dilation. The vessel-to-vessel variation is very high with dilation observed to span the range of approximately 1.1 to 2.5. In some cases the amount of vessel distention over time does not appear to be steady, and appears to increase with time post-thaw. In these vessels the time at which maximal dilation is seen to occur (5-10 minutes post-thaw), coincides with the onset of secondary stasis in these vessels (4.5–6 minutes post-thaw). In other cases, by the time vessels could be resolved in images (~ 3 minutes after thaw) they already appeared distended. This tended to be true only in cases where the vessel distention never exceeded 1.5. Some extravasation of red blood cells was observed to occur immediately post-thaw, but severe hemorrhage did not occur until 30 to 40 minutes post-thaw.

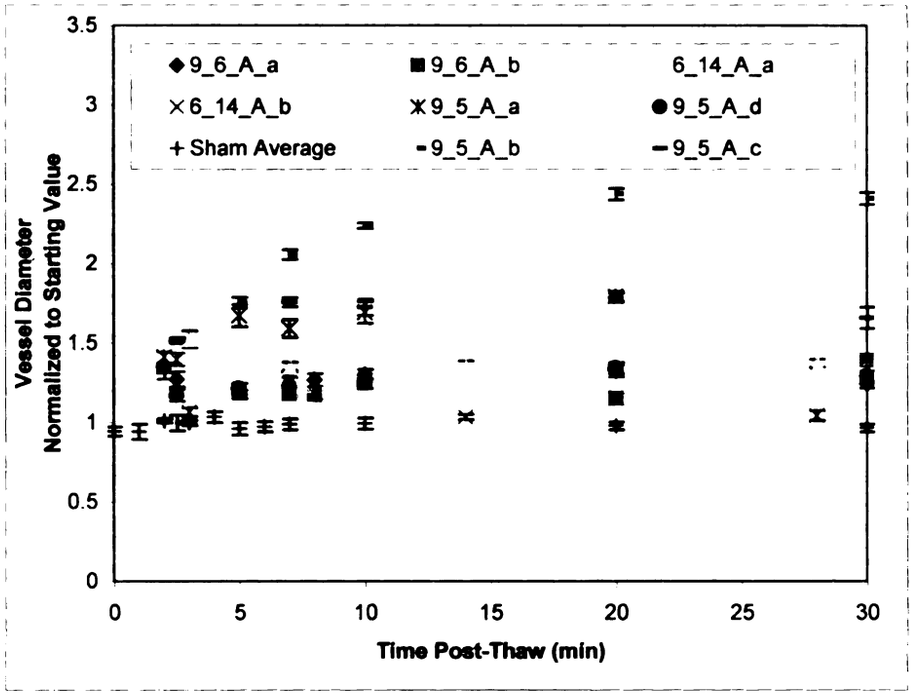

Figure 9.8 Individual vessel measurements from treated animals, normalized to the starting diameter of each vessel, are compared to a baseline of pooled sham animal data. For the sham animals the error bars represent the standard deviation of three animals. Remaining measurements represent the average and standard deviation of five repeated measurements of the same vessel.

9.6.4 Time Course of Injury Based on GFP Intra-vital Viability Assay

Only two animals in the treated group were found to have suitable tumor growth for analysis. As can be seen in the image series in Figure 9.9, fluorescence loss from GFP-transfected tumor cells was gradual, with a minimal loss minutes after freezing, and progressive changes occurring over several hours. The change was seen to be most dramatic in the first three hour time period. By two hours post thaw, the skin flaps were

observed to be extremely swollen and in some cases the tissue was beginning to blacken, consistent with the gross character of frostbite injury and appearing consistent with the *in vivo* observations. To quantify the time course of GFP intensity change in the two treated animals that grew tumors, gray scale intensity values normalized to the starting intensity values were acquired of the central region of the tumor tissue in each image. These results are plotted in Figure 9.10. The GFP signal reduction for both animals is very similar, with very little change occurring after 4 hours. The tumor appears to have a considerable amount of viable cells immediately after the thaw, but these cells slowly die over the subsequent three hours.

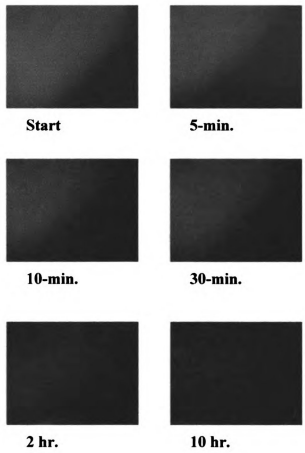

Figure 9.9 Micrograph series of GFP intensity change over time in a centrally located DSFC tumor treated with slow freezing to –18 °C.

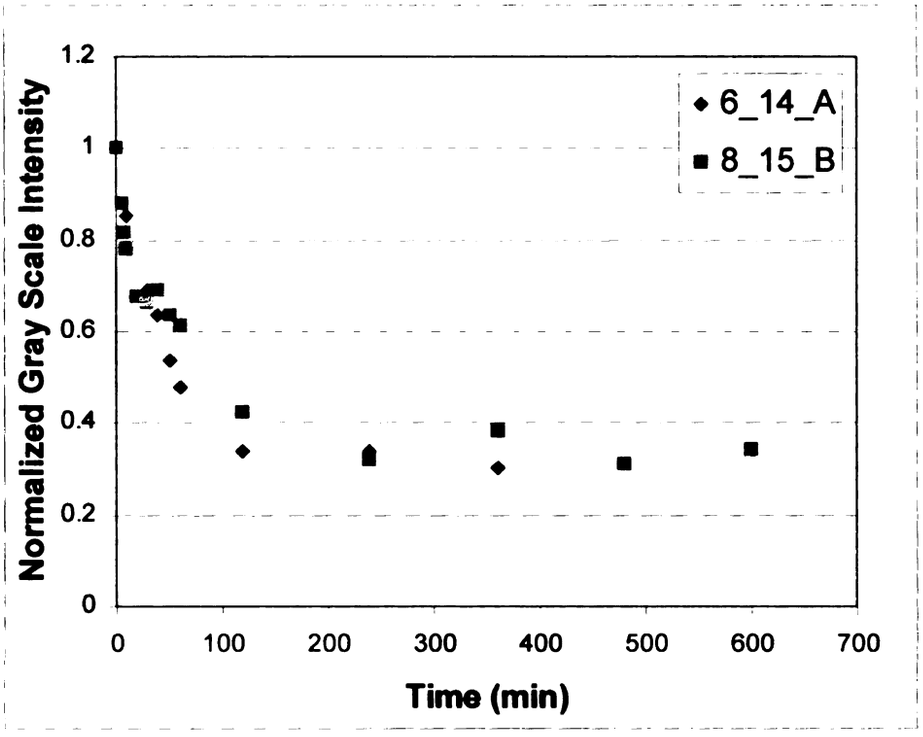

Figure 9.10 Normalized gray scale intensity plots of GFP fluorescence intensity loss of cells following slow freezing to –18 °C.

9.6.5 Histology

As can be seen in Figure 9.11, histological sections from sham-treated tissue demonstrated vessels of normal patency. Fibroblast cells in these specimens had the expected spindle morphology and flattened nuclei. In contrast, histological sections from treated tissue were seen to have dilated and engorged vessels and significant hemorrhage. Figure 9.12(A) illustrates the extent of red blood cell extravasation that was typically observed. The engorged vessel seen in Figure 9.12(A) appears to have been mechanically damaged, perhaps from dilation beyond physically tolerable limits. The

nuclei were seen to be condensed in treated tissue, consistent with tissue necrosis. These histology images were consistent with both gross observation and intra-vital measurements and observations, as both vessel distention and severe hemorrhage was observed, the latter being resolved at both microscopic and macroscopic levels.

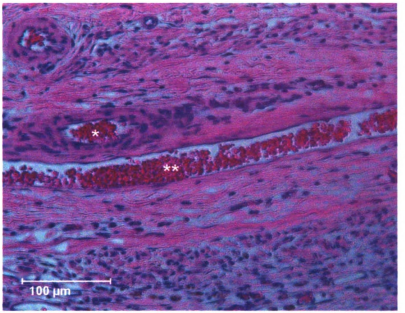

(a)

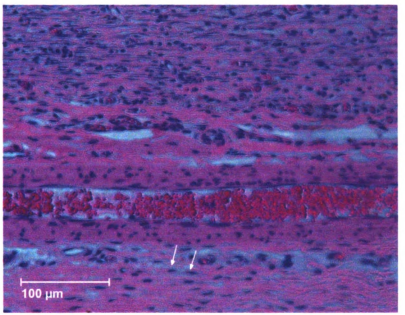

(b)

Figure 9.11 Micrographs of sham-treated tissue from the dorsal skin flap chamber, showing no evidence of necrosis, and blood vessels of normal patency. (a) Transverse (*) and longitudinal (**) sections of blood vessels can be seen. (b) Fibroblast nuclei (arrows) are normal in appearance.

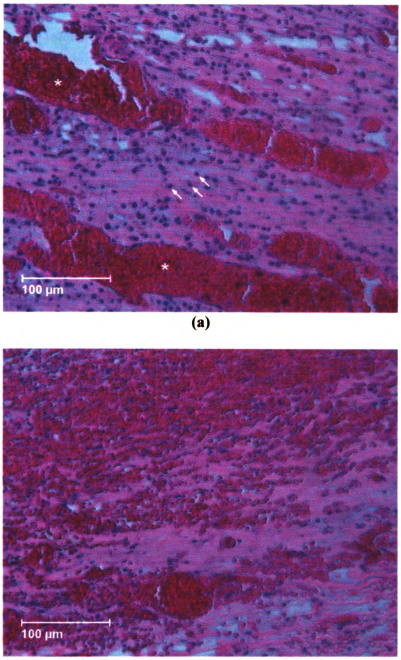

Figure 9.12 Micrographs of dorsal skin flap chamber tissue frozen at ~ 3 °C/min to – 18 °C. (a) Congestion and engorgement of blood vessels (*) and condensed nuclei (arrows) were observed, indicating both microvascular injury and tissue necrosis. (b) Extravasated red blood cells can be seen to dominate this severely hemorrhaged section.

9.7 Discussion

The results of this study suggest that temperatures as high as -18 °C can cause severe disruption of microvasculature integrity and functionality, which may be effecting cell changes that manifest on a time scale consistent with this injury, i.e. some hours delayed. Vessel dilation was observed to occur post-thaw to varying extents, as evidenced by both offline analysis of intravital images and histopathology specimens.

The intravital microvascular observations of this study are very similar to those reported by Rabb *et al.* (1974) in their studies in the hamster cheek model. They observed constriction of venules and arterioles and sluggish blood flow as the tissue was cooled, with freezing taking place from –3 to –9 °C. Upon thaw, circulation commenced from 0 to –3 °C. Consistent with our observations, they also reported vasodilatation beginning shortly after thaw and continuing throughout the observation period. Hemostasis was observed to begin at 1 minute after thaw with flow stoppage in small vessels by 20 minutes attributed to platelet occlusions. In the current study the earliest episode of secondary stasis that occurred could be seen 4.5 minutes following thaw. Although they reported return of blood flow after 30 minutes, this was not observed in our experiments, as vessels remained static throughout the ten-hour observation period.

Shuder et al. (1999), in their investigation of the response of hepatic microcirculation to cryosurgery, found complete stasis at the center of the lesion directly following freeze injury, whereas the sinusoids at the edge of the lesion were heterogenously perfused. This region experienced progressive failure as parenchymal cell aggregates lodged in the sinusoidal lumens and caused terminal blockages. Microvascular perfusion failure was associated with Ito cell disintegration and possible

loss of Ito-cell regulated vasomotor control. Consistent with the results of the current study, marked dilation of sinusoids (15.6 vs. 8.8 microns) was also observed following freeze-thaw.

This increase in sinusoidal diameter was also observed by Rubinsky (1987) in studies on freeze-substituted liver sections that had been previously directionally solidified at various freezing rates. Rubinsky subsequently modeled this response as a biophysical response (1990). The general basis for his theory is that during slow freezing ice crystals would form first in the microvasculature, resulting in an exclusion of solutes, thereby establishing a concentration gradient that would result in water transport into the blood vessels from the extra-cellular space. This model therefore predicts an increase in the diameter of the sinusoids as a direct consequence of this water transport, consistent with his experimental observations in frozen section.

The Rubinsky theory does not address the expected thawing response, but it is possible that water will leave the vascular when the system melts and returns to ambient temperatures. Whether the vessels are dilated or not when the system thaws is not clear from the studies done on liver tissue, therefore it is difficult to extrapolate to the current case. It is worth noting that liver tissue has the unique feature of being a relatively homogenous tissue compared to many other tissue types. Hepatic tissue is uniformly perfused with vessels of very similar diameters. In contrast the tissue studied in this work has vessels of many sizes coursing through the tissue and are very irregularly spaced. The fact that the window chamber is implanted in a wound results in a dynamically changing vascular bed. The relevance of this environment to a 'normal' tumor vasculature needs exploration from the standpoint of mass transfer, but also begs the

question of how other tissues compare to the hepatic blood vessel architecture, and whether the Rubinsky model can be considered valid for other tissue types. In any event, if the freezing events have created mechanical damage to the microvasculature, the stress on the vessels appears to be further augmented by dilation post-thaw. The likely mechanism for the post-thaw swelling is the plugging of vessels and subsequent mounting of hydrostatic pressure gradients as blood from the uninjured microvasculature tries to make its way into this region.

9.8 Summary and Conclusions

This pilot study provided the first *direct* *in vivo* evidence that cells frozen to –18°C at a slow freezing rate are not being immediately damaged by the freezing protocol, but that the damage manifests at a later time. Only two animals were able to grow tumors adequately for GFP intensity changes to be studied together with vascular changes, therefore, statistical conclusions cannot be drawn about the GFP signal from this small subset. The information provided from these pilot studies, together with experience gleaned from the animal series described in Chapter 7, can however be used to develop strategies for future experimental design. The GFP assay provided a measure of injury dynamics in the living system that prior to now has not been possible. This represents a significant advance in uncoupling the effects of direct and indirect cellular injury following freezing. Based on these results, cell injury associated with high sub-zero temperatures and slow freezing rates can be seen to occur on a time scale of several hours. This is not inconsistent with the predictions of Hoffman and others that microvascular injury is indirectly bringing about the death of cells that would otherwise

survive the initial freezing insult. However, the timing of viability loss does not preclude the effects of solute injury, which have been observed in this study to progress over a period of hours following hypertonic exposure. The possibility of osmotic and thermal shock induction of apoptosis is also not ruled out. The pilot results obtained do suggest however that the relevant time scale to explore these slow freezing primary and secondary injury mechanisms is on the order of hours and not days. This information alone can directly improve the experimental efficiency of future studies, independent of the particular hypotheses of injury that might be explored.

Although –18°C was the temperature used in this study, it is possible that higher sub-zero temperatures may bring about as much lethality.

The vascular injury model was shown to be highly reproducible with all treated tissues demonstrating signs of severe vascular hemorrhage. Tissues with vessels of adequate resolution for monitoring blood flow were seen to undergo secondary stasis in a very narrow time range post-thaw, specifically, 4.5 to 8 minutes. Marked vessel dilation (~2-fold) was observed in many of the vessels, though this was not true for all vessels. This variation may be due to the different vessel sizes analyzed as well as variation in the distance between vessels. These results did not support nor refute the hypothesis of Rubinsky that distention is occurring during freezing, as it was not possible to measure dilation during the frozen period as the ice obscures the sample. Some vessels appeared to be consistent with the model of water transport into vessels during freezing as they appeared dilated directly after thawing, yet others appeared to dilate over time and appeared to coincide with the onset of secondary stasis. It is likely that both mechanisms are contributing to the overall microvascular injury that occurs.

Chapter 10

Summary, Conclusions and Future Work

10.1 Summary

At the onset of this work, it was hypothesized that GFP transfection of tumor cells prior to introduction into animal models could provide the basis for a tissue viability assay in the mature tumor. It was speculated that the presence of GFP within transfected tumor cells would indicate that two features of cell viability exist: a metabolically functioning system capable of producing the GFP and an intact cell membrane. Because of the unique tertiary structure of the GFP molecule, we postulated that the molecule itself would remain stable with respect to freezing and that the attenuation of intracellular GFP fluorescence would occur when protein synthesis was disrupted or when membrane damage caused leakage of cytoplasmic contents, including the GFP molecules. Freezing is known to affect the cell in such a way that the membrane is either directly impaired, or the cell is damaged such that necrosis and/or apoptosis will prevail, inducing a cascade that inevitably leads to both metabolic failure and eventual membrane degradation. The

results obtained following freezing of both isolated cells and tumors grown in the rodent dorsal skin flap chamber confirmed these hypotheses.

It was established that GFP fluorescence is lost from isolated transfected R3230AC cells following exposure to cryosurgically relevant freezing and thawing rates. The presence of GFP fluorescence in these tumor cells correlated very well ($0.91 < R^2 < 0.94$) with several standard cell survival assays such as ethidium bromide and Trypan Blue. This level of correlation compared very favorably with correlations made between non-GFP-based viability indicators (Yang *et al.*, 1998), suggesting that the GFP-based approach is comparable to established standard methods. GFP fluorescence was also lost following exposure to hypertonic stresses comparable to those experienced during these freeze/thaw conditions. The correlation between GFP fluorescence as a measure of viability and the other common viability indicators used was very high not only for static, end point measures of viability but throughout the dynamics of the apparent loss of viability.

The GFP-expressing rat tumor cells were used to produce fluorescent tumors *in vivo* in a rodent-implanted dorsal skin flap chamber. At the time of chamber implant, the tissue inside the chamber was bathed with a solution of tumor cells in media. The animals were placed in a warm room (91°F) for 6-11 days to grow large tumors (~ 10 mm diameter) in the skin flap window chamber. The tumors were then treated using three cycles of freezing and thawing. GFP intensity fields were measured before, during, and after the cryosurgery protocol. The tissue was also biopsied for hematoylin and eosin (H&E) staining. Histopathology evaluation presented evidence for direct cell injury at locations near the cryoprobe where the tissue is expected to experience the most rapid

freezing rates. In these regions the histology revealed nearly complete ablation of the tumor tissue, with only nuclear and cytoplasmic remnants scattered within a congested connective tissue matrix. The GFP fluorescence signal was also diminished to background levels in these same central regions. The loss of fluorescence occurred within seconds to minutes. Thus, cells that presented as definitively dead in the histopathology also presented as dead in the intra-vital GFP microscopy. Likewise, outside of the region of treatment, cells unaffected by therapy as demonstrated by unaltered levels of GFP fluorescence presented as viable and highly mitotic in histopathology. The histopathology revealed a mixed population of healthy cells and cells in various stages of necrosis (evidenced by nuclear pyknosis, karyorrhexis, and cytoplasmic eosinophilia) in a band between the definitively dead tissue and the healthy tissue in the margin. A region of similar 'mixed' character (average GFP signal diminished to levels above background) was identified during intravital GFP microscopy.

It was hypothesized that the GFP assay would have characteristics that likened it to two classes of existing viability assays: membrane integrity assays and protein synthesis assays. The detection of intracellular GFP directly following insult would correspond to retention of membrane integrity. Although membrane integrity is generally accepted as a reasonable indicator that the cell will survive, it is a necessary but not sufficient condition. Because the transfected cells continuously produce GFP, the maintenance of GFP synthesis following insult was hypothesized to be a second indicator of cell survival. To implement this feature accurately it was first necessary to understand the half-life of the GFP inside the cell. Experiments with cycloheximide, a protein synthesis inhibitor, were undertaken to measure the half-life of GFP in R3230AC cells.

The half-life was not definitely established, as cells began to die and leak their contents before GFP turnover was observed. However it was established that the half-life was greater than 16 hours.

Experiments were performed to establish the stability of pure recombinant GFP to freezing. Successive rapid plunge freezing of aqueous solutions of rEGFP in liquid nitrogen and slow thawing at ambient conditions revealed a minimal loss of fluorescence intensity after three cycles, suggesting that cold denaturation of the GFP molecule was not occurring to an appreciable extent under these conditions. An analysis of extracellular green fluorescence intensity before and after cell lysis revealed an increase in background fluorescence intensity that was directly proportional to the volume fraction of GFP-transfected cells in the starting cell suspension prior to lysis. Consequently a conservation of fluorescence was established, indicating that intracellular GFP was not being destroyed during this process.

A number of supporting studies were also completed that provided the foundation for the work previously described. Linking the thermal history of the tissue during cryosurgery to the biophysical and physiological responses is understood to be critical to a better understanding of tissue freezing and thawing. The biophysical characteristics of the GFP-R3230AC line were determined for individual cells to predict biophysical behavior. These results indicated that the cell membrane permeability for cultured cells was quite high (L_p = 302 μm/s, 22 °C) suggesting that rapid freezing rates will be necessary to induce intracellular ice in these cells. The magnitude of the activation energy (Ea = 4.2 kcal/mol) together with the high Lp values, were consistent with the presence of aquaporins.

An annular cryo-probe system was developed that allowed the application of slow freezing rates to high sub-zero temperatures. The initial design objective was met and freezing rates between 1 and 10 °C/min were achieved. At the fastest pumping rates the freezing apparatus was capable of achieving a surface temperatures of –130 °C on the surface of the annular probe, and when in contact with the dorsal skin flap chamber, –110 °C on the inner surface of the chamber. Temperature gradients within the optical port of the DSFC were determined to be small thereby facilitating a more accurate experimental determination of localized thermal history. A numerical model of freezing in the dorsal skin flap chamber was developed and compared to discrete thermocouple measurements in phantom systems. Because of the symmetrical nature of the apparatus and the fact that reproducible and uniform freezing rate results were measured on the inner ring of the DSFC, the temperature profiles could be computed for a ¼ section of the DSFC. These results were representative of the temperature profiles in the full geometry but were computed with less computational time than a full grid would have required. The similarity of experimental and computational results suggested that the numerical model was suitably accurate to use for future experimental design.

The concluding work in this study was the application of the new GFP viability assay together with the new freezing device to evaluate the hypothesis that cells in the periphery of cryo-lesions (i.e. high sub-zero freezing rates) do not die from the immediate effect of freezing but are the result of delayed or secondary effects (solute damage or ischemia/inflammation). High sub-zero temperatures and slow freezing rates were chosen because they were not expected to induce significant intracellular ice formation. In the eight animals studied the microvascular injury induced was significant. Vessel

dilation, stasis, edema, and hemorrhage characterized the vascular lesion. In the two cases where GFP tumors were grown and treated using this same protocol, GFP fluorescence intensity in the cells did not decrease immediately following thawing, but instead the fluorescence was gradually lost over several hours. These preliminary results indicated that the time scale for this cellular injury was ~2 hours.

10.2 Conclusions

The principal conclusion based on the results of *in vitro* studies with GFP-transfected R3230AC cells was that GFP fluorescence could be used as a viability indicator to monitor the dynamic loss of viability in a population of cells with a predictive ability equal to that of conventional assays. This work was the first application of a GFP-based viability assay to cryobiological problems (Elliott *et al.*, 2000b).

Studies on the application of the GFP viability assay to tissues also established a good correlation between the loss of fluorescence intensity from tumors grown from GFP-transfected cells and tissue damage as assessed by histological methods. To the author's best knowledge this work represented the first time the validity of this assay was established in tissues, and as well the first utilization of the GFP viability protocol for *in vivo* assessment of tissue damage following injury (Elliott *et al.*, 2000a).

In terms of the nature of the viability assay, i.e. whether it functioned as a membrane integrity assay, as a metabolic indicator, or as a combination of both, it was established that its primary utility was as a membrane integrity assay. Because the half-life of GFP inside the R3230AC cells was found to exceed 16 hours, this suggested that if freezing (or some other stress) impaired protein synthesis *without* damaging the membrane, the GFP signal would likely not decay significantly until necrosis progressed

to the stage where cell leakage occurred. The continuous nature of the assay would thus be in the tracking of membrane degradation over time. These results suggested that in instances where membrane damage was not expected after an injurious stress, but instead some other component of the cell stressed or injured (eg. nuclear damage), the appropriate time to assay for lethality of injury would be greater than 16 hours after the insult. More specifically it would be on the time scale of necrosis and/or apoptosis in that system.

It was concluded on the basis of pure recombinant GFP protein stability studies together with a conservation of fluorescence signal analysis that the mechanism responsible for the attenuation of the GFP signal following cell injury was diffusion and dilution. A basic 1-D model of GFP diffusion in aqueous solutions and in hindered cellular environments yielded time constants that agreed in an order-of-magnitude sense with characteristic attenuation times generally observed in experiments. All the experiments and analyses performed were consistent with a leakage, diffusion, and dilution model of GFP fluorescence attenuation following injury. Cold denaturation of the protein was ruled out as a significant mechanism of fluorescence attenuation under the circumstances studied.

Although the conclusions presented so far represent the most significant contributions of this work, several other pieces of work were completed in support of both the short-term and long-term goals of this project. The thermophysical characterization work that was performed as part of this comprehensive study allowed the conclusion that fast freezing rates (order 100-1000°C/min) were necessary to induce definitive IIF injury in cultured cells. However, the extrapolation of *in vitro* behavior to

in vivo behavior is not straightforward. It is possible that the high permeability associated with cultured R3230AC cells will not translate into identical freezing behavior *in vivo*. The interesting result that came out of this study was that the cultured cells appear to possess AQP channels for transporting water, and it is therefore likely that the *in vivo* cells possess the same channels. If the water channel transport is the dominant means of moving water across the cell, it can be hypothesized that the *in vivo* tumor cells will have high water permeabilities and consequently also require very rapid freezing rates to induce significant IIF within cells in the tissue. Differences between cultured cells and *in vivo* cells that might result in differences in passive diffusion of water across the cell membrane may not be relevant for water transport when AQPs are present. This hypothesis that *in vivo* cells will parallel *in vitro* cells in their freezing response remains to be tested however.

The AFA device that was developed was able to achieve freezing rates and temperatures in the range desired, without sacrifice of optical access in the DSFC. Moreover a significant portion of the tissue could be treated uniformly, thereby minimizing the challenges associated with measuring temperature in small systems amidst large temperature gradients. This development represents a contribution to the state-of-the-art in small-scale cryosurgical probes, as well as extends the utility of DSFC preparations. There were limitations with this device however, the most significant being the magnitude of the injury it induced. By virtue of the device design, the tissue surrounding the experimental region was also damaged to the same extent as the tissue in the experimental window. In instances where the volume of tissue damaged can come to

bear on the variables being studied, this AFA leaves little room for control, and consequently the AFA would not be reccomended for such studies.

The new GFP technology that was developed in this work was used together with the novel AFA to perform a pilot study on a relevant problem in the cryosurgery field, namely freeze injury at high sub-zero temperatures. At temperatures of –18.0 °C significant vascular injury was observed, supporting the hypothesis that vascular injury can contribute significantly to the overall lesion that forms following a cryosurgery, consequently killing cells that otherwise would be expected to remain viable. Although only 2 of the 8 animals that were kept in the study group grew tumors of suitable fluorescence for transient injury observations, the GFP attenuation response post-injury was very similar in the two cases. Complete attenuation was seen to occur by ~2 hours. This was a somewhat unexpected result, and suggests that although vascular injury may be playing a role, it is possible that the cells may by dying as the result of a more direct mechanism. Despite the lack of statistical significance due to the small group size (n=2) these preliminary results are valuable with respect to future experimental design. Experiments to delineate the nature of this high sub-zero injury should not focus solely on vascular injury as the dominant mechanism, without first ruling out such possible alternatives as delayed primary injury (e.g. osmotic shock induced apoptosis or accumulative solute injury).

10.3 Future Work

While GFP technology has revolutionized biological research in many application areas, we believe that we are the first to use it as a tissue viability assay and the first to

apply it to cryobiology problems. The results presented here suggest that the GFP-based viability assay is not limited to isolated cells but can be used as the basis of a tissue viability assay as well, and moreover can be used *in vivo*. This tool should allow the dynamics of cellular injury to be quantitatively evaluated continuously and dynamically, *in vivo,* without sacrifice of the host animal, wherever optical access is possible. This opens the door for obtaining unprecedented information in time and space about cryosurgical tissue injury. The application of GFP technology to a number of fundamental and applied research areas in the field of cryobiology appears to have excellent potential. Moreover, this assay has possible utility for assessing viability following a diversity of tissue injury modalities. The next steps of this research would involve exploring the application of this assay to other modes of injury. Because other applications may involve injury mechanisms and tissue changes that could impair GFP diffusion *in vivo*, it would be prudent to explore GFP diffusion dynamics in the context of several different types of injury.

Both modeling and experimental evidence suggested differences in the threshold levels to be used for the *in vitro* and *in vivo* experimental cases. The signal-to-noise ratio in the *in vivo* case was poor (2:1) due to the background green autofluorescence of biological tissue. In future work it would be advisable to explore different colors of fluorescent protein to improve the signal-to-noise ratio *in vivo*.

Long-term follow up studies *in vivo* would be advisable to evaluate re-growth potential after cells are deemed non-viable by the GFP assay. All cell culture experience to date has implicated no potential for re-growth once GFP has been lost as a result of injury, however this hypothesis remains to be tested in any long-term study in an animal

model. Because of the extent of the edema seen in the skin flaps following freezing it would be advisable to implement an intra-vital tissue model that is not constrained inside a device for such studies. The liver model of Shuder *et al.* (2000) is one such example, however to the author's knowledge this system has not yet been suitably developed for long-term or chronic studies. Using an *in vivo* model that is not as prone to hemorrhage during instrumentation with thermocouples would also be desirable. A preparation that does not require removal of a window could improve the experimental efficiency of the DSFC system as utilized in this work. Establishing the limitations of the GFP technique for trans-epithelial imaging without a dorsal skin flap chamber could open up potential new intravital applications of the GFP assay.

Perhaps the single greatest advance in this area would be the development of non-contact methods for measuring thermal field information *in vivo*, in conjunction with the intravital information. The AFA developed in the present work creates a uniform temperature field during slow freezing of tissue within the DSFC. This allows thermocouples to be used to quantify local temperature and freezing rates with a low sensitivity to placement error. Also, the optical access provided by the annular shape of the device allows thermocouples to be placed in a manner that minimizes fin effect error. If this device is implemented for rapid freezing, the temperature gradients are not expected to be as uniform, and therefore accurate temperature sensing becomes more challenging. In experimental situations where the environment is not amenable to accurate thermocouple measurements, other methods of temperature sensing are necessary. Avoiding the use of thermocouples also minimizes the risk of microvascular

hemorrhage. Novel methods of measuring temperature that require less manipulation of the DSFC or the underlying tissue would be advantageous.

Initial feasibility tests performed by other researchers in the Low Temperature Biology Lab, suggest that infrared thermography and FERIT technology can be applied successfully to measure the temperature field on the surface of the window of the dorsal skin flap chamber or on the rat skin tissue itself if the window is removed. It has been shown that these thermography methods can be performed during freezing and thawing of tissue and tumors within the dorsal skin flap chamber. The application of thermography has several advantages compared to the use of thermocouples. The method is non-contacting, the method is not subject to the fin-effect artifacts that arise from the use of thermocouples and the data are in the form of a complete field rather than discrete points. The continued development and application of these technologies would help improve the ability the correlate thermal history information in time and space with viability information, could improve the overall efficiency of the experimental systems when using the DSFC to study thermal injury.

APPENDICES

APPENDIX A

DIFFCHAM Program

```
(*DiffCham_Check*)
(*****************************************************************)
(*       This program checks the results of Diffcham                *)
(*****************************************************************)
Areacellinit = .
Concsaltext = .
Concsaltextinit = .
Concsaltinit = .
Lp = .
Lpmod = .
Nsaltinit = .
R = .
ri = .
t = .
T = .
Vb = .
vsalt = .
Vbcell = .
Vbcelli = .
Vwinit = .
(*****************************************************************)
(*Parameters that generally remain constant*)

R=8.31 (*J/K/mol*) (*Universial Gas Constant*);

(*Properties requiring definition per cell type*)

Lp=13.2 (*μm/min/atm*) (*Membrane Permeability Constant*);
Vb=0.33(*dimensionless) (*Osmotically-Inactive Volume Fraction*);
T=295 (*K*) (*Temperature*);
ri=9.05 (*μm*) (*Initial Cell Radius*);

(*Experimental conditions that must be specified*)

(*Define initial extracellular salt concentration*)
(*Note: Conversion of Osm to moles/μm^3 with 10^-15 factor*);

Concsaltexti = 0.308 * 10^-15 (*Salt conc, moles/μm^3*);
vsalt = 17.7 * 10^-12 (*NaCl*) (*μm^3/mole*);

(*****************************************************************)
```

```
(*********************************************************************)
(*      Adjustment for mass transfer through the dialysis membrane     *)
(*********************************************************************)
Clear [Concsaltext];
Concsaltext = (0.308 + 0.592*(1-Exp[-0.038*t]))*10^-15;
(*Salt conc, moles/μm^3*)
(*********************************************************************)
Plot [Concsaltext, {t,0,180}, PlotRange → {0.0,1 * 10^-15},
      AxesLabel → {"Time (Sec)", "Ext Concn (moles/μm^3)"}]
```

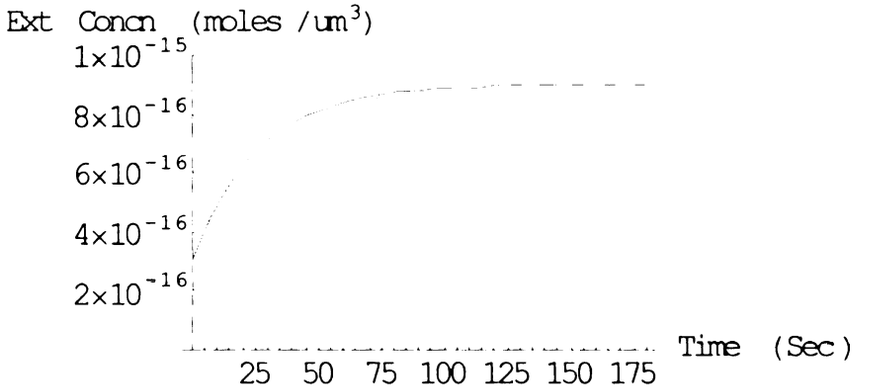


```
(*Necessary Conversions*)
Lpmod=R*T*Lp*(10^18)*(1/60)*(10^-5)(*μm^4/mol/sec*);
(*10^18 for m^3 to μm^3; 1/60 for min to sec; 10^-5 for atm to (N/m^2)*);
Vcelli=(4/3)*3.14*ri^3 (*assuming spherical, μm^3*);
Areacellinit=4*3.14*ri^2 (*μm^2*);
Vbcell=Vcelli*Vb (*μm^3*);
(*Define Lpmod*A factor; (μm^4/mol/sec)*μm^2*) ;
(*Calc initial volume of cell water, μm^3; Assume Vcell=Vw+Vsalt+Vb*)
Vwinit=(Vcelli-Vbcell)/(1+(vsalt*Concsaltexti));
(*Calc initial number of moles of intracellular salt*);
Nsaltinit=Concsaltexti*Vwinit;
(*Define instantaneous intracellular salt conc (mol/μm^3)*)
(*Where y[t] below is Vcell*)
Concsaltint=(Nsaltinit)/(y[t]-Vbcell-Nsaltinit*vsalt);

Clear[y, sol]
sol=NDSolve[{y'[t] = = -Lpmod*Areacellinit*((Concsaltext)-Concsaltinit),
      y[0] = = Vcelli}, y[t], {t,0,180}]

(*********************************************************************)
```

```
Plot[Evaluate[y[t]/Vcelli)/.sol], {t,0,60}, PlotRange → {0.0, 1.0},
    AxesLabel →{"Time (Sec)", "Normalized Volume"}]
```

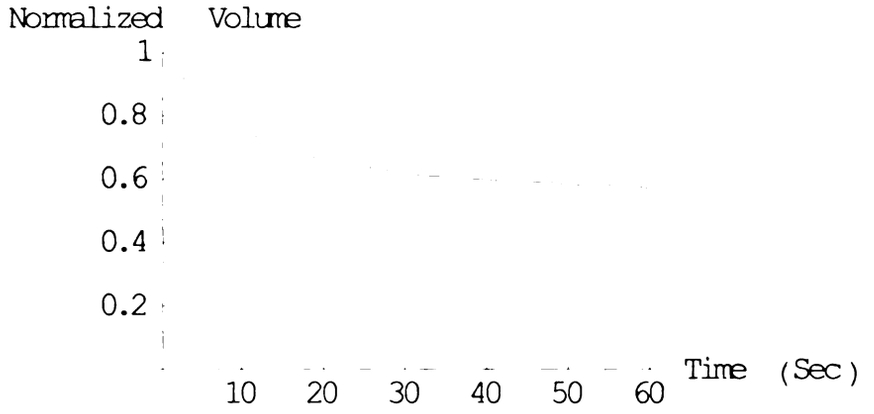

APPENDIX B

Vc_Freeze Program

```
(*Vc_Freeze*)

(*****************************************************************)
(*      This program simulates the biophysical response          *)
(*      of cells to freezing.                                    *)
(*****************************************************************)

ELp=.
ELp1=.
Lp=.
Lpg=.
Lpmod=.
B=.
R=.
T=.
TR=.
ri=.
H=.
H1=.
A=.
V=.
Vi=.
Vb=.
Vbcell=.
vs=.
vw=.
concexini=.
concex=.
nsalt=.

(*****************************************************************)
(*      Parameters that generally remain constant                *)
(*****************************************************************)

R=8.314 (*J/K-mol*) (*Universial Gas Constant*);
vw=18.0*10^12 (*μm^3/mol*);
H1=333 (*latent heat of fusion; kJ/kg*);

(*****************************************************************)
```

```
(*****************************************************************)
(*      Reference Conditions                                     *)
(*****************************************************************)

Lpg=7.466 (*μm/min-atm*);
TR=273.15 (*Temperature in K*);

(*****************************************************************)
(*      Cell Parameters                                          *)
(*****************************************************************)

ri=9.0 (*μm*);
ELp1=4.2 (*kcal/mol*);
Vb=0.33 (*osmotically-inactive volume fraction*);

(*****************************************************************)
(*      Experimental conditions that must be satisfied           *)
(*****************************************************************)

concexini=0.154*10^-15;
(*initial extracellular salt concentration; μm^3/mole*)

(*****************************************************************)
(*      Conversions to ensure consistent units                   *)
(*****************************************************************)

ELp=ELp1*4.184*10^3 (*J/mol*);
H=H1*18.015 (*J/mol*);

(*****************************************************************)
(*      Calculations                                             *)
(*****************************************************************)

A=4*3.14*ri^2 (*μm^2*);
Vi=(4/3)*3.14*ri^3;
Vbcell=Vb*Vi;
nsalt=concexini*(Vi-Vbcell);
Lp=Lpg*Exp[(ELp/R)*((1/TR)-(1/T))];
Lpmod=Lp*R*T*10^13 (*μm^4/mol-atm*);

(*****************************************************************)
```

```
(*****************************************************************)
(*      Plots of Calculations                                    *)
(*****************************************************************)

Plot[Lp, {T, 274, 253}, PlotRange → {0.0, 8.0},
      AxesLabel → {"Temp(K)", "Lp (μm/min-atm)"}];
```

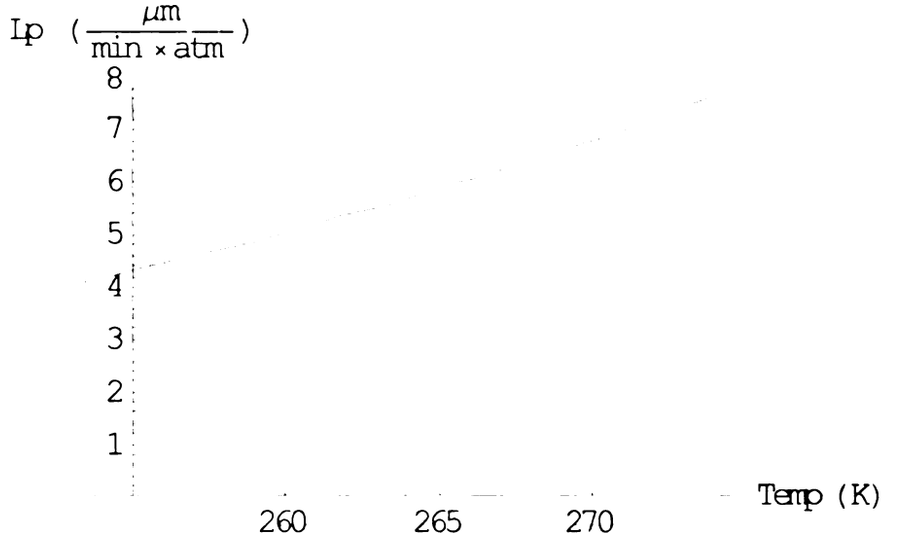


```
(*****************************************************************)

Clear [B];
B=100 (*Cooling rate in °C/min*);

(*****************************************************************)
(*      Solution                                                 *)
(*****************************************************************)

sol=NDSolve[{V'[T] = = ((Lpmod*A)/(vw*B))*
      ((Log[(V[T]-Vbcell)/((V[T]-Vbcell)+(2*vw*nsalt))]) –
            (H/R)*((1/TR)-(1/T))), V[272.4] = = Vi}, V[T],
                  {T, 272.4, 253}]

(*****************************************************************)
(*      Results                                                  *)
(*****************************************************************)
```

```
Plot[Evaluate [((V[T])/Vi)/.sol], {T, 272, 253},
        PlotRange → {0, 1.1}, AxesLabel →
                {"Temp(K)", "Normalized Volume"}]

Table[(V[T]/Vi)/.sol, {T, 253, 272}];
TableForm[%]
```

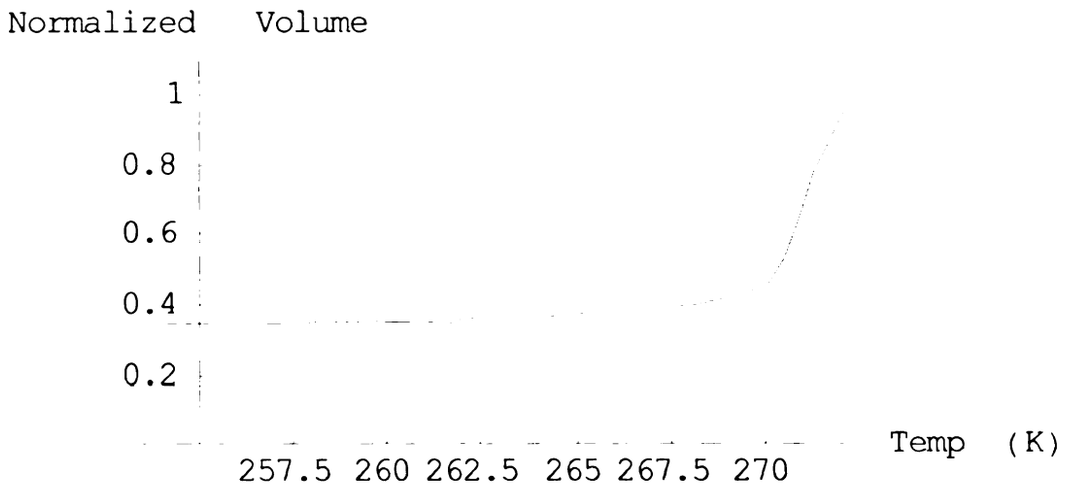


```
0.345868
0.346861
0.347964
0.349196
0.350581
0.352151
0.353943
0.356009
0.358418
0.361261
0.364669
0.36883
0.374027
0.380705
0.389618
0.402163
0.421334
0.462304
0.699509
0.956958
```

APPENDIX C

Mechanical Drawing of AFA

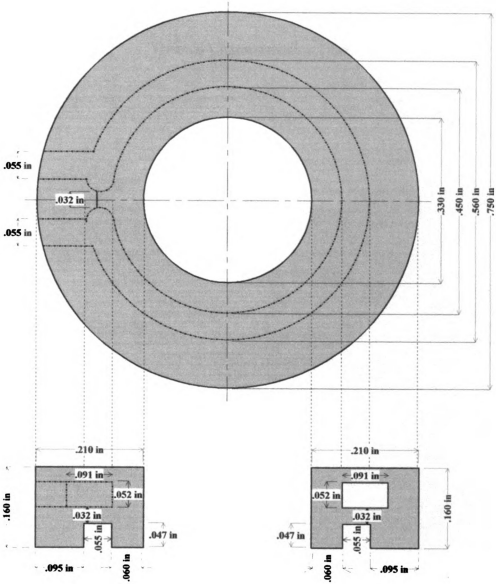
.055 in
.032 in
.055 in
.330 in
.450 in
.560 in
.750 in
.210 in
.091 in
.052 in
.160 in
.032 in
.055 in
.047 in
.095 in
.060 in
.210 in
.091 in
.052 in
.160 in
.032 in
.047 in
.055 in
.060 in
.095 in

APPENDIX D

Thermal Characterization Data

Characterization of AFA using processed meat (n=3)

Latent Heat Release (onset temperature)

	TC1	TC2	TC3	TC4	TC5	TC6
gloria5.log	-8.38	-8.25	-6.45	-0.92	-1.25	-0.66
gloria6.log	-8.67	-8.49	-7.32	-5.04	-4.67	-3.48
gloria7.log	-4.01	-4.38	-3.9	-8.75	-9.17	-6.55
					AVE	-5.57444
					SD	2.844756
					SEM	0.670515

Lowest Minimum Temperature

	TC1	TC2	TC3	TC4	TC5	TC6
gloria5.log	-87.77	-88.65	-85.7	-81.94	-82.03	-80.99
gloria6.log	-86.03	-86	-83.72	-82.65	-82	-79.95
gloria7.log	-79.62	-79.92	-79.01	-85.49	-86.3	-82.88
					AVE	-83.3694
					SD	2.957273
					SEM	0.697036

Maximum Spatial Variation

	A	B	C	D	E	F
gloria5.log	3.02	3.29	3.55	1.35	1.18	1.81
gloria6.log	2.96	2.76	2.5	0.83	3.17	2.4
gloria7.log	0.53	1.01	1.37	1.17	3.31	4.05
					MAX	4.05
					SD	1.085254
					SEM	0.255797

Average Spatial Variation

	A	B	C	D	E	F
gloria5.log	0.288491	1.260677	1.352935	0.219724	0.399332	0.57878
gloria6.log	0.179767	1.04299	0.871832	0.322239	1.158316	0.978596
gloria7.log	0.15163	0.398218	0.431064	0.220152	1.091823	1.29634
					AVE	0.680161
					SD	0.439946
					SEM	0.103696

Symmetry

(three T/Cs per side averaged, then differences summarized)

	AVE	MAX
gloria5.log	2.81	7.84
gloria6.log	1.72	4.94
gloria7.log	0.72	2.08
AVE	1.75	4.95

AVE=average difference between sides
MAX=maximum difference between sides
A=TC1-TC2 D=TC4-TC5
B=TC2-TC3 E=TC4-TC6
C=TC1-TC3 F=TC5-TC6

APPENDIX E

Neumann Program

```
(*NeumannV1.nb*)
(*************************************************************)
(*      This program finds the solution to the Neumann 2-phase      *)
(*      solidification problem, with constant properties            *)
(*************************************************************)

Clear[rho1, rho2, k1, k2, a1, a2, c1, c2, T1, T2, Tf, To, Ts, l, L, lam, X]

(*************************************************************)
(* properties; 1=solid region, 2=liquid region*)

(*water*)
rho1=1000; (*kg/m^3*)
rho2=1000; (*kg/m^3*)
k1=1.88; (*W/mK*)
k2=0.61; (*W/mK*)
c1=2.04 10^3; (*J/kgK*)
c2=4.18 10^3; (*J/kgK*)
l=333.4 10^3; (*J/m^3*)

(*************************************************************)
(*boundary, initial, and phase change conditions; 1=solid region,
      2=liquid region*)

Tf=269 (*K*);
To=310 (*K*);
Ts=77(*K*);

(*************************************************************)

a1=k1/(rho1 c1);
a2=k2/(rho2 c2);
a12=a1/a2;
k21=k2/k1;

(*************************************************************)

FindRoot[(1/(Exp[lam^2] Erf[lam]))-(k21*a12^0.5*(To-Tf))/((Tf-Ts)
      *Exp[a12*(lam^2)] Erfc[a12^0.5*lam]) = =
            l* lam*(Pi^0.5)/(c1*(Tf-Ts)), {lam, 0.01, 0.01, 100}]

(*************************************************************)
9.21569x10^-7
      {lam→0.545159}
```

```
(*************************************************************)
(*      With knowledge of the root the position of the interface at      *)
(*      any given time can be computed.                                  *)
(*                                                                       *)
(*      Note: a1 needs to be re-written from the previous sub-routine    *)
(*************************************************************)
```

Table[(2*0.545159*((t*9.21569 10^{-7})$^{0.5}$)), {t, 0, 22, 1}]

```
(*************************************************************)

0
0.00104669
0.00148024
0.00181292
0.00209338
0.00234046
0.00256385
0.00276928
0.00296048
0.00314006
0.00330992
0.00347147
0.00362583
0.00377389
0.00391635
0.0040538
0.00418675
0.0043156
0.00444072
0.00456241
0.00468093
0.00479653
0.0049094
```

```
(*************************************************************************)
(*      For a given time/interface position the temperature distribution  *)
(*      can be determined.                                                *)
(*************************************************************************)
Clear [rho1, rho2, k1, k2, a1, a2, c1, c2, T1, T2, Tf, To, Ts, l, L, lam, X];

rho1=1000; (*kg/m^3*)
rho2=1000; (*kg/m^3*)
k1=1.88; (*W/mK*)
k2=0.61; (*W/mK*)
c1=2.04 10^3; (*J/kgK*)
c2=4.18 10^3; (*J/kgK*)
l=333.4 10^3; (*J/m^3*)

Tf=269 (*K*);
To=310 (*K*);
Ts=77(*K*);

a1=k1/(rho1 c1);
a2=k2/(rho2 c2);
a12=a1/a2;
k21=k2/k1;

T1= Ts + (((Tf-Ts)*(Erf[x/(2*(a1*22)^0.5])))/(Erf[0.545159]));
T2=To – (((To-Tf)*(Erfc[x/(2*(a2*22)^0.5])/(Erfc[0.545159*(a12^0.5)])));

plot1=Plot[T1, {x, 0, 0.0049094}]
plot2=Plot[T2, {x, 0.004904, 0.01}]
Show [plot 1, plot2]
```

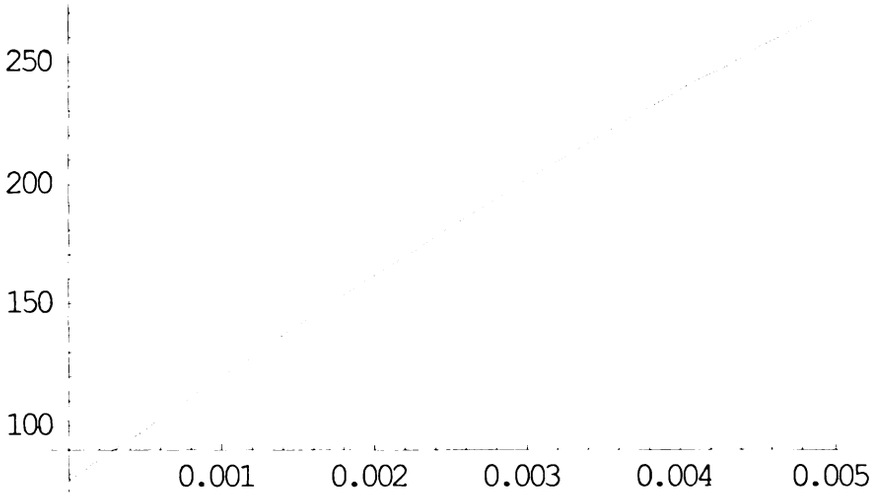

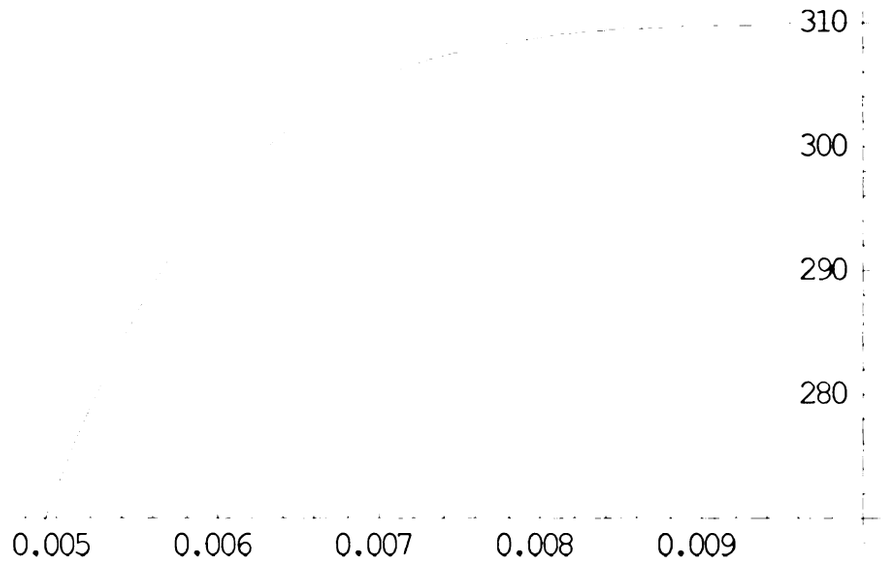
310
300
290
280
0.005
0.006
0.007
0.008
0.009

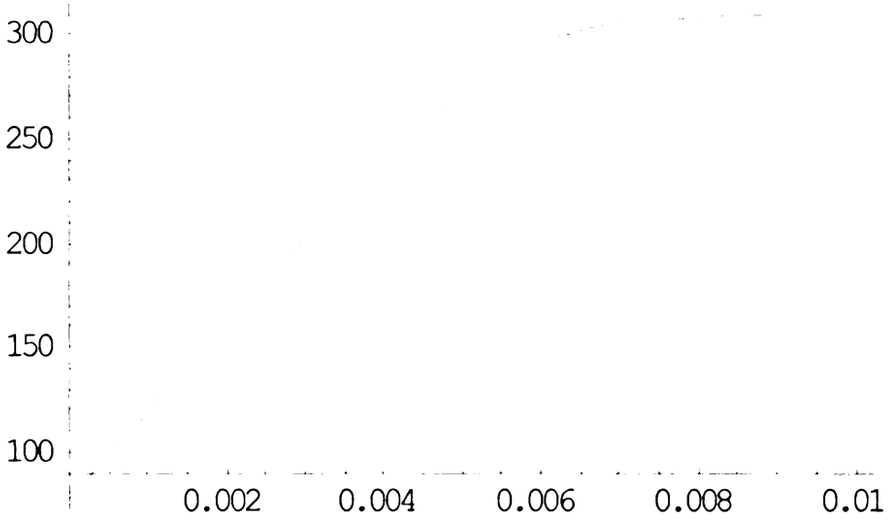
300
250
200
150
100
0.002
0.004
0.006
0.008
0.01

APPENDIX F

Cho and Sutherland Program

```
(*Neumann 3 phase.v1*)
(*****************************************************************)
(*      This program provides the exact solution to the Neumann  *)
(*      problem with a melting temperature range,                 *)
(*      infinite slab geometry                                    *)
(*****************************************************************)
ClearAll[a1, a2, a3, a12, a21, a13, a23, a31, c1, c2, c3, eta, f, k1, k2, k21,
k31, k32, l, lam, rho, t, T1, T2, T3, To, Tfl, Tfs, x]

(*****************************************************************)
(*      Material properties                                       *)
(*      1=solid phase; 2=mush; 3=liquid phase                     *)
(*****************************************************************)
(*      Define properties                                         *)
(*****************************************************************)
k1=1.88 (*W/mK*);
k2=1.245 (*W/mK*);
k3=0.61 (*W/mK*);
rho=1000 (*kg/m^3*);
c1=2040 (*J/kgK*);
c2=3110 (*J/kgK*);
c3=4180 (*J/kg/K*);
Tfs=265 (*K*);
Tfl=272 (*K*);
To=310 (*K*);
Ts=77 (*K*);
f=1 (*dimensionless*) (* =1 pure water  =eutectic concn for mixtures*);
l=334000(*J/kg*);
(*****************************************************************)
(*      Conversions                                               *)
(*****************************************************************)
a1=k1/(rho*c1);
a2=k2/(rho*c2);
a3=k3/(rho*c3);
a12=a1/a2;
a21=a2/a1;
a23=a2/a3;
a32=a3/a2;
a31=a3/a1;
k12=k1/k2;
k21=k2/k1;
k23=k2/k3;
k32=k3/k2;
(*****************************************************************)
```

```
(*****************************************************************)
(*      Solution                                                 *)
(*****************************************************************)

FindRoot [
 { e^(-lam^2) / Erf[lam] + (Sqrt[π] k21 f l) / (2 c2 (Tfs - Ts) (eta - lam)) -
   (k21 * (Tfl - Tfs + l f / c2) e^(-lam^2/a21)) / (Sqrt[a21] * (Tfs - Ts) * (Erf[eta/Sqrt[a21]] - Erf[lam/Sqrt[a21]])) ==
   Sqrt[π] (1 - f) l lam / (c1 (Tfs - Ts)),
   (Tfl - Tfs + l f / c2) e^(-eta^2/a21) / (Erf[eta/Sqrt[a21]] - Erf[lam/Sqrt[a21]]) - (Sqrt[π] * a21 * l * f) / (2 * c2 * (eta - lam)) ==
   (To - Tfl) k32 Sqrt[a23] e^(-eta^2/a31) / Erfc[eta/Sqrt[a31]] },
 {eta, 0.45}, {lam, 0.4},
 MaxIterations -> 800, DampingFactor -> 0.2]
```

(*NOTE: Do not set eta=lam. It will generate an infinity term*)

{eta → 0.55469, lam →0.531195}

eta=0.55469;
lam=0.531195;

(********** TEST ROOTS **********)

$$EQ1 = \left(\frac{e^{-lam^2}}{Erf[lam]}\right) + \left(\frac{\sqrt{\pi}\ k21\ f\ l}{2\ c2\ (Tfs - Ts)\ (eta - lam)}\right) - \left(\frac{\left(k21 * \left(Tfl - Tfs + \frac{l\ f}{c2}\right) e^{-\frac{lam^2}{a21}}\right)}{\sqrt{a21} * (Tfs - Ts) * \left(Erf\left[\frac{eta}{\sqrt{a21}}\right] - Erf\left[\frac{lam}{\sqrt{a21}}\right]\right)}\right) - \frac{\sqrt{\pi}\ (1 - f)\ l\ lam}{c1\ (Tfs - Ts)}$$

$$EQ2 = \left(\frac{\left(Tfl - Tfs + \frac{l\ f}{c2}\right) e^{-\frac{eta^2}{a21}}}{Erf\left[\frac{eta}{\sqrt{a21}}\right] - Erf\left[\frac{lam}{\sqrt{a21}}\right]}\right) - \left(\left(\frac{1}{2}\sqrt{\pi\ a21}\right) *\right.$$

$$\left.((1 * f / (c2 * (eta - lam))))\right) - \frac{(To - Tfl)\ k32\ \sqrt{a23}\ e^{-\frac{eta^2}{a31}}}{Erfc\left[\frac{eta}{\sqrt{a31}}\right]}$$

(**********)
(* Roots solved in the previous equation need to be defined below *)
(**********)

eta=0.55469
lam=0.53195

(**********)
(* The next segment solves for the temperature distribution at a *)
(* pre-determined time *)
(**********)

t=22; (*sec*)

(**********)

$$T1 = \left(\frac{\mathrm{Erf}\left[\frac{x}{2*\sqrt{a1*t}} \right]}{\mathrm{Erf}[lam]} \right) * (Tfs - Ts) + Ts;$$

$$T2 =$$

$$\left(1 - \frac{1*f*\left(\frac{x}{2*\sqrt{a1*t}} - lam \right)}{c2*(Tfs - Ts)*(eta - lam)} \right) +$$

$$\left(\frac{\left(Tfl - Tfs + \left(\frac{1*f}{c2} \right) \right)}{(Tfs - Ts)} \right) * \left(\frac{\left(\mathrm{Erf}\left[\frac{x}{2*\sqrt{a2*t}} \right] - \mathrm{Erf}\left[\frac{lam}{\sqrt{a21}} \right] \right)}{\left(\mathrm{Erf}\left[\frac{eta}{\sqrt{a21}} \right] - \mathrm{Erf}\left[\frac{lam}{\sqrt{a21}} \right] \right)} \right)$$

$$* (T fs - T s) + T s;$$

$$T3 = To - (To - Tfl) * \left(\frac{\left(\mathrm{Erfc}\left[\frac{x}{2*\sqrt{a3*t}} \right] \right)}{\left(\mathrm{Erfc}\left[\frac{eta}{\sqrt{a31}} \right] \right)} \right);$$

```
(*****************************************************************)
(*      Plotting: need to solve for the location of the mushy region      *)
(*      limits                                                            *)
(*****************************************************************)


Xs = 2 * lam * √ al * t ;


Xl = 2 * eta * √ al * t ;
```

Xs
Xl

0.00478365
0.00499523

```
(*****************************************************************)
(*      Using these limits the results can then be appropriately          *)
(*      plotted                                                           *)
(*****************************************************************)

plot1=Plot[T1, {x, 0, 0.00478365}]
plot2=Plot[T2, {x, 0.00478366, 0.00499523}]
plot3=Plot[T3, {x, 0.00499524, 0.01}]
Show[plot1, plot2, plot3]
```

BIBLIOGRAPHY

Aggarwal, S.J., Shah, S.J., Diller, K.R., and Baxter, C.R. Fluorescent digital microscopy of interstitial molecular diffusion in burn injury. *Comput. Biol. Med.* **19**(4), 245-261 (1989).

Agre, P., Brown, D., and Nielson, S. Aquaporin water channels: unanswered questions and unresolved controversies. *Curr. Opin. Cell. Biol.* **7**, 472-483 (1995).

Altman N.H., and Goodman D.G. *In* "The Laboratory Rat" (H.J. Baker, J.R. Lindsey, and S.H. Weisbroth, Eds.), pp. 361-362. Academic Press, Orlando, 1979.

Aran, J.M., Gottesman, M.M., and Pastan, I. Construction and characterization of bicistronic retroviral vectors encoding the multi-drug transporter and b-galactosidase or green fluorescent protein. *Cancer. Gene Ther.* **5**, 195-206 (1998).

Baumstark-Khan, C., Palm, M., Wehner, J., Okabe, M., Ikawa, M., and Horneck, G. Green fluorescent protein (GFP) as a marker for cell viability after UV irradiation. *Journal of Fluorescence* **9**(1), 37-43 (1999).

Baust, J., Gage, A.A., Ma, H., and Zhang, C.M. Minimally invasive cryosurgery-technological advances. *Cryobiology* **34**, 373-384 (1997).

Baust, J.G., Clarke, D., Chatterjee, S., Baust, J.M., Friedland, D.M., Cohen, J.K., and VanBuskirk, R. Cryosurgical modeling: sequenced cryo-chemotherapy increases human prostate cancer cell death. *Cryobiology* **41**, 358-359 (2000).

Beavis, A.J., and Kalejta, R.F. Simultaneous analysis of the cyan, yellow, and green fluorescent proteins by flow cytometry using single-laser excitation at 458 nm. *Cytometry* **37**, 68-73 (1999).

Bellman, S., and Adams-Ray, J. Vascular reactions after experimental cold injury: a microangiographic study on rabbit ears. *Angiology* **7**, 329-367 (1956).

Bischof, J., Christov, K., and Rubinsky, B. A morphological study of cooling rate response in normal and neoplastic human liver tissue: cryosurgical implications. *Cryobiology* **30**, 482-492 (1993).

Bischof, J., Smith, D., Pazhayannur, P.V., Manivel C., and Hulbert, J. Cryosurgery of Dunning AT-1 rat prostate tumor: thermal, biophysical, and viability responses at the cellular and tissue level. *Cryobiology* **34**, 42-69 (1997).

Bird, H.M. James Arnott, M.D. (Aberdeen) 1797-1833: A pioneer in refrigeration analgesia. *Anesthesia* **4**, 10-17 (1949).

Bokman, S.H., and Ward, W.W. Renaturation of *Aequorea* Green fluorescent protein. *Biochem. Biophys. Res. Commun.* **101**, 1372-1380 (1981).

Bonacina, C., Comini, G., Fasano, A., and Primicerio, M. On the estimation of thermophysical properties in nonlinear heat conduction problems. *Int. J. of Heat & Mass Transfer* **17**, 861-867 (1974).

Brewis, N., Phelan, A., Webb, J., Drew, J., Elliott, G., and O'Hare, P. Evaluation of VP22 spread in tissue culture. *Journal of Virology* **74**(2), 1051-6 (2000).

Brown, N.J., Bayoo, P., and Reed M.W.R. Effect of cryosurgery on liver blood flow. *Br. J. Cancer* **68**, 10-12 (1993).

Brown, N.J., Pollack, K.J., Bayoo, P., and Reed M.W.R. The effect of cryotherapy on the cremaster muscle microcirculation *in vivo*. *Br. J. Cancer* **68**, 10-12 (1994).

Bourne, M.H., Piepkorn, M.W., Clayton, F., and Leonard, L.G. Analysis of microvascular changes in frostbite injury. *J. of Surgical Research* **40**, 26-35 (1986).

Budman, H., Shitzer, A., and Dayan, J. Analysis of the inverse problem of freezing and thawing of a binary solution during cryosurgical processes. *JBME* **117**, 193-202 (1995).

Chalfie, M., Tu, Y., Euskirchen, G., Ward, W., and Prasher, D.C. Green fluorescent protein as a marker for gene expression. *Science* **263**, 802-805 (1994).

Chida, D., Miura, O., Yoshimura, A., and Miyajima, A. Role of cytokine signaling molecules in erythroid differentiation of mouse fetal liver hematopoietic cells: functional analysis of signaling molecules by retrovirus-mediated expression. *Blood* **93**, 1567-1578 (1999).

Chishima, T., Miyagi, Y., Li, L., Tan, Y., Baranov, E., Yang, M., Shimada, H., Moossa, A.R., and Hoffman, R.M. Use of histoculture and green fluorescence protein to visualize tumor cell host interaction. *In vitro Cell. Dev. Biol.* **33**, 745-747 (1997a).

Chishima, T., Miyagi, Y., Wang, X., Baranov, E., Tan, Y., Shimada, H., Moossa, A.R., and Hoffman, R.M. Metastatic patterns of lung cancer visualized live and in process by green fluorescence protein expression. *Clin. Exp. Metastasis* **15**, 547-552 (1997b).

Chishima, T., Miyagi, Y., Wang, X., Tan, Y., Shimada, H., Moossa, A.R., and Hoffman, R.M. Visualization of the metastatic process by green fluorescent protein expression. *Anticancer Research* **17**, 2377-2384 (1997c).

Chishima, T., Miyagi, Y., Wang, X., Yamaoka, H., Shimada, H., and Moossa, A.R. Cancer invasion and micrometastasis visualized in live tissue by green fluorescent protein expression. *Cancer Res.* **57**, 2042-2047 (1997d).

Chishima, T., Yang, M., Miyagi, Y., Li, L., Tan, Y., Baranov, E., Shimada, H., Moossa, A.R., Penman, S., and Hoffman, R.M. Governing step of metastasis visualized *in vitro*. *Proc. Natl. Acad. Sci. USA* **94**, 11573-11576 (1997e).

Cho, S.H. and Sutherland, J.E. Heat conduction problems with melting or freezing. *Journal of Heat Transfer*, **91**, 421-426 (1969).

Chou, C.L., Ma, T., Yang, B., Knepper, M.A., and Verkman, A.S. Fourfold reduction of water permeability in inner medullary collecting duct of aquaporin-4 knockout mice. *Am. J. Physiol.* **274** (2), C549-554 (1998).

Chou, C.L., Knepper, M.A., van Hoek, A.N., Brown, D., Yang, B., Ma, T., and Verkman, A.S. Reduced water permeability and altered ultrastructure in thin descending limb of Henle in aquaporin-1 null mice. *J. Clinical Investigation* **103** (4), 491-496 (1999).

Clarke, D.M., Baust, J.M., VanBuskirk, R, and Baust, J.G. Cryo-chemo combination therapy: an adjunctive model for the treatment of prostate cancer. *Cryobiology* **42,** 274-285 (2001).

Clontech Protocol # PT2040-1, Version #PR67195

Cody, C.W., Prasher, D.C., Westler, W.M., Prendergast, F.G., and Ward, W.W. Chemical structure of the hexapeptide chromophore of the *Aequorea* green fluorescent protein. *Biochemistry* **32**, 1212-1218 (1993).

Coombe, D.R., Nakhoul, A.M., Stevenson, S.M., Peroni, S.E., and Sanderson, C.J. Expressed luciferase viability assay (ELVA) for the measurement of cell growth and viability. *J. of Immun. Methods* **215**, 145-150 (1998).

Cooper, I.S. Cryobiology as viewed by the surgeon. *Cryobiology* **1**, 44-54 (1964).

Cooper, T.E., and Trezek, G.J. Analytical prediction of the temperature field emanating from a cryogenic surgical cannula. *Cryobiology* **7**, 79-93 (1970).

Cormack, B.P., Valdivia, R.H., and Falkow, S. FACS-optimized mutants of the Green Fluorescent Protein (GFP). *Gene* **173**, 33-38 (1996).

Creighton, T.E. "Proteins, Structures, and Molecular Properties, second edition" W.H. Freeman and Company, New York, 1996.

Cubitt, A.B., Heim, R., Adams, S.R., Boyd, A.E., Gross, L.A., and Tsien, R.Y. Understanding, improving and using Green Fluorescent Proteins. *Trends in Biochemical Science* **20,** 448-455 (1995).

De Giorgi, F., Ahmed, Z., Bastianutto, C., Brini, M., Jouaville, L.S., Marsault, R., Murgia, M., Pinto, P., Pozzan, T., and Rizzuto, R. Targetting GFP to organelles. *In* "Methods in Cell Biology: Green Fluorescent Proteins" (K.F. Sullivan, and S.A. Kay, Eds.), Vol. 58, pp. 75-85. Academic Press, San Diego, 1999.

Devireddy, R.V., Raha, D., and Bischof, J.C. Measurement of water transport during freezing in cell suspensions using a differential scanning calorimeter. *Cryobiology* **36,** 124-155 (1998).

Diller, K.R., and Hayes, L.J. Analysis of tissue injury by burning: comparison of *in situ* and skin flap models. *Int. J. Heat Mass Transfer* **34,** 1393-1406 (1991).

Elliott, G.D., and J.J. McGrath. Freezing response of mammary tissue: a mathematical study. *Advances in Heat and Mass Transfer in Biotechnology.* HTD-Vol. 363/BED-Vol. 44, 59-64 (1999).

Elliott, G.D., Fron, D., Seip, C., McGrath, J.J., and Crockett-Torabi, E. Development of a novel *in vivo* assay of tissue viability: a cryosurgery application. *Advances in Heat and Mass Transfer in Biotechnology*, HTD-Vol. 368, BED-Vol.47, 149-155 (2000a).

Elliott, G., McGrath, J., and Crockett-Torabi, E. Green Fluorescent Protein: A novel viability assay for cryobiological applications *Cryobiology* **40,** 360-369 (2000b).

Endo, M., Jain, R.K., Witwer, B., and Brown, D. Water channel (Aquaporin 1) expression and distribution in mammary carcinomas and glioblastomas. *Microvascular Research* **58**, 89-98 (1999).

Falk, M.M., and Lauf, U. High resolution, fluorescence deconvolution microscopy and tagging with the autofluorescent tracers, CFP, GFP, and YFP to study structural composition of gap junctions in living cells. *Microscopy Research and Technique* **52**(3), 251-262 (2001).

Frerichs, N. Independent Study, Department of Mechanical Engineering, Michigan State University, 2001.

Fron, D. Independent Study, Department of Mechanical Engineering, Michigan State University, 2000.

Gaber, M.H., Wu, N.Z., Hong, K., Huang, S.K., Dewhirst, M.W., and Papahadjopoulos, D. Thermosensitive liposomes: extravasation and release of tumor contents in tumor micro-vascular networks. *Int. J. Radiat. Oncol. Biol. Phys.* **36**(5), 1177-1187 (1996).

Gage, A.A. Cryosurgery in the treatment of cancer. *Surg. Gynecol. Obstet.* **174,** 73-92 (1992).

Gage, A.A. History of cryosurgery. *Seminars in Surgical Oncology* **14**, 99-109 (1998).

Gage, A. and Baust, J. Mechanisms of tissue injury in cryosurgery. *Cryobiology* **37**, 171-186 (1998).

Gilbert J.C., Rubinsky B., Wong S.T.S., Brennan K.M., Pease G.R., and Leung P.P. Temperature determination in the frozen region during cryosurgery of rabbit liver using MR image analysis. *Magnetic Resonance Imaging* **15**, 657-667 (1997).

Gonzalez, D.G., and Ward, W.W. Large-scale purification of recombinant green fluorescent protein from *Escherichia coli*. *In* "Methods in Enzymology: Bioluminescence and Chemiluminescence Vol. 305(C)" (M.M. Ziegler and T.O. Baldwin, Eds.) pp. 212-223, Academic Press, San Diego, 2000.

Gordon-Kamm W.J., Steponkus P.L. Lamellar-to-hexagonal$_{II}$ phase transitions in the plasma membrane of isolated protoplasts following freeze-induced dehydration. *Proc. Natl. Acad. Sci., USA* **81**, 6373-6377 (1984).

Gourgouliatos, Z.F., Welch, A.J., and Diller, K.R. Microscopic instrumentation and analysis of laser-tissue interaction in a skin flap model. *JBME* **113**, 301-307 (1991).

Gross, J.F., Roemer, R., Dewhirst, M., and Meyer, T. A uniform thermal field in a hyperthermia chamber for microvascualr studies. *Int. J. Heat Mass Transfer* **25** 1313-1320 (1982).

Haupts, U., Maiti, S., Schwille, P., and Webb, W.W. Dynamics of fluorescence fluctuations in green fluorescent protein observed by fluorescence correlation spectroscopy. *Proc. Natl. Acad. Sci. USA* **95**, 13573-13578 (1998).

Haas, J., Park, E.C., and Seed, B. Codon usage limitation in the expression of HIV-1 envelope glycoprotein. *Curr. Biol.* **6**(3) 315-324 (1996).

Heim, R., Prasher, D.C., and Tsien, R.Y. Wavelength mutations and post-translational auto-oxidation of Green Fluorescent Protein. *Proc. Natl. Acad. Sci. USA* **91**, 12501-12504 (1994).

Hempling, H.G., Thomson, S., and Dupre, A.M. Osmotic properties of human lymphocytes. *J. Cell Physiol.* **93** 293-302 (1977).

Higashijima, S., Hotta, Y., and Okamoto, H. Visualization of cranial motor neurons in live transgenic zebrafish expressing green fluorescent protein under the control of the islet-1 promoter/enhancer. *J. Neuroscience* **20**(1), 206-218 (2000).

Hilf, R., Freeman, J.J., Michel, I., and and Borman, A. Characterization of a transplantable lactating mammary tumor: endocrinological, morphological, and biochemical aspects. *Cancer Res.* **24**, 812-824 (1964).

Hilf, R., Michel, I., Bell, C.F., and Borman, A. Biochemical and morphologic properties of a new lactating mammary tumor line in the rat. *Cancer Res.* **25**, 286-299 (1965).

Hoffman, N., Swanlund, D. and Bischof, J. Observation of vascular injury after freezing: investigating the response of normal skin and subcutaneous AT-1 tumor tissue to cryosurgery in the dorsal skin flap chamber. *Advances in Heat and Mass Transfer in Biotechnology*, HTD-Vol. 363/BED-Vol. 44, 39-42 (1999).

Hoffman, N., and Bischof, J. Cryosurgery of normal and tumor tissue in the dorsal skin flap chamber: part I-thermal response. *J. of Biomechanical Engineering* **123**, 301-309 (2001).

Hoffman, N., and Bischof, J. Cryosurgery of normal and tumor tissue in the dorsal skin flap chamber: part II-injury response. *J. of Biomechanical Engineering* **123**, 310-316 (2001).

Hong J., and Rubinsky B. Patterns of ice formation in normal and malignant breast tissue. *Cryobiology* **31**, 109-120 (1994).

Hong J., Wong S., Pease G., and Rubinsky B. MR imaging assisted temperature calculations during cryosurgery. *Magn. Reson. Imaging* **12**(7), 1021-1031 (1994).

Hunt, L., Jordan, M., De Jesus, M., and Wurm, F.M. GFP-expressing mammalian cells for fast, sensitive, non-invasive cell growth assessment in a kinetic mode. *Biotechnol. & Bioeng.* **65**(2), 201-205 (1999).

Jacob, G., Kurzer, M.N., and Fuller, B.J. An assessment of tumor cell viability after *in vitro* freezing. *Cryobiology* **22**, 417-426 (1985).

Jain, R.K. Transport of molecules in the tumor interstitium: a review. *Cancer Res.* **47** 3039-51 (1987).

Jain, R.K., Stock, R.J., Chary, S.R., and Reuter, M. Convection and diffusion measurements using fluorescence recovery after photobleaching and video analysis: *in vitro* calibration and assessment. *Microvascular Research* **39**, 77-93 (1990).

Jain, R.K., Weissbrod, J.M., and Wei, J. Mass transport in tumors: characterization and applications to chemotherapy. *Advances in Cancer Research* **33**, 251-311 (1998).

Jain, R.K. Transport of molecules, particles, and cells in solid tumors. *Ann. Rev. Biomed. Eng.* **1**, 241-263 (1999).

Jakobs, S., Subramaniam, V., Schonle, A., Jovin, T.M., and Hell, S.W. EGFP and DsRed expressing cultures of *Escherichia coli* imaged by confocal, two-photon and fluorescence lifetime microscopy. *FEBS Letters* **479**, 131-135 (2000).

Kac, E. GFP Bunny. *In* "Telepresence, Biotelematics, and Transgenic Art" (P.T. Dobrila, Ed.) Kibla, Maribor, Slovenia, 2000.

Kain, S.R. Enhanced variants of the Green Fluorescent Protein for greater sensitivity, different colors, and detection of apoptosis. *In* "Fluorescent and Luminescent Probes, 2nd Edition", pp. 284-292, Academic Press, 1999.
Kay, J. Intracellular protein degradation. *Biochem. Soc. Trans.* **6,** 789-797 (1978).

Kedem, O. and Katcalsky, A. Thermodynamic analysis of the permeability of biological membranes to non-electrolytes. *Biochimica et Biophysica ACTA* **27**, 229-246, (1958).

Kleinhans, F.W. Membrane permeability modeling: Kedem-Katchalsky vs. a two-parameter formalism. *Cryobiology* **37**(4), 271-89 (1998).

Kolb, V.A., Makeyev, E.V., Ward. W.W., and Spirin, A.S. Synthesis and maturation of green fluorescent protein in a cell-free translation system. *Biotechnology Letters* **18,** 1447-1452 (1996).

LeFebvre, J.H., and Folke, L.E. Effects of subzero temperatures on the microcirculation in the oral mucous membrane. *Microvascular Research* **10**, 360-372 (1975).

Lehninger, A. "Biochemistry, The Molecular Basis of Cell Structure and Function, Second Edition". Worth Publishers, Inc., New York (1976).

Levin, R.L., Cravalho, E.G., and Huggins, C.E. A membrane model describing the effect of temperature on the water conductivity of erythrocyte membranes at subzero temperatures. *Cryobiology* **13**, 415-429 (1976).

Levin, R.L. Water permeability of yeast cells at subzero temperatures. *Journal of Membrane Biology* **46,** 191-214 (1979).

Levonson, V.V., Transue, E.D.E., and Roninson, I.B. Internal ribosomal entry site - containing retroviral vectors with green fluorescent protein and drug resistance markers. *Hum. Gen. Ther.* **9**, 1233-1235 (1998).

Li, X., Zhang, G., Ngo, N., Zhao, X., Kain, S.R., and Huang, C.C. Deletions of the *Aequorea victoria* Green Fluorescent Protein define the minimal domain required for fluorescence. *J. Biol. Chem.* **272**, 28545-28549 (1997).

Li, X., Zhao, X., Fang, Y., Jiang, X., Duong, T., Fan, C., Huang, C-C., Kain, S.R. Generation of destabilized Green Fluorescent Protein as a transcription reporter. *J. Biol. Chem.* **273**(52), 34970-34975 (1998).

Li, C-Y., Shan, S., Huang, Q., Braun, R., Lanzen, J., Hu, K., Lin, P. and Dewhirst, M. Initial stages of tumor cell-induced angiogenesis: evaluation via skin window chambers in rodent models. *Journal of the National Cancer Institute* **92**(2), 143-7 (2000).

Lim, C.R., Kimata, Y., Oka, M., Nomaguchi, K., and Kohno, K. Thermosensitivity of green fluorescent protein fluorescence utilized to reveal nuclear-like compartments in a mutant nucleoporin NSP1. *J. Biochem.* **118**, 13-17 (1995).

Lunardini, V. Heat Transfer in Cold Climates. Van Nostrand Reinhold Company, New York, (1981).
Lunardini, V. Heat Transfer with Freezing and Thawing. Elsevier, Amsterdam, (1991).

Manson, P.N., Jesudass, R., Marzella, L., Bulkley, G.B., Im, M.J., and Narayan, K.K. Evidence for an early free-radical mediated reperfusion injury in frostbite. *Free Radical Biology & Medicine* **10**, 7-11 (1991).

Mansoori, G.A. Kinetics of water loss from cells at subzero centigrade temperature. *Cryobiology* **12**, 34-45 (1975).

Marshall, J., Molloy, R., Moss, G.W.J., Howe, J.R., and Hughes, T.E. The jellyfish green fluorescent protein: a new tool for studying ion channel expression and function. *Neuron* **14**, 211-215 (1995).

Martinez de Maranon, I., Gervais, P., and Molin, P. Determination of cells' water membrane permeability: unexpected high osmotic permeability of *Saccharomyces cerevisiae*. *Biotechnology and Bioengineering* **56** (1), 62-70 (1997).

Marzella, L., Jesudass, R.R., Manson, P.N., Myers, R.A., and Bulkley, G.B. *Plast. Reconstr. Surg.* **83** (1), 67-76 (1989).

Mazur, P. Kinetics of water loss from cells at subzero temperatures and the likelihood of intracellular freezing. *Journal of General Physiology* **14**, 347-369 (1963).

Mazur, P. Theoretical and experimental effects of cooling and warming velocity on the survival of frozen and thawed cells. *Cryobiology* **2**(4), 181-92 (1966).

Mazur, P. The role of intracellular freezing in the death of cells cooled at supraoptimal rates. *Cryobiology* **14**, 251-272 (1977).

Mazur P. Freezing of living cells: mechanisms and implications. *Amer. J. Physiol.* **247**, C125-C142 (1984).

McGrath, J.J., Cravalho, E.G., and Huggins, C.E. An experimental comparison of intracellular ice formation and freeze-thaw survival of Hela S-3 cells. *Cryobiology* **12**, 540-550 (1975).

McGrath, J.J. Preservation of biological material by freezing and thawing. *In* "Heat Transfer in Medicine and Biology" (A Shitzer, and R.C. Eberhart, Eds.) Plenum, New York, 1985.

McGrath, J.J. Membrane transport properties. *In* "Low Temperature Biotechnology: Emerging Applications and Engineering Contributions" (J.J. McGrath and K.R. Diller, Eds.) pp. 271-330. ASME Press, New York, 1988.

McGrath, J.J. Low temperature injury processes. *In* "Advances in Bioheat and Mass Transfer: Microscale Analysis of Thermal Injury Processes, Instrumentation, Modeling, and Clinical Applications" ASME-HTD **268**, 125-132 (1993).

Meryman, H.T. Mechanics of freezing in living cells and tissues. *Science* **124**, 515-521 (1956).

Meryman H.T. The exceeding of a minimum tolerable cell volume in hypertonic suspension as a cause of freezing injury. *In* "The Frozen Cell" (G.E. Wolstenholme, M. O' Conner, Eds.) pp. 51-67. J. & A. Churchill, London, 1970.

Miller, J.P., and Selverston, A.I. Rapid killing of single neurons by irradiation of intracellularly injected dye. *Science* **206**, 702-704 (1979).

Morise, H., Shimomura, O., Johnson, F.H., Winant, J. Intermolecular energy transfer in the bioluminescent system. *Biochemistry* **13**(12), 2656-2662 (1974).

Muldrew, K., and McGann, L.E. Mechanisms of intracellular ice formation. *Biophys J.* **57**, 525-532 (1990).

Muldrew, K., Hurtig, M., Novak, K., Schachar, N., and McGann, L. Localization of freezing injury in articular cartilage. *Cryobiology* **31**, 31-38 (1994).

Nardid,O., Dyubko, T, and Repina, S. A comparative study of the effect of freeze-thawing on peripheral and integral membrane proteins. *Cryobiology* **34**, 107-113 (1997).

Netti, P.A., Berk, D.A., Swartz, M.A., Grodzinsky, A.J., and Jain, R.K. Role of extracellular matrix assembly in interstitial transport in solid tumors. *Cancer Research* **60**, 2497-2503 (2000).

Niswender, K.D., Blackman, S.D., Rhode, L., Magnuson, M.A., and Piston, D.W. Quantitative imaging of green fluorescent protein in cultured cells: comparison of microscopic techniques, use in fusion proteins, and detection limits. *J. Microbiol.* **180**, 109-116 (1995).

Nugent, L.J., and Jain, R.K. Pore and fiber-matrix models for diffusive transport in normal and neoplastic tissues. *Microvascular Research* **28**, 270-274 (1984).

Okabe, M., Ikawa, M., Kominami, K., Nakanishi, T., and Nishimune, Y. 'Green mice' as a source of ubiquitous green cells. *FEBS Lett* **407**, 313-319 (1997).

Papanek, T.H. in The Water Permeability of the Human Erythrocyte in the Temperature Range +25 C to -10 C, PhD dissertation, Massachusetts Institute of Technology (1978).

Papenfuss, H.D., Gross, J.F., Intaglietta, M., and Treese, F.A. A transparent access chamber for the rat dorsal skin fold. *Microvascular Research* **18**(3), 311-318 (1979).

Patterson, G.H., Knobel, S.M, Sharif, W.D., Kain, S.R., and Piston, D.W. Use of the green fluorescent protein and its mutants in quantitative fluorescence microscopy. *Biophysical Journal* **73**, 2782-2790 (1997).

Pegg, D.E. Viability assays for preserved cells, tissues, and organs. *Cryobiology* **26**, 212-231 (1989).

Prasher, D.C., Eckenrode, V.K., Ward, W.W., Prendergast, F.G., and Cormier, M.J. Primary structure of the *Aequorea* victoria Green Fluorescent Protein. *Gene* **111**, 229-233 (1992).

Prendergast, F.G., and Mann, K.G. Chemical and physical properties of Aequorin and the Green Fluorescent Protein isolated from *Aequorea forskalea. Biochemistry* **17**, 3448-3453 (1978).

Rabb, J.M., Renaud, M.L., Brandt, P.A., and Witt, C.W. Effect of freezing on the microcirculation capillary endothelium of the hamster cheek pouch. *Cryobiology* **11**(6), 508-18 (1974).

Rabin, Y., and Korin, E. An efficient numerical solution for the multi-dimensional solidification (or melting) problem using a microcomputer. *Int. J. Heat and Mass Transfer* **36**(3), 673-683 (1993).

Rabin, Y., and Shitzer, A. Exact solution to the one-dimensional inverse Stefan problem in non-ideal biological tissues. *Journal of Heat Transfer* **117**, 425-431 (1995).

Rabin, Y., and Shitzer, A. Combined solution of the inverse Stefan problem for successive freezing/thawing in non-ideal biological tissues. *JBME* **119**, 146-152 (1997).

Rabin, Y., Julian, T.B., Olson, P., Taylor, M.J., and Wolmark, N. Evaluation of post cryosurgery injury in a sheep breast model using the vital stain 2,3,5-triphenytetrazolium chloride. *Cryo-Letters* **19**, 255-262 (1998).

Rabin, Y., and Shitzer, A. Numerical solution of the multi-dimensional freezing problem during cryosurgery. *JBME* **120**, 32-37 (1998).

Rand R.W., Rand R.P., Eggerding F.A., Field M., DenBesten L., King W., and Camici S. Cryolumpectomy for breast cancer: an experimental study. *Cryobiology* **22**, 307-318 (1985).

Rand RW, Rand RP, Eggerding F, DenBesten L, King W. Cryolumpectomy for carcinoma of the breast. *Surg. Gynecol. Obstet.* **165**, 392-396 (1987).

Reite, O.B. Functional qualities of small blood vessels in tissue injured by freezing and thawing. *Acta. Physiol. Scand. (Suppl)* **63**, 111-120 (1965).
Riddell, S.R., Elliott, M., Lewinsohn, D.A., Gilbert, M.J., Wilson, L., Manley, S.A., Lupton, S.D., Overell, R.W., Reynolds, T.C., Corey, L., and Greenberg, P.D. T-cell mediated rejection of gene-modified HIV-specific cytotoxic T lymphocytes in HIV-infected patients. *Nature Medicine* **2**(2), 216-223 (1996).

Rizzuto, R., Brini, M., Pizzo, P. Murgia, M., and Pozzan, T. Chimeric green fluorescent protein as a tool for visualizing subcellular organelles in living cells. *Current Biology* **5** (6), 635-642 (1995).

Rizzuto, R., Brini, M., DeGiorgi, F., Rossi, R., Heim, R., Tsien, R.Y., and Pozzan, T. Double labelling of subcellular structures with organelle-targeted GFP mutants *in vivo*. *Current Biology* **6** (2), 183-8 (1996).

Roberts, K.P., Smith, D., Ozturk, H., Kazem, A., Pazhayannur, P., Hulbert, J.C., and Bischof, J.C. Biochemical alterations and tissue viability in AT-1 tumor tissue after *in vitro* cryo-ablation. *Cryo-letters* **18**, 241-250 (1997).

Rubinsky B., and Ikeda M. A cryomicroscope using directional solidification for controlled freezing of a biological material. *Cryobiology* **22**, 55-68 (1985).

Rubinsky, B., Lee, C.Y., Bastacky, J., and Hayes, T.L. The mechanism of freezing in biological tissue: the liver. *Cryo-letters*, **8**, 370-381 (1987).

Rubinsky, B., and Pegg, D. A mathematical model for the freezing process in biological tissue. Proceedings of the Royal Society (1988).

Rubinsky, B. The energy equation for freezing of biological tissue. *Journal of Heat Transfer* **111**, 988-997 (1989).

Rubinsky, B., Lee, C.Y., Bastacky, J., and Onik, G. The process of freezing and the mechanism of damage during hepatic cryosurgery. *Cryobiology* **27**, 85-97 (1990).

Rubinsky B., and Onik G. Cryosurgery: advances in the application of cold to medicine. *Int. J. of Refrigeration* **14**, 190-199 (1991).

Scandurra, R., Consalvi, V., Chiaraluce, R., Politi, L., and Engel, P. Protein stability in extremophilic archaea. *Frontiers in Bioscience* **5**, d787-795 (2000).

Schuder, G., Vollmar, B., Richter, S., Pistorus, G., Fehringer M., Feifel, G., and Menger, M.D. Epi-Illumination fluorescent light microscopy for the *in vivo* study of rat hepatic microvascular response to cryothermia. *Hepatology* **29** (3), 801-808 (1999).

Schuder, G., Pistorius, G., Fehringer, M., Feifel, G., Menger, M.D., and Vollmar, B. Complete shutdown of microvascular perfusion upon hepatic cryothermia is critically dependent on local tissue temperature. *Br. J. Cancer* **82**(4), 794-799 (2000).

Schwartz, G.J., and Diller, K.R. Osmotic Response of Individual Cells During Freezing. II. Membrane Permeability Analysis. *Cryobiology* **20** (1983).

Schwartz, G.J., and Diller, K.R. Analysis of the water permeability of human granulocytes at subzero temperatures in the presence of ice. *JBME* **105**, 360-366 (1983).

Shabana, M., and McGrath, J.J. Cryomicroscope investigation and thermodynamic modeling of the freezing of unfertilized hamster ova. *Cryobiology* **25**, 338-354 (1988).

Shepherd J.P., and Dawber R.P.R. Wound healing and scarring after cryosurgery. *Cryobiology* **21**, 157-169 (1984).

Sherban, K.D. Application and analysis of a microscope diffusion chamber. M.S. Thesis, Mechanical Engineering Department, Michigan State University, 1987.

Shimura, O. Structure of the chromophore of *Aequorea* Green Fluorescent Protein. *FEBS Letters* **104** (2), 220-222 (1979).

Silvares, O.M., Cravalho, E.G., Toscano, W.M., and Huggins, C.E. The thermodynamics of water transport from biological cells during freezing. ASME Journal of Heat Transfer **97**, 582-588 (1975).

Sjostrom, B., Weatherly-White, R.C.A., and Paton, B.C. Experimental studies in cold injury I. The individual response to a standard cold environment. *JSR* **IV** (1), 12-16 (1964).

Smith, D.J., Fahssi, W.M., Swanlund, D.J., and Bischof, J.C. A parametric study of freezing injury in AT-1 rat prostrate tumor cells. *Cryobiology* **39**, 13-28 (1999).

Snider, R.L., and Porter, J.M. Treatment of experimental frostbite with intra-arterial sympathetic blocking drugs. *Surgery* **77**(4), 557-561 (1975).

Steponkus P.L., Dowgert M.F., and Gordon-Kamm W.J. Destabilization of the plasma membrane of isolated plant protoplasts during a freeze-thaw cycle: the influence of cold acclimation. *Cryobiology* **20**, 448-465 (1983).

Stripecke, R., del CarmenVillacres, M., Skelton, D.C., Stake, N., Halene, S., and Kohn, D.B. Immune response to green fluorescent protein: implications for gene therapy. *Gene Therapy* **6**, 1305-1312 (1999).

Swaminathan, R., Bicknese, S., Periasamy, N., and Verkman, A.S. Cytoplasmic viscosity near the cell plasma membrane: translational diffusion of a small fluorescent solute measured by total internal reflection-fluorescence photobleaching recovery. *Biophys. J.* **71**, 1140-1151 (1996).

Swaminathan, R., Hoang, C.P., and Verkman, A.S. Photobleaching recovery and anisotropy decay of green fluorescent protein GFP-S65T in solution and cells: cytoplasmic viscosity probed by green fluorescent protein translational and rotational diffusion. *Biophys. J.* **72**, 1900-1907 (1997).

Tatsutani, K., Rubinsky, B., Onik, G., and Dahiya, R. Effect of thermal variables on frozen human primary prostatic adenocarcinoma cells. *Urology* **48**(3), 441-447 (1996).

Terwillinger, T.C., and Solomon, A.K. Osmotic water permeability of human red cells. *J. Gen. Physiol.* **77**, 549-570 (1981).

Toscano, W.M., Cravalho, E.G., Silvares, O.M., and Huggins, C.E. The thermodynamics of intracellular ice nucleation in the freezing of erythrocytes. *ASME Journal of Heat Transfer* **97**, 326-332 (1975).

Toner, M., and Cravalho, E. Thermodynamics and kinetics of intracellular ice formation during freezing of biological cells. *J. Appl. Phys.* **67** (3), 1582-1593 (1990).

Toner, M., Tompkins, R.G., Cravalho, E.G., and Yarmush, M.L. Transport phenomena during freezing of isolated hepatocytes. *Amer. Inst. of Chem. Eng. J.* **38**, 1512-1522 (1992).

Toner, M. Nucleation of ice inside biological cells. *In* "Advances in Low-Temperature Biology, Vol. 2" pp. 1-51, JAI Press Ltd, 1993.

Tsien, R., Pozzan, T., and Rink, T.J. *J. Cell. Biol.* **94**, 325-334 (1982).

Ushiyama, M., Cravalho, E.G., Diller, K.R., Huggins, C.E., Intracellular water content of *Saccharomyces cerevisae* during freezing at constant cooling rates. *Cryobiology* **10**, 517 (1973).

Voller, V.R., and Prakash, C. A fixed grid numerical modeling methodology for convection-diffusion mushy region phase-change problems. *Int. J. Heat Mass Transfer* **30**(8), 1709-1719 (1987).

Voller, V.R., Brent, A.D., and Prakash, C. Modeling the mushy region in a binary alloy. *Appl. Math. Modeling*, **14**, 320-326 (1990).

Voller, V.R. An overview of numerical methods for solving phase change problems. *In* "Advances in Numerical Heat Transfer", 1995.

Wachsmuth, M., Waldeck, W., and Langowski, J. Anomalous diffusion of fluorescent probes inside living cell nuclei investigated by spatially-resolved fluorescence correlation spectroscopy. *J. Mol. Biol.* **298**, 677-689 (2000).

Wanner, G.A., Mica, L.L., Wanner-Schmid, E., Kolb, Stefan A., Hentze, H.; Trentz, O., and Wolfgang, E. Inhibition of caspase activity prevents CD95-mediated hepatic microvascular perfusion failure and restores Kupffer cell clearance capacity. *FASEB J.* **13**, 1239-1248 (1999).

Ward, W.W., and Cormier, M.J. An energy transfer protein in coelenterate bioluminescence. *J. Biol. Chem.* **274** (3), 781-788 (1979).

Ward, W.W. Properties of the coelenterate green-fluorescent protein. *In* "Bioluminescence and Chemiluminescence" (M.A. DeLuca and W.D. McElroy, Eds.) pp. 235-242. Academic Press, New York, 1981.

Waris, T., and Kyosala, K. Cold injury of the rat skin. *Scand. J. Plast. Reconstr. Surg.* **16**, 1-9 (1982).

Weatherly-White, R.C.A., Sjostrom, B., and Paton, B.C. Experimental studies in cold injury: the pathogenesis of frostbite. *J. Surg. Res.* **4** (1), 17-22 (1964).

Weatherly-White, R.C.A., Knize, D.M., Geisterfer, D.J., and Paton, B.C. Experimental studies in cold injury. V. circulatory hemodynamics. *Surgery* **66** (1), 208-214 (1969).

White, A.C. Liquid air: its application in medicine and surgery. *Med. Rec.* **56**, 109-112 (1899).

Whittaker, D.W. Ice crystals formed in tissues during cryosurgery. I. Light microscopy. *Cryobiology* **11**, 192-201 (1974).

Whittaker, D.W. Ice crystals formed in tissues during cryosurgery. II. Electron microscopy. *Cryobiology* **11**, 202-217 (1974).

Windoffer, R., Leube, R.E. Detection of cytokeratin dynamics by time-lapse fluorescence microscopy in living cells. *J. Cell Sci.* **112**, 4521-4534 (1999).

Woods, E.J., Liu, J., Derrow, C., Smith, F.O., Williams, D.A., and Critser, J.K. Osmometric and permeability characteristics of human placental /umbilical cord blood CD34+ cells and their applications to cryopreservation. *J. of Hematotherapy and Stem Cell Research* **9**, 161-173 (2000).

Wu, N., Ross, B., Gulledge, C., Klitzman, B., and Dewhirst, M. Differences in leucocyte-endothelium interactions between normal and adenocarcinoma-bearing tissues in response to radiation. *Br. J. Cancer Research* **69**, 883-889 (1994).

Xian, M., Honbo, N., Zhang, J., Liew, C-C., Karliner, J.S., and Lau, Y-F.C. The green fluorescent protein is an efficient biological marker for cardiac myocytes, *J. Mol. Cell. Cardiol.* **31**, 2155-2165 (1999).

Yang, F., Moss, L.G., and Phillips, G.N., Jr. The molecular structure of Green Fluorescent Protein. *Nature Biotechnology* **14**, 1246-1251 (1996).

Yang, H., Acker, J., Chen, A., and McGann, L. *In situ* assessment of cell viability. *Cell Transplantation* **7** (5), 443-451 (1998a).

Yang, M., Hasegawa, S., Jiang, P., Wang, X., Tan, Y., Chishima, T., Shimada, H., Moossa, A.R., and Hoffman, R.M. Widespread skeletal metastatic potential of human lung cancer revealed by Green Fluorescent Protein expression. *Cancer Res.* **58**, 4217-4221 (1998b).

Yang, M., Jiang, P., Sun, F., Hasegawa, S., Baranov, E., Chishima, T., Shimada, H., Moossa, A.R., and Hoffman, R.M. A fluorescent orthotopic bone metastasis model of human prostate cancer. *Cancer Res.* **59** (4), 781-6 (1999).

Yokoe, H., and Meyer, T. Spatial dynamics of GFP-tagged proteins investigated by local fluorescence enhancement. *Nature Biotechnology* **14**, 1252-1256 (1996).

Yuan, F., Leunig, M., Berk, D. A. and Jain, R. K. Microvascular permeability of albumin, vascular surface area, and vascular volume measured in human adenocarcinoma LS174T using dorsal chamber in SCID mice. *Microvascular Research* **45**, 269-289 (1993).

Zacarian, S.A., Stone, D., and Clater, M. Effects of cryogenic temperatures on microcirculation in the golden hamster cheek pouch. *Cryobiology* **7**, 27 (1970).

Zhang, G., Gurtu, V., and Kain, S. An enhanced green fluorescent protein allows sensitive detection of gene transfer in mammalian cells, *Biochemical and Biophysical Research Communications* **227**, 707-711 (1996).

Zhang, Z., Rydel, R.E., Drzewieke, G.J., Fuson, K., Wright, S., Wogulis, M., Audia, J.E., May, P.C., and Hyslop, P.A. Amyloid β-mediated oxidative and metabolic stress in rat cortrial neurons: no direct evidence for a role of H_2O_2 generation. *J. Neurochemistry* **67**, 1595-1606 (1996).

Zook, N., Hussmann, J., Brown, R., Russell, R., Kucan, J., Roth, A., and Suchy, H. Microcirculatory studies in frostbite injury. *Annals of Plastic Surgery* **40** (3), 246-255 (1998).